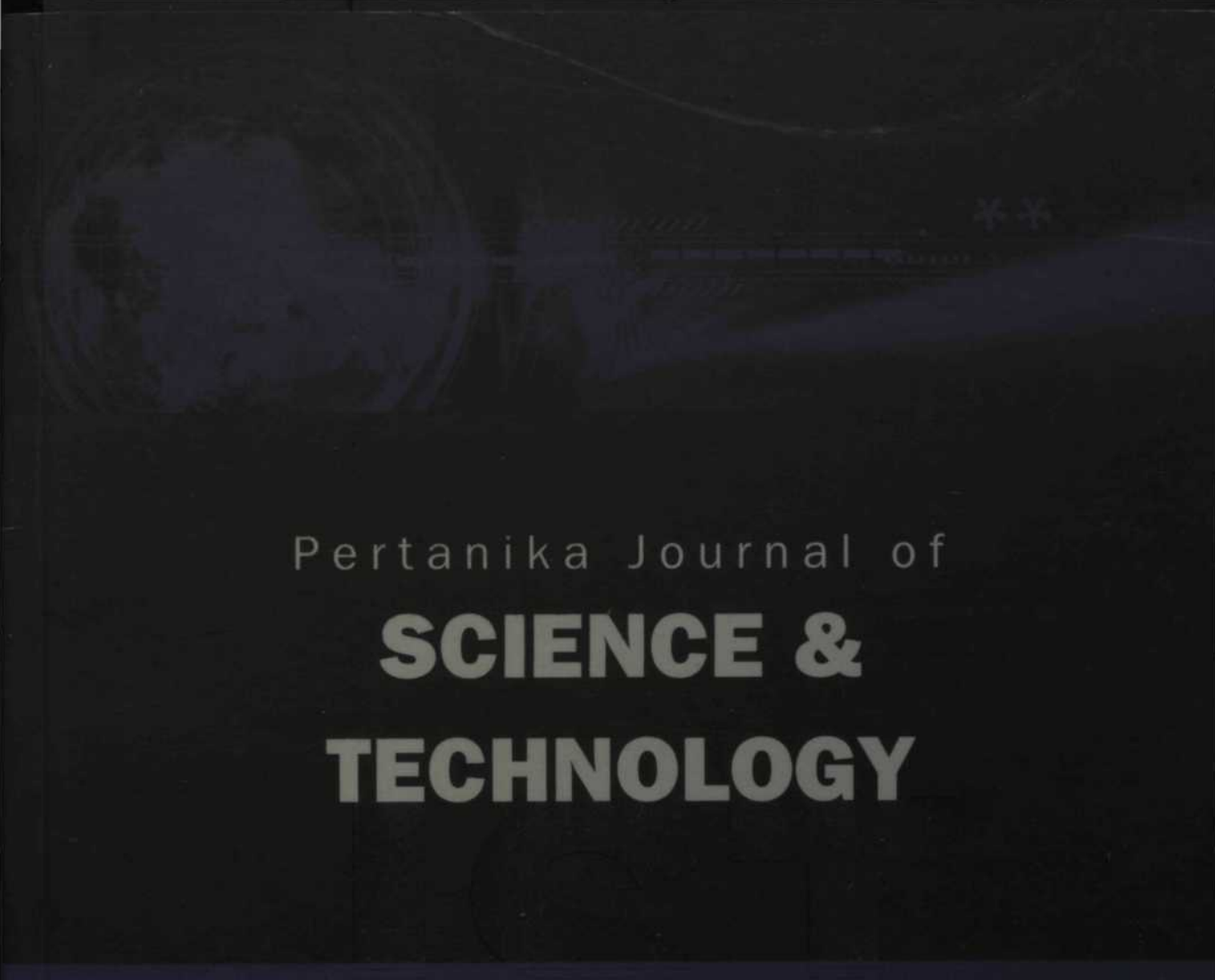

Pertanika Journal of

SCIENCE & TECHNOLOGY

VOLUME 17 NO. 2 • JUL. 2009

A scientific journal published by Universiti Putra Malaysia Press

About the Journal
Pertanika is an international peer-reviewed journal devoted to the publication of original papers, and it serves as a forum for practical approaches to improving quality in issues pertaining to tropical agriculture and its related fields. Pertanika Journal of Tropical Agricultural Science began publication in 1978. In 1992, a decision was made to streamline Pertanika into three journals to meet the need for specialised journals in areas of study aligned with the interdisciplinary strengths of the university. The revamped, Pertanika Journal of Science & Technology (JST) is now focusing on research in science and engineering, and its related fields. Other Pertanika series include Pertanika Journal of Tropical Agricultural Science (JTAS); and Pertanika Journal of Social Sciences and Humanities (JSSH).

JST is published in **English** and it is open to authors around the world regardless of the nationality. It is currently published two times a year i.e. in **January** and **July**.

Goal of Pertanika
Our goal is to bring the highest quality research to the widest possible audience.

Quality
We aim for excellence, sustained by a responsible and professional approach to journal publishing. Submissions are guaranteed to receive a decision within 12 weeks. The elapsed time from submission to publication for the articles averages 5-6 months. JST is an international journal indexed in EBSCO.

Future vision
We are continuously improving access to our journal archives, content, and research services. We have the drive to realise exciting new horizons that will benefit not only the academic community, but society itself.

We also have views on the future of our journals. The emergence of the online medium as the predominant vehicle for the 'consumption' and distribution of much academic research will be the ultimate instrument in the dissemination of the research news to our scientists and readers.

Aims and scope
Pertanika Journal of Science and Technology aims to provide a forum for high quality research related to science and engineering research. Areas relevant to the scope of the journal include: *bioinformatics, bioscience, biotechnology and bio-molecular sciences, chemistry, computer science, ecology, engineering, engineering design, environmental control and management, mathematics and statistics, medicine and health sciences, nanotechnology, physics, safety and emergency management*, and related fields of study.

Editorial Statement
Pertanika is the official journal of Universiti Putra Malaysia. The abbreviation for Pertanika Journal of Science & Technology is *Pertanika J. Sci. Technol.*

Editorial Office
Pertanika, Research Management Centre (RMC), 4th Floor, Administration Building
Universiti Putra Malaysia, 43400 Serdang, Selangor, Malaysia
Tel: +603 8946 6192, 8946 6185 • Fax: +603 8947 2075
E-mail: *ndeeps@admin.upm.edu.my*

Publisher
The UPM Press
Universiti Putra Malaysia
43400 UPM, Serdang, Selangor, Malaysia
Tel: +603 8946 8855, 8946 8854 • Fax: +603 8941 6172
penerbit@putra.upm.edu.my
URL : *http://penerbit.upm.edu.my*

Pertanika Journal of Science & Technology
Vol. 17 (2) Jul. 2009

Contents

ISSN: 0128-7680
Pertanika J. Sci. & Technol. **17 (2)**: 201 – 210 (2009)

Review Paper

Characterization of Fusion Welded Joint: A Review

Nur Azida Che Lah*, Aidy Ali and Napsiah Ismail
Department of Mechanical and Manufacturing Engineering,
Faculty of Engineering, Universiti Putra Malaysia,
43400 UPM, Serdang, Selangor, Malaysia
**E-mail: nurazida@yahoo.com*

ABSTRACT

Welding process is most widely used in joining components or structures in industry. Although welding is part of a larger category called metals joining, the weld itself still gives significant problems to engineers, researchers and manufacturers until today. Several widely used welding processes, such as the Metal Inert Gas (MIG), Tungsten Inert Gas (TIG), and Manual Metal Arc (MMA), were studied. In the present paper, the characterization of the macrostructure, microstructure, hardness and residual stress distribution are highlighted and discussed to achieve a better understanding of the welded quality which is crucial in determining the welded products.

Keywords: **Fusion welding, macrostructure, microstructure, hardness and residual stress**

ABBREVIATIONS

MIG	Metal Inert Gas
TIG	Tungsten Inert Gas
MMA	Manual Metal Arc
BM	base metal
HAZ	heat-affected zone
WM	weld metal
FZ	fusion zone
RS	residual stress

INTRODUCTION

Development in welding has been greatly investigated since 1800. During the late 1800s, gas welding and arc welding were developed and became a practical joining process. The variation and implementation of knowledge give a high value in the development of welding industry and therefore, provide new findings of welding applications, i.e. from conventional to the newest process such as friction and laser welding (Stephens *et al*., 2001; Suresh, 1998).

Significantly, versatility of welding provides maximum application process in joining metals such as stainless steel, low alloy steel and high strength steel. Appropriate welding control techniques, with a maximum penetration, commonly produced good weld qualities. Some examples of these applications include welding of industrial piping in petrochemical refineries, constructions and repair of nuclear power facilities, ship building, aerospace and ground vehicles.

Received: 30 April 2008
Accepted: 23 August 2008
*Corresponding Author

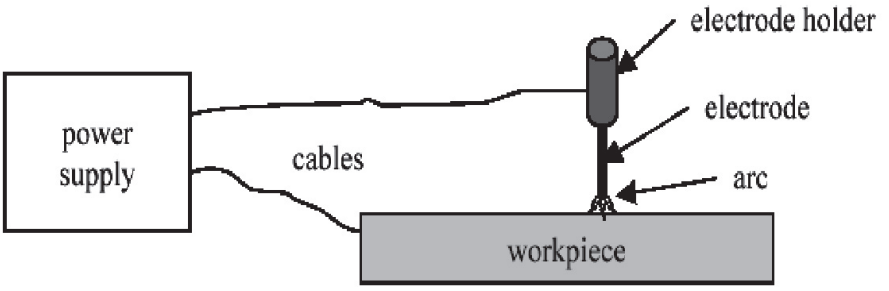

Fig. 1: Illustration of a simplified welding circuit (David et al., 2003)

Qualification of the welder and the structural code of welding procedures have been well covered by the standard welding specification to provide standardized specific information of welding procedure for the last 200 years. Engineers come out with a common code used in the welding industry, such as the American Welding Society Standard for Welding Procedure and Performance Qualification (AWS B2.1) which covers the qualification of the welder and welding procedure. In contrast, the AWS Structural Welding Code for steel provides a structural code for the use of steel welding procedure specification (Burgess, 1989).

OVERVIEW OF FUSION WELDING

Without any doubt, fusion welding is the oldest welding technique. It plays an important role in machine tools nowadays, particularly in the fabrication of joining engineering structures especially steels. Due to the advancement of technology, there are many ways in which the process can be carried out, but it is interesting to note that most of them involve the same parameters. For many years, engineers have been aware that most common type of fusion welding include manual metal arc (MMA), metal inert gas (MIG), and tungsten inert gas (TIG) welding (Weber, 2001).

Of course it is known now that the entire arc welding processes utilise variation of electrical circuits, but are still controlled by the same parameters. Power source cables are connected to the work piece and electrode. The power source creates a current through the welding circuit and an arc is created between the electrode and the work piece. *Fig. 1* shows a simple illustration of a simplified welding circuit (David *et al*., 2003).

CHARACTERISTIC OF FUSION WELDED JOINTS

In general, fusion welding consists of three distinct zones, namely the base metal (BM), heat-affected zone (HAZ) and weld metal (WM) or fusion zone (FZ), as depicted in *Fig. 2* (David, 2003).

WM is a part of a weldment which melts during welding process. It comprises a metal from the original work piece and may contain filler metal which is melted during the process. Near the weld area but outside the fusion weld is the HAZ. Volume of metal in this regime does not melt, but it is still being recognized as a part of the FZ. The HAZ area was affected mainly by the heat produced during the welding process. The third region is known as the BM or the parent plate region which is unaffected by any heating operation during the welding processes.

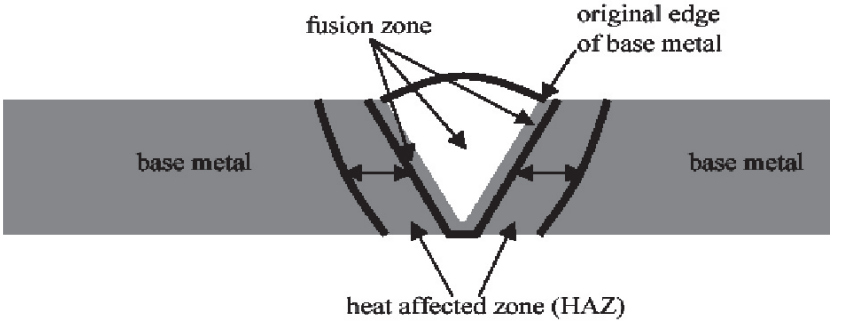

Fig. 2: Three zones of fusion welded joint (David et al., 2003)

MACROSTRUCTURE AND MICROSTRUCTURE OF FUSION WELDED JOINTS

In welding, there have been many attempts on observations of fusion welded joint microstructures by engineers, scientist and manufacturers. Yet again, it is well established that during welding process, the microstructure properties vary from region to region when the heat input interacts with the metal. For example, the macrostructure of the above mentioned three main regions for the low carbon steel fusion welded joint is as shown in *Fig. 3* (John *et al*., 2006).

As it progressed, instead of the three main recognized regions in fusion weld, the researchers again segregated the fusion weld region into six zones which could be discerned in the welded area and the BM adjacent to it, as illustrated in *Fig. 4*. These zones were created because they had been subjected to a kind of different degrees of heat treatment in the welding process. However, to simplify, one can group them into six basic zones, as follows:

1.	Deposited Metal Zone	Weld Metal Zone
2.	Fusion Zone	
3.	Grain Growth Zone	The Heat Affected Zone
4.	Grain Refinement Zone	
5.	Transition Zone	
6.	Unaffected Zone	Base Metal

The question remains is, how can an engineer differentiate them? Indeed, up to the best of authors' knowledge, the FZ was observed to normally consist of a fine dendritic network, as shown and labelled in *Fig. 5*. The edge of the FZ exhibits a more columnar structure growing in from the FZ boundary (Lefebvre *et al*., 2005).

The structure closed to WM in Mg/Al TIG welded joints is columnar crystal, which grows into the WM. There is an obvious boundary between the Mg substrate and WM, as shown in *Fig. 6a*. Moreover, *Fig. 6b* shows the columnar crystals which are closed to the WM, and the length of the crystals is almost half of the FZ width. The microstructure of the WM and the region were observed to mainly compose of the dendrite crystals, as illustrated in *Fig. 5* (Liu *et al*., 2007), and is also in agreement with the finding by Lefebvre *et al*. (2005).

In the previous research, the microstructure of the cross-sectional structures of the MIG welded joints was investigated. In that attempt, two kinds of specimens were used, namely the low carbon steel of 0.1C, and ferritic stainless steels of 18Cr-1Mo-Ti. The samples were welded with three types of welding material; the ferritic welding wire of 16Cr (W1), austenitic welding wire of 23Cr-12Ni (W2) and flux cored wire of 23Cr-12Ni (W3). It is interesting to discover that in each

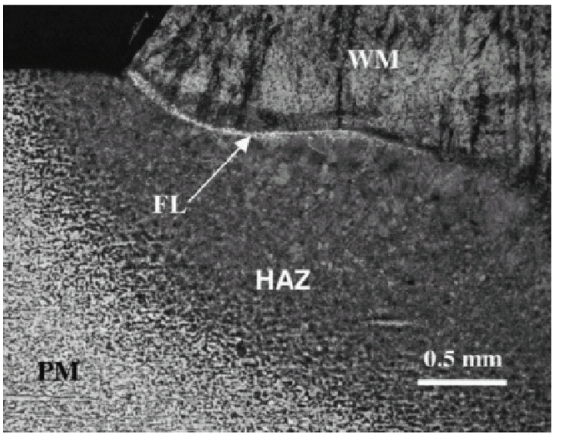

Fig. 3: Typical optical micrograph through welded section showing fusion line, FL, base metal or parent metal, PM, weld metal, WM, and heat affected zone, HAZ (John et al., 2006)

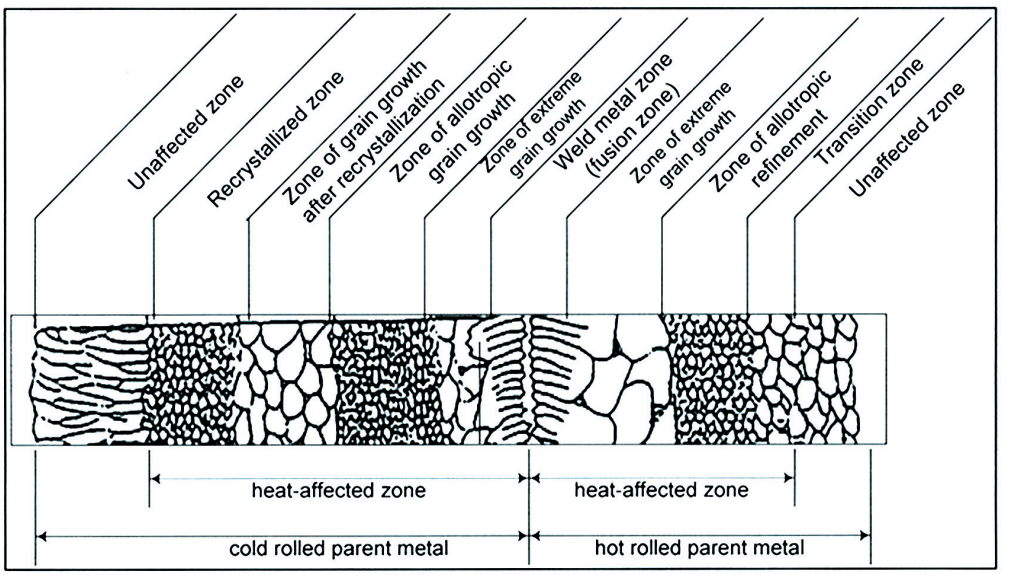

Fig. 4: Schematic diagram showing six micro-structural zones in the welded steel (Metallography, 2002)

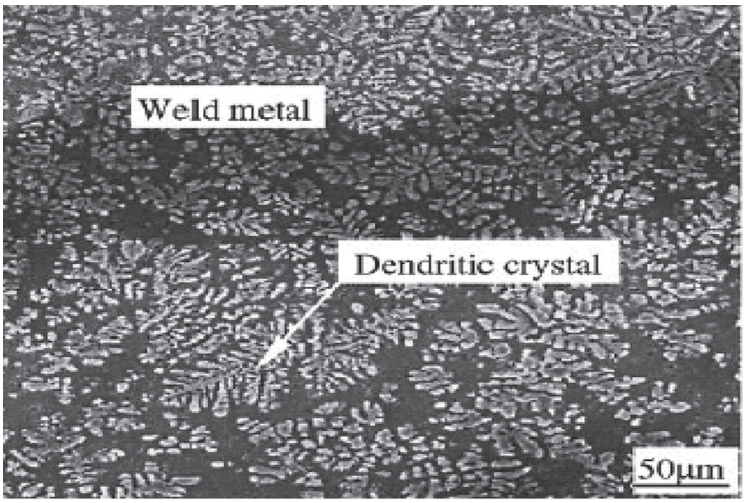

Fig. 5: The microstructure of weld metal for Mg/Al TIG welded joints (Peng Liu et al., 2007)

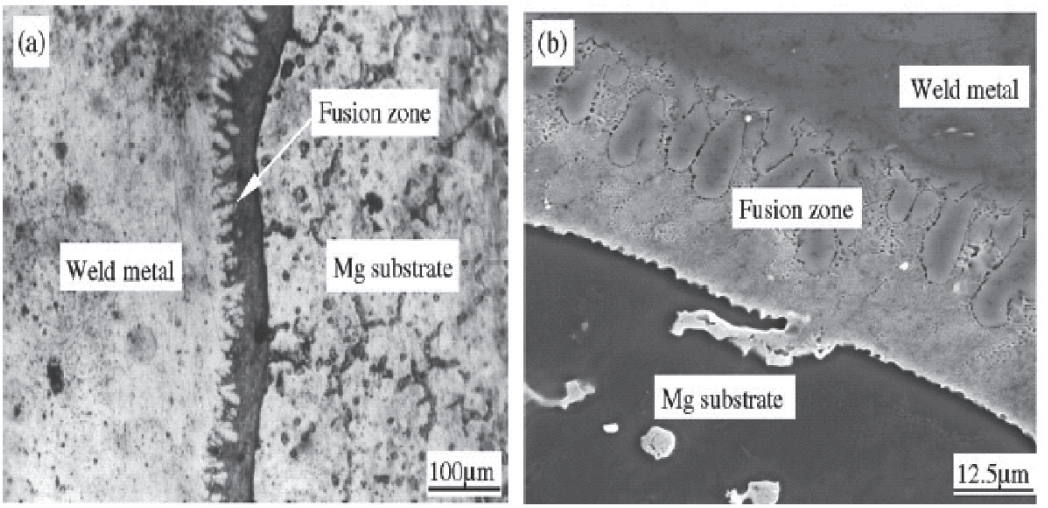

Fig. 6: The microstructure near the fusion zone of Mg side for Mg/Al TIG welded joint, (a) Metallography structure, (b) SEM structure (Peng Liu et al., 2007)

deposited zone, the columnar structure was developed from the HAZ of the BM. Nevertheless, the cell dendrite structure or oxidation inclusion admixed from the flux was also observed (Xiaoguang *et al*., 2003).

HARDNESS CHARACTERISATION

There have been numerous works in hardness characterisation. It is evident that the hardness distribution has strong influences on the strength and toughness of the welded joints (Liu and Bhole, 2002).

As can be noticed in *Fig. 7a*, the micro-hardness near the FZ of Mg side is higher than the Mg substrate region. In addition, *Fig. 7b* also shows the increase in the hardness of FZ between the WM and Al substrates. Their work indicated that the Mg and Al substrates, which are close to the FZ, are affected by the welding thermal cycle, and consequently the hardness increases gradually. Moreover, the brittleness phase with high hardness may be formed near the FZ (Liu *et al*., 2007).

The hardness value in the pressure vessel steel weld zones is indicated in *Fig. 8*. The hardness value in the HAZ region is higher than that in both BM and WM, which was also agreed by Liu *et al*. (2007), John *et al*. (2006) as well as Liu and Bhole (2002). According to John *et al*. (2006), a high hardness value indicates quite severe cooling conditions in the heat affected area in the low carbon steel weldment. These observations are different when compared to the experiment done by Itoh *et al*. (1989) who found that the Vickers hardness distributions were high in the WM, followed by the HAZ region and BM, respectively.

In previous work done by Itoh *et al*. (1989), the FZ region was clearly shown to present a minimum hardness value based on the hardness value obtained in the MIG weld, and it yielded a similar result. The hardness peak was noticed in the HAZ region, whereby the hardness level was greater than the BM (Lefebvre *et al.*, 2005).

Particularly, the HAZ is a transition zone on the welded joints and it is rationale to suggest that there is a risk of cracking along this zone. The HAZ readings were consistently higher than both the BM and WM readings, depending on the welding type (Yayla *et al*., 2006).

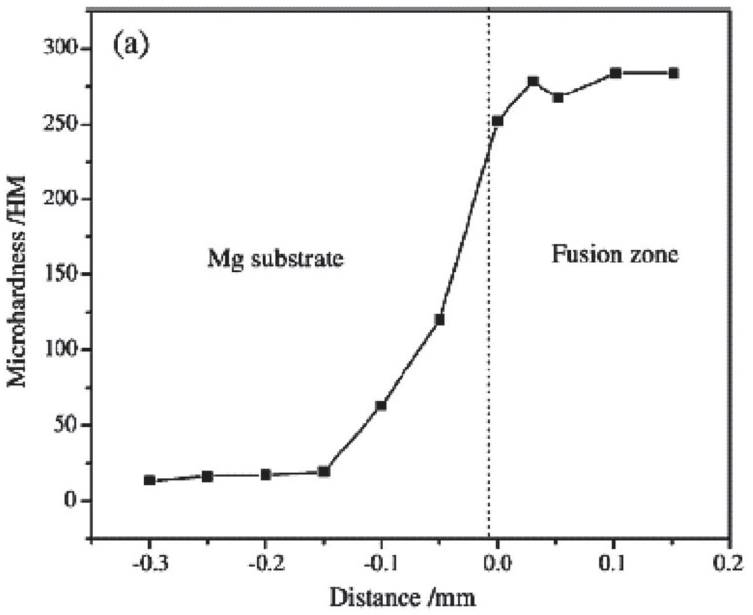

Fig. 7a: Micro-hardness for Mg fusion zone of Mg/Al TIG welded joint (Peng Liu et al., 2007)

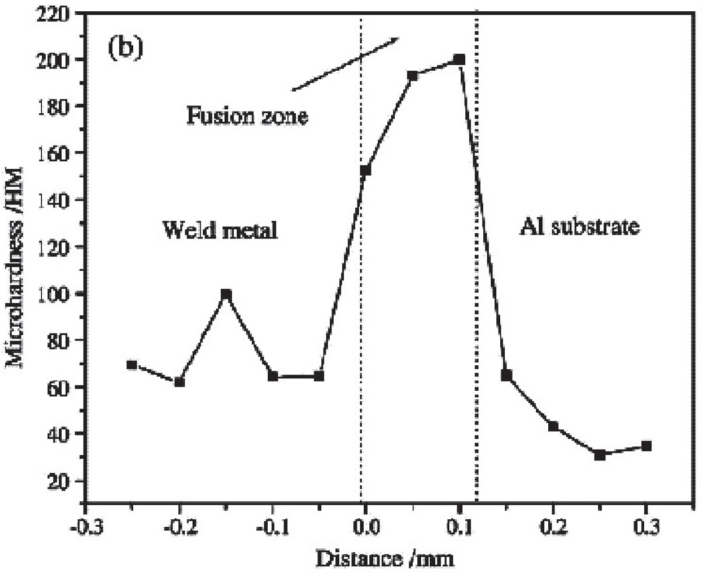

Fig. 7b: Micro-hardness for Al fusion zone of Mg/Al TIG welded joint (Peng Liu et al., 2007)

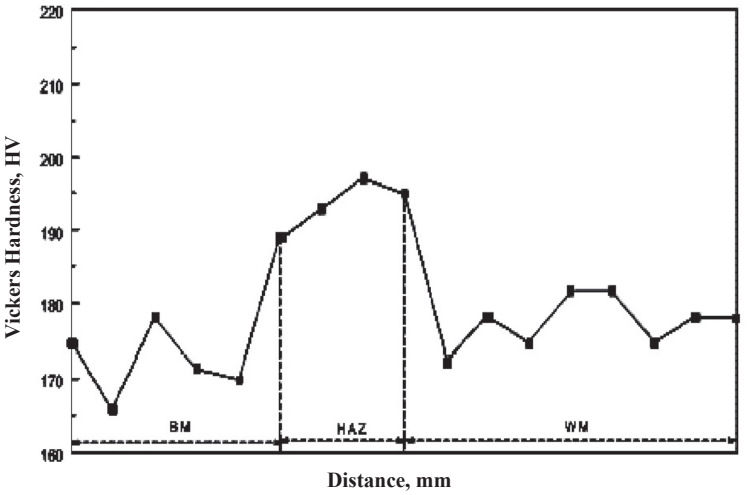

Fig. 8: Hardness distributions in pressure vessel steel weld (Liu and Bhole, 2002)

RESIDUAL STRESSES CHARACTERISATION

In welding, residual stresses (RS) are the stresses which remain after the welded members have cooled down to the normal temperature. The RS have also been called "self-equilibrating stresses" because they are in equilibrium within a part, without any external load. The tensile residual stresses have to be relieved to prevent cracking or fracture in the weld, which majority believed to have caused the crack to open. Several processes were used to relieve this stress; these include pre-heating, post-heating, as well as full annealing and peening (Stephens *et al*., 2001).

The RS which are formed in a weld pad are dependent on (i) thermal conditions like peak temperatures, rate of cooling and the temperature of the base material; (ii) material properties like coefficient of thermal expansion and modulus of elasticity; and (iii) restraint conditions, whether the material is restrained or left free to allow them to deform.

The RS distribution increases with the increase in the thickness of the weld pad for both low carbon steel and stainless steel weld pad. The increment is more pronounced in a low carbon steel weld pad due to the higher heat input during the welding process. This experiment shows that there is a correlation between two welding parameters, heat input and geometry of material which characterize the RS (Murugan *et al*., 2001).

In this study, the RS were measured using the Neutron Diffraction Technique for the low carbon steel and it was found that the maximum tensile residual stress was near the middle of the weld, as shown in *Fig. 9*. High RS may lead to the loss of performance in corrosion, fatigue and fracture (John *et al*., 2006).

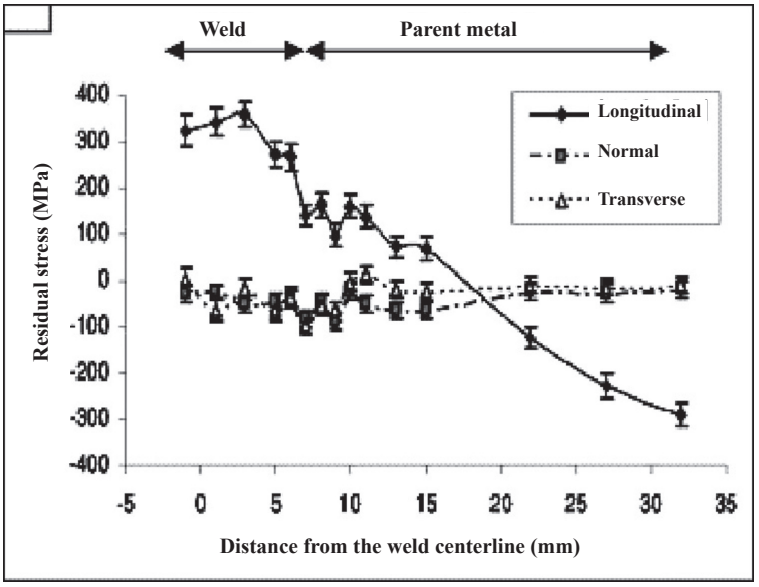

Fig. 9: The longitudinal, transverse and normal components of strains measured by Neutron Diffraction against distance from the weld centerline (John et al., 2006)

The RS distribution was also investigated in welded butt joints in carbon-manganese-silicon steel (SS41) and austenitic stainless steel (SUS304). The result revealed that the RS distribution was rather inhomogeneous in the longitudinal and transverse direction of the weld, as well as across the thickness of the weld, particularly for the transverse direction (Itoh *et al*., 1989).

It is clearly proven that the tensile residual stresses are located in the HAZ, in the area of WM. From these maximum values, the tensile residual stresses decrease in the BM adjacent to the HAZ area, which contains compressive residual stresses. As the distance from the weld area increases, the RS is then gradually changed into the initial stress state of the BM.

CONCLUSIONS

In this paper, the macrostructure, microstructure distribution, hardness and residual stresses of fusion welded joints were investigated and discussed to better understand and clarify the characterization of fusion welded joints. In the weld failure assessment, a profound knowledge in the weld characterization is required to determine the mechanisms of the weld failure and what can be done to prevent them. Without any doubt, a study and a deeper analysis should be performed through experimental and analytical methods as suggested from the past investigations. Undoubtedly, the inspections and proper precautions still need to be taken seriously to prevent such weld damages.

ACKNOWLEDGEMENT

The authors wish to thank the technical staff of the Department of Mechanical and Manufacturing Engineering in carrying out this research at Universiti Putra Malaysia.

REFERENCES

Burgess, N.T. (1989). *Quality Assurance of Welded Construction* (Second Edition). London: Elsevier Applied Science Publishers Ltd.

David, S.A., Babu, S.S. and Vitek, J.M. (2003). Welding: Solidification and microstructure. A hypertext-enhanced article. *JOM Journal, 55*(6), 14.

Itoh, Y.Z., Suruga, S. and Kashiwaya, H. (1989). Prediction of fatigue crack growth rate in welding residual stress field. *Journal of Engineering Fracture Mechanics, 33*(3), 397-407.

John, W.H.P., Anna, M.P., Ibrahim, I. and Trevor, R.F. (2006). Residual stresses evaluation in welds and implications for design for pressure vessel applications. *Journal of Pressure Vessel Technology*, *128,* 638-643.

John, W.H.P., Anna, P., Suraj, J. and Trevor, F. (2006). Residual stresses measurement by neutron diffraction and theoretical estimation in a single weld bead. *International Journal of Pressure Vessels and Piping*, *83,* 381-387.

Lefebvre, F., Ganguly, S. and Sinclair, I. (2005). Micromechanical aspects of fatigue in a MIG welded aluminium airframe alloy. *Material Science & Engineering A, 397,* 338-345.

Liu, C. and Bhole, S.D. (2002). Fracture behavior in a pressure vessel steel weld. *Journal of Materials and Design*, *23,* 371–376.

Metallography. (2002). Department of Mechanical and Production Engineering, National University of Singapore. *http://www.me.nus.edu.sg*

Murugan, S., Sanjai K.R., Kumar, P.V., Jayakumar, T., Raj, B. and Bose, M.S.C. (2001). Temperature distribution and residual stresses due to multipass welding in Type 304 stainless steel and low crabon steel weld pads. *International Journal of Pressure Vessels and Pipings, 78,* 307-317.

Peng Liu, Yajiang Li, Haoran Geng and Juan Wang. (2007). Microstructure characteristics in TIG welded joint of Mg/Al dissimilar materials. *Journal of Materials Letter, 61,* 1288–1291.

Stephens, R.I., Fatemi A., Stephens, R.R. and Fuchs, H.O. (2001). *Metal Fatigue in Engineering* (Second Edition). United States of America: John Wiley & Sons Inc.

Suresh, S. (1998). *Fatigue of Material* (Second Edition). United Kingdom: Cambridge University Press.

Weber, R. (2001). Here's why weld cracking is so crucial. *http://trailer-bodybuilders.com*

Xiaoguang, W., Hisayuki, I. and Kiyokazu, S. (2003). Fatigue and microstructure of welded joints of metal sheets for automotive exhaust system. *JSAE of Japan, 24,* 295-301.

Yayla, P., Kaluc, E. and Ural, K. (2007). Effects of welding processes on the mechanical properties of HY 8 steel weldments. *Materials and Design, 28,* 1898-1906.

ISSN: 0128-7680
Pertanika J. Sci. & Technol. **17 (2)**: 211 – 218 (2009)

Review Paper

Modelling of Residual Stress Relaxation: A Review

Omar Suliman Zaroog[1*], Aidy Ali[1,2], B.B. Sahari[1, 2] and Rizal Zahari[3]
[1]Dpartment of Mechanical and Manufacturing Engineering, Universiti Putra Malaysia,
[2]Institute of Advanced Technology (ITMA), Universiti Putra Malaysia,
[3]Aerospace Engineering, Faculty of Engineering, Universiti Putra Malaysia,
43400 UPM, Serdang, Selangor, Malaysia
[*]E-mail: omarzaroog@gmail.com

ABSTRACT

Compressive residual stress, induced by mechanical surface treatment, may relax during component operation life, due to thermal or mechanical mechanism. Fatigue life prediction for the components which have residual stress will be misled and inaccurately predicted the phenomenon of residual stress relaxation is not considered. Despite putting an effort on incorporating the residual stress relaxation, the issues remain concerned with the technical challenge of measuring and quantifying the magnitude of residual stress relaxation as well as redistribution during the loading cycling itself. In this paper, the residual stress relaxation and its models were reviewed and discussed to picture the best knowledge related to this topic, i.e. whether relaxation is a cause or an effect.

Keyword: **Residual stress, relaxation of residual stress, modelling of residual stress relaxation**

INTRODUCTION

Residual stresses are those stresses which exist along a cross-section of a component without applied external forces (Sigwart, 1957). These can be inherent in the product from the manufacturing process or induced in the finished product. Welding, machining, forming, hardening, casting and forging can lead to residual stresses in the product. Beneficial compressive residual stresses (which increase the fatigue life of the component) can be added to the component using several methods such as shot peening, laser peening, low plasticity burnishing, ultrasonic impact treatment and deep rolling.

Meanwhile, the fatigue life of metallic materials can be extended by the near-surface macroscopic compressive residual stresses (Juijerm and Altenberger 2006), as they retard fatigue crack initiation and crack growth (Niku-Lari, 1987; Altenberger, 2005; Wagner, 1999).

By using shot peening, Ali *et al*. (Aidy Ali, 2005; Aidy Ali *et al*., 2007a; Aidy Ali *et al*., 2007b; Aidy Ali and Brown, 2006) successfully improved the fatigue life of 2024-T351 Aluminium alloy aircraft friction stir welding joints. Yet again, the problem remains is the initial residual stress field inherent in or induced in the finished product may not remain stable during residual stressed component operation life. These residual stresses may decrease and redistribute, and this reduction is called relaxation. Residual stress relaxation can occur due to several reasons including thermal, static mechanical load, cyclic load and crack extension effects.

Received: 24 June 2008
Accepted: 28 January 2009
[*]Corresponding Author

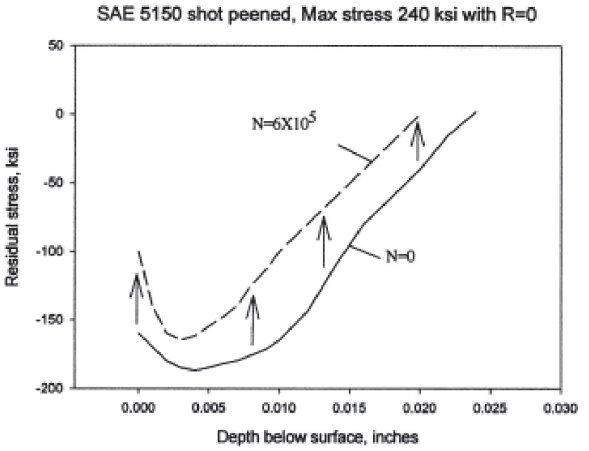

Fig. 1: Residual stress relaxation, before and after cyclic loading (10)

Many years ago, cyclic residual stress relaxation was observed by Mattson and Coleman (1954), and this is shown in *Fig. 1*. Nevertheless, the beneficial effects on fatigue life still remain because the relaxation is a partial relaxation of the compressive residual stress.

THERMAL RELAXATION

Leverant *et al*. (1979) found approximately 20% of the relaxation of the residual stresses induced by Shot Peening on Ti-6Al-4V caused by 600° F (316°C) thermal exposure alone. A primary approach for modelling the thermal stability of peening residual stresses, known as the Zener–Wert–Avrami function (V¨ohringer, 1983), has widely been used (V¨ohringer *et al*., 1984; Hoffmann *et al*., 1987; Schulze *et al*., 1993); it has a general form:

$$\frac{\sigma^{RS}(T,t)}{\sigma_0^{RS}} = \exp\left[-(At)^m\right] \tag{1}$$

Where σ^{RS}(T,t) is the residual stress after annealing at temperature T for time t, σ_0^{RS} is residual stress value before annealing, *m* is a numerical parameter dependent on the dominant relaxation mechanism (the parameter m has been found to change with aging temperature), A is a function of material and temperature according to

$$A = C\exp\left(-Q/kT\right) \tag{2}$$

Where *C* is a velocity constant, *Q* is the activation enthalpy for the relaxation process, and *K* is the Boltzmann constant. It is used to fit an experimental data for the surface thermal residual stresses. This approach does not appear to have been extended to subsurface changes in residual stresses. Therefore, individual experimental results cannot be regarded as being entirely general, because the thermal stability of peening residual stresses is dependent on several critical peening parameters, including coverage, intensity and the resulting cold work.

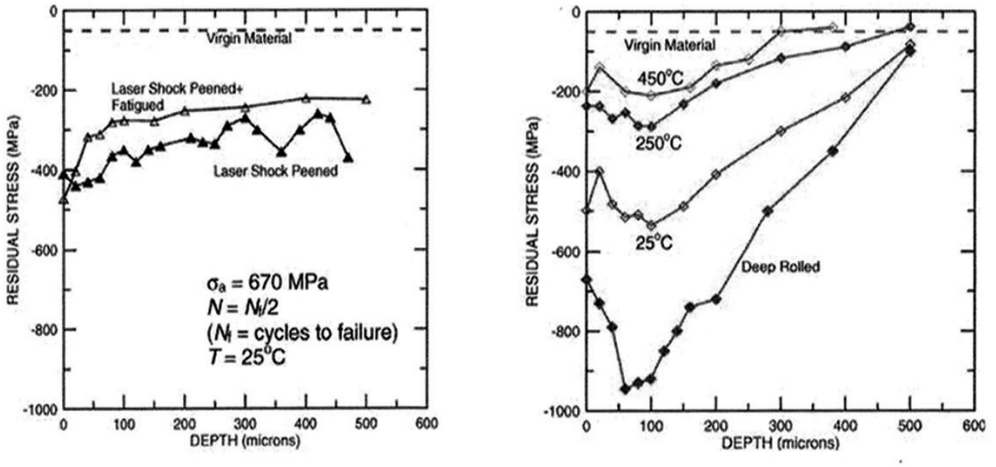

Fig. 2: Residual stress profiles, before and after fatigue cycling in Ti-6Al-4V for laser shock peening (left) and deep rolling (right) at various temperatures (17)

CYCLIC RELAXATION

If the summation of the applied stress and residual stress is more than the yield stress of the residual stress component, relaxation and redistribution of the residual stress will occur due to macroscopic plastic deformation (Han *et al*., 2002). It is worth to note that in repeated cyclic load, which is important for many mechanical components, the relaxation will also exist even when the individual mechanical load cycles do not cause deformation of macroscopic plastic.

After the first cycle in fatigue cycle for Ti-6Al-4V sheet, V¨ohringer *et al*. (1984) found a limited residual stress relaxation. For the same material, at several different temperatures for both deep rolling and laser shock peening, Nalla *et al*. (2003) showed relaxation of the residual stress profiles after fatigue cycling at load ratio of $R = -1$. As shown in *Fig. 2*, the room temperature cyclic relaxation was small for the laser shot peening and medium for deep rolling, but this was large for both processes at high temperature.

Zinn and Scholtes (1999) observed that the most relaxation changes occurred on the first cycle for the reversed bending of shot peening residual stress in several aluminium alloys (2017, 5083, 5754, 6082 and 7020), followed by a moderate relaxation (up to 30 to 40%) by the end of the fatigue life. Furthermore, a large relaxation of the compressive residual stress was found in the first fatigue cycle observed by several researchers (Taira and Murakami, 1960; Kodama, 1972; Wick *et al*., 2000; Qui and Wang, 1987), which was apparently due to the static effect, when the yield condition was less than that of the summation of residual stress and applied stress of the same sign of applied load. The followed gradual relaxation is due to true cyclic effects.

In another work by Wick *et al*. (2000), the measured surface residual stress for AISI 4140 steel after 1 cycle and after 10^4 cycles of fatigue loading at different stress amplitudes as shown in *Fig. 3*.

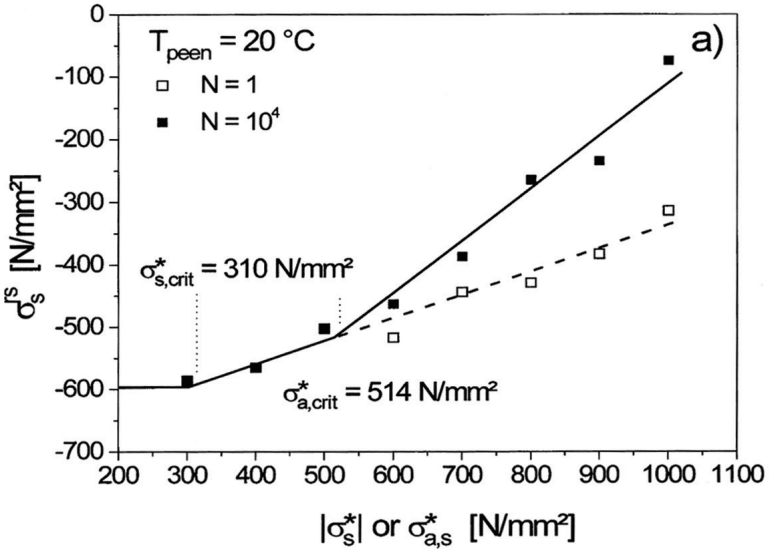

Fig.3: Surface residual stress, as a function of fatigue stress amplitude after 1 cycle and 10^4 cycles (21)

MODELLING OF RESIDUAL STRESS RELAXATION

The benefits of surface engineering residual stresses are reduced by cyclic relaxation of compressive residual stress (Mattson and Coleman, 1954). The cyclic relaxation is affected mainly by:

(1) Initial magnitude and gradient of the residual stress field and degree of cold working,
(2) Fatigue stress amplitude, mean stress ratio and number of cycles, and
(3) Material cyclic stress-strain response and degree of cyclic work hardening/softening (Zhuang and Halford, 2001)

Morrow and Sinclair (1958) conducted strain-controlled fatigue tests to quantify the cyclic residual stress relaxation and proposed a relationship between the mean stress and the load cycle, as follows:

$$\frac{\sigma_{mN}}{\sigma_{m1}} = \frac{\sigma_y - \sigma_a}{\sigma_{m1}} - \left(\frac{\sigma_a}{\sigma_y}\right)^b \log N \qquad (3)$$

Where σ_{mN} is the mean stress at the Nth cycle, and σ_{ml} is the mean stress at the first cycle. σ_a is the alternating stress amplitude, σ_y is the material yield strength, and b is a constant dependent on material softening and applied strain range $\Delta\varepsilon$. Eq. (3) is not applicable for load ratio R≠-1 because the surface residual stress is only analogous to the mean stress when the material is subjected to completely reversed loading. The experimental results were only supported by Eq. (3) for $N>10^6$ and $\sigma_{mN} < 20$ MPa.

A linear reduction in the residual stress as a function of the exponent of the number of cycles, N was proposed by Seungho Han *et al*. (2002) for welded steel components by the relationship between the ratio of the residual stress, after a single load cycle to the initial residual stress, $(\sigma_{res})_{1cycle} / (\sigma_{res})_{ini}$, and $\{(\sigma_{res})_{ini} + \sigma_{app})/\sigma_y\}$, as follows:

$$(\sigma_{res})_{relax}/(\sigma_{res})_{1cycle} = N^{k} \quad (4)$$

For $\{(\sigma_{res})_{ini} + \sigma_{app})/\sigma_y\} < 1$

$$(\sigma_{res})_{relax} = (\sigma_{res})_{in}.N^{-0.004} \quad (5)$$

For $\{(\sigma_{res})_{ini} + \sigma_{app})/\sigma_y\} \geq 1$,

$$(\sigma_{res})_{relax} = (\sigma_{res})_{ini}.(-1.6[\{(\sigma_{res})_{ini} + \sigma_{app})/\sigma_y\}]+2.6).N^{-0.004} \quad (6)$$

They found that the residual stress relaxed by the first cycle load was large and the amount of the residual stress relaxation by the repetition of cyclic load was small enough to be neglected in an application of fatigue strength estimation.

Jhansale and Topper (1973) suggested the following relationship between the mean stress and the load cycle to quantify the cyclic residual stress relaxation:

$$\sigma_{mN} = \sigma_{ml}(N)^{B} \quad (7)$$

where B is the relaxation exponent dependent on the material softening and applied strain range $\Delta\varepsilon$.

Kodama (1972) measured the residual stress decrease on the surface of the shot-peened specimens using the X-ray diffraction techniques, and proposed the following linear logarithm relationship:

$$\sigma^{re}{}_{N} = A + m \log N \quad (8)$$

where $\sigma^{re}{}_{N}$ is the surface residual stress after N cycles. A and m are material constants, which are depending on the stress amplitude σ_a. It was noted that the experimental data which supported the linear logarithm decreased the relationship between residual stress and the load cycles only after the first cycle.

Using the finite element method, Zhuang and Halford (2001) proposed an analytical model for the relaxation of residual stress. The model could predict the relaxation with R=0 and R=-I very close to that obtained by the finite element method. The model incorporates the initial cold work effect. An equation for the prediction of residual stress relaxation is therefore proposed:

$$\frac{\sigma_N^{re}}{\sigma_0^{re}} = A\left(\frac{\sigma_{\max}\sigma_a}{(C_w\sigma_y)^2}\right)^{m}(N-1)^{B} - 1 \quad (9)$$

where C_w is a parameter which accounts for the degree of cold working. Material constant m is dependent on the cyclic stress and strain response, where material constant A is also dependent on the cyclic stress and strain response. Constant B controls the relaxation rate versus loading cycles. The initial residual stress is $\sigma^{re}{}_{0}$. To obtain the effect of loading ratio R on the relaxation, Eq. (5) can therefore be rewritten in the following form:

$$\frac{\sigma_N^{re}}{|\sigma_0^{re}|} = A\left(\frac{2\sigma_a^2}{(1-R)(C_w\sigma_y)^2}\right)^{m}(N-1)^{B} - 1 \quad (10)$$

However, an experimental study on the cycle-dependent residual stress relaxation is still required to validate the analytical and numerical models for validation.

DISCUSSION

The modelling of the residual stress relaxation by Morrow and Sinclair (1958) and Jhansale and Topper (1973) [as in equations (3) and (7)] did not incorporate the stress ratio into account because in their axial tests, the mean stresses were dictated by the initially applied mean strain which was kept constant.

As noted earlier, Kodama's (1972) experimental data supported the linear logarithmic decrease relationship between the residual stress and the load cycles only after the first cycle. Based on the data presented in *Fig. 4*, the relaxation of the compressive residual stress in the first cycle is approximately 50%. However, Kodama's model did not predict this large amount of the first cycle relaxation.

For $\{(\sigma_{res})_{ini}+\sigma_{app})/\sigma_y\}<1$, the residual stress relaxation is influenced by the micro-plastic deformation in the micro-structural levels. This microstructure mechanism did not take into account in the Seungho Han's model.

Reducing the load amplitude in Zhuang and Halford (2001) analytical models will cause the relaxation to slow down. The model can be used to predict the residual stress relaxation trends, but it requires validation by an experimental study on the cycle-dependent residual stress relaxation.

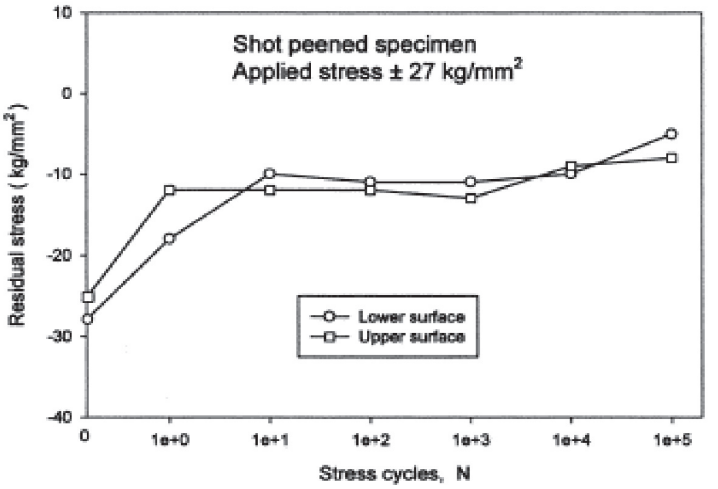

Fig. 4: Residual stress relaxation at the surface of a specimen (20)

CONCLUSIONS

In this review, it appeared that the residual stresses relaxed during the operation life of the component and this relaxation reduced the benefits of the compressive residual stresses. Despite the relaxation of the residual stresses, there are still benefits from the remaining residual stresses. There are no definitive explanations or models for all the relaxation phenomena for the cyclic relaxation. As a general observation, the large amount of relaxation occurred in the first few cycles. This was particularly due to static for the load with the same direction as the residual stress direction. After

the static relaxation, it then went to gradual cyclic relaxation. The numerical model proposed for the cyclic relaxation requires some further detailed study to evaluate its practicality. Experimental models are useful to characterize cyclic relaxation. Accordingly for an accurate life modelling, characterizing and employing a correct residual stress field is important.

ACKNOWLEDGEMENTS

The authors wish to thank the technical staff at the Department of Mechanical and Manufacturing Engineering, UPM, for their support.

REFERENCES

Aidy Ali. (2005). Improving the fatigue life of aircraft components by using surface engineering. PhD thesis, Sheffield University, UK.

Aidy Ali, Brown, M.W. and Gardiner, S. (2006). Microstructure and precipitates studies on 2024-T351 friction stir welding loints. FEIIC Seminar on Engineering and technology (SET 2006) (p. 363-373). 4-5th September 2006, Putrajaya, Malaysia.

Aidy Ali, An, X., Rodopoulos, C.A., Brown, M.W., O'hara P., Levers, A. and Gardiner, S. (2007a). The effect of controlled shot peening on the fatigue behaviour of 2024-T3 aluminium friction stir welds. *International Journal of Fatigue*, *29*(8), 1531-1545

Aidy Ali, Brown, M.W., Rodopoulos, C.A. and Gardiner, S. (2007b). Characterization of friction stir welding 2024-T351 Aluminium Alloy. *Journal of Failure Analysis and Prevention, ASM International, 6*(4), 83-96.

Altenberger, I. (2005). Deep rolling - The past, the present and the future. In *Proceedings of the 9th International Conference on Shot Peening (ICSP9)* (pp. 144–155). September 6-9, 2005, Paris, Marne la Vallée, France.

Han, S., Lee, T. and Shin, B. (2002). Residual stress relaxation of welded steel components under cyclic load. *Materials Technology (Steel Research), 73*(9), 414-420.

Hoffmann, J., Scholtes, B., V¨ohringer, O. and Macherauch, E. (1987). Thermal relaxation of shot peening residual stresses in the differently heat treated plain carbon steel Ck 45. In H. Wohlfahrt, R. Kopp and O. V¨ ohringer (Eds.), *Proceedings of the 3rd International Conference on Shot Peening (ICSP3)*. Garmisch-Partenkirchen, Germany, DGM.

Jhansale, H.R. and Topper, T.H. (1973). Engineering analysis of the inelastic stress response of a structural metal under variable cyclic strains. In *Cyclic Stress–Strain Behavior—Analysis, Experimentation, and Failure Prediction ASTM STP 519* (pp. 246–270). American Society for Testing and Materials.

Juijerm, P. and Altenberger, I. (2006). Residual stress relaxation of deep-rolled Al–Mg–Si–Cu alloy during cyclic loading at elevated temperatures. *Journal of Scripta Materialia, 55*(12), 1111-1114.

Kodama, S. (1972). The behaviour of residual stress during fatigue stress cycles. In *Proceedings of the International Conference of Mechanical Behaviour of Materials* (Vol. II, p. 111–118).

Leverant, G.R., Langer, B.S., Yuen, A. and Hopkins, S.W. (1979). Surface residual stresses, surface topography and the fatigue behaviour of Ti-6Al-4V. *Metallurgical and Materials Transactions, 10A,* 251–257.

Mattson, R.L. and Coleman, W.S. (1954). Effect of shot peening variables and residual stresses on fatigue life of leaf spring specimens. *Transactions, Society of Automotive Engineers, 62,* 546–556.

Morrow, J. and Sinclair, G.M. (1958). Cycle-dependent stress relaxation. In *Symposium on Basic Mechanisms of Fatigue, ASTM STP 237*. American Society for Testing and Materials.

Nalla, R.K., Altenberger, I., Noster, U., Liu, G.Y., Scholtes, B. and Ritchie, R.O. (2003). On the influence of mechanical surface treatments—deep rolling and laser shock peening—on the fatigue behavior of TI-6AL-4V at ambient and elevated temperatures. *Material Science Engineering, A355,* 216–230.

Niku-Lari, A. (Ed.). (1987). *Advances in Surface Treatments*. Oxford: Pergamon Press.

Qui, Q. and Wang, R. (1987). Changes in the state of the material by shot peening. In H. Wohlfahrt, R. Kopp and O. V¨ ohringer (Eds.), *Proceedings of the 3rd International Conference on Shot Peening (ICSP3)* (pp. 231–238). Garmisch-Partenkirchen, Germany, DGM Informationsgesellschaft Verlag, Oberursel.

Sigwart, H. (1957). Influence of residual stresses on the fatigue limit. In *Proceedings of the International Conference on Fatigue of Metals*. Institution of Mechanical Engineers, London, UK.

Schulze, V., V¨ ohringer, O. and Macherauch, E. (1993) Thermal relaxation of shot peening induced residual stresses in a quenched and tempered steel 42 Cr Mo 4. In D. Kirk (Ed.), *Proceedings of the 5th International Conference on Shot Peening (ICSP5)* (pp. 265–274). Oxford, UK.

Taira, S. and Murakami, Y. (1960). On the changes in residual stresses due to repeated stressing. In *Proceedings of the 3rd Japan Congress on Testing Materials* (pp. 52–55). Kyoto, Japan.

V¨ ohringer, O. (1983). Relaxation of residual stresses. In E. Karlsruhe, W. Macherauch and V. Hauk (Eds.), *Proceedings of European Conference on Residual Stresses* (pp. 47–80). DGM Information sgesellschaft,

V¨ ohringer, O., Hirsch, Th. and Macherauch E. (1984.) Relaxation of shot peening induced residual stresses of TiAl6V4 by annealing or mechanical treatment. In *Proceedings of the 5th International Conference on Titanium, Munich, FRG, 4*, 2203–2210.

Wagner, L. (1999). Mechanical surface treatments on titanium, aluminium and magnesium alloys. *Materials Science and Engineering, A 263(2, 15),* 210-216.

Wick, A., Schulze, V. and V¨ ohringer, O. (2000). Effects of warm peening on fatigue life and relaxation behaviour of residual stresses in AISI 4140 steel. *Material Science Engineering, A, A293,* 191–197.

Zhuang, W.Z. and Halford, G.R. (2001). Investigation of residual stress relaxation under cyclic load. *International Journal of Fatigue, 23,* S31–S37.

Zinn, W. and Scholtes, B. (1999). Mechanical surface treatments of lightweight materials effects on fatigue strength and near-surface microstructures. *Journal of Materials Engineering and Performance, 8,* 145–151.

ISSN: 0128-7680
Pertanika J. Sci. & Technol. **17 (2)**: 219 – 230 (2009)

Modelling of Precast Concrete Composite Slab Using Finite and Interface Elements

M.S. Jaafar, J.N. Wong, J. Noorzaei* and W.A. Thanoon
Department of Civil Engineering, Faculty of Engineering,
Universiti Putra Malaysia, 43400 UPM, Serdang, Selangor, Malaysia
**E-mail: jamal@eng.upm.edu.my*

ABSTRACT

This study presents an efficient finite element analysis technique which shows great versatility in modelling of precast composite flooring system subjected to static loadings. The method incorporates sliding and opening in the analysis of composite structures using the interface element which was specifically designed to simulate the actual behaviour at the interfaces between contacting materials. A three-dimensional finite element model of the precast composite slab which exhibits discontinuous behaviour was performed to demonstrate the potential and applicability of the proposed method of analysis. The results of the analysis demonstrate that the overall response of a discontinuous system to external loading is significantly affected by the bonding condition at the interfaces between the contacting materials.

Keywords: Finite element method, interface, isoparametric, composite, precast

INTRODUCTION

The viability of the finite element method, for the analysis and design of composite structures, has been proven by several researchers. For example, Tzamtzis *et al*. (2004a, b) model the interfacial behaviour between the brick and mortar, in case of masonry walls, under static and dynamic loadings. Different imperfect transmission conditions which model a thin intermediate layer, between two bonded materials with dissimilar material properties, were carried out by Mishuris *et al*. (2005) using interface element. Meanwhile, three-dimensional simulation of the crack in beams was carried out by Hanson *et al*. (2003) using interface element. The steel-concrete composite plate girders, under the action of shear and bending, were investigated by Baskar *et al*. (2003) using shell and interface elements through ABAQUS commercial software. A similar work was also reported by Nassif *et al*. (2004).

This investigation presents a computational model used for the discretisation of the composite flooring/roofing system. The slab unit is composed of precast and *in situ* concrete.

FORMULATION OF THE JOINT ELEMENT

Proposed finite element modelling:
The precast composite slabs are constructed into two layers, namely the precast and *in situ* layers. Each layer has different material properties.

Received: 6 July 2007
Accepted: 19 January 2009
*Corresponding Author

The following elements were used to discretize the precast composite slab:

i. Sixteen noded three-dimensional isoparametric finite elements to model the top and bottom layers
ii. Sixteen noded isoparametric interface element

Hence, this study was carried out to model each layer separately and to account for the interfacial behaviour between the layers, in which a special joint/interface element (sandwiched between the two sixteen noded isoparametric brick elements shown in *Fig. 1a*) was formulated. A brief formulation of this element (*Fig. 1*) is presented in the following discussion.

$$X = \sum_{i=1}^{n} N_i X_i;\ Y = \sum_{i=1}^{n} N_i Y_i;\ Z = \sum_{i=1}^{n} N_i Z_i \tag{1}$$

For corner nodes:

$$N_i = \frac{1}{4}(1 + \xi\xi_i)(1 + \zeta\zeta_i)(\xi\xi_i + \zeta\zeta_i - 1);\ i = \text{I, III, V and VII} \tag{2}$$

For midside nodes:

(a) $\xi = 0.0$

$$N_i = \frac{1}{2}(1 + \zeta\zeta_i)(1 - \xi^2);\ i = \text{II and VI} \tag{3}$$

(b) $\zeta = 0.0$–

$$N_i = \frac{1}{2}(1 + \xi\xi_i)(1 - \zeta^2);\ i = \text{IV and VIII} \tag{4}$$

$$U = \sum_{i=1}^{n} N_i U_i;\ V = \sum_{i=1}^{n} N_i V_i;\ W = \sum_{i=1}^{n} N_i W_i \tag{5}$$

where X, Y, Z and ξ, η, ζ are global and natural coordinate systems, respectively.

U, V and W are the displacement components with respect to global coordinate system.

n is the number of nodes.

N_i are the shape functions.

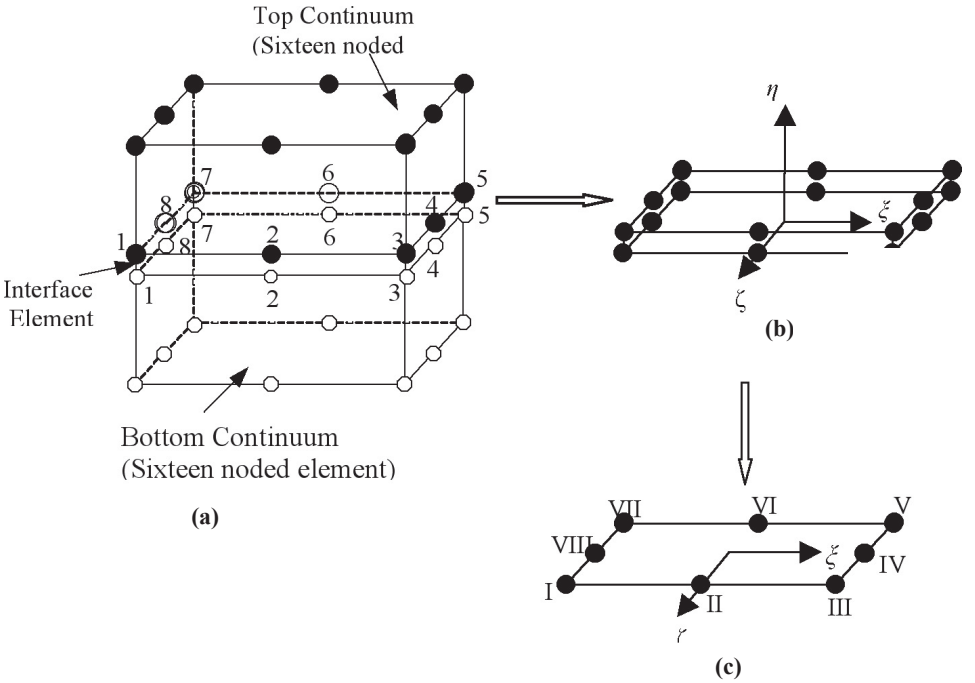

Fig. 1: Interface elements sandwiched between two horizontal layers

The interface nodes of the top and bottom continuum possess the same coordinates, that is zero thickness, and their relative displacements are given by:

$$\{\Delta\}=[I,-I]\{\delta\} \tag{6}$$

where $[I]$ = Identity matrix

Defining $[T] = [I, -I]$, so this can written as follows:

$$\{\Delta\} = [T]_{16*48} \quad \{\delta\}_{48*1} \tag{7}$$

Here, $\{\Delta\}$ is defined as:

$$\{\Delta U_1, \Delta V_1, \Delta W_1, ..., \Delta U_{VIII}, \Delta V_{VIII}, \Delta W_{VIII}\} \tag{8}$$

The present interface element, formulated for the use at the interface between two sixteen node isoparametric brick element (in ξ-ζ plane), and the typical parabolic interface element is shown in *Fig. 1b*. The pairs of 1-1, 2-2, …., 8-8 are usually close to each other.

$$\Delta U_I = U_2^t - U_2^b;\ \Delta V_I = V_2^t - V_2^b;\ \Delta W_I = W_2^t - W_2^b \tag{9}$$

Suffixes *t* and *b* denote the top and bottom continuum. Similar expression can be written for the other relative displacement, i.e. for node II, III, IV, ……, VIII. In the case of the interface element, the strains can be expressed as:

$$\{\varepsilon\} = \{\Delta U, \Delta V, \Delta W\} \tag{10}$$

$$\text{where } \Delta U = \Delta U = \sum_{i=1}^{n} N_i \Delta U_i;\ \Delta V = \sum_{i=1}^{n} N_i \Delta V_i\ ;\ \Delta W = \sum_{i=1}^{n} N_i \Delta W_i \tag{11}$$

i = I, II, III, IV, V, VI, VII and VIII

$$\begin{Bmatrix} \Delta U \\ \Delta V \\ \Delta W \end{Bmatrix} = \begin{Bmatrix} N_I & 0 & 0 & N_{II} & 0 & 0 & \cdots\cdots \\ 0 & N_I & 0 & 0 & N_{II} & 0 & \cdots\cdots \\ 0 & 0 & N_I & 0 & 0 & N_{II} & \cdots\cdots \end{Bmatrix}_{3*48} \{\Delta\}_{48*1} \tag{12}$$

i.e. $\{\varepsilon\} = [N]\{\Delta\}$ (13)

Using Eq. (7),

$$\begin{aligned} \{\varepsilon\} &= [N]_{3*16}[T]_{16*48}\{\delta\}_{48*1} \\ &= [B_J]_{3*48}\{\delta\}_{48*1} \end{aligned} \tag{14}$$

where $[B_J]$ = Shape function matrix for joint element.

The stress-strain relation is expressed as in standard form:

$$\{\sigma\} = [D]\{\varepsilon\} \tag{15}$$

In the case of interface element, elasticity matrix is presented as:

$$[D] = \begin{bmatrix} K_{nn} & 0 & 0 \\ 0 & K_{ss} & 0 \\ 0 & 0 & K_{ss} \end{bmatrix}_{3*3} \tag{16}$$

where K_{nn} and K_{ss} are the normal and shear stiffness, respectively.

The stiffness matrix for joint element is given by:

$$[K] = \int_v [B_J]^T [D][B_J] dv \tag{17}$$

DEVELOPMENT OF FINITE ELEMENT CODE

The finite element code, which was written by Noorzaei *et al*. (2003), was further modified by including the 16-noded joint element which modelled the contact/interfacial behaviour between the two 16-noded isoparametric brick elements, two 20-noded or one 16-noded and one 20-noded isoparametric brick elements. The program runs under a master MAIN. The overall flowchart of this finite element code is presented in *Fig. 2*.

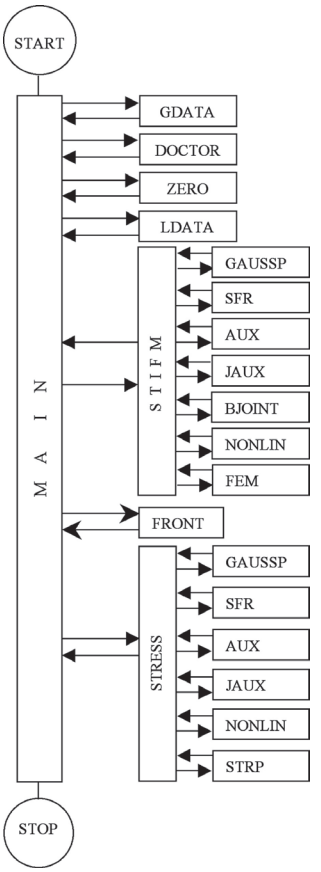

Fig. 2: Flow chart 3-D finite element code

PROBLEM ANALYSED

The plan view of the precast composite flooring system, together with the material properties for the precast layer and *in situ* layer, is shown in *Fig. 3*.

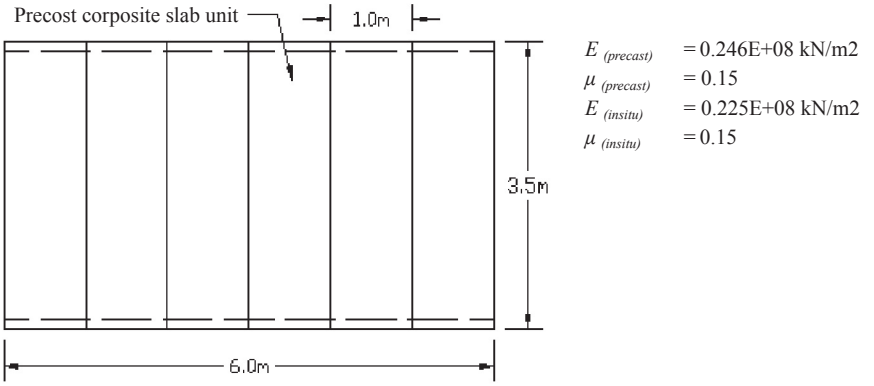

Fig. 3: Plan view of the precast composite flooring system

Only one unit of the precast composite slab was taken for the finite element analysis. For a single composite slab unit, the thickness of the precast layer is 75 mm and the cast *in situ* layer is 75 mm. As for the realistic finite element modelling of the composite slab unit, the interface element was used to account for the frictional behaviour between the two different layers of the composite slab modelled using 16-noded isoparametric brick element. *Fig. 4* shows the finite element mesh of the composite slab, with and without the interface elements.

In order to account for the composite action between the two layers, this example was analysed for different cases as presented in Table 1. Based on the investigation carried out by Pande *et al*. (1979) and Viladkar (1994), it was suggested that for full bond case $K_{ss} = K_{nn} = 10^6$-10^9 kN/m^2 could be assumed in absence of the experiment data. Meanwhile, for the no bond case, $K_{nn} = 10^6$-10^9 kN/m^2 and $K_{ss} = 0.0$.

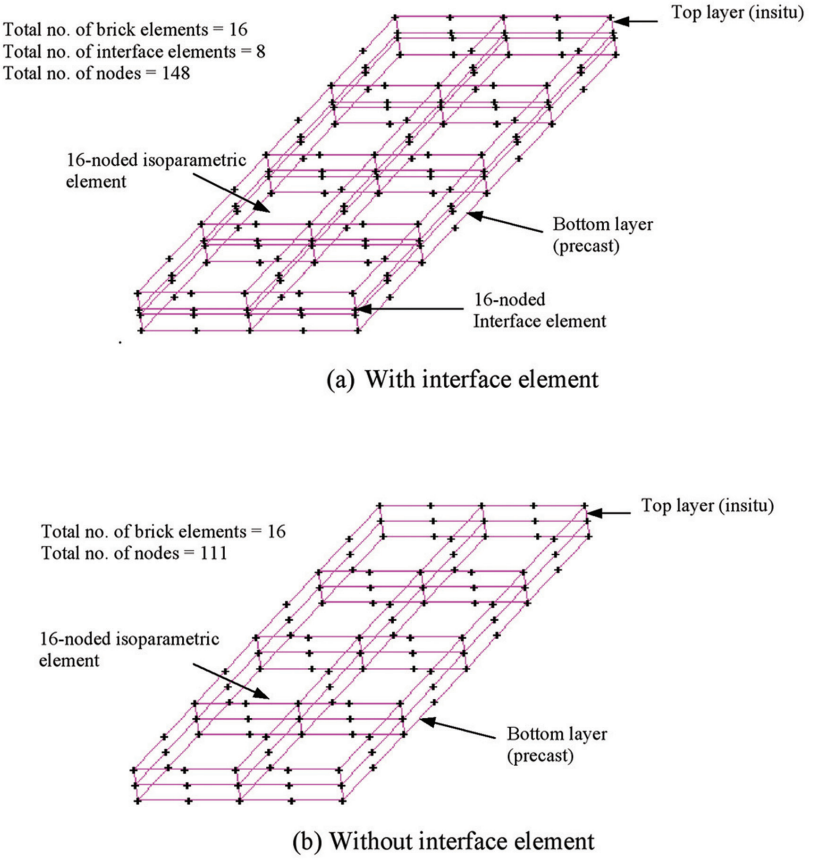

Fig. 4: Finite element mesh of the precast composite slab unit

TABLE 1
The value of normal and shear stiffness

Case No.	Normal Stiffness, K_{nn} (kN/m^2)	Shear Stiffness, K_{ss} (kN/m^2)
I	10e7	10e7
II	10e7	10e5
III	10e7	10e4
IV	10e7	100
V	10e7	50
VI	10e7	10
VII	10e7	0
VIII	without interface	without interface

DISCUSSION OF RESULTS

The structural behaviour of the composite slab has been discussed, with respect to displacements, strains, principal stresses and normal stresses.

Figs. 6 and *7* show the variations of vertical displacement of the precast composite slab along section A-A and B-B (*Fig. 5*), respectively. The variations of displacement for Case III, IV, V, VI, and VII gave almost the same results. It could also be seen from these plots that as the value of K_{ss} had reduced, while the deflections were increasing. Furthermore, the variations of displacement for Case I with high value of shear stiffness (K_{ss} = 10e7) are almost similar to the results where no interface elements (Case VIII) were involved.

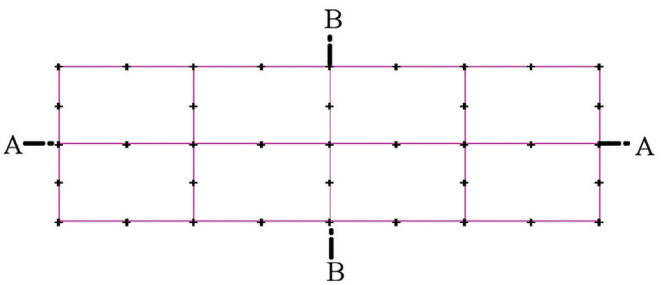

Fig. 5: Section lines for displacement analysis

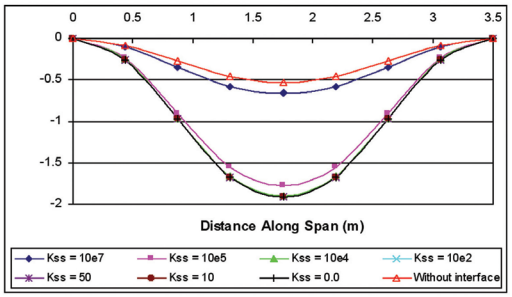

Fig. 6: Vertical displacement (A-A)

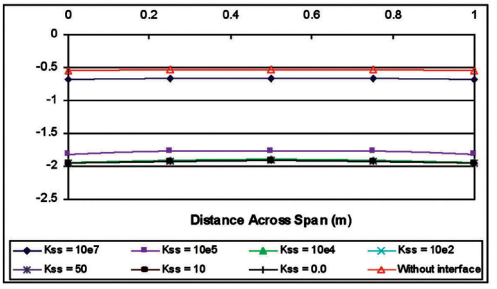

Fig. 7: Vertical displacement (B-B)

Strains

The complete composite action, with respect to strain variation along the depth (thickness) of the slab, is presented in this section. The strains are plotted along the depth of the composite slab at two Gaussian points, namely Point (I) and Point (II), as indicated in *Fig. 8* (i.e. the nearest Gauss point to C-C).

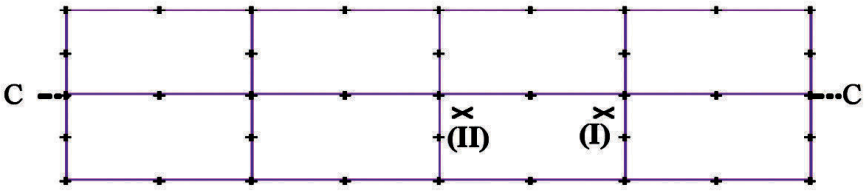

Fig. 8: Location for the strain analysis

The variation of the strain along the depth is shown in *Figs. 9* and *10*. It can be seen that case VIII shows a similar trend of behaviour as i.e. full bond case I when there is no interface, and the slab behaves as one unit. Meanwhile, when there is partial bond or no bond (case II to VII), the plots clearly shows that the two layers behave independently.

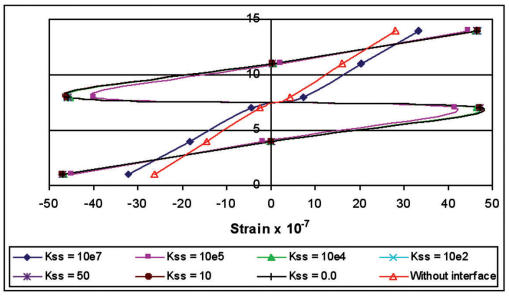

Fig. 9: Strain along depth (Point I)

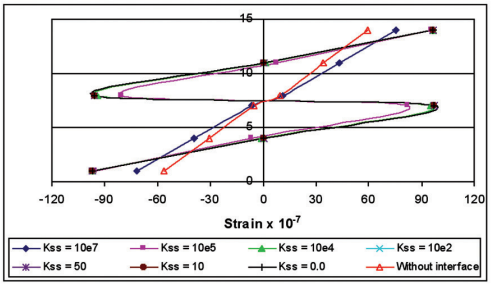

Fig. 10: Strain along depth (Point II)

Stresses

The variations of the maximum principal stresses (σ_1) and the minimum principal stresses (σ_3), to the nearest Gaussian integration point to section D-D and E-E (*Fig. 11*), are shown in *Figs. 12* to *15*. The above stresses were plotted for different layers, the *in situ* (top) and precast (bottom), which were plotted separately.

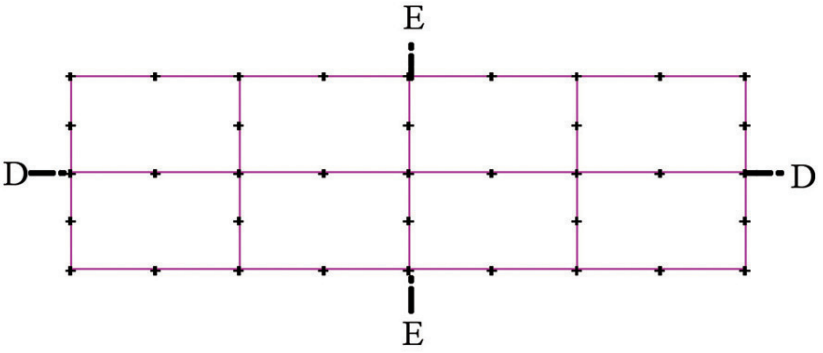

Fig. 11: Section lines for stress analysis

Figs. 12 and *13* show the patterns of the variation for the maximum stresses along section D-D and E-E. It is evident from these plots that Case I and Case VIII have resulted in the same behaviour. Similarly, it is also clear from these plots that both the layers have exactly opposite signs, and in the middle portion, the top layer is in compression while the bottom layer in tension.

The minimum principal stresses σ_3 (kN/m2) were plotted for the similar sections as σ_1 and these are illustrated in *Figs. 14* and *15* below.

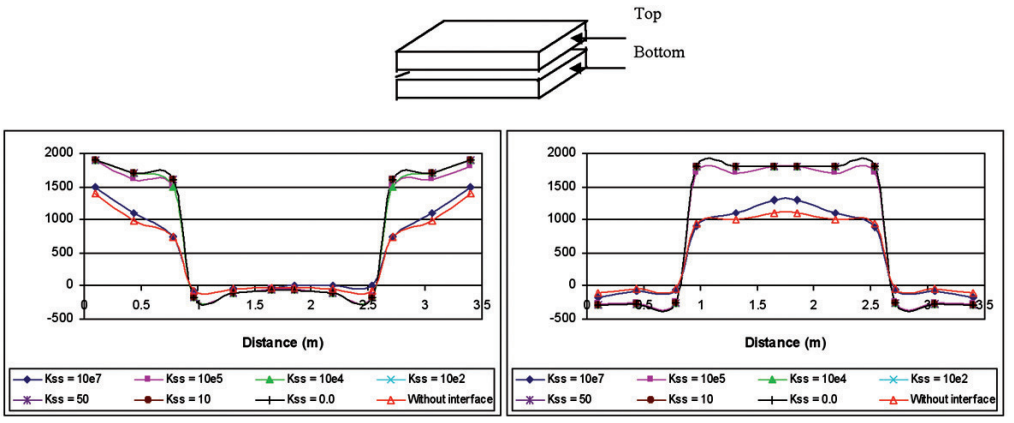

(a) Top Layer (b) Bottom Layer

Fig. 12: Variations of the maximum principal stress, σ_1 along Section D-D

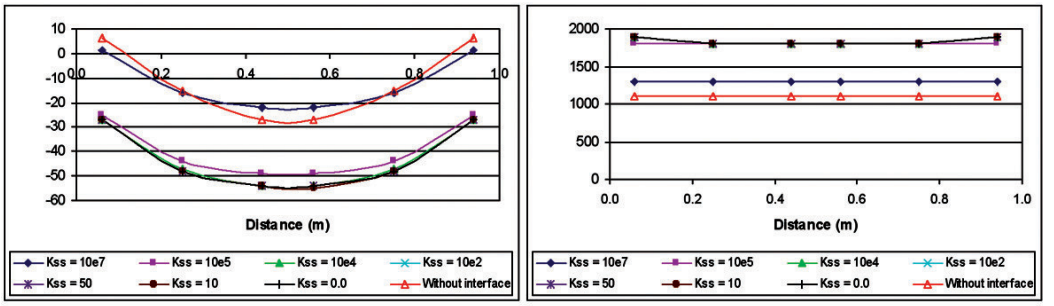

(a) Top Layer (b) Bottom Layer

Fig. 13: Variations of the maximum principal stress, σ_1 along Section E-E

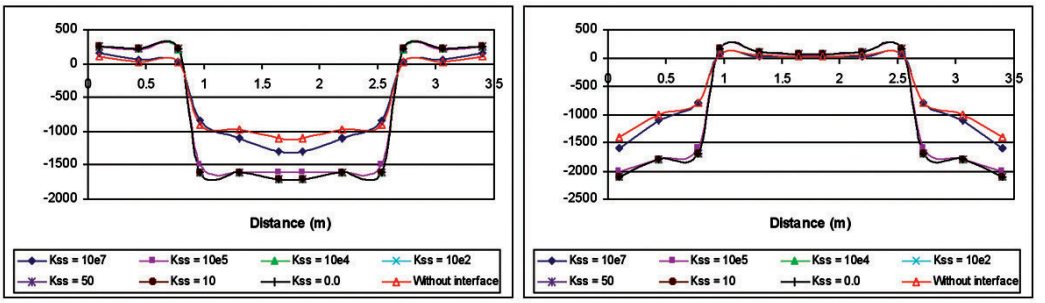

(a) Top Layer (b) Bottom Layer

Fig. 14: Variations of the minimum principal stress, σ_3 along Section D-D

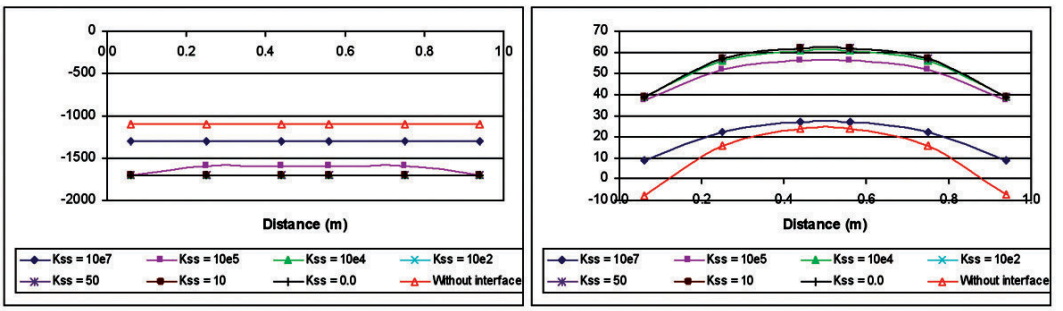

(a) Top Layer (b) Bottom Layer

Fig. 15: Variations of the minimum principal stress, σ_3 along Section E-E

THE STUDY OF THE NORMAL AND SHEAR STRESSES AT CONTACT SURFACE

In the formulation of the interface element, it was seen that there were one normal stress σ_n and two shear stresses τ_{n1} and τ_{n2}. In this study, the variation of the normal stress σ_n, along Section N-N and O-O (*Fig. 16*), are as shown in *Figs. 17* and *18*. These plots indicate that there is no separation between the layers and the complete contact is due to their nature of the loadings.

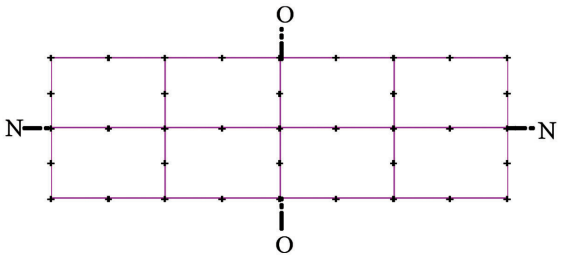

Fig: 16: Section lines for the interface element analysis

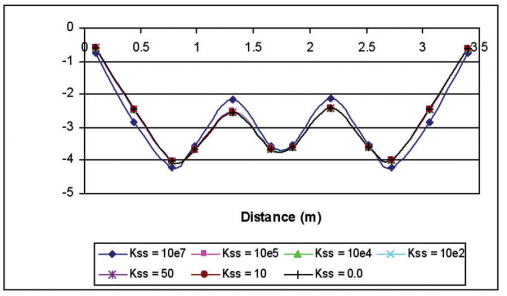

Fig. 17: Normal Stress, σ_n (N-N)

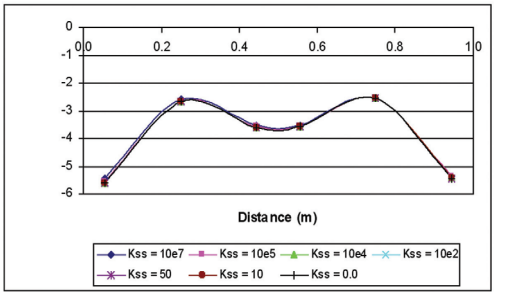

Fig. 18: Normal Stress, σ_n (O-O)

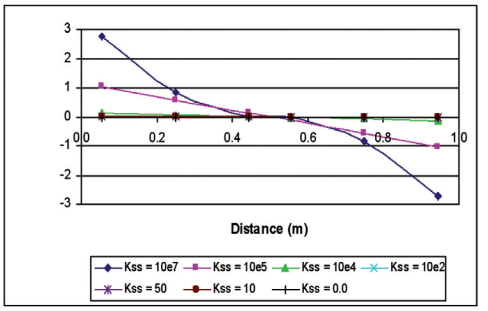

Fig. 19: Shear Stress, τ_{n1} (N-N)

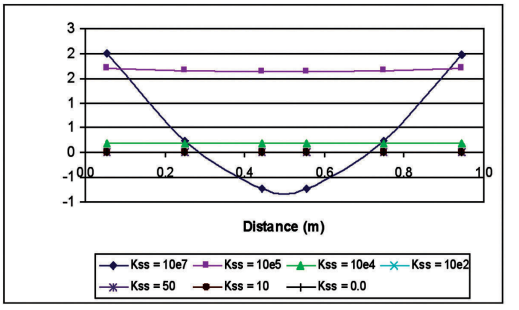

Fig. 20: Shear Stress, τ_{n1} (O-O)

Figs. 19 and *20* show the variations of the shear stress, τ_{n1} i.e. the shear stress in *x*-direction. From these plots, it is clear that the shear stress reduces when the value of shear stiffness is lower. As for the case where K_{ss} = 10 and K_{ss} = 0.0, the value of τ_{n1} is almost equal to zero and for the high value of K_{ss}, the linear variation follows the same path as that of the shear force

Figs. 21 and *22* below illustrate the variations of τ_{n2} (shear stress in z-direction), along the length of the slab (Section E-E) and across the slab (Section F-F). It can be stated that the resistance of the slab in the two-directions is according to the values of shear stiffness K_{ss}.

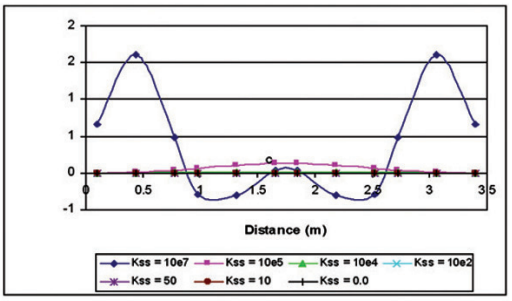

Fig. 21: Shear Stress, τ_{n2} (N-N)

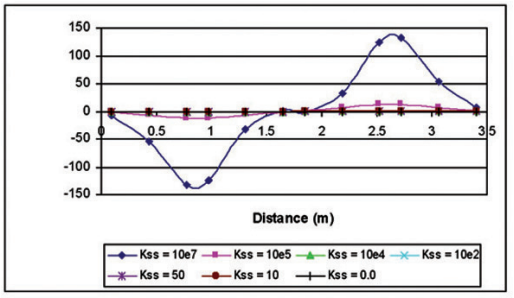

Fig. 22: Shear Stress, τ_{n2} (O-O)

CONCLUSIONS

In the case of the composite slab, the slab consists of two layers which are constructed at different stages (the precast layer in industry and the other layer cast at the construction site). In this situation, it is necessary to model the interfacial behaviour between the two layers, using the interface element. Therefore, this study has given a special attention to this particular type of slab by considering each layer separately and connecting them mathematically through the interface element. Based on the findings, it is revealed that the slab acts as a single unit in the case of full bond.

REFERENCES

Baskar, K. and Shanmugam, N.E. (2003). Steel-concrete composite plate girders subject to combined shear and bending. *Journal of Constructional Steel Research, 59*(4), 531-557.

Hanson, J.H., Bittencourt, T.N. and Ingraffea, A.R. (2004). Three-dimensional influence co-efficient method for cohesive crack simulations. *Engineering Fracture Mechanics, 71*(15), 2109-2124.

Mishuris, G. and Öchsner, A. (2005). Edge effects connected with thin interphases in composite materials. *Composite Structures*, *68*(4), 409-417.

Nassif, H.H. and Najm, H. (2004). Experimental and analytical investigation of ferrocement-concrete composite beams. *Cement & Concrete Composites*, *26*(7), 787-796.

Noorzaei, J., Jaafar, M.S., Thanoon, W.A. and Ghafouri, H.R. (2003). Software development for the analysis of arch dams under static and dynamic loads. *IEM Journal*, *64*(2), 31-39.

Pande, G.N. and Sharma, K.G. (1979). On joint/interface element and associated problems of numerical ill-conditioning. *International Journal Analysis and Numerical Method in Geomechanics*, *2*(3), 293-300.

Tzamtzis, A.D. and Asteris, P.G. (2004). FE analysis of complex discontinuous and jointed structural systems (Part 1: Presentation of the method – A state-of-the-art review). *Electronic Journal of Structural Engineering*, *4,* 75-92.

Tzamtzis, A.D. and Asteris, P.G. (2004). FE analysis of complex discontinuous and jointed structural systems (Part 2: Application of the method-development of a 3D model for the analysis of unreinforced masonry walls). *Electronic Journal of Structural Engineering*, *4,* 93-107.

Viladkar, Noorzaei, J. and Godbole, P.N. (1994). Modelling of interface for soil structure interaction studies. *International Journal of Computer and Structures, Pergamon, United Kingdom*, *52*(4), 765-779.

ISSN: 0128-7680
Pertanika J. Sci. & Technol. **17 (2)**: 231 – 243 (2009)

The Performance of Expectation Maximization (EM) Algorithm in Gaussian Mixed Models (GMM)

Mohd. Izhan Mohd. Yusoff[1*], Mohd. Rizam Abu Bakar[2] and Abu Hassan Shaari Mohd. Nor[3]

[1]*Operation Support Systems Program, Applied Research Division, Telekom Research & Development Sdn Bhd, TMR&D Innovation Centre, Lingkaran Teknokrat Timur, 63000 Cyberjaya, Selangor, Malaysia*

[2]*Department of Mathematics, Faculty of Science, Universiti Putra Malaysia, 43400 UPM Serdang, Selangor, Malaysia*

[3]*Faculty of Economics and Business, Universiti Kebangsaan Malaysia, 43600 UKM, Bangi, Selangor, Malaysia*

[*]*E-mail: izhan@tmrnd.com.my*

ABSTRACT

Expectation Maximization (EM) algorithm has experienced a significant increase in terms of usage in many fields of study. In this paper, the performance of the said algorithm in finding the Maximum Likelihood for the Gaussian Mixed Models (GMM), a probabilistic model normally used in fraud detection and recognizing a person's voice in speech recognition field, is shown and discussed. At the end of the paper, some suggestions for future research works will also be given.

Keywords: Expectation Maximization (EM), Gaussian Mixed Models (GMM), Box and Muller Transformation

INTRODUCTION

Every year, telecommunication companies register heavy loses due to fraud activities amounting to million of dollars. Vendors, seeing the above as an opportunity not to be missed, compete to provide data mining applications which could detect the said activity effectively using methods such as OLAP, deviation based outlier detection, Hidden Markov Model, and the model which became the focal area of this paper, the Gaussian Mixed Models (GMM).

GMM is best known in providing a robust speaker representation for the difficult task of speaker identification on *short-time speech spectra*, which is a cosine, transformed of log energy filter outputs from processed magnitude spectrum from a 20 ms short time segment of speech, by simulated me-scale filter-bank (Reynolds *et al*., 1995). Its function is further extended to detect fraud activities on daily number of calls and length of calls occurring during the office hours, the evening hours and the night hours for both national and international calls (Mohd Yusoff *et al*., 2006; Tanigushi *et al*., 1998).

Maximum likelihood estimation for GMM is difficult to find and the solution is Expectation Maximization (EM) algorithm. The EM algorithm was first introduced by Dempster *et al*. (1977) and since then, there has been a significant increase in terms of its usage, particularly in finding the

Received: 5 September 2007
Accepted: 27 February 2009
[*]Corresponding Author

Maximum Likelihood for probabilistic models (such as missing data, grouping, censoring, truncation, and finite mixtures). The main issue with respect to the EM algorithm is finding the right choice of initial parameters and the number of components. This particular issue or problem is illustrated in several examples in this paper.

The subsequent sections provide a brief introduction of the EM algorithm and GMM, generate the simulation univariate and multivariate data with clear and hidden components, present the results gathered from the GMM and EM algorithm where the emphasis given on the choice of the initial parameters and the number of components, and some suggestions for future research works.

The Gaussian Mixed Models (GMM) and Expectation Maximization (EM) Algorithm

Let $x \in R^d$ and K be the number of components where each component having its own prior probability (weight) a and probability density function with the mean μ and covariance Σ. All of them are mixed resulting in the following formula, which is also known as the Gaussian Mixed Models (GMM):

$$\sum_{i=1}^{K} a_i \phi(\mathrm{x} \mid \mu_i, \Sigma_i) = \sum_{i=1}^{K} a_i \frac{1}{\sqrt{(2\pi)^d \mid \Sigma_i \mid}} \exp\left(\frac{-(\mathrm{x}-\mu_i)^t \Sigma_i^{-1} (\mathrm{x}-\mu_i)}{2} \right) \tag{1}$$

where prior probability (weight) of component i that is a_i satisfy the constraint $\sum_{i=1}^{K} a_i = 1$.

For the case of voice recognition, assuming there are n number of speakers. The m number of samples were collected from each speaker. Equation (1) is derived for each sample, where its parameters were kept in the database for comparison purposes. Fraud detection would follow similar steps.

From equation (1), the likelihood function and log likelihood function by $L(\mathrm{X} \mid \theta) = \prod_{j=1}^{n} f(\mathrm{x}_j \mid \theta)$ and, $l(\mathrm{X} \mid \theta) = \log L(\mathrm{X} \mid \theta) = \sum_{j=1}^{n} \log\left(\sum_{i=1}^{K} a_i \phi(\mathrm{x}_j \mid \mu_i, \Sigma_i) \right)$ were defined, respectively. The maximum likelihood estimation (m.l.e) aimed at finding $\hat{\theta}$ which maximized $l(x|\theta)$, with respect to θ (Mardia *et al*., 1979). The expression $\log\left(\sum_{i=1}^{K} a_i \phi(\mathrm{x}_j \mid \mu_i, \Sigma_i) \right)$ in the log likelihood function is difficult to solve, and in order to overcome this problem, the Expectation Maximization (EM) algorithm was used.

In the EM algorithm, the distribution of X needs to be estimated in the sample space χ, but X can only be observed indirectly through Y in the sample space Y. In many cases, there is a mapping $x \rightarrow y(x)$ from χ o Y, and x is only known to lie in a subset of χ, denoted by $\chi(y)$, which is determined by equation $y = y(x)$. The distribution of X is parameterized by a family of distributions $f(x|\theta)$, with parameters $\theta \in \Omega$ or x. The distribution of Y, $g(y|\theta)$ is therefore:

$$g(y \mid \theta) = \int_{\chi(y)} f(x \mid \theta) dx \tag{2}$$

The EM algorithm aims at finding θ which maximizes $g(y|\theta)$ given an observed y. Let the function

$$Q(\theta' \mid \theta) = E(\log f(x \mid \theta') \mid y, \theta) \tag{3}$$

be the expected value of $\log f(x|\ \theta')$ given y and θ. The expectation was assumed to exist for all the pairs (θ', θ). In particular, it was assumed that $f(x|\theta) > 0$ for $\theta \in \Omega$.

EM Iteration

E-Step: Compute $Q(\theta|\ \theta^{(p)})$

M-step: Choose $\theta^{(p+1)}$ to be a value of $\theta \in \Omega$ that maximizes $Q(\theta|\theta^{(p)})$ (Dempster *et al*., 1977). In the case of GMM, it was defined that $Q(\theta'|\ \theta) = E\left[\log \prod_{i=1}^{n} a'_{y_i} \phi(\mathrm{x}_i|\mu'_{y_i}, \Sigma'_{y_i}) \middle| \mathrm{X}, \theta\right]$, where $y_i \in \{1,2,\ldots, K\}$, $y_i = k$ if the i^{th} sample was generated by the k^{th} mixture component. It was simplified using (among other) the Bayes formula which is $f(\theta|x) \propto f(x|\theta)P(\theta)$, where $f(\theta|x)$ = posterior probability, $f(x|\theta)$ = likelihood function, and $P(\theta)$ = prior probability (Tsay, 2005; Bilmes, 1997) to the following equations:

$$Q(\theta'|\theta) = \sum_{i=1}^{n}\sum_{k=1}^{K} p_{i,k} \log a'_k + \sum_{i=1}^{n}\sum_{k=1}^{K} p_{i,k} \log \phi(\mathrm{x}_i|\mu'_k, \Sigma'_k) \tag{4}$$

where

$$p_{ik} = \frac{a_k \phi(\mathrm{x}_i|\mu_k, \Sigma_k)}{\sum_l a_l \phi(\mathrm{x}_i|\mu_l, \Sigma_l)} \tag{5}$$

and

$$\phi(\mathrm{x}_i|\mu_k, \Sigma_k) = \frac{1}{\sqrt{(2\pi)^d |\Sigma_k|}} \exp\left(\frac{-(\mathrm{x}_i - \mu_k)^t \Sigma_k^{-1} (\mathrm{x}_i - \mu_k)}{2}\right) \tag{6}$$

The EM Iteration (for GMM)

E-Step:

Equation (5) is calculated.

M-Step:

The following formulas (derived from the Lagrange multipliers, $\frac{\partial Q}{\partial \mu_j} = 0$ and $\frac{\partial Q}{\partial \Sigma_j^{-1}} = 0$, respectively) are calculated. Further details are given in Appendix A.2.

$$a_j = \frac{1}{n}\sum_i p_{ij} \tag{7}$$

$$\mu_j = \frac{\sum_i p_{ij} \mathrm{x}_i}{\sum_i p_{ij}} \tag{8}$$

$$\Sigma_j = \frac{\sum_i p_{ij}(\mathrm{x}_i - \mu_j)(\mathrm{x}_i - \mu_j)^t}{\sum_i p_{ij}} \tag{9}$$

The above steps (i.e. E-step and M-step) were repeated until a convergence was achieved.

SIMULATION DATA

A program called "Simulate" was developed (using C++ language) to generate simulation data for equation (1) with the parameters as per given in Table 1 (taken from Everitt *et al*., 1981, with modifications) using Box and Muller Transformation (Box *et al*., 1958) and Equation (10). The simulation data were then labelled as "Sample1", "Sample2", "Sample3" and "Sample4", and their histograms are shown in *Figs. 1* and *2*.

$$z_j = \mu + (-2\sigma^2 \log u_j)^{\frac{1}{2}} \cos 2\pi u_{j+1}$$

$$z_{j+1} = \mu + (-2\sigma^2 \log u_j)^{\frac{1}{2}} \sin 2\pi u_{j+1}, u_j, u_{j+1} \sim U(0,1) \tag{10}$$

The "Simulate" program would generate one random number, denoted by U_1, from the uniform distribution *U(0,1)*, and check whether it was less than say a_i (i=1,2). If the answer is "yes", the two random numbers, denoted by U_2 and U_3, are generated from the uniform distribution *U(0,1)* and used in the computing equation (10), along with the corresponding μ_i and σ_{ii}, taken from Table 1. In this study, these steps were repeated until 1000 observations were obtained. For "Sample 4", apart from equation (10), the formulas given in Appendix A.1 (in the matrix format) were also used.

In *Fig. 1.1*, two humps are observed and these represent two components: $(\mu_1, \sigma_{11}) = (0.0, 1.0)$ and $(\mu_2, \sigma_{22}) = (2.0, 0.25)$. Both of them are well-separated, in which the observations for the latter component are grouped around the mean.

One would never expect to find the two components in *Fig. 1.2*. The histogram is dominated by the component $(\mu_1, \sigma_{11}) = (0.0, 1.0)$ due to the fact that $a_1 = 0.85$.

In *Fig. 1.3*, two humps are vividly displayed and they represent two components: $(\mu_2, \sigma_{22}) = (-1.0, 0.25)$ and $(\mu_3, \sigma_{33}) = (4.0, 4.0)$. The third component, $(\mu_1, \sigma_{11}) = (0.0, 1.0)$, is hidden from the view by the two components indicated earlier. The observations are grouped around the mean for the component $(\mu_2, \sigma_{22}) = (-1.0, 0.25)$.

The histograms in *Figs. 2.1* and *2.2* appear to split into two representing components $(\mu_{11}, \mu_{21}) = (5.01, 5.91)$ and $(\mu_{22}, \mu_{32}) = (2.78, 2.95)$, respectively; whereas *Figs. 2.3 and 2.4* into three representing components $(\mu_{13}, \mu_{23}, \mu_{33}) = (1.46, 4.2, 5.48)$ and $(\mu_{14}, \mu_{24}, \mu_{34}) = (0.25, 1.3, 1.98)$, respectively.

TABLE 1

a's, μ's, $\boldsymbol{\mu}$'s, $\boldsymbol{\sigma}$'s and $\boldsymbol{\Sigma}$'s for each sample used in the "Simulate" program. The number of observations generated by the program is given in the bracket

"Sample1" (N=1000)	$a_1=0.4$ $a_2=0.6$	$\mu_1=0.0$ $\mu_2=2.0$	$\sigma_{11}=1.0$ $\sigma_{22}=0.25$
"Sample2" (N=1000)	$a_1=0.85$ $a_2=0.15$	$\mu_1=0.0$ $\mu_2=2.0$	$\sigma_{11}=1.0$ $\sigma_{22}=0.25$
"Sample3" (N=1000)	$a_1=0.33$ $a_2=0.33$ $a_3=0.34$	$\mu_1=0.0$ $\mu_2=-1.0$ $\mu_3=4.0$	$\sigma_{11}=1.0$ $\sigma_{22}=0.25$ $\sigma_{33}=4.0$
"Sample4" (N=1000)	$a_1=0.33$	$\mu_1 = \begin{bmatrix} 5.01 \\ 3.43 \\ 1.46 \\ 0.25 \end{bmatrix}$	$\Sigma_1 = \begin{bmatrix} 0.12 & 0.1 & 0.02 & 0.01 \\ & 0.14 & 0.01 & 0.13 \\ & & 0.03 & 0.01 \\ & & & 0.3 \end{bmatrix}$
	$a_2=0.30$	$\mu_2 = \begin{bmatrix} 5.91 \\ 2.78 \\ 4.2 \\ 1.3 \end{bmatrix}$	$\Sigma_2 = \begin{bmatrix} 0.27 & 0.1 & 0.18 & 0.05 \\ & 0.09 & 0.09 & 0.04 \\ & & 0.2 & 0.06 \\ & & & 0.03 \end{bmatrix}$
	$a_3=0.37$	$\mu_3 = \begin{bmatrix} 6.54 \\ 2.95 \\ 5.48 \\ 1.98 \end{bmatrix}$	$\Sigma_3 = \begin{bmatrix} 0.38 & 0.09 & 0.3 & 0.06 \\ & 0.11 & 0.08 & 0.05 \\ & & 0.32 & 0.07 \\ & & & 0.08 \end{bmatrix}$

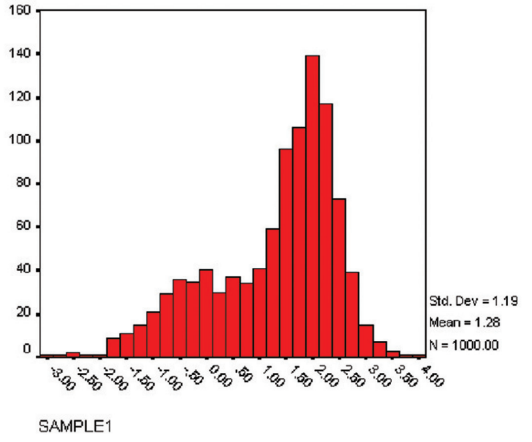

(1.1)

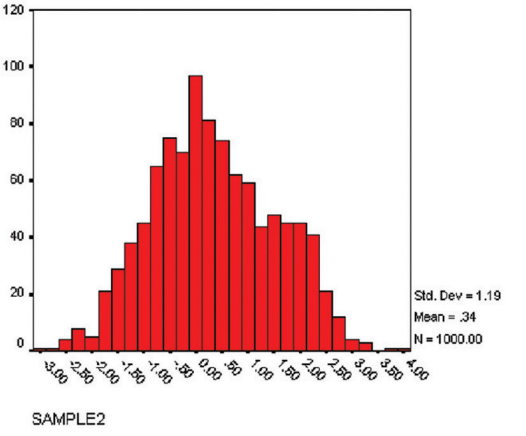

(1.2)

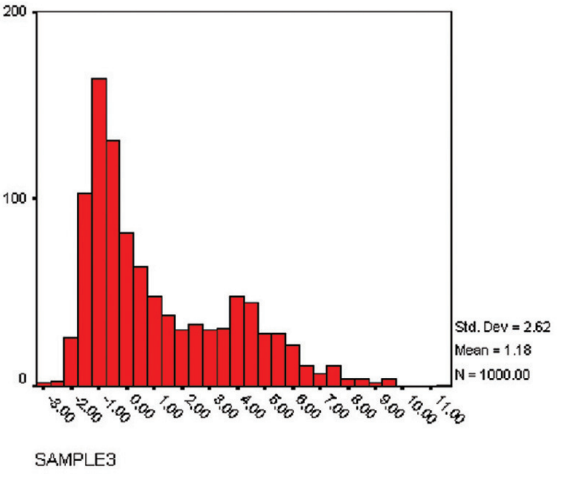

(1.3)

Fig. 1: The histograms of "Sample1" (with overall mean and standard deviation equal to 1.28 and 1.19, respectively); "Sample2" (with overall mean and standard deviation equal to 0.34 and 1.19, respectively); and "Sample3" (with overall mean and standard deviation equal to 1.18 and 2.62, respectively)

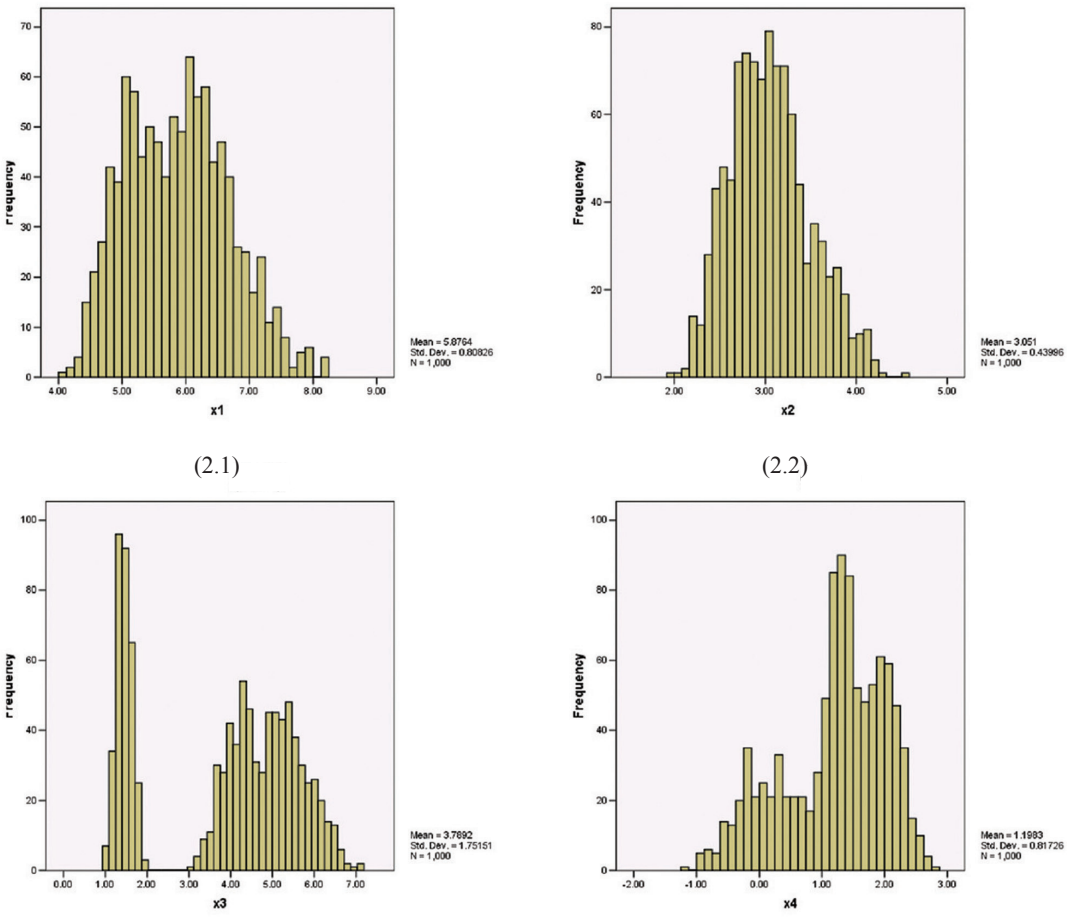

Fig. 2: The histograms of "Sample4" x_1 (with overall mean and standard deviation equal to 5.88 and 0.81, respectively); x_2 (with overall mean and standard deviation equal to 3.05 and 0.44, respectively); x_3 (with overall mean and standard deviation equal to 3.79 and 1.75, respectively); and x_4 (with overall mean and standard deviation equal to 1.2 and 0.82, respectively)

RESULTS

A program known as the "GMM" was developed using the Java language to find the parameters of equation (1) by employing the EM algorithm, where iteration is stopped when $|\theta^{i+1}-\theta^{i}|<0.000001$. Other methods involved in the calculation of EM algorithm include the Cholesky method (Mardia *et al*., 1979). In this section, two scenarios are therefore presented.

Scenario 1: In Table 2, with the exception of "Sample4" (where initial parameters were taken from Everitt *et al*., 1981), the initial parameters for "Sample1", "Sample2" and "Sample3" were determined using visual inspection of the histograms given in *Fig. 1*. This was done by concentrating on the observation(s) that gave the highest frequency, as shown by the components which were clearly displayed.

TABLE 2
a's, μ's, $\boldsymbol{\mu}$'s, σ*'s and* $\boldsymbol{\Sigma}$*'s* for each sample used in the GMM program, where they were treated as the initial parameters

"Sample1"	a_1=*0.5*	μ_1=0.0	σ_{11}=1.0
	a_2=*0.5*	μ_2=2.0	σ_{22}=1.0
"Sample2"	a_1=*0.5*	μ_1=0.0	σ_{11}=1.0
	a_2=*0.5*	μ_2=1.5	σ_{22}=1.0
"Sample3"	a_1=*0.33*	μ_1=0.0	σ_{11}=1.0
	a_2=*0.33*	μ_2=-1.0	σ_{22}=1.0
	a_3=*0.34*	μ_3=4.0	σ_{33}=1.0
"Sample4"	a_1=0.33	$\mu_1 = \begin{bmatrix} 4 \\ 4 \\ 2 \\ 1 \end{bmatrix}$	$\Sigma_1 = \begin{bmatrix} 1 & 0 & 0 & 0 \\ & 1 & 0 & 0 \\ & & 1 & 0 \\ & & & 1 \end{bmatrix}$
	a_2=0.30	$\mu_2 = \begin{bmatrix} 7 \\ 2 \\ 3 \\ 2 \end{bmatrix}$	$\Sigma_2 = \begin{bmatrix} 1 & 0 & 0 & 0 \\ & 1 & 0 & 0 \\ & & 1 & 0 \\ & & & 1 \end{bmatrix}$
	a_3=0.37	$\mu_3 = \begin{bmatrix} 8 \\ 4 \\ 5 \\ 3 \end{bmatrix}$	$\Sigma_3 = \begin{bmatrix} 1 & 0 & 0 & 0 \\ & 1 & 0 & 0 \\ & & 1 & 0 \\ & & & 1 \end{bmatrix}$

The values given in Table 2 were used by the "GMM" program as the initial parameters to find the final ones for the simulation data, as shown in *Figs. 1* and *2*. The results are as tabulated below.

TABLE 3
$\hat{a}$'s, $\hat{u}$'s, $\hat{u}$'s, $\hat{\sigma}$'s and $\hat{\Sigma}$'s for each sample produced by the "GMM" program, using (Table 2) as the initial parameters. The "GMM" program converged is given in the bracket

"Sample1" *(Converged at iteration no 156)*	$\hat{a}_1$=0.34 $\hat{a}_2$=0.66	$\hat{\mu}_1$=-0.05 $\hat{\mu}_2$=1.98	$\hat{\sigma}_{11}$=0.85 $\hat{\sigma}_{22}$=0.28
"Sample2" *(Converged at iteration no 389)*	$\hat{a}_1$=0.82 $\hat{a}_2$=0.18	$\hat{\mu}_1$=-0.02 $\hat{\mu}_2$=1.97	$\hat{\sigma}_{11}$=0.93 $\hat{\sigma}_{22}$=0.30
"Sample3" *(Converged at iteration no 316)*	$\hat{a}_1$=0.29 $\hat{a}_2$=0.31 $\hat{a}_3$=0.40	$\hat{\mu}_1$=-0.1 $\hat{\mu}_2$=-1.01 $\hat{\mu}_3$=3.76	$\hat{\sigma}_{11}$=0.89 $\hat{\sigma}_{22}$=0.22 $\hat{\sigma}_{33}$=4.71
"Sample4" *(converged at iteration no 32)*	$\hat{a}_1$=0.32 $\hat{a}_2$=0.33 $\hat{a}_3$=0.35	$\hat{\boldsymbol{\mu}}_1 = \begin{bmatrix} 5.05 \\ 3.46 \\ 1.45 \\ 0.23 \end{bmatrix}$ $\hat{\boldsymbol{\mu}}_2 = \begin{bmatrix} 5.93 \\ 2.77 \\ 4.22 \\ 1.30 \end{bmatrix}$ $\hat{\boldsymbol{\mu}}_3 = \begin{bmatrix} 6.58 \\ 2.94 \\ 5.53 \\ 1.99 \end{bmatrix}$	$\hat{\boldsymbol{\Sigma}}_1 = \begin{bmatrix} 0.13 & 0.11 & 0.03 & 0.02 \\ & 0.15 & 0.02 & 0.14 \\ & & 0.03 & 0.01 \\ & & & 0.31 \end{bmatrix}$ $\hat{\boldsymbol{\Sigma}}_2 = \begin{bmatrix} 0.26 & 0.09 & 0.17 & 0.05 \\ & 0.08 & 0.09 & 0.04 \\ & & 0.21 & 0.06 \\ & & & 0.03 \end{bmatrix}$ $\hat{\boldsymbol{\Sigma}}_3 = \begin{bmatrix} 0.36 & 0.08 & 0.28 & 0.06 \\ & 0.10 & 0.08 & 0.05 \\ & & 0.29 & 0.06 \\ & & & 0.08 \end{bmatrix}$

It is crucial to note that for the univariate samples, the convergence was achieved with more than 100 iterations, while for the multivariate samples, less than 100 iterations were required. The choice of the initial parameters might play an important role in making the convergence process faster, as illustrated by the latter.

The "GMM" program managed to find (final) parameters even in cases where the components were hidden from the view, but this is provided that the number of components and the observations which give the highest frequency for the identifiable components are known.

Scenario 2: Great care should be taken when choosing the initial parameters (to start the EM algorithm) as well as the number of components, where wrong choice will lead to the situation exemplified in Table 4. Other examples can be found in Everitt *et al*. (1981) and Reynolds *et al*. (1995).

TABLE 4
The initial (1st row) and final (2nd row) parameters for "Sample 3" (chosen for having hidden components), where: two components were used for (4.1), four components were used for (4.2), and six components were used for (4.3) and (4.4). The actual number of the components is three

"Sample3"	$a_1=0.5$ $a_2=0.5$	$\mu_1=-1.0$ $\mu_2=4.0$	$\sigma_{11}=1.0$ $\sigma_{22}=1.0$
"Sample3" (Converged at iteration no 99)	$\hat{a}_1=0.51$ $\hat{a}_2=0.49$	$\hat{\mu}_1=-0.75$ $\hat{\mu}_2=3.21$	$\hat{\sigma}_{11}=0.45$ $\hat{\sigma}_{22}=5.58$

(4.1)

"Sample3"	$a_1=0.25$ $a_2=0.25$ $a_3=0.25$ $a_4=0.25$	$\mu_1=-1.0$ $\mu_2=4.0$ $\mu_3=0.0$ $\mu_4=0.0$	$\sigma_{11}=1.0$ $\sigma_{22}=1.0$ $\sigma_{33}=1.0$ $\sigma_{44}=1.0$
"Sample3" (Converged at iteration no 186)	$\hat{a}_1=0.31$ $\hat{a}_2=0.41$ $\hat{a}_3=0.14$ $\hat{a}_4=0.14$	$\hat{\mu}_1=-1.01$ $\hat{\mu}_2=3.76$ $\hat{\mu}_3=-0.1$ $\hat{\mu}_4=-0.1$	$\hat{\sigma}_{11}=0.22$ $\hat{\sigma}_{22}=4.71$ $\hat{\sigma}_{33}=0.89$ $\hat{\sigma}_{44}=0.89$

(4.2)

"Sample3"	$a_1=0.17$ $a_2=0.17$ $a_3=0.17$ $a_4=0.17$ $a_5=0.17$ $a_6=0.17$	$\mu_1=-1.0$ $\mu_2=4.0$ $\mu_3=0.0$ $\mu_4=0.0$ $\mu_5=0.0$ $\mu_6=0.0$	$\sigma_{11}=1.0$ $\sigma_{22}=1.0$ $\sigma_{33}=1.0$ $\sigma_{44}=1.0$ $\sigma_{55}=1.0$ $\sigma_{66}=1.0$
"Sample3" (Converged at iteration no 312)	$\hat{a}_1=0.31$ $\hat{a}_2=0.41$ $\hat{a}_3=0.07$ $\hat{a}_4=0.07$ $\hat{a}_5=0.07$ $\hat{a}_6=0.07$	$\hat{\mu}_1=-1.01$ $\hat{\mu}_2=3.76$ $\hat{\mu}_3=-0.1$ $\hat{\mu}_4=-0.1$ $\hat{\mu}_5=-0.1$ $\hat{\mu}_6=-0.1$	$\hat{\sigma}_{11}=0.22$ $\hat{\sigma}_{22}=4.71$ $\hat{\sigma}_{33}=0.89$ $\hat{\sigma}_{44}=0.89$ $\hat{\sigma}_{55}=0.89$ $\hat{\sigma}_{66}=0.89$

(4.3)

(4.3)

"Sample3"	a_1=0.17 a_2=0.17 a_3=0.17 a_4=0.17 a_5=0.17 a_6=0.17	μ_1=0.0 μ_2=0.0 μ_3=0.0 μ_4=0.0 μ_5=0.0 μ_6=0.0	σ_{11}=1.0 σ_{22}=1.0 σ_{33}=1.0 σ_{44}=1.0 σ_{55}=1.0 σ_{66}=1.0
"Sample3" (Converged at iteration no 2)	$\hat{a}_1$=0.17 $\hat{a}_2$=0.17 $\hat{a}_3$=0.17 $\hat{a}_4$=0.17 $\hat{a}_5$=0.17 $\hat{a}_6$=0.17	$\hat{\mu}_1$=1.18 $\hat{\mu}_2$=1.18 $\hat{\mu}_3$=1.18 $\hat{\mu}_4$=1.18 $\hat{\mu}_5$=1.18 $\hat{\mu}_6$=1.18	$\hat{\sigma}_{11}$=6.88 $\hat{\sigma}_{22}$=6.88 $\hat{\sigma}_{33}$=6.88 $\hat{\sigma}_{44}$=6.88 $\hat{\sigma}_{55}$=6.88 $\hat{\sigma}_{66}$=6.88

(4.4)

Notice that Table 4.2's $\hat{\mu}_3 = \hat{\mu}_4 = -0.1$ and $\hat{\sigma}_{33} = \hat{\sigma}_{44} = 0.89$ and if $\hat{a}_3 + \hat{a}_4$ were computed, 0.28 would therefore be obtained, and this is no far different from the ones given in Table 3. Table 4.3 also shows similar results, where $\hat{u}_3 = \ldots = \hat{\mu}_6 = -0.1$, $= \hat{\sigma}_{33} = \ldots = \hat{\sigma}_{66} = 0.89$ and $\hat{a}_3 = \ldots = \hat{a}_6 = 0.07$ where $\hat{a}_3 + \ldots + \hat{a}_6 = 0.28$. Despite converging at iteration no. 2 (the lowest so far), the final parameters shown in Table 4.4 are completely different from those in Table 3, and this is a direct consequence from ignoring the characteristics shown by the observations in the histograms.

CONCLUSIONS

In the previous sections, "Sample1", "Sample2", "Sample3", and "Sample4" (using a program called "Simulate") were generated with known number of both components and parameters. Using the same information, particularly on the number of components and determining the initial parameters to start the EM algorithm by inspecting the histograms, the final parameters produced from the EM algorithm (using the program known as the "GMM") are similar to the real ones.

Just to show how important the process of choosing the initial parameters is (to start the EM algorithm) and the number of components, "Sample3" was selected for having hidden components, while the process of determining the initial parameters to start EM algorithm (i.e. by inspecting the histograms) and reducing the number of components was repeated; the final parameters produced were incorrect. The same results were also obtained when the number of components was increased; for the initial parameters to start the EM algorithm, let the mean equals to 0 and the standard deviation equals to 1 (a common mistake done by most of the practitioners).

In contrary to the above, when the number of components was increased and the initial parameters to start the EM algorithm was determined by inspecting the histograms and for the rest (especially the hidden components) by letting the mean equals to 0 and standard deviation equals to 1, the final parameters produced (with minor adjustments) were similar to the real ones (a "characteristic" where some might consider it as unimportant and therefore choose to ignore).

The determination of the initial parameters to start the EM algorithm could be made easier and faster using the graphical techniques such as plotting $\log \frac{\phi_{i+1}}{\phi_i}$ against x_i where each approximately straight line, with negative slope represents an area where one component dominates and the kernel

method defined by $f(\hat{t}_k) = \sum_{l=-\frac{m}{2}}^{\frac{m}{2}} \exp\left(-\frac{2\pi ikl}{m}\right)\exp\left(-\frac{1}{2}h^2\left(\frac{2\pi l}{b-a}\right)^2\right)\left(\frac{1}{m}\sum_{k=0}^{m-1}\xi_k \exp\left(\frac{2\pi ikl}{m}\right)\right)$, $m = 2^r$ (Everitt *et al*., 1981; Bhattacharya, 1967; Silverman, 1986). Nevertheless, the main disadvantage of both methods is that they can not be used to detect hidden components.

Appendix A

A.1 "Simulate" program uses the following formulas to produce "Sample4" (where the subscript represents the dimension of the matrix).

$$X_{nx1} = C_{nxn} Z_{nx1} + \mu_{nx1}, \Sigma_{nxn} = C_{nxn} C_{nxn}{}^{t}$$

where $c_{ij} = \begin{cases} \dfrac{\sigma_{ij} - \sum_{k=1}^{j-1} c_{ik}c_{jk}}{\left(\sigma_{jj} - \sum_{k=1}^{j-1} c_{jk}c_{jk}\right)^{\frac{1}{2}}} & ,j \le i \\ 0 & ,i < j \end{cases}$ and z_i, ith component of Z, is as per defined in equation (10), where μ and σ are set/fixed at 0 and 1, respectively.

A.2 Derivation of Equations (7), (8) and (9)

A.2.1 Using Lagrange multipliers defined by *max/min F(x,y,z)* subject to $\Phi(x,y,z)=0$, $G(x,y,z)=F(x,y,z)+\lambda\Phi(x,y,z)$, $\frac{\partial G}{\partial x} = 0, \frac{\partial G}{\partial y} = 0, \frac{\partial G}{\partial Z} = 0$ (Spiegel, 1974) on $max \sum_i \sum_j p_{ij} \log(a_j)$ subject to $\sum_j a_j = 1$ (or $\left(\sum_j a_j - 1\right) = 0$, Equation (7) would be obtained.

A.2.2 From $\frac{\partial}{\partial \mu_j}\left(\frac{1}{2}\sum_i \sum_j p_{ij}(\mathbf{X}_i - \boldsymbol{\mu}_j)^t \Sigma_j^{t-1}(\mathbf{X}_i - \boldsymbol{\mu}_j)\right) = 0$, equation (8) would be obtained using the following matrix properties, $\frac{\partial \mathbf{x}^t \mathbf{A}\mathbf{y}}{\partial \mathbf{x}} = \mathbf{A}\mathbf{y}, \frac{\partial \mathbf{a}^t \mathbf{x}}{\partial \mathbf{x}} = \mathbf{a}$

A.2.3 The first and second expressions of

$\frac{\partial}{\partial \boldsymbol{\Sigma}_j^{-1}}\left(\frac{1}{2}\sum_i \sum_j p_{ij}(\mathbf{X}_i - \boldsymbol{\mu}_j)^t \boldsymbol{\Sigma}_j^{-1}(\mathbf{X}_i - \boldsymbol{\mu}_j)\right) + \frac{\partial}{\partial \boldsymbol{\Sigma}_j^{-1}}\left(\frac{1}{2}\sum_i \sum_j p_{ij} \log\left|\boldsymbol{\Sigma}_j^{-1}\right|\right) = 0$ use the following matrix properties, $\frac{\partial tr(\mathbf{xy})}{\partial \mathbf{x}} = \mathbf{y} + \mathbf{y}^t - Diag(\mathbf{y})$, and $\sum \mathbf{X}_i^t \mathbf{A}\mathbf{x}_i = tr\left(\mathbf{A}\sum \mathbf{x}_i \mathbf{x}_i^t\right)$ to get equation (9). (Mardia *et al*., 1979).

REFERENCES

Bhattacharya, C.G. (1967). A simple method of resolution of a distribution into Gaussian components. *Biometrics*, *23,* 115-35.

Bilmes, J.A. (1997). A Gentle tutorial of the EM algorithm and its application to parameter estimation for Gaussian Mixture and Hidden Markov Models. Technical Report, University of Berkeley, ICSI-TR-97-021.

Box, G.E.P. and Muller, M.E. (1958). A note on the generating of random normal deviates. *Annals of Mathematical Statistics*, *29,* 610-611.

Dempster, A.P., Laird, N.M. and Rubin, D.B. (1977). Maximum Likelihood from incomplete data via the EM algorithm. *Journal of Royal Statistics Society*, *39*(1), 1-21.

Everitt, B.S. and Hand, D.J. (1981). *Finite Mixture Distributions*. London: Chapman and Hall Ltd.

Mardia, K.V., Kent, J.T. and Bibby, J.M. (1979). *Multivariate Analysis*. London: Academic Press Inc. Ltd.

Mohd Yusoff, M.I., Abu Bakar, M.R. and Mohd Nor, A.H.S. (2007). Fraud detection in telecommunication using Data Mining application. In *Proceedings of 9th Islamic Countries Conference on Statistical Sciences 2007 (ICCS-IX)*.

Reynolds, D.A. and Rose, R.C. (1995). Robust text-independent speaker identification using Gaussian Mixture Speaker Models. *IEEE Transactions on Speech and Audio Processing, 3*(1), January 1995.

Silverman, B.W. (1986). *Density Estimation for Statistics and Data Analysis*. London: Chapman and Hall Ltd.

Spiegel, M.R. (1974). *Shaum's Outline Series: Theory and Problems of Advanced Calculus*: SI (Metric) edition. Mc Graw-Hills, Inc.

Tanigushi, M., Haft, M., Hollmen, J. and Tresp, V. (1998). Fraud detection in communications networks using neural and probabilistic methods. In *Proceeding of the 1998 IEEE International Conference in Acoustics, Speech and Signal Processing (ICASSP'98)*, *II,* 1241-44.

Tsay, R.S. (2005). *Analysis of Financial Time Series: Financial Econometrics*. John Wiley and Sons.

ISSN: 0128-7680
Pertanika J. Sci. & Technol. **17 (2)**: 245 – 262 (2009)

Target Detection in Forward Scattering Radar

Mohamed Khalaf alla Hassan Mohamed,
Raja Syamsul Azmir Raja Abdullah* and M.F.A. Rasid
Microwave, Millimetre Wave and Radar System Laboratory,
Department of Computer and Communication Systems, Faculty of Engineering,
Universiti Putra Malaysia, 43400 UPM, Serdang, Selangor, Malaysia
**E-mail: rsa@eng.upm.edu.my*

ABSTRACT

This paper analyses electromagnetic signal scattered from the target crossing the Forward Scattering Radar (FSR) system baseline. The aim of the analysis was to extract the Doppler signal of a target under the influence of high ground clutter and noise interference. The extraction was used for the automatic target detection (ATD) in the FSR system. Two extraction methods, namely Hilbert Transform and Wavelet Technique, were analyzed. The detection using the Hilbert Transform is only applicable for some conditions; however, the detection using the Wavelet Technique is more robust to any clutter and noise level. From 55 sets of signal, only 4% of false alarm was detected or occurred when the Wavelet Technique was applied as a detection scheme. Two sets of field experimentation were carried out and the target's signal under the influence of high clutter had successfully been detected using the proposed method.

Keywords: Forward Scattering Radar, Hilbert Transform, Wavelet Denoise, target detection

ABBREVIATIONS

FSR: Forward scattering radar
FSCS: Forward scattering cross-section
RCS: Radar cross section

INTRODUCTION

Forward scattering radar (FSR) is an operational mode of bistatic radar which corresponds to the case when the bistatic angle is nearly 180°. The FSR offers a number of peculiarities which make it a viable interest. Its most attractive feature is the steep rise in the target radar cross section (RCS) as compared to the traditional monostatic radar (Glaser, 1985; Stimson, 1983; Jackson, 1986), and this particular feature improves the sensitivity of the radar system. The forward scattering RCS mainly depends on the target's physical cross section and the wavelength, and at the same time, it is independent on the surface shape of target and any radar absorbing material (RAM) coating which reduces the RCS of the target in the traditional radar (Boyle, 1994). This feature has made the FSR robust to stealth technology. In addition, the FSR only requires a relatively simple hardware and has a long coherent interval of the received signal. Moreover, the FSR receiver can utilise radiation from non-cooperative transmitter, without revealing its location. In a hostile environment, this is

Received: 21 January 2008
Accepted: 16 July 2008
*Corresponding Author

highly desirable as the receiver may be used covertly. All these advantageous features create a 'come back' interest to the FSR after it was abandoned since World War II (Willis, 1995). As far as the authors' knowledge is concerned, only a few researchers and research labs are seriously working in this area (e.g. Abdullah *et al*., 2004; Blackman, *et al*., 2000; Cherniakov *et al*., 2006).

The basics of the FSR can be found in the works of Willis (1995) and Chernyak (1998), whereas research on target detection, coordinate estimation and automatic classification can be found in Abdullah *et al*. (2004), Raja Abdullah *et al*. (2005) and Cherniakov *et al*., 2006). Despite the results reported in the stated literature, most studies carried out on the FSR have only been carried out in a small number of scenarios and most publications dedicated to the FSR studied on airborne. The more recent studies, which focused on ground application (Abdullah *et al*., 2004; Cherniakov *et al*., 2006), did not assume any denoising process of different noise levels masking the received signal in which it made the detection process more difficult.

This paper concentrates on the method of extracting signal scattered from the ground target crossing the FSR baseline. Typical ground vehicle (car) has been used as a target. The signal scattered from the target is embedded and hidden inside the high clutter and noise interferences. Two methods, namely the Hilbert Transform and Wavelet with the capability of denosing, were analyzed to predict the existence of a target. Using these techniques has been shown to effectively predict target crossing the FSR baseline. To the best knowledge of the authors, this paper is amongst the earliest documented discussion dedicated to ground clutter rejection in the FSR. Thus, using FSR for detection and classification of ground targets, together with its low cost system, various applications in civil, defense, medical and security systems could be found.

FORWARD SCATTERING RADAR BASIC AND THEORY

This section summarizes the basic technical aspects in the FSR and more details can be found in Abdullah *et al*. (2004) and Cherniakov *et al*. (2006). As discussed in the earlier section, the FSR introduces a specific case of a more general class of radar, namely the bistatic radar (BR). The key peculiarity of the FSRs is that, in contrast to their monostatic and bistatic counterparts, they exploit an effect of electromagnetic wave shadowing a target, rather than scattering from the target. This fact puts an essential restriction on the FSR topology, since the target shadow exists within a relatively narrow corridor of <20° around the baseline, that is, the line connecting the transmitter and the receiver. Another consequence is that the system loses its range resolution. The FSR system, as shown in *Fig. 1*, comprises of a transmitter (*Tr*) with *fc* central frequency and an appropriate wavelength (λ), and of a receiver (*Re*) separated by a distance (*b*) from the transmitter. The target (*Ta*) is assumed to be moving along a trajectory which crosses the baseline with speed (V), has zero elevation and the system operates in a ground plane (Cherniakov *et al*., 2006; RSA Raja Abdullah *et al*., 2003). Assuming the transmitting signal bandwidth Δf, the bistatic range resolution ΔR_{BR} could be specified by:

$$\Delta R_{BR} = \frac{c}{2\Delta f_t \cos(\beta/2)} \tag{1}$$

Where c is the speed of light, β is the bistatic angle and for the FSR.

$$\Delta R_{br} \rightarrow \infty \ \beta \rightarrow 180^{o}$$

TABLE 1
Example of vehicle types used in experiment

Mercedes E-class - W124	
Proton Savy	
Proton Myvi	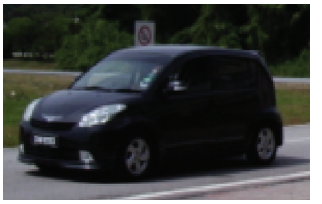

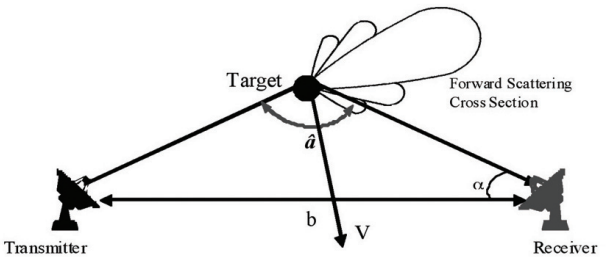

β - bistatic angle

Fig. 1: Forward Scattering Radar general layout (top view), α is the angle on the horizontal plane

As one can see, the transmitting signal bandwidth in the limiting case does not influence the range resolution, and a continuous wave (CW) can effectively be used in the FSR. It is important to mention that in the case of moving targets, the shadow signal experiences Doppler shift, f_{dbr}. This can be evaluated (Willis, 1995) as:

$$f_{dbr} = 2v \frac{1}{\lambda} \cos \delta \cos (\beta/2) \quad (2)$$

The maximal Doppler shift occurs for the target trajectory normal to the baseline $\delta = 0^o$. Even in this case, the absolute value of the f_{dbr} is essentially less than its maximal rate $f_{dmax} = 2v/\lambda$ corresponding to a monostatic radar. For $\beta = 170^o$ to be considered as a boundary of the FS corridor, the absence of a range resolution and low Doppler shift, even for relatively high-speed targets, introduces a big threat for the FSR from the ground clutters. At the time that β approaches 180^o, the target blocks part of the transmitted signal (i.e. the direct signal from the transmitter), leading to a reduction in the received signal power. In this case, the target acts as an aperture antenna with a maximum gain equal to:

$$G = \frac{4\pi A}{\lambda^2} \tag{3}$$

Where $\lambda = c/f_c$ is the signal wavelength, which is assumed to be small as compared to the dimensions of the target, and A is the target shadow silhouette area projection on the transmitter-target line. When $\beta = 180^0$, the level of received signal, comprising of the scattered signal from the target and transmitted signal, reaches its maximum. Similarly, at this condition, the target radar cross section can be characterized by a forward scattering cross-section (FSCS), which is also dependent upon the target shadow silhouette area A (Cherniakov *et al*., 2006).

$$\sigma_b = \frac{4\pi A^2}{\lambda^2} \tag{4}$$

Using practical numbers, it could be shown that the FSCS is essentially bigger than the corresponding monostatic RCS. For a small car (ground target), with a physical area $A \sim 4\text{m}^2$ at frequency 900 MHz, $\sigma_b = 2000\text{m}^2$ could then be expected when a similar target in the monostatic case had about 50m^2 RCS. This and the robustness to stealth targets are considered as one of the main advantages of the FSR. When the bistatic angle decreases, the FSCS follows the appropriate equivalent antenna pattern. The first null in this pattern occurs at the angular distance (Cherniakov *et al*., 2006).

$$\alpha = \lambda / l_{\max} \tag{5}$$

Where, l_{max} is the maximum length of the target. Equation 5 is a good approximation only for the optical region, that is, where $l_{max} > \lambda$. In the resonance region, $l_{max} \sim \lambda$, forward scattering still exists but this equation is not accurate. Using rectangular targets with different lengths as examples, it was theoretically shown and experimentally confirmed that the cross-section of the target $\sigma_b(\varphi)$, $\varphi = \pi = \beta$, approximately followed the appropriate antenna pattern with a rectangular aperture (RSA Raja Abdullah *et al*., 2003). The received forward-scattering signature is a function of the observation angle α (angular distance in terms of Radar Cross Section). When the target crosses the baseline, it has a maximal cross-section, and this region can be used as the parameters to evaluate the target detect ability. Alternatively, if the bistatic angle never reaches 180^o, an appropriate σ_b reduction should be taken into account and the detection via FSCS side lobes can then take place. For example, for a rectangular silhouette, the cross section reduction follows the $\sin^2(\beta/\Delta\beta)/(\beta/\Delta\beta)^2$ function (Cherniakov *et al*., 2006). This means that if the waveforms are processed using the third side lobe of the FSCS, a signal reduction from 22 dB to 23 dB is expected (Cherniakov *et al*., 2006). It is obvious that the forward scattering components of a moving target introduce a Doppler shift. This can be used for moving target selection, as well as for its speed determination. This

information is also used in the FSR for the trajectory reconstruction and classification of target. The Doppler shift depends mainly on the target velocity vector components and the carrier frequency. The general equation which describes the received waveform, that is, the target signature from the moving sample target (rectangular shape) can be found in Cherniakov *et al*. (2006).

EXPERIMENTAL SET UP AND DATA COLLECTION

In this section, the experimental set-up is described and the method used for data collection is presented. Two experimental setups were implemented to collect the FSR signal. The different parameter between the setups are in the transmitter–receiver distance, types of antenna and height of antenna. Details of the experimental setup are presented in the next sub-sections. Typical cars in the public road were used as examples for the target. Table 1 shows the example of the targets used in the experiment.

Experimental Setup: Layout 1

Fig. 2 illustrates the FS sensor block diagram, the system topology and a typical scene during experimentation used for data collection. The transmitter generates a 20 dBm CW signal at an ISM band carrier frequency of 900 MHz with vertical polarization. In the layout, two directional flat antennas, as shown in *Fig. 3*, were used as the transmitting and receiving antennas. At the receiver end, the vehicle signature is detected via non-linear processing, whereby the arriving signal, containing both direct signal and the signal with the Doppler components, is passed through an amplitude detector. The low-pass filter allows only this Doppler component to pass through. This waveform is the vehicle signature which is stored for further processing.

Experimental Setup: Layout 2

In general, the experimentation in Layout 2 is similar to Layout 1, but the differences are:

i. In the second setup, two omni-directional antennas, with lower gain at 2dbi and wider beamwidth as shown in *Fig. 4*, were used. It is desirable for any radar sensor to have a wide coverage area. In this case, employing the Omni-directional antenna enabled the forward scattering network to cover up to 360^{o} angle. This could happen with a specially designed sensor network topology.
ii. The separation distance, between the transmitter and the receiver, was increased up to ~40m. The transmitter–receiver distance in the initial layout was restricted to only ~15m. As the transmitter receiver distance increases, this will reduce the power received at the receiver, and the signal is highly corrupted with noise. To increase the transmitter receiver, the baseline distance is one of the important requirements in a practical radar system.
iii. The antenna was mounted on the pole and was elevated to ~1m from the ground in the first case (*Fig. 3*), whereas the antenna was directly elevated on the ground in the second experimentation, as shown in *Fig. 4*. With this position, the antenna could be covert and was also less cumbersome due to the non-mounting mechanism, hence is easy to deploy and incurs low cost.

The difference between the two experimental set ups is summarized in Table 2. These differences, especially in the experimental Layout 2, make the process of extracting the Doppler frequencies more difficult. The scenario restricts the power density incident onto the target surface, beside the higher noise level and the ground clutter which is added to the received signal. The choice of using carrier frequency at 900 MHz increases the difficulty of extracting the Doppler signals; this is due to the tendency to experience strong interference, especially from the cellular services. An example of the received signal is shown in the next section.

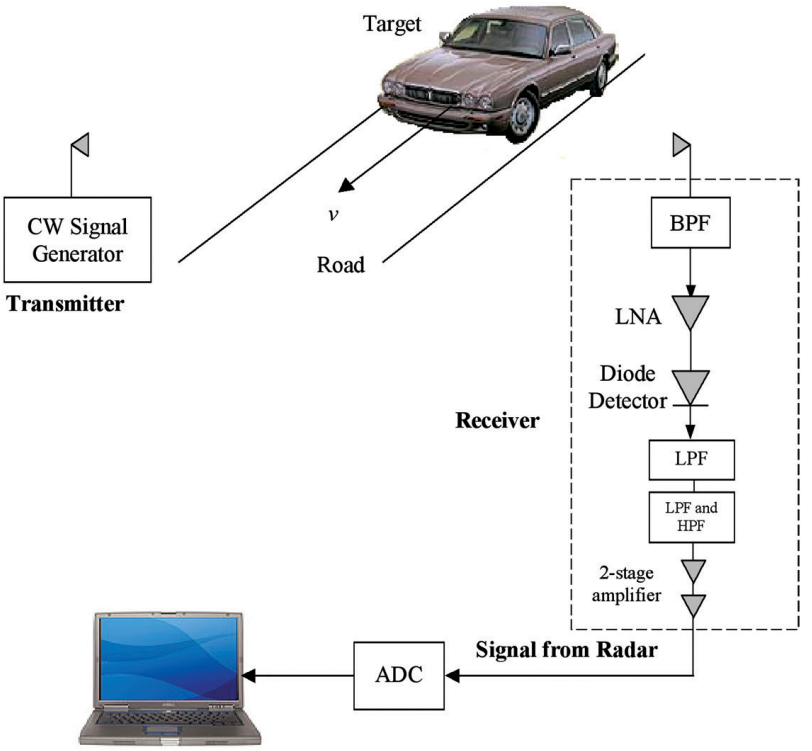
Target
v
Road
CW Signal Generator
Transmitter
BPF
LNA
Diode Detector
Receiver
LPF
LPF and HPF
2-stage amplifier
Signal from Radar
ADC

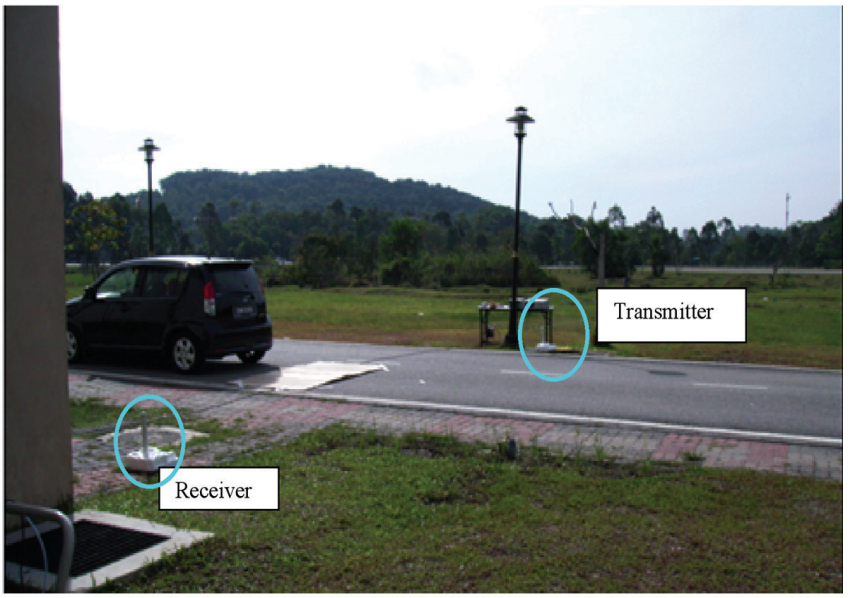
Transmitter
Receiver

(a)

(b)

Fig.2: (a) General experiment layout for the FSR detection, (b) Scene for the FSR target detection experiment

TABLE 2
The difference set up between the two layouts

Factors	Layout 1	Layout 2
Antenna	High gain directional	Low gain omni directional
Tx-Rx separation Distance	Up to 15 m	Up to 40 m
Antenna elevation	Elevated to ~1m from the ground	directly elevated on the ground

TARGET DETECTION IN THE FORWARD SCATTERING RADAR

In the FSR system, as shown in *Fig. 1*, the electromagnetic wave scattered from the target carries Doppler information to the receiver, as a result of the changes in the transmitter-target-receiver distance. The Doppler frequency is determined by the carrier wavelength, λ, while the target's speed relative to the receiver is as given by Equation 2 in Section 2. In the case of the FSR, by looking at Equation 2 and as illustrated in *Fig. 5* (using a point target), the Doppler frequency scattered by the target is zero whenever the target is exactly on the transmitter – receiver baseline (position 'C', f_{Dc}=0). Hence, the first detection technique of the target's existence within the FSR corridor is

Fig. 3: Directional antenna used in Layout 1

Fig. 4: Dipole omni directional antenna

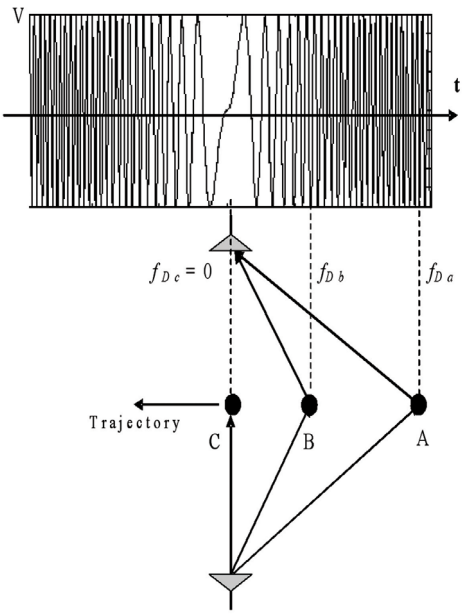

Fig. 5: Doppler frequency variation relative to the scattering point on the vehicle

based on the high amplitude of zero Doppler frequency (DC component) at the receiver, i.e. when the target is exactly on the transmitter–receiver baseline. The Doppler frequency at the receiver increases as the target moves away from the baseline.

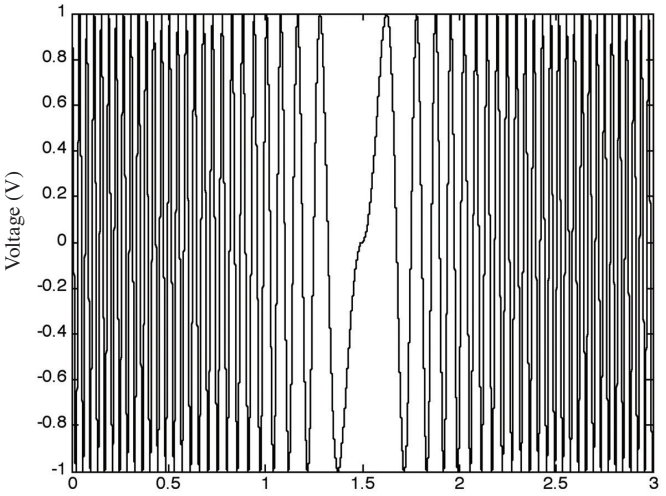

(a)

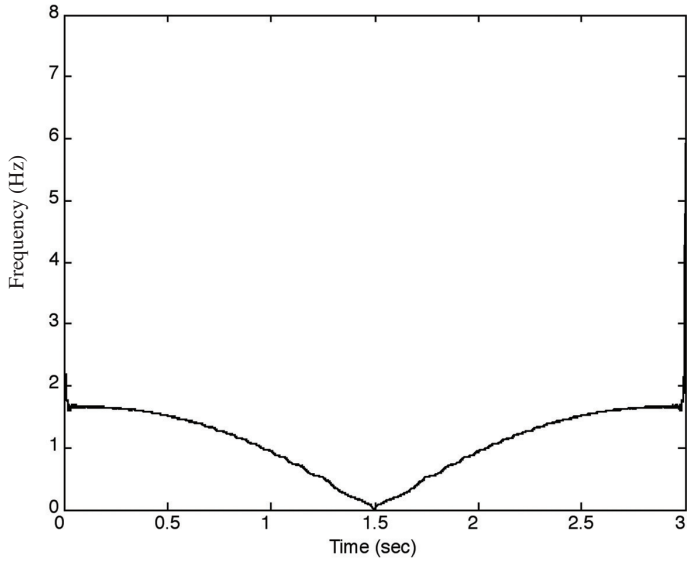

Fig. 6: Ideal analytical signal in (a) time domain and (b) its instantaneous frequency

By employing the Hilbert transform to the received signal, it produces a relationship between the instantaneous frequencies with respect to time, reflecting the position of the target. From the discussion in Section 2 and the assumption given above, zero frequency or very low frequency is created at the time that the object passes through the FSR baseline, and using the frequency–time relationship from Hilbert, the target can then be detected. The effectiveness of the proposed method is presented first by testing to the analytical result, and followed by the real experimental data.

To calculate the instantaneous frequency, f_i the Hilbert Transform of the received signal, x(t) was performed and given by: (Marple, 1999)

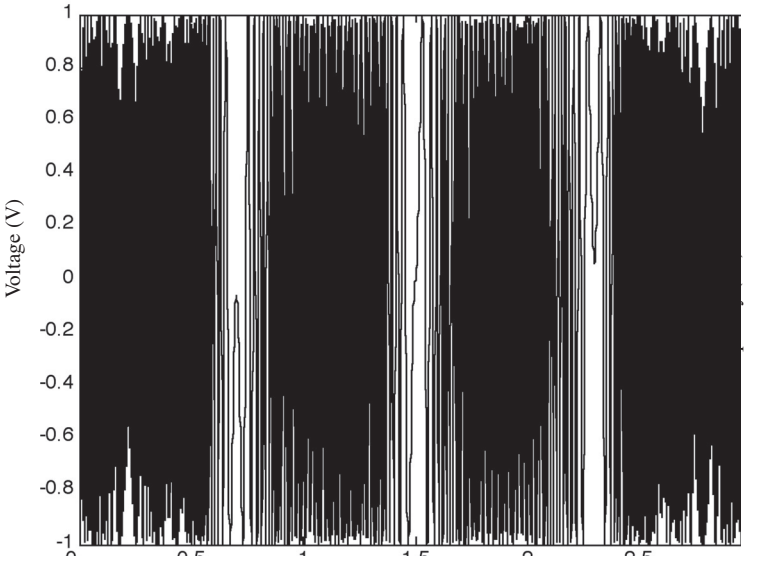

(a)

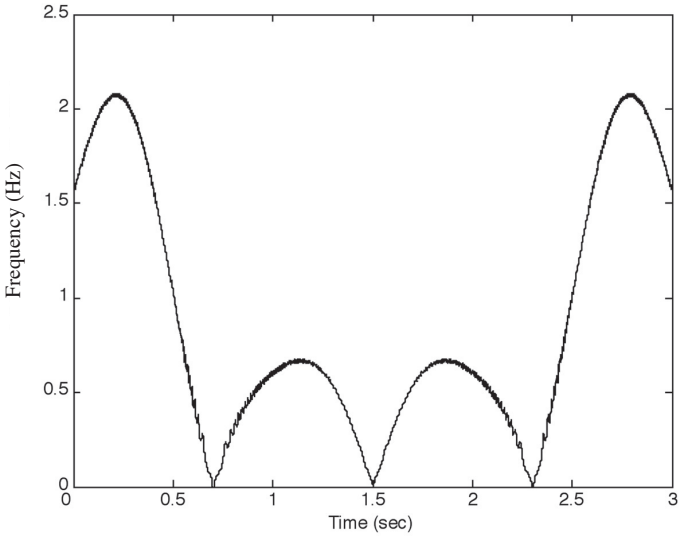

Fig. 7: Analytical signal from the three targets in (a) time domain and (b) its instantaneous frequency

$$z(t) = x(t) + i \times y(t) \tag{6}$$

Where $z(t)$ is the notation for the Hilbert Transform, and $y(t)$ represents the complex conjugate of $x(t)$. In this case, the instantaneous frequency is defined as the rate of phase change of the angle between y(t) and x(t), divided by 2π. *Figs. 6a* and *6b* show n theoretical ideal received Doppler signal, from one target and its frequency-time relationship, respectively. Another example in *Fig.*

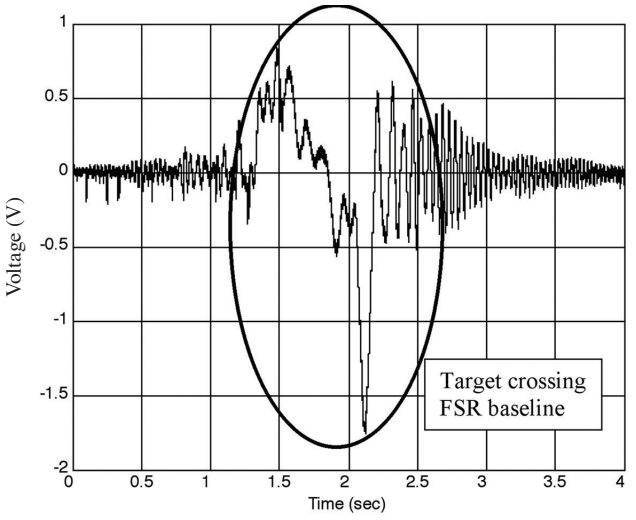

(a)

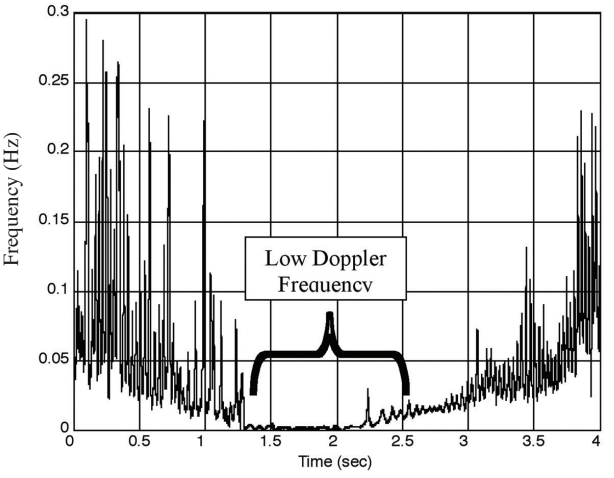

(b)

Fig. 8: Received signal from Layout 1 (a) time domain (b)its instantaneous frequency

7a shows the theoretical received signal from three targets and the frequency-time relationship is presented in *Fig. 7b*. The plots showing the instantaneous frequency-time relationship (*Figs. 6b* and *7b*) clearly show the target crossing the baseline (zero Doppler frequency) correlates with the position in the time domain signal (*Figs. 6a* and *7a*). Thus, this technique can be used for target detection in the FSR.

Next, the frequency–time relationship is produced by performing the Hilbert Transform to the real received signal from the experiment using Layout 1. *Fig. 8a* shows an example of the received signal in time domain from Layout 1. The frequency-time relationship, after the Hilbert Transform, is shown in *Fig. 8b*. Again, from the example, the proposed method and assumption were validated.

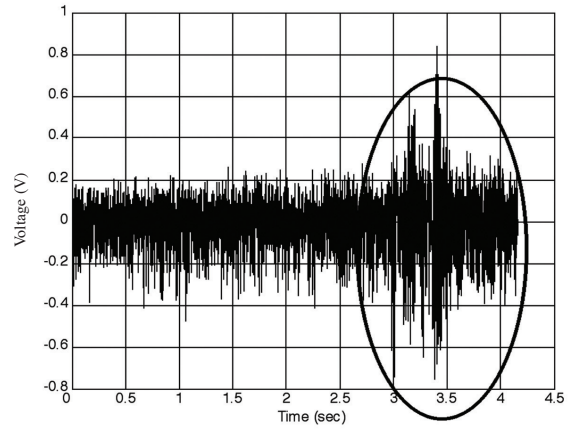

(a)

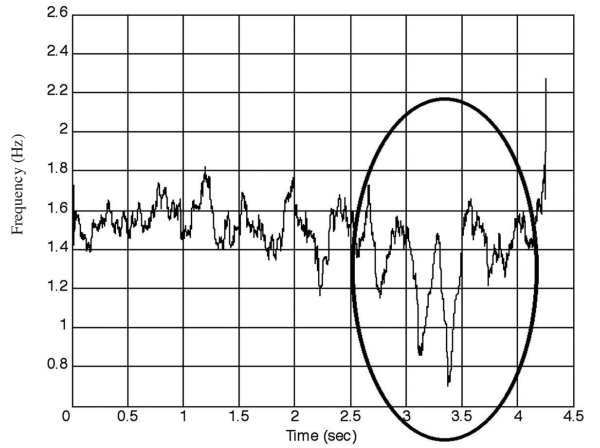

(b)

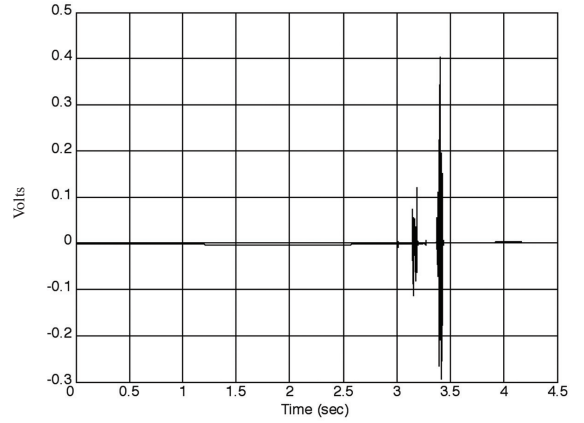

(c)

Fig. 9: Received signal from Layout 2 20m separation distance (a) time domain, b) Its instantaneous frequency, (c) Wavelet denoised received signal

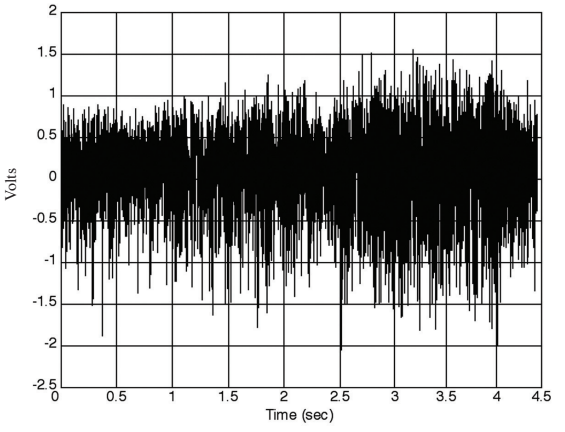

(a)

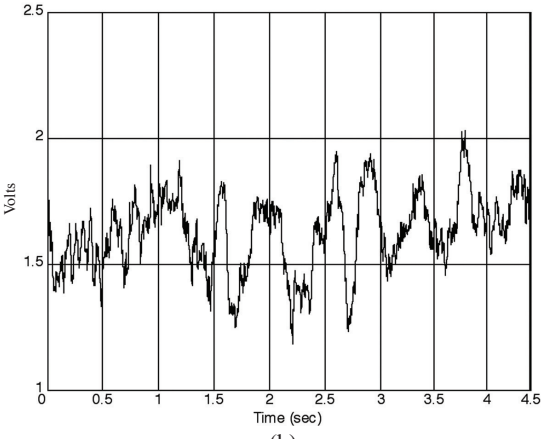

(b)

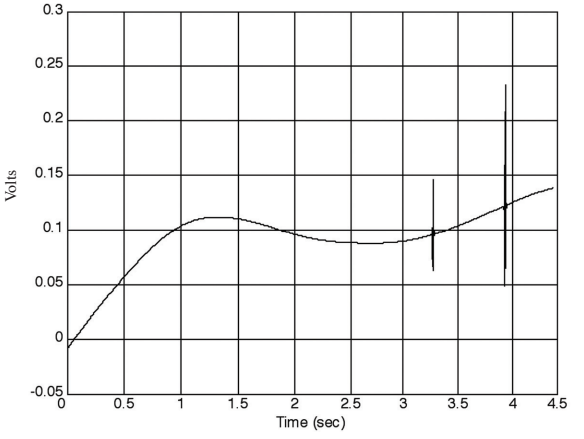

(c)

Fig.10: Received signal from Layout 2 20m separation distance (a) time domain (b) Its instantaneous frequency and (c)Wavelet denoised received signal

Zero and very low Doppler frequency is clearly seen from the trace in the graph of *Fig. 8b*. Thus, the detection of a target is possible and the crossing time can also be predicted.

The instantaneous frequency-time relationship, using the Hilbert Transform to this signal sample, does not give a huge significant contribution. This is due to the huge interruption on the time domain signal (*Fig. 8a*). Nevertheless, this exercise has at least shown a reliable assumption and a possibility to detect the presence of target using the proposed procedure. This is also amongst the first documented result to show the instantaneous frequency-time relationship in the practical FSR system for a better understanding.

The next step is to apply the same procedure to the FSR data, using the experimentation given in Layout 2. In this experiment, the transmitter-receiver distance was increased to ~40m and the antennas were placed directly on the ground. During the experimentation, two targets with a separation distance of approximately ~3m were crossing the baseline at a speed ~20km/h. The two targets were almost similar in shape and they had at least the same maximum height. *Fig. 9a* shows the received signal in time domain. The plot shows that the signals from the targets are under the influence of high noise and can barely be seen by human visualization.

Fig. 9b shows the trace of the instantaneous frequency–time relationship from the Hilbert Transform as in the previous case. This figure reveals a promising indicator, based on the two lowest frequencies, between 3 and 3.5 sec. The positions of these two minimum peaks do correlate with the expected target's signal in time domain. Each low peak represents each car which passes the FSR baseline. The result is considered good, provided the target existence is known beforehand. However, if these plots (*Fig. 9a*) are to be processed by an automatic detection, a few more parameters have to be taken into account, for example, the frequency threshold (acceptable lowest frequency) before any decision can be made, and the minimum difference between the frequency from the target and clutter. These factors will create uncertainties and false alarm in the radar system.

Based on these examples, if the transmitter receiver distance is further increased or transmitting signal power is reduced, or both, the Doppler information will completely be hidden and embedded inside the ground clutter. Thus, it is less efficient if the target existence is predicted using the frequency–time relationship. This relationship is illustrated in *Fig. 10* for the increased transmitter receiver distance, and *Fig. 11* for the reduced transmitted power. An example of these signals will be given in the subsequent section, while an alternative method to detect the existence of target in the FSR system will also be discussed.

DENOISING USING WAVELET

To overcome the uncertainties in decision making, a denoising technique of the received signal using wavelet is proposed. This procedure can increase the confidence in target detection in the FSR system. Lehmann and Teschlke (2001) gave an example of using the wavelet for denoising in a radar system. In this paper, the wavelet denoise was used to automatically remove both ground and intermittent clutters (air plane echoes) from wind profiler radar data.

The signal denoising using wavelet comprises of three steps, namely Decomposition, Threshold Detail Coefficients and Reconstruct. After the signal decomposition using wavelet transform, the signal is left with a set of wavelet coefficients which correlate to the high frequency sub-bands. These high frequency sub-bands consist of the details in the signal. If these details were small enough, they might be omitted without substantially affecting the main features of the signal. However, these small details are often associated with noise; therefore, by setting these coefficients to zero, the noise are essentially filtered out from the signal. This is the idea of thresholding, setting all subs band frequency coefficients which are less than a particular threshold to zero, and using these coefficients in an inverse wavelet transformation to reconstruct the signal.

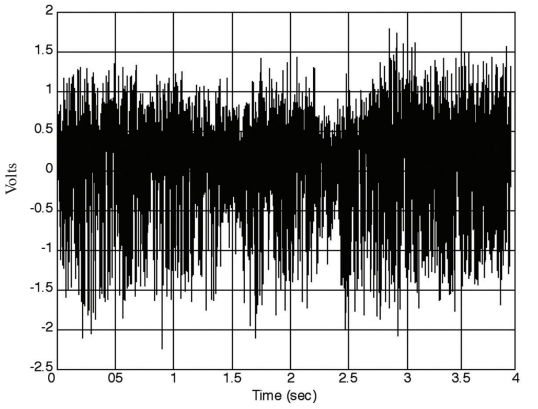

(a)

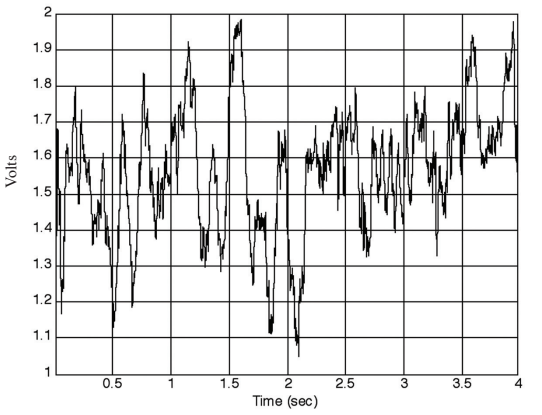

(b)

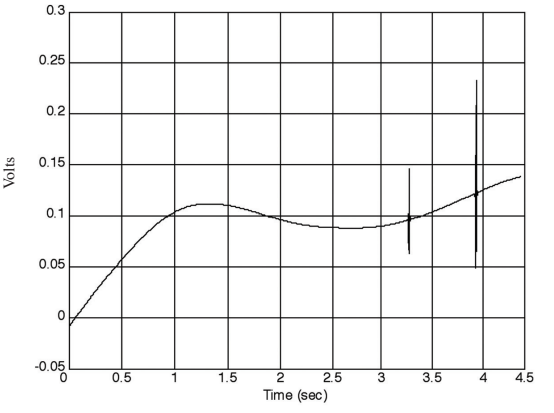

(c)

Fig. 11: Received signal from Layout 2 20m separation distance and reduced transmit power (0 dBm) a) time domain, (b) its instantaneous frequency, (c) Wavelet denoised received signal

The following sub-section explains the mathematical descriptions for the wavelet denoise, and how it is applied in the detection technique in the FSR. Let the first level of decomposition denoted by A_j where *j* is the number of decomposition, and assume $(A_k^j)_k \in z$ as the coordinates of the vector A_j and k could be time in this case.

The initialization is carried out using $A_k^0 = s(k)$, where *s(k)* is the signal value at time *k*. By equating s(t) = s(k), where s(t) is the received signal from target at the receiver, it is given by (RSA Raja Abdullah *et al*., 2003):

$$s(t) = \frac{k\lambda}{2\pi vt(d)} \sin\left(\frac{2\pi}{\lambda}\{\frac{vt}{d}\}\right) e^{-j\frac{4\pi}{\lambda}(d)} \tag{7}$$

Hence, we have

$$A = \sum_k A_k^{(j)} \phi_{j,k} \tag{8}$$

Where $\phi_{j,k}$ scaling function is used to calculate the approximations, and $A_k^{(j+1)}$ is the coordinate of the vector A_{j+1}, then

$$A_{J+1} = \sum_K A_K^{(J+1)} \phi_{J+1,K} \tag{9}$$

Where $A_k^{(j+1)}$ is calculated using the formula

$$A_K^{(J+1)} = \sum h_{n-2k} A_n^{(J)} \tag{10}$$

This formula resembles a convolution formula. Now let us define
$\tilde{h}(k) = h(-k)$, and $F^{(j+1)} = \sum_n \tilde{h}_{k-n} A_n^{(j)}$

The sequence $F^{(j+1)}$ is the filtered output of the sequence A^j by the filter $\tilde{h}$. Hence,

$$A_k{}^{(J+1)} = F_{2k}^{(j+1)} \tag{11}$$

We have to take the even index values of *F*, this is down sampling of the version $F^{(j+1)}$. The initialization is carried out using, $A_K^{(0)} = s(k)$ where *s(k)*is the signal value at time k. The details will follow the same procedure, but instead of filter *h*, filter *g* will be used. Setting to zero, the values above define the threshold, the final denoised signal will be:

$$s = A_j + \sum_{j \le J} D_J \tag{12}$$

Where D is the 'Detail' of the Decomposition.

By denoising the signal in *Fig. 9a*, the signal is left with two peaks and most of the high frequency noises have been filtered out, as shown in *Fig. 9c*. The position of the two very clear high peaks correlated with *Figs. 9a* and *9b*. This validates the denoising process and is adequate for target detection.

To test the feasibility of both the proposed procedures in target detection, similar experiment using Layout 2 had been conducted with the increased transmitter and receiver distance (*Fig. 10*) and also reduced transmit power (*Fig. 11*). This was done to make sure that the signal scattered from target had completely been masked by the clutter and noise. In this example, the scattered

signal was completely masked by the clutter and it was almost impossible to detect the existence of the target within the coverage area. This makes the detection using frequency-time relationship (*Figs. 10b* and *11b*) and denoising more challenging.

Using the denoising technique on the received signal, it is clear that there are two high peaks which correspond to the two targets, as shown in *Figs. 10c* and *11c*. This proves that the proposed technique has worked and successfully detected the target. All the signals, results and traces for the 'before' and 'after' denoising were verified using a video camera capturing the experimentation scene. During the experimentation, all the vehicles which passed through the sensor baseline were recorded using a video camera. This allowed the researchers to associate a captured vehicle signature with the respective vehicle.

Based on the analysis and the examples, the target detection in the FSR has been shown to be influenced by the level of power and the hardware used. This effect can be seen in the example using a high gain and narrow beam width antenna. In this case, the Doppler signature is clear due to the low noise levels and high SNR. In the second example, the detection process is more difficult when the antenna is replaced by low gain and wide beam width omni directional antenna with the same level of transmit power due to the low SNR. This factor becomes clearer when the transmit power is decreased, and it is impossible to detect the existence of a target directly without using an advanced signal processing to denoise the signal. Thus, signal processing using wavelet technique, which contains high pass and low pass filter coefficients in the example shown in this paper, has successfully denoised the complex signals.

CONCLUSIONS

In this paper, a signal processing and experimental study for extracting the Doppler signature in the FSR for ground target detection have been presented. The target signal under the influence of high clutter has successfully been detected using the proposed method. The detection using the Hilbert Transform is only applicable if the raw signal has significant difference from the average noise level, but detection using the wavelet denoising becomes more robust to any clutter and noise. The results again confirmed the feasibility of the FSR to be employed as an automatic ground target detection system. However, to make the FSR ready to be realized in real applications, more work still needs to be done, including practical cross range resolution in the FSR and an advanced classification technique.

REFERENCES

Abdullah, R., Cherniakov, M. and Jancovic, P. (2004). Automatic vehicle classification in Forward Scattering Radar. In *First International Workshop on Intelligent Transportation WIT* (pp. 7-12). Hamburg, Germany.

Blackman, A.B. and Runova, I.A. (1999). Forward scattering radiolocation, Bistatic RCS and Target Detection. In *Radar Conference*, *1999. The Record of the 1999 IEEE*, pp. 203-208.

Blackman, A.B., Ryndyk, A.G. and Sidorov, S.B. (2000). Forward Scattering Radar moving object coordinate measurement. *Proc. Int.Radar Conf*., pp. 678–682. Washington, DC, USA.

Boyle, R.J. (1994). Comparison of mononstatic and bistatic bearing estimation performance for low RCS targets. *IEEE Transactions on Aerospace and Electronic System, 30*(3), 962-968.

Chapurskiy V.V. and Sablin, V.N. (2000). SISAR: Shadow Inverse Synthetic Aperture Radiolocation. *International Radar Conference*, *The Record of the IEEE 2000 International*, pp. 322 – 328.

Cherniakov, M., Chapurskiy, V.V., Raja Abdullah, R.S.A., Jancovic, P. and Salous, M. (2004). Short-range Forward Scattering Radar, *International Radar Conference*, The Record of the IEEE International, pp. 322 – 328.

Cherniakov, M., Salous, Kostylev and Abdullah, R.S.A. (2005). Analysis of Forward Scattering Radar for ground target detection. *European Radar Conference*, pp.145 – 148.

Cherniakov, M., Abdullah, R.S.A.R., Jancˇovicˇ, P., Salous, M. and Chapursky, V. (2006). Automatic ground target classification using Forward Scattering Radar, *IEE Proc.- Radar Sonar Navig*., *153*(5), 427 – 437.

Chernyak. (1998). *Fundamentals of Multisite Radar Systems*. Gordon and Breach Science Publishers.

Chesnokov, Y.S. and Krutikov, M.V. (1996). Bistatic RCS of aircrafts at the forward scattering. Radar, 1996. *Proceedings, CIE International Conference of Radar*, pp. 156 – 159.

Glaser, J.I. (1985). Bistatic RCS of complex objects near forward scatter. *IEEE Transactions on Aerospace and Electronic System, AES-21*(1), 70-78.

Gould, D.M., Orton, R.S. and Pollard, R.J.E. (2002). Forward Scatter Radar detection. *RADAR 2002*, 15-17, pp. 36 – 40.

Jackson, M.C. (1986). The geometry of bistatic radar systems. *IEE Proceedings, 133*(7), 604-612.

Lehmann, V. and Teschlke, G. (2001). Wavelet based methods for improved wind profiler signal processing. *Annals Geophysical, 19*, 825-836(c). European geophysical society.

Marple, S.L. (1999). Computing the discrete-time analytic signal via FFT. *IEEE Transactions on Signal Processing, 47*(9), 2600-2603.

Raja Abdullah, R.S.A. and Cherniakov, M. (2003). Forward Scattering Radar for vehicles classification. *VehCom International Conference, VehCom2003*, pp. 73-78. Birmingham, UK.

Siegel, K.M. (1985). Bistatic radars and forward scattering. *National Conference Proceeding in Aeronautical Electronics*, pp. 286-290. Ohio.

Stimson, G.W. (1983). Introduction to Airborne Radar. Hughes Aircraft Company, El Segundo, California, pp. 3.

Willis N. J. (1995). Bistatic Radar. Technology Service Corporation.

ISSN: 0128-7680
Pertanika J. Sci. & Technol. **17 (2)**: 263 – 268 (2009)

Unusual Spawning Behaviour of the Horseshoe Crab (*Tachypleus gigas,* Müller) after the Tsunami along Orissa Coast, India

Anil Chatterji* **and Faizah Shaharom**
Institute of Tropical Aquaculture, Universiti Malaysia Terengganu,
21030 Kuala Terengganu, Terengganu, Malaysia
**E-mail: anilch_18@yahoo.co.in*

ABSTRACT

The central coast of Tamil Nadu, Andaman and Nicobar Islands, along with other regions, was severely hit by the tsunami on 26 December 2004. A strange spawning behaviour of the Indian horseshoe crabs (*Tachypleus gigas,* Müller) was observed after the tsunami disturbance. Along the northeast coast of India, the horseshoe crabs normally migrate towards the shore in large numbers coinciding with the tidal height and grain size of the sediment and spawn in nests made in sand. The spawning behaviour was normal until November 2004 and throughout that period about 35 to 45 nests in 200 m^2 of area of the breeding beach were examined. However, no nesting was observed from December 2004 to March 2005, i.e. after the occurrence of tsunami. The number of nests per 200 m^2 of area (~82) and the number of eggs per nest (750-1000 eggs) were increased considerably when the normal conditions were restored in April 2005. The absence of spawning migration, from December 2004 to March 2005, is totally an unusual behaviour and this happened for the first time during the past several years of the study period.

Keywords: Indian horseshoe crab, unusual spawning behaviour, tsunami

INTRODUCTION

Many of the Asian and Pacific developing countries are situated in the world's hazardous belts and they are vulnerable to natural disasters which occur periodically as a result of climatic and seismic activities (ESCAP, 1995). In the recent years, more and different kinds of natural disasters such as earthquakes, super cyclones, cloud bursts, floods and tsunami have occurred. These disasters kill thousands of people and destroy habitat as well as properties worth million of dollars each year. The rapid growth of the world's population and its increasing concentration along the coastal belt accelerate the problems of hazard, leading to both frequency and severity of natural disasters (ESCAP, 1995).

On 26 December 2004, the central coast of Tamil Nadu, Andaman and Nicobar Islands in India, along with several other countries in South-East Asia, were severely hit by the tsunami (*Fig. 1*). The massive tsunami was triggered by an underwater earthquake with a magnitude of about 9.3 Richter scale, off the coast of the northern Sumatra Island, Indonesia (Lay *et al.*, 2005). The impact of its tidal waves, measuring up to 7 m to 10 m high, caused seawater surges and severe flooding which led to widespread environmental and infrastructure damages along Nagapattinam and Cuddalore districts of India. Although several studies have been carried out to study on the impact of this particular disaster, no study has been carried out to investigate the behavioural changes of the inter-tidal and sub-tidal marine animals due to tsunami disturbance (Lay *et al.*, 2005). Therefore

Received: 3 March 2008
Accepted: 2 July 2008
*Corresponding Author

Fig. 1: A map of India (dots show tsunami affected areas)

an attempt was made to study the impact of tsunami on the spawning behaviour of the horseshoe crabs in the present study.

MATERIALS AND METHODS

In India, horseshoe crabs (*Tachypleus gigas*, Müller) are found in abundance along the Balramgari coast (Lat 21° 27'N, Long 87° 04' E) (Chatterji, 1994). They regularly migrate towards the shore in large numbers to spawn in nests made in sand, depending upon the tidal height (Chatterji *et al*., 1992). A 200 m^2 area at the Balramgari beach was regularly monitored by the researchers for the past several years to study the nesting behaviour of the horseshoe crabs. The nest of the horseshoe crab was a depression in the sand made by female brooders for laying their gametes. The number of depressions, along with number of eggs in each depression, was counted every time during the full moon tides at monthly intervals, and this was done regularly to study the nesting frequency of the horseshoe crabs. Replicate sediment samples were also collected from the nesting area during the low tide, while grain size analysis was done following the method as described by Chauhan and Chaubey (1989). The same area was monitored immediately after the tsunami disturbance, following the same protocol as described above.

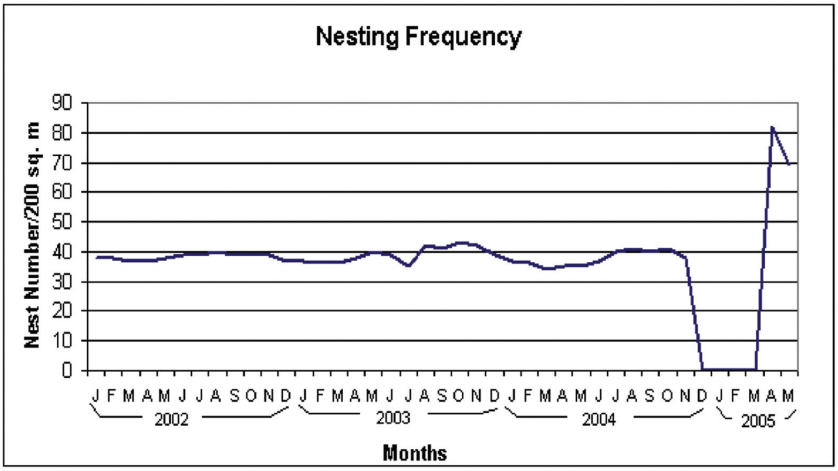

Fig. 2: The number of nests per 200 m² area, from January 2002 to May 2005

RESULTS

The breeding behaviour of the horseshoe crabs was found to be normal during January 2001 to November 2004 (*Fig. 2*). During these months, the tidal heights ranged from 2.53 to 2.99 mm, with the grain size of sand from 0.182 to 0.221 mm. Meanwhile, the average number of nests ranged from 35 to 45 in 200 m^2 of the area with the number of eggs varied from 18 to 258 in each nest. After the occurrence and disturbance of tsunami, not a single nest was found from December 2004 till March 2005 on the breeding beach of Balramgari (*Fig. 2*). Nevertheless, the re-appearance of nests on this beach was started only in April 2005, when surprisingly about 82 nests in 200 m^2 of the area were encountered. In each nest, about 750-1000 eggs were released by a single brooder, as compared to our previous observations whereby only 18-258 eggs $nest^{-1}$ were encountered. In May 2005, the same trend was repeated when 69 nests in 200 m^2 of the area, with a range of 550-990 eggs $nest^{-1}$ were observed. The tidal amplitude during these months was found to be between 2.60 and 2.85 m, whereas the sand grain size was between 0.182 and 0.221 mm. Although the condition of the beach was ideal for normal spawning during December 2004 to March 2005, surprisingly no spawning migration of the horseshoe crabs was observed after the tsunami. The absence of their nests from December 2004 to March 2005 was entirely an unusual behaviour which was observed for the first time during the past several years of the study period.

DISCUSSION

In India, though the impact of tsunami was not very bad along the coastal villages off Balramgari in Orissa, a strange spawning behaviour of the horseshoe crabs was observed after the occurrence of tsunami. In particular, the Balramgari coast has always experienced semidiurnal tides ranging between 215 and 325 cm. The intertidal exposure at Balramgari is large, and this can extend up to several kilometres, depending upon the changing tidal range. Thus the area has the characteristics of a tidal flat and provides a suitable ground for nest building of the horseshoe crabs. The dominant rains, associated with the southwest monsoon, subside after September and therefore, the beach provides a more suitable environment for sand deposition and this makes the beach ideal for spawning (Chatterji, 1994).

Plate 1: Breeding beach showing settlement of thick clay just after the tsunami

Plate 2: Breeding beach after the recovery of the breeding beach

In India, the horseshoe crabs breed for a prolonged period during the year on sandy beaches. In our previous study, spawning migration was observed to be directly related with the tidal amplitude and this occurred around the highest high water mark of the high tides of the new and full moon (Chatterji *et al*., 1992). The researchers also observed that the selection of the nesting sites by the horseshoe crabs was also related to the grain size of the sediment. For instance, *Tachypleus gigas* (Müller) appears to be selective and prefers a grain size ranging from 0.182 to 0.203 mm for nesting. Any increase in this range does not seem to favour nesting (Rudloe and Herrnkind, 1976). However, there were some unusual changes observed in the beach characteristics of Balramgari, and these were due to the seismic activities caused by tsunami making the beach unfavourable for nest building by the horseshoe crabs (Plate 1). This might have prevented the horseshoe crabs to migrate to the shore for breeding purposes. There could be another reason related to an increase in salinity due to a sudden penetration of giant sea waves into the coastal waters. This might have also

been one the reasons terminating the spawning. There was also a possibility that during December 2004 to April 2005 the horseshoe crabs might have shifted their breeding ground to an unknown place on the account of unfavourable condition along the Balramgari beach and once the beach became suitable they started migrating to the place again for breeding (Plate 2).

It has been a well known fact that there are some specific physical factors such as wave characteristic, seabed slope, beach gradient, near shore currents, geochemical and geophysical profiles which play an important role, singly or collectively, in the spawning migration of marine animals (Botton *et al*., 1988; Chatterji *et al*., 1996). Any major change in these factors, which are due to sudden disturbances of the sea, may affect the normal behavioural activity of these animals. Moreover, the relationship between the breeding activities and the characteristics of the beach sediment has been discussed in detail in several other marine species (Henning *et al*., 1982; Fleming and Fricke, 1983).

There have been only a few observations made along the affected areas in Sri Lanka to study on the impacts of tsunami on the behaviour of marine animals (Bambaradeniya, 2005; Sandun *et al*., 2005). A heavy mortality was encountered in the estuarine fishes due to the sudden increase in salinity in Rekawa lagoon in Sri Lanka after the tsunami (Bambaradeniya, 2005). It was also found that many species of the marine fishes, which were not previously inhabitants of this lagoon, are now occurring in the water (Sandun *et al*., 2005). A large number of turtle nests in the Rekawa beach were also been destroyed by the tsunami waves. The nesting of the Green Turtle (*Chelonia mydas*) and the Olive Ridley (*Lepidochelys olivaceae*) was also severely affected. Now, these turtles have started migrating towards the beaches to lay eggs, and this probably indicates a gradual recovery of the normal nesting behaviour. However, the number of migrating turtles for breeding was reported to have reduced considerably as compared to the pre-tsunami situation (Sandun *et al*., 2005).

CONCLUSIONS

There have been several attempts made by some scientists to study the behaviour of the animals before or after the occurrence of earthquakes and tsunamis. In a country like Japan, which is considered to be one of the world's most earthquake-prone countries, researchers have been continuing for the past several decades, to understand the behaviour of animals in relation to sudden disturbances caused by this natural disaster. Japanese scientists are primarily interested in knowing and discovering specific factors which responsible for the changes in the normal behaviour of the animals, before or after the earthquakes. Some American seismologists are still sceptical about these studies, although there have been documented cases of strange animal behaviour prior to the earthquakes. The United States Geological Survey, which provides scientific information about the earth, states that a reproducible connection between a specific behaviour of the animal and the occurrence of an earthquake or tsunami has never been properly documented. Thus, more researches are needed to determine and understand the strange behaviour of the animals on the account of earthquakes and tsunami. These researches in the near future may be useful as a prediction tool to forecast earthquakes and tsunami.

ACKNOWLEDGEMENTS

The author is grateful to the Director of the National Institute of Oceanography, Goa, for providing the necessary laboratory facilities, to Dr. S. Z. Qasim for his valuable comments on the manuscript and Ms Reena Rodrigues of NIO, Goa, for the help she has rendered in the preparation of this manuscript. I am also thankful to the Life Science Research Board of Defence Research Development Organization, Government of India, for providing the financial support to undertake the work.

REFERENCES

Bambaradeniya, C.N.B. (2005). Impacts of the recent tsunami on the Bundala national Park – the first Ramsar Wetland in Sri Lanka, IUCN – The World Conservation Union, Sri Lanka Country Office.

Botton, M.L., Loveland, R.E. and Jacobsen, T.R. (1988). Beach erosion and geochemical factors: influence on spawning success of horseshoe crab (*Limulus polyphemus*). *Marine Biology, 99***,** 325-332.

Chatterji, A., Vijayakumar, R. and Parulekar, A.H. (1992). Spawning migration of the horseshoe crab, *Tachypleus gigas* (Muller), in relation to lunar cycle. *Asian Fisheries Science, 5***,** 123-128.

Chatterji, A. (1994). The Horseshoe crab − A Living Fossil. A Project Swarajya Publication (p. 157).

Chatterji, A., Parulekar, A.H. and Qasim, S.Z. (1996). Nesting behaviour of the Indian horseshoe crab, *Tachypleus gigas* (Müller) (Xiphosura). In S.Z. Qasim and G.S. Roonwal (Eds.), *India's Exclusive Economic Zone* (p. 142). New Delhi.

Chauhan, O.S. and Chaubey, A.K. (1989). Comparative studies of the moment, graphic studies and phi measures on the sand of the east coast beaches, India. *Sedimentary Geology, 65*, 183-185.

ESCAP. (1995). The State of the Environment in Asia and the Pacific 1995. *ESCAP*. Bangkok.

Fleming, J.H. and Fricke, A.H. (1983). Beach and near shore habits as a function of internal geometry, primary sediment structures and grain size. In A. Malachlan and A. Erasmus (Eds.), *Sandy Beaches Ecosystem* (p. 115-132).

Henning, H.K., Ericke, A., Greenwood, H.P.J. and Eagle, G.A. (1982). Relationship between meio-faunal population densities and physiochemical properties of unpolluted beaches. *Environmental Monitoring and Assessment, 1*, 337-344.

Lay, T., Kanamori, H., Ammon, C., Nettles, M., Ward, S., Aster, R., Beck, S., Bilek, S., Brudzinski, M., Butler, R., Deshon, H., Ekström, G., Satake, K. and Sipkin, S. (2005). The Great Sumatra-Andaman Earthquake of December 26, 2004. *Science*, *308*, 1127–1133**.**

Rudloe, A. and Herrnkind, W. F. (1976). Orientation of *Limulus polyphemus* in the vicinity of breeding beaches. *Marine Behavioural Physiology, 4***,** 75-89.

Sandun, M., Perera, J., Bambaradeniya, C.N.B., Ekanayake, S.P. and Roshan, K.V. (2005). Impacts of the recent tsunami on the Rekawa proposed coastal sanctuary and turtle refuge, IUCN – The World Conservation Union, Sri Lanka Country Office.

ISSN: 0128-7680
Pertanika J. Sci. & Technol. **17 (2)**: 269 – 289 (2009)

Study of CNG Combustion Under Internal Combustion Engines Conditions Part I: Using Quasi-Dimensional Modelling

Y. Bakhshan[1*] and Shahrir Abdullah[2]
[1]Department of Mechanical Engineering,
University of Hormozgan,
P.O.Box 3995,
[2]Department of Mechanical and Material Engineering,
Universiti Kebangsaan Malaysia,
43600 UKM Bangi, Selangor, Malaysia
[*]E-mail: y_bakhshan@yahoo.com

ABSTRACT

An in-house quasi-dimensional code has been developed which simulate the overlap, intake, compression, combustion, as well as expansion and exhaust processes of a homogeneous charged internal combustion engine (ICE). A detailed chemical kinetic mechanism, constituting of 39 species and 148 elementary reactions, has been used in conjunction with above code to study the combustion of CNG under IC engine conditions. Two different criteria, based on pressure rise and mass of fuel burned, are used to detect the onset of ignition. Parametric studies are conducted to show the effect of compression ratio, initial pressure, intake temperature and equivalence ratio, on the time of ignition and fuel burning rate. The results obtained from the modelling show a good agreement with the experimental data.

Keywords: Natural gas, auto-ignition, quasi-dimensional, chemical kinetic, modelling

NOTATION

θ	Crank angle (Deg.)
φ	Equivalence ratio
C_v, C_p	Specific heat capacity (Kj/Kg.K)
A_v	Area (m^2)
h	Enthalpy (Kj/Kg)
h_f	Enthalpy of formation (Kj/Kg)
A	Air (Kg)
B	Cylinder bore (m)
F	Fuel (kg)
W	Molecular weight (Kg)
m	Mass (Kg)
$\dot{m}_i$	Mass flows rate into the cylinder (Kg/s)
$\dot{m}_e$	Mass flows rate out of the cylinder (Kg/s)
ρ	Density (Kg/m^3)
V	Volume (m^3)

Received: 3 March 2008
Accepted: 25 February 2009
[*]Corresponding Author

t Time (s)
T Temperature (K)
$E_{fn,rn}$ Activation energy (J/mol)
$\beta_{fn,rn}$ Reaction constant
K_{fn},K_{rn} Reaction rate Constants

SUBSCRIPTS AND SUPERSCRIPTS

g Gas
fn Forward
rn Backward

ABBREVIATIONS

NOx Oxides of nitrogen
TDC Top dead center
ATDC After top dead center
BBDC Before bottom dead center
BTDC Before top dead center
ABDC After bottom dead center
ICE Internal combustion engine
CNG Compressed natural gas

INTRODUCTION

Natural gas is an economical and clean burning fuel, whose advantages as an alternative fuel for internal combustion engines have been well documented (Papageorgakis, 1997; Emad Boshra Fawzy Khalil, 2000; Bade Shrestha, 1999). Experiments in a combustion bomb have shown that auto-ignition of natural gas, under diesel-like conditions, requires a temperature as high as 1100-1200K (Papageorgakis, 1997). This high temperature requirement mandates that either a high compression ratio (about 23:1) or a high intake air temperature be used, both of which have negative effects on the performance and durability of engine. Obviously, knowing at what conditions of temperatures, pressures, and compositions, a methane-air mixture can have auto-ignition, or whether ignition assists in the form of glow plug, is very important. A fundamental understanding of the thermodynamics and fuel composition-related factors influencing ignition in internal combustion engines can only be obtained from a detailed study of the processes leading up to auto-ignition. However, the inherent transient nature of this starting process, with reactants and evolving towards a steadily burning flame, makes its theoretical treatment difficult. Recourse must almost always be made the numerical techniques involving the solution time-dependent equations of mass, momentum and energy which include the effect of chemical reactions and account for molecular transport, thermodynamics and convection. The usual approach used in studying the problem of ignition has either been to ignore the details of chemistry or to ignore the details of flow, the overriding concern being the enormous computational costs involved in combining the two, while the importance of detailed chemistry in homogeneous studies of ignition and flame propagation is well-documented (Emad Boshra Fawzy Khalil, 2000). Sloane and Ronny (Zhou, 1993) showed that although properly-calibrated one-step models are able to describe flame speed for planar flame propagation reasonably well, they are very inadequate in accurately predicting the minimum ignition energy and induction time. In fact, the induction time for homogeneous ignition of methane-air mixture, predicted using the one-step models, was about 60 to 1500 times lower than the one predicted using a detailed kinetic mechanism over a range of temperatures (1500 to 2222 K) (Zhou, 1993).

The objectives of this work were to explain the predictive ability of the coupled model in simulating the auto- ignition of natural gas injected in an ICE, and to study the effect of important parameters on the ignition of a CNG engine.

GOVERNING EQUATIONS

Quasi-Dimensional Engine Simulation

This simulation starts with a thermodynamic-based in-cylinder model. The structure of this type of engine simulation is as follows. The model divides the complete cycle into overlap, intake, compression, combustion, expansion and exhaust processes. Some of the applied equations in this simulation are as follow:
Work is defined by:

$$\dot{W} = P\dot{V} \tag{1}$$

and specific enthalpy by

$$\dot{h} = C_P\dot{T} + \frac{\partial h}{\partial P}\dot{P} + \frac{\partial h}{\partial \varphi}\dot{\varphi} \tag{2}$$

State equation:

$$\begin{aligned} &PV = MR_gT \\ &\frac{\dot{P}}{P} + \frac{\dot{V}}{V} = \frac{\dot{M}}{M} + \frac{\dot{T}}{T} \\ &R_g = R_g(T,P,\varphi) \end{aligned} \tag{3}$$

Energy equation for an open system:

$$\dot{E} = \dot{Q} - \dot{W} + \dot{M}_{in}h_{in} - \dot{M}_{out}h_{out} \tag{4}$$

The volume constraint is given by:

$$\dot{V} = \sum_{i=1}^{n} \dot{V}_i \tag{5}$$

and the equivalence ratio is:

$$\dot{\varphi}_i = \frac{\varphi_i(t+\Delta t) - \varphi(t)}{\Delta t} \tag{6}$$

and,

$$\varphi_i(t+\Delta t) = \frac{F_i / A_i}{(F/A)_s} \tag{7}$$

Where, F_i and A_i are the quantity of fuel and air, respectively.

Gas Exchange Model

A one-dimensional quasi-steady compressible flow model is used to describe the gas exchange between the engine cylinder and intake and exhaust manifolds.

The governing equations can be written as follows:

$$\dot{m} = C_v A_v \left(\frac{RT_o}{P_o}\right)\left(\gamma RT_o\right)^{1/2} * \left\{\left(\frac{2}{\gamma-1}\right)\left[\left(\frac{P_2}{P_o}\right)^{2/\gamma} - \left(\frac{P_2}{P_o}\right)^{\frac{\gamma+1}{2}}\right\}^{\frac{1}{2}} \quad (8)$$

For choked flow

$$\dot{m} = C_v A_v \left(\frac{RT_{oc}}{P_{oc}}\right)\left(\gamma RT_o\right)^{1/2} * \left\{\left(\frac{2}{\gamma+1}\right)^{\frac{\gamma+1}{\gamma-1}}\right\}^{\frac{1}{2}} \quad (9)$$

More details about the quasi-dimensional modeling can be found in other papers by authors in references (Mansouri and Bakhshan, 2000; Mansouri and Bakhshan, 2001; Mansouri and Heywood, 1980; Mansouri and Bakhshan, 2000; Bakhshan, Karim and Mansouri, 2002; Bakhshan, Karim and Mansouri, 2003).

Chemical Kinetic Modelling

There has been a significant and progress made in recent years in the status of chemical kinetic modelling of the combustion of hydrocarbon fuels under engine-like conditions. These enable the derivation of comprehensive chemical kinetic models for hydrocarbons. Such schemes can be incorporated into a variety of predictive models so as to analyse the performance of engine under operating and design conditions, with a reasonable level of confidence. They may also be used to validate the results of other models which employ only reduced kinetic schemes for a wide range of fuel mixtures commonly encountered in natural and industrial gases.

In this investigation, a scheme with 39 species (Appendix A) and 148 elementary reactions (Appendix B) was used for a kinetic scheme represented mathematically by the set of elementary reactions:

$$\sum_{m=1}^{M} \upsilon'_{mn} \chi_m \Leftrightarrow \sum_{m=1}^{M} \upsilon''_{mn} \chi_m \quad (10)$$

Where,

υ'_{mn}, υ''_{mn} are stoichiometric coefficients of the *mth* species appearing in the reactants and products of the *nth* reaction, respectively, and X is the chemical presentation of species m taking part in the reaction.

With definition

$$\dot{C_m} = \sum_{n=1}^{N} \upsilon'_{mn} k_{rn} \prod_{m=1}^{M} [\mathrm{X}_m]^{\upsilon'_{mn}} + \sum_{n=1}^{N} \upsilon''_{mn} k_{fn} \prod_{m=1}^{M} [\mathrm{X}_m]^{\upsilon'_{mn}} \quad (11)$$

$$\dot{D_m} = \sum_{n=1}^{N} \upsilon'_{mn} k_{fn} \prod_{m=1}^{M} [\mathrm{X}_m]^{\upsilon'_{mn}} + \sum_{n=1}^{N} \upsilon''_{mn} k_{rn} \prod_{m=1}^{M} [\mathrm{X}_m]^{\upsilon''_{mn}} \quad (12)$$

The rate of production or destruction of species can be calculated as follow:

$$\dot{\rho_m} = \dot{\omega_m} W_m \tag{13}$$

$$\dot{\omega_m} = \dot{C_m} - \dot{D_m} \tag{14}$$

Where the k_{fn} and k_{rn} are forward and backward reaction rate constants and are given as follow:

$$k_{fn} = A_{fn} T^{\beta_{fn}} \exp\left(-\frac{E_{fn}}{RT}\right) \tag{15}$$

$$k_{rn} = A_{rn} T^{\beta_{rn}} \exp\left(-\frac{E_{rn}}{RT}\right) \tag{16}$$

By considering the enthalpy of the formation of each species, the heat release from the chemical reactions can therefore be calculated in each crank angle. The chemical heat release term in the energy equation is given by:

$$\dot{Q_c} = \sum_{n=1}^{N} Q_n \dot{q_n} \tag{17}$$

Where Q_n is the negative of the heat of reaction at a reference temperature, given by:

$$Q_n = \sum_{m=1}^{M} (\upsilon'_{mn} - \upsilon''_{mn})(\Delta h^{\circ}_f)_m W_m \tag{18}$$

$$\dot{q_n} = k_{fn} \prod_{m=1}^{M} [\mathrm{X}_m]^{\upsilon'_{mn}} - k_{rn} \prod_{m=1}^{M} [\mathrm{X}_m]^{\upsilon''_{mn}} \tag{19}$$

$$\dot{Q_c} = \sum_{n=1}^{N} \left[\sum_{m=1}^{M} (\upsilon'_{mn} - \upsilon''_{mn})(\Delta h^{\circ}_f)_m W_m \right]_n \dot{q_n} \tag{20}$$

$$\dot{Q_c} = - \sum_{m=1}^{M} \dot{\omega_m} (\Delta h^{\circ}_f)_m W_m \tag{21}$$

RESULTS AND DISCUSSION

In this investigation, a complete cycle simulation of the physical processes in motored engine was initially developed. For this, the Pride 1300cc engine was chosen and its data are shown in Table 1. After the zero-dimensional code had been developed, it was validated using the experimental data which were determined in the MEGA-MOTORS Company on the above engine.

TABLE 1
Engine data

Cylinder bore	7.1cm
Connecting rod	13.6cm
Stroke	8.36cm
Clearance volume	$38cm^3$
Piston cup radius	1.34cm
Inlet valve open(IVO)	14BTDC
Inlet valve close(IVC)	52ABDC
Exhaust valve open(EVO)	52BBDC
Exhaust valve close(EVC)	14ATDC
Inlet valve diameter	3.2cm
Exhaust valve diameter	2.8cm
Maximum valve lifting	8.5mm

In order to validate the quasi-dimensional code, the calculated in-cylinder pressure was compared with the experimental data presented in *Fig. 1*. The calculated pressure is in good agreement with the experimental data and the prepared program can be used for other studies in motored engine. *Fig. 2* shows the variations of the temperature and pressure of the in-cylinder gas of a Pride engine through its operating cycle. The detailed chemical kinetic mechanism was coupled with the zero-dimensional code after its validation and the results were extracted in three cases:

1. Constant pressure
2. Constant volume
3. In a motored engine

Fig. 3 shows the bulk temperature variation in a constant pressure case. The temperature rise at the ignition point shows the start of CNG combustion and this combustion will continue up to the equilibrium point, where the maximum temperature will be obtained. In this investigation, the experimental data derived by Zhou *et al.* (1993) were used to validate the calculated data. *Figs. 4* and *5* show the variations of H_2O, H_2, CO and CO_2 species concentrations with equivalence ratio. A good agreement was obtained between the calculated concentrations and the experimental data, and the maximum error is about 2 percent in these curves.

The auto-ignition time variation with equivalence ratio is shown in *Fig. 6*. As depicted in the figure, a good agreement is shown between the model and experimental data in the range of spark ignition engines operation (0.8~1.4). With the increasing equivalence ratio, the initial mass of the natural gas in the mixture increases and the auto-ignition time decreases. *Fig. 7* shows the equilibrium temperature variations with the equivalence ratio and the maximum temperature is obtained at the stoichiometric condition ($\varphi \sim 1.0$). *Figs. 8, 9* and *10* show the important effects of the parameters (initial temperature, initial pressure and equivalence ratio) on the auto-ignition time in either constant volume or constant pressure. With the increase in all the three parameters T_i, P_i and φ, the auto-ignition time decreases but the effect of the initial temperature on the auto-ignition is very important because the dependence of the reaction rates on temperature is high. With the increase in the initial temperature, the kinetic energy of the species and the number of collisions between species also increases rapidly, while the combustion starts much earlier than the other cases. Nevertheless, it is crucial to noted increasing the intake temperature will decrease the volumetric efficiency and output power of the engine.

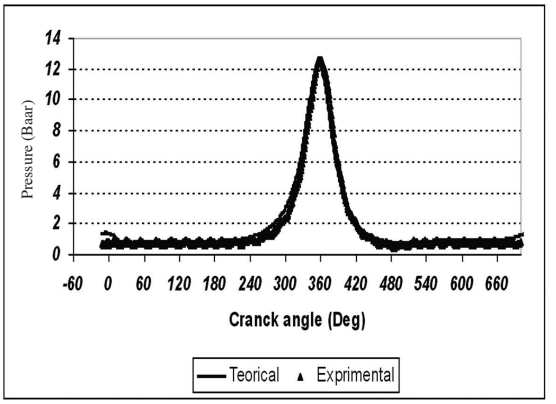

Fig. 1: The comparison between the calculated in-cylinder pressure and the experimental data

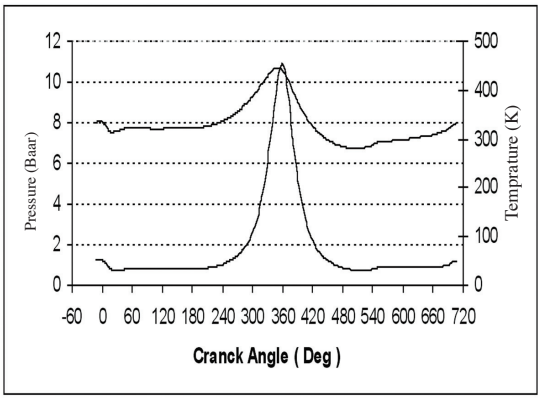

Fig. 2: Variation of calculated in-cylinder pressure and temperature through the engine cycle

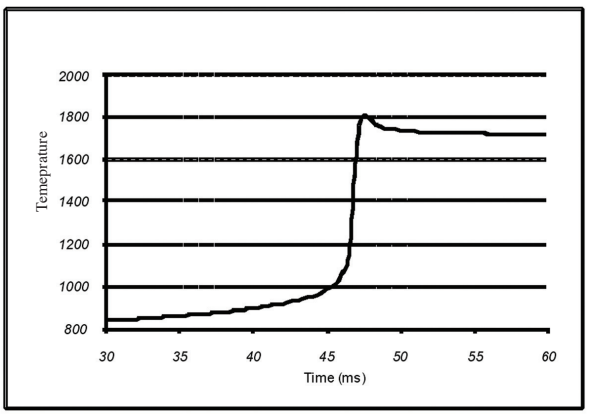

Fig. 3: Variation of temperature in constant pressure with considering the chemical kinetic vs. time at equivalence ratio (φ=2.5)

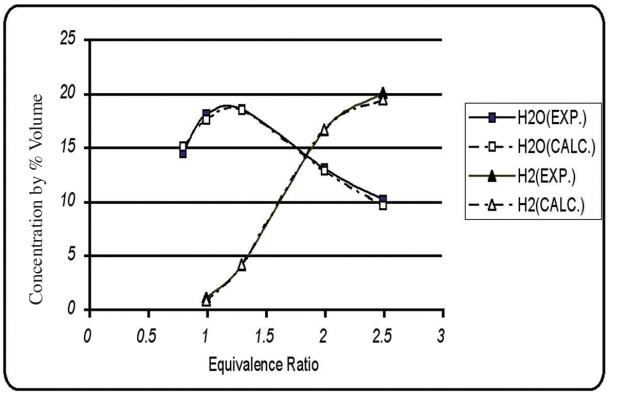

Fig. 4: Comparison of calculated concentration of H_2O, H_2 species with experimental data at constant pressure vs. equivalence ratio

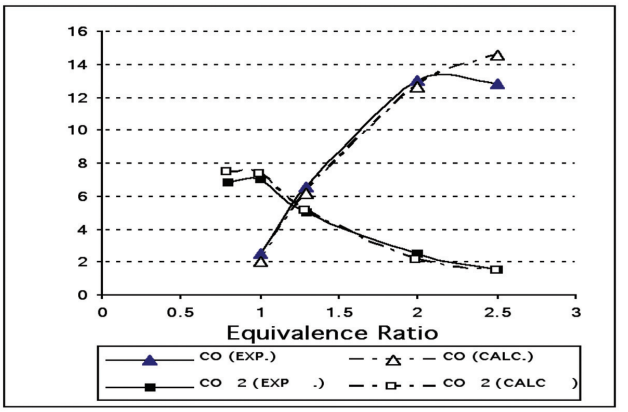

Fig. 5: Comparison of calculated concentration of CO_2, CO species with experimental data at constant pressure vs. equivalence ratio

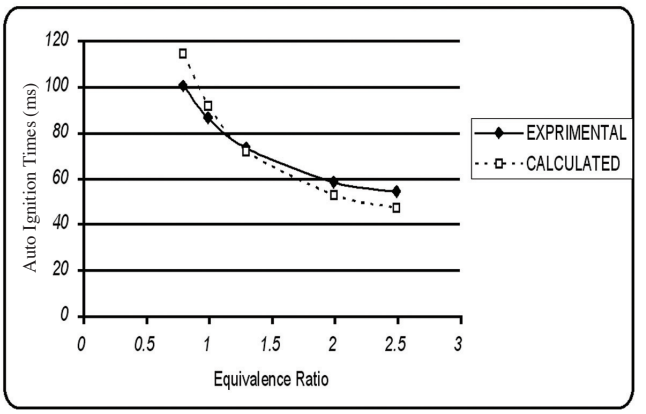

Fig. 6: Effect of equivalence ratio on auto-ignition time in constant pressure

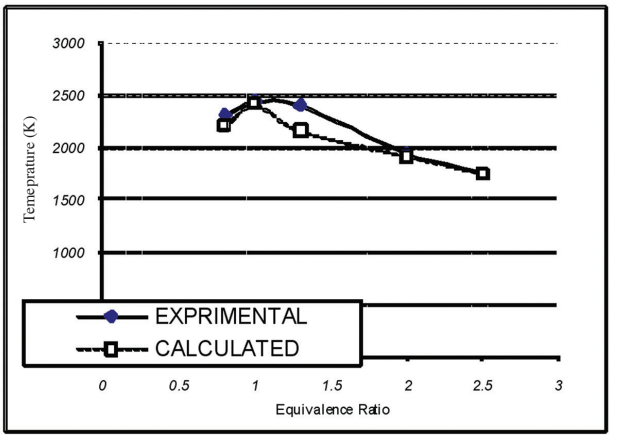

Fig. 7: Variation of equilibrium temperature after combustion with equivalence ratio

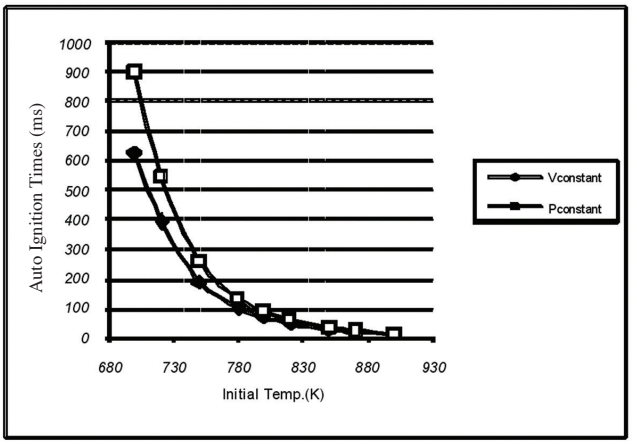

Fig. 8: Effect of initial temperature on auto-ignition time

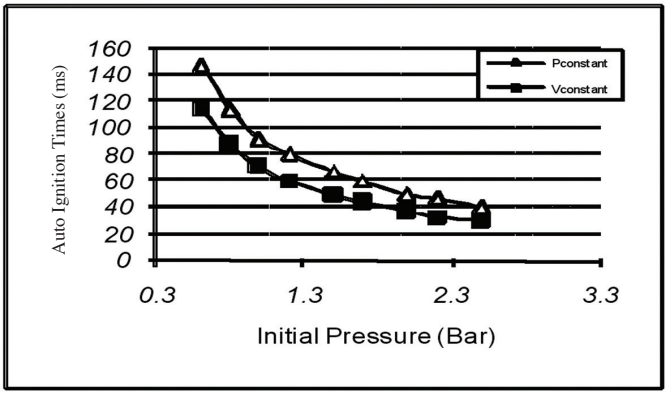

Fig. 9: Effect of initial pressure on auto-ignition time

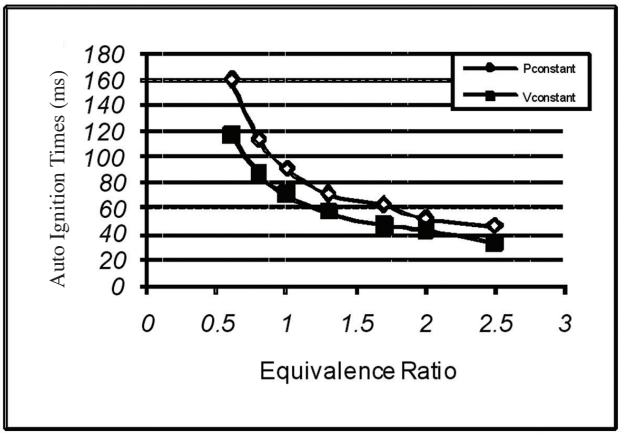

Fig. 10: Effect of equivalence ratio on auto-ignition time

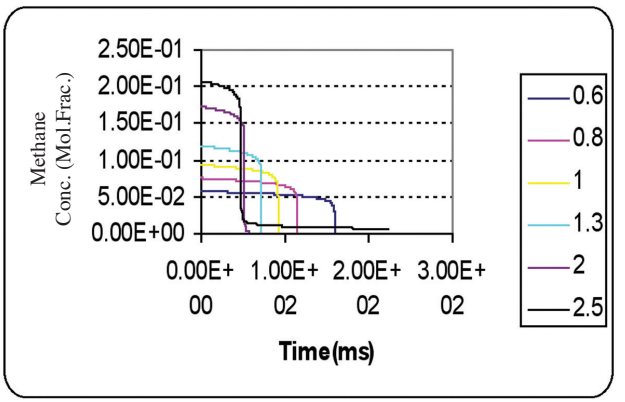

Fig. 11: Variation of CH4 concentration versus time at different equivalence ratios

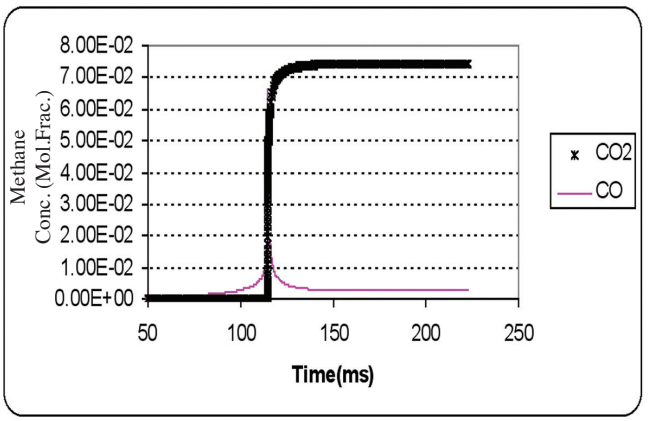

Fig. 12: Variation of CO2 and CO concentration with time in the combustion chamber (Lean mixture φ=0.8)

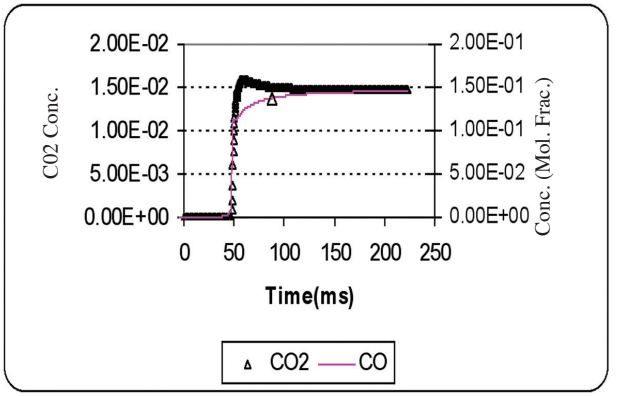

Fig. 13: Variation of CO_2 and CO concentration with time in the combustion chamber (Rich mixture φ=2.5)

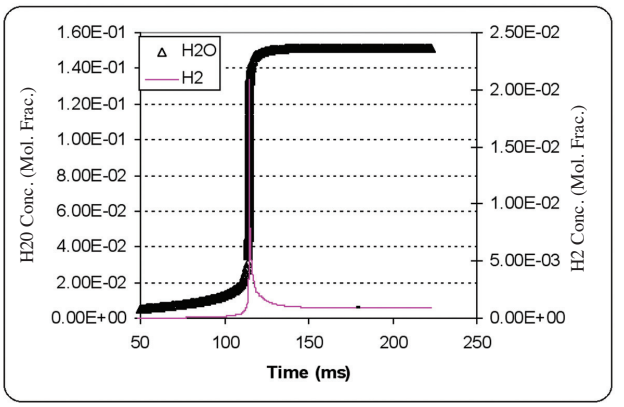

Fig. 14: Variation of H_2O and H_2 concentration with time in the combustion chamber (Lean mixture φ=0.8)

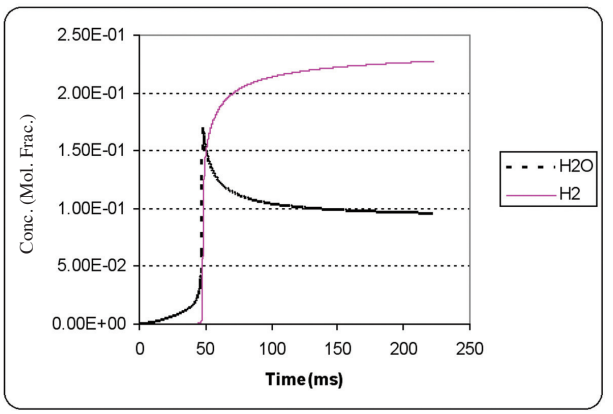

Fig. 15: Variation of H_2O and H_2 concentration with time in the combustion chamber (Rich mixture φ=2.5)

Fig. 11 shows the CH_4 concentration with time at different equivalence ratios. The sudden decrease of methane mass indicates the start of combustion and the auto-ignition point; this shows that the method can be used as a criterion to detect the auto-ignition. *Fig. 12* shows the variation of CO and CO_2 concentrations with time. It was found that the CO value increased rapidly at the start of combustion, but after the combustion completion, the oxidation of CO had taken more speed and its concentration would therefore decrease. Similarly, the CO_2 concentration will increase through oxidation of CO. *Fig. 13* shows the variation of both the CO and CO_2 concentrations in a rich mixture. Meanwhile, *Figs. 14* and *15* show the variation of H_2O and H_2 species in the lean and rich mixtures.

The nitrogen oxides (NOx) are important pollutants in internal combustion engines. The variation of nitrogen oxides (NO_x) are shown in *Fig. 16*. At the stoichiometric point, the concentrations took the maximum values and this was a result of higher combustion temperature at this condition. When the mixture is richer, the concentration of oxygen decreases, while the maximum temperature as well as the concentrations of NOx will decrease, whereas, when the mixture is leaner, the maximum temperature decreases. The variations of OH, H and O concentrations with equivalence ratio are shown in *Fig. 17*. In the combustion of methane–oxygen mixture, the OH radical has important role than H radical; while in the combustion of methane, air the role of H radical is further. This is shown in *Fig. 17*, in which the rich mixture in the production of H radical is further than the OH radical. The stable intermediate species of C_2H_2, C_2H_4 and C_2H_6 concentration variations with equivalence ratio are shown in *Fig. 18*, while some concentration variations of species are shown in *Fig. 19*. Using the detailed chemical kinetic presented for the motoring cycle of an engine (1300cc), a part of pressure and temperature rise of in-cylinder gas can be from the heat release from the chemical reactions in each crank angle. In each crank angle, the following can therefore be written:

$$\Delta P \text{ (total)} = \Delta P \text{ (piston motion)} + \Delta P \text{ (heat release from chemical reactions)} \quad (22)$$

$$\Delta T \text{ (total)} = \Delta T \text{ (piston motion)} + \Delta T \text{ (heat release from chemical reactions)} \quad (23)$$

The rise in pressure and temperature at the ignition point can be used as the criteria to detect that particular point. *Figs. 20* and *21* compare the pressure and temperature variations in a motored engine with the application of detailed chemical kinetic and without its application. The separation of the curves at the ignition point is illustrated in the figures.

The variations of ΔT and ΔP, adjusted with the heat release from the chemical kinetic reactions, are shown in *Fig. 22*. When the combustion was started at ignition point, the values of ΔT and ΔP increased rapidly. The effect of compression ratio on ΔP is shown in *Fig. 23*; the increase in the compression ratio caused the ΔP to increase. The variations in the temperature of the in-cylinder gas are shown in *Fig. 24* at two different equivalence ratios. This figure shows that no combustion occurs at this compression ratio and pressure. As discussed in the earlier section, the initial temperature is one of the important parameters which greatly affects the auto-ignition time. *Fig. 25* shows the effect of the initial mixture temperature on the auto-ignition on the pressure curve at same compression ratios and other engine operating parameters. When the temperature is increased, the activation energy will also increase and the ignition occurs at the early stage of the compression.

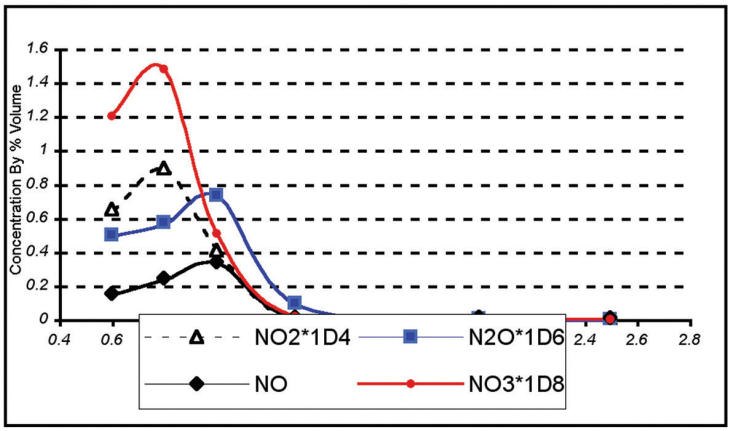

Fig. 16: Variation of nitrogen oxides (NOx) concentrations with equivalence ratio

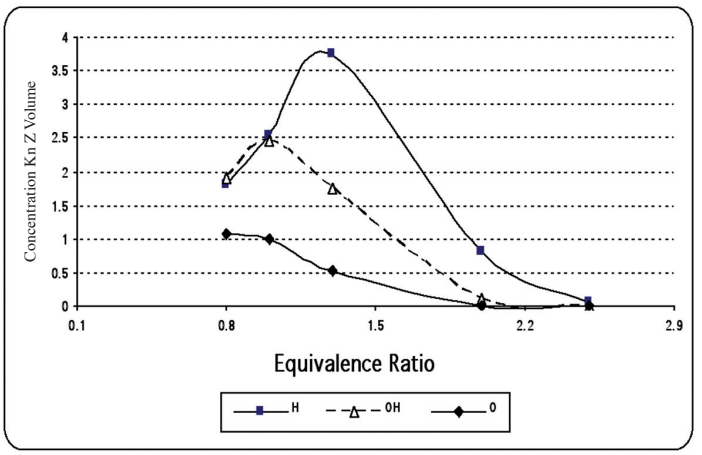

Fig. 17: Variation of H, OH and O radicals values with equivalence ratio

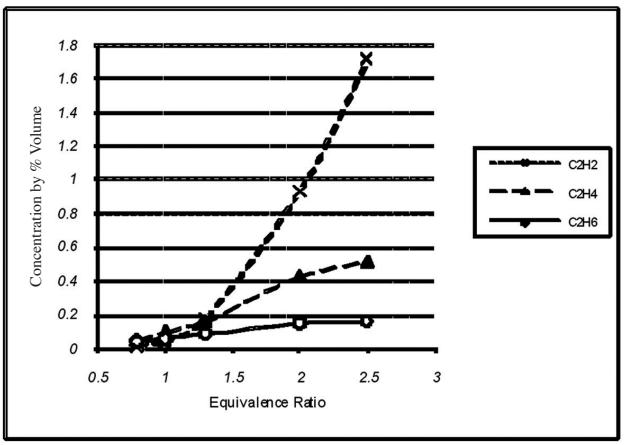

Fig. 18: Variation of intermediate species C_2H_2, C_2H_4 and C_2H_8 with equivalence ratio

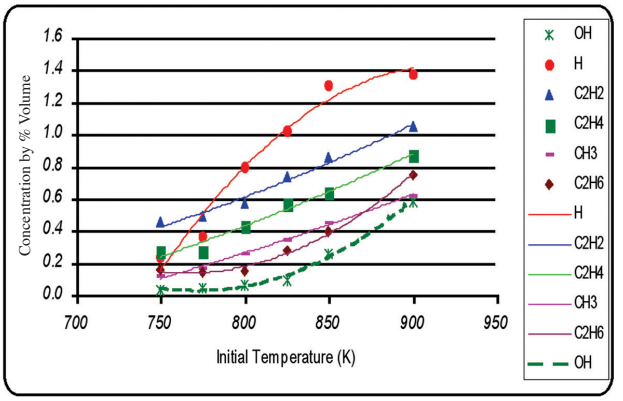

Fig. 19: Variation of some species with initial temperature

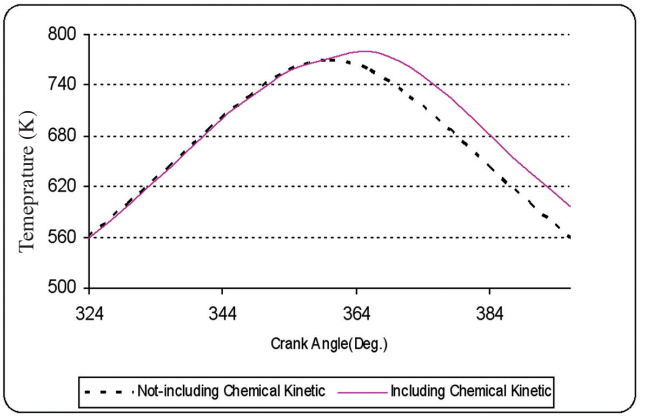

Fig. 20: Variation of in-cylinder gas bulk temperature vs. crank angle

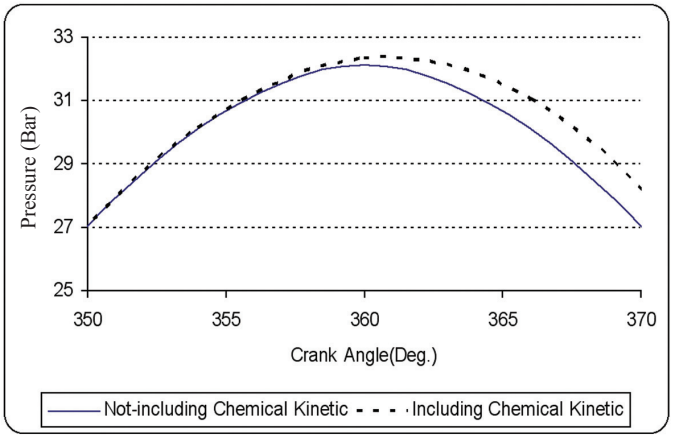

Fig. 21: Variation of in-cylinder gas pressure vs. crank angle

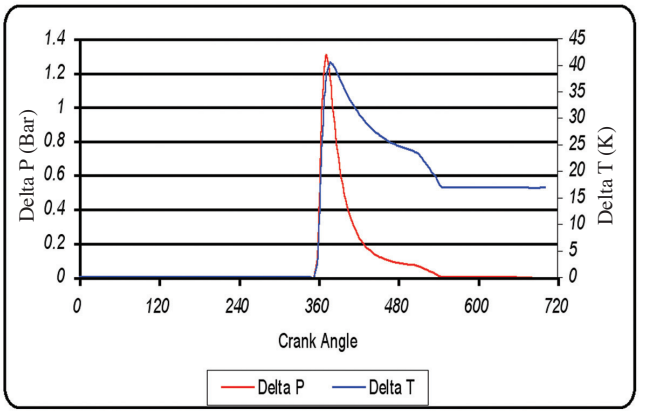

Fig. 22: Variation of ΔP and ΔT with crank angle

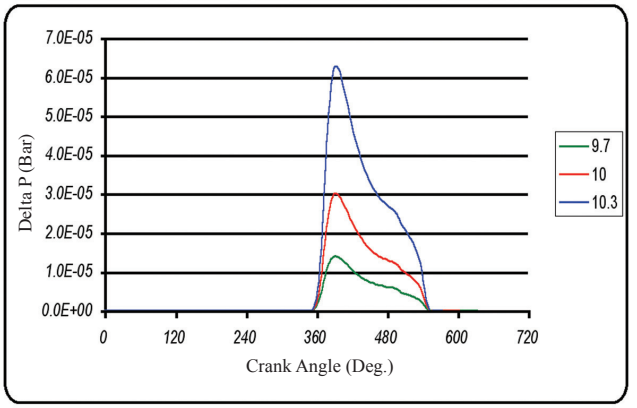

Fig. 23: Variation of ΔP with crank angle at different compression ratios

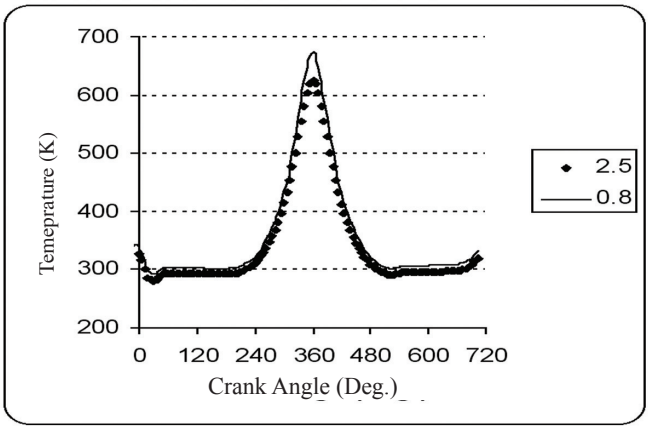

Fig. 24: Variation of in-cylinder gas bulk temperature with crank angle at different equivalence ratios

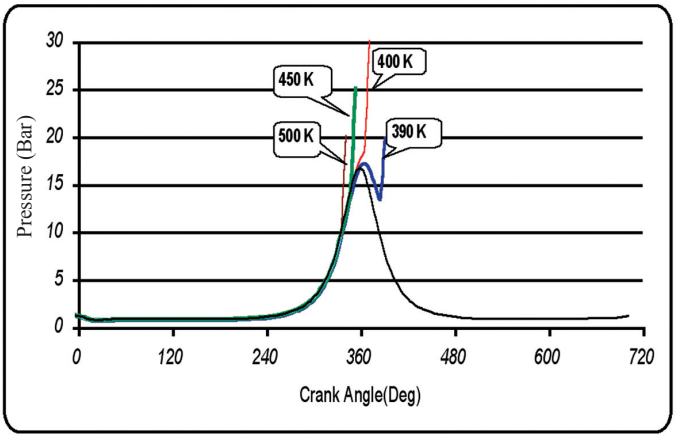

Fig. 25: Variation of in-cylinder pressure to show the effect of initial temperature on auto-ignition time

CONCLUSIONS

An in-house quasi-dimensional code was developed to simulate the physical processes of a CNG engine, in conjunction with a detailed chemical kinetic scheme, to predict the auto-ignition condition of that particular engine. In this study, the calculated results were found to have a good agreement with the experimental data. In more specific, the prepared code can be used to predict the auto-ignition point in the CNG engine satisfactory. Similarly, this code can also be used in parametric study to show the effects of important design and operating parameters on auto-ignition time.

REFERENCES

Bade Shrestha S.O. (1999). A predictive model for gas fueled spark ignition engine application. PhD. Thesis, Department of Mechanical Engineering, University of Calgary, Canada.

Bakhshan, Y., Karim, G.A. and Mansouri, S.H. (2002). Unsteady Heat Transfer during the Rapid Compression and Expansion of Air. ASME paper ETCE2002/CAE-29015.

Bakhshan, Y. and Mansouri, S.H. (2003). Comparison between zero and multi-dimensional turbulence models for internal combustion engine application. In *Proceeding of ISME2003*, Mashad, Iran.

Bakhshan, Y., Karim, G.A. and Mansouri, S.H. (2003). Study of instantaneous unsteady heat transfer in a rapid-compression-expansion machine using zero-dimensional turbulence model. Accepted for publication in Iranian Journal of Science and Technology, Shiraz, Iran.

Emad Boshra Fawzy Khalil. (2000). Modelling the chemical kinetic of combustion of higher hydrocarbon fuels in air. Ph.D. Thesis, Department of Mechanical Engineering, University of Calgary, Canada.

Heywood, J.B. (1988). *Internal Combustion Engine Fundamental.* New York: McGraw-Hill.

Higgin, R. and William, A. (1969). A shock tube investigation of the ignition of lean methane and n-Butane mixtures with oxygen. In *12th Symposium (International) on Combustion* (p. 579), the Combustion Institute, Pittsburg, Pa.

Jenning, M.J. and Jeske, F.R. (1994). Analysis of the injection process in direct injected natural gas engines:part II Effects of injector and combustion chamber design. *J. Eng. Gas. Turb. Power*, *116,* 806-813.

Jenning, M.J. and Jeske, F.R. (2004). Analysis of the injection process in direct injected natural gas engines:part I study of unconfined and in cylinder plume behavior. *J. Eng. Gas. Turb. Power*, *116,* 799-805

Karim, G.A. (2002). *Personal Communications*.

Karim, G.A., Hanafi, A. and Zhou, G. (1992). A kinetic investigation of the oxidation of low heating value fuel mixtures of methane and diluents. In *Proceeding of the 15th Annual ASME/ETCE*, Houston, Texas.

Khalil, E., Samuel, P. and Karim, G.A. (1996). An analytical examination of chemical kinetic of the combustion of n-heptane-methane air mixtures. SAE Paper No.961932.

Mansouri, S.H. and Bakhshan, Y. (2000). The k-epsilon Turbulence modelling of heat transfer and Combustion processes in a Texaco Controlled Combustion Stratified Charge Engine. *Journal of Automobile Engineering, ImechE,* PartD, *214*.

Mansouri, S.H. and Bakhshan, Y. (2001). Studies of Nox, CO, Soot formation and oxidation from direct-injection Stratified-Charge Engine Using k-epsilon Turbulence Model. *Journal of Automobile Engineering*, ImechE, PartD, *215*, UK.

Mansouri, S.H. and Heywood, J.B. (1980). Correlation for the viscosity and Prandtl number of hydrocarbon -air combustion products. *Combust. Sci.Technology*, *23,* 251-256.

Mansouri, S.H. and Bakhshan, Y. (2000). Prediction of soot formation and oxidation in a direct-injection Stratified-Charge Engine. *Proceeding of ISME2001*, Sharif University of Technology, Tehran, Iran.

Mozaffari, A., Bakhshan, Y. and Agdasi, N. (2003). Simulation of methane combustion with using detailed chemical kinetic. In *Proceeding of ISME2003*, Mashad, Iran.

Papageorgakis, G.C. (1997). Turbulence modelling of gaseous injection and mixing in DI engines. Ph.D Thesis, Ann Arbor, Michigan.

Papageorgakis, G.C. and Dennis, N.A. (1998). Optimizing gaseous fuel-air mixing direct injection engines using an RNG based model. SAE Paper 980135.

Ramos, J.I. (1988). *Internal Combustion Engine Modelling*. New York: Hemisphere Pub. Corp.

Turns, S.R. (1996). *An Introduction to Combustion*. McGraw-Hill.

Westbrook, C.K. and Pitz, W.J. (1998). Detailed kinetic modelling of auto ignition chemistry. *Transacation of SAE*, *96*(7), 559.

Zhou, G.R. (1993). Analytical studies of methane combustion and the production of hydrogen and/or synthesis gas by thr uncatalysed partical oxidation of methane. Ph.D. Thesis, Department of Mechanical Engineering, University of Calgary, Canada.

APPENDIX A
Chemical species considered in this investigation

No.	Species	Chemical	Molecular
1	Methane	CH_4	16.043
2	Ethynyl	C_2H	25.0303
3	Acetylene	C_2H_2	26.0382
4	Vinyl	C_2H_3	27.0462
5	Ethylene	C_2H_4	28.0542
6	Ethyl	C_2H_5	29.0622
7	Ethane	C_2H_6	30.0701
8	Methylidene	CH	13.0191
9	Methylene	CH_2	14.0270
10	Ketene	CH_2CO	42.0376
11	Formaldehyde	CH_2O	30.0265
12	Methyl	CH_3	15.0351
13	Acetaldehyde	CH_3CHO	44.0536
14	Acetyl	CH_3CO	43.0456
15	Methyloxide	CH_3O	31.0345
16	Ketyl	CHCO	41.0297
17	Carbon Monoxide	CO_2	28.0106
18	Carbon Dioxide	CO	44.0100
19	Hydrogen Atom	H	1.00797
20	Hydrogen Molecule	H_2	2.01594
21	Steam	H_2O	18.0153
22	Hydrogen Peroxide	H_2O_2	34.0147
23	Formyl	HCO	29.0185
24	Hydroperoxo	HO_2	33.0068
25	Oxygen	O_2	31.9988
26	Oxygen Atom	O	15.9994
27	Hydroxyl	OH	17.0074
28	Carbon	C	12.0110
29	Cyanogen	CN	26.0180
30	Nitrogen	N_2	28.0134
31	Nitrogen Atom	N	14.0067
32	Hydrogen Cyanide	HCN	27.0260
33	Hydrogen Isocyanate	HCNO	43.0250
34	Nitric Acid	HNO_3	63.0130
35	Imidogen	NH	15.0150
36	Nitrogen Oxide	NO	30.0060
37	Nitrogen Dioxide	NO_2	46.0060
38	Nitrous Oxide	N_2O	44.0130
39	Nitrogen Trioxide	NO_3	62.0050

APPENDIX B
Chemical Kinetics Reactions Mechanism (SI Units)

No.	Chemical Reactions	A_{fn}	β_{fn}	E_{fn}	A_{rn}	β_{rn}	E_{rn}
1	$CH_4 + OH \Leftrightarrow CH_3 + H_2O$	2.200E+07	0.000	2.093E+03	3.750E+06	0.000	9.251E+04
2	$CH_4 + H \Leftrightarrow CH_3 + H_2$	6.900E+07	0.000	4.940E+04	2.480E+07	0.000	5.986E+04
3	$CH_4 + O \Leftrightarrow CH_3 + OH$	1.000E+07	0.000	3.374E+04	1.550E+05	0.000	3.375E+04
4	$CH_4 + HO_2 \Leftrightarrow CH_3 + H_2O_2$	2.000E+07	0.000	7.535E+04	1.050E+06	0.000	6.061E+04
5	$CH_4 + O_2 \Leftrightarrow CH_3 + HO_2$	1.000E+07	0.000	2.300E+05	1.480E+06	0.000	-1.126E+03
6	$CH_4 \Leftrightarrow CH_3 + H$	1.000E+15	0.000	4.200E+05	1.026E+05	0.000	-7.100E+04
7	$CH_3 + O \Leftrightarrow HCO + H_2$	1.000E+08	0.000	0.000E+00	9.372E+07	0.000	3.943E+05
8	$CH_3 + O \Leftrightarrow CH_2O + H$	1.300E+08	0.000	8.400E+03	1.590E+09	0.000	2.901E+05
9	$CH_3 + O_2 \Leftrightarrow CH_2O + OH$	1.000E+05	0.000	0.000E+00	8.450E+04	0.000	2.117E+05
10	$CH_3 + OH \Leftrightarrow CH_2O + H_2$	8.000E+06	0.000	0.000E+00	2.940E+09	-0.300	3.043E+05
11	$CH_3 + O_2 \Leftrightarrow CH_3O + O$	4.786E+07	0.000	1.214E+05	3.019E+08	0.000	3.050E+03
12	$CH_3 + HO_2 \Leftrightarrow CH_3O + OH$	2.000E+07	0.000	0.000E+00	1.000E-06	0.000	0.000E+00
13	$CH_3 + OH \Leftrightarrow CH_3O + H$	4.520E+08	0.000	6.488E+04	4.750E+10	-0.130	8.836E+04
14	$CH_3 + CH_3 \Leftrightarrow C_2H_4 + H_2$	5.000E+09	0.000	1.339E+05	1.540E+14	-0.750	3.794E+05
15	$CH_3 + CH_3 \Leftrightarrow C_2H_5 + H$	2.400E+09	0.000	1.113E+05	3.210E+48	10.770	1.650E+05
16	$CH_3 + CH_3 \Leftrightarrow C_2H_6$	6.830E+16	-3.36	5.774E+03	3.680E+34	-5.730	3.893E+05
17	$CH_3 + NO_2 \Leftrightarrow CH_3O + NO$	1.300E+07	0.000	0.000E+00	2.460E+07	0.000	7.535E+04
18	$CH_3 + OH \Leftrightarrow CH_2 + H_2O$	7.500E+00	2.000	2.093E+04	4.980E+07	0.000	7.610E+04
19	$CH_3 + H \Leftrightarrow CH_2 + H2$	9.000E+07	0.000	6.312E+04	1.500E+07	0.000	4.113E+04
20	$CH3 + N \Leftrightarrow H + H + HCN$	5.000E+07	0.000	0.000E+00	5.058E+06	0.000	4.644E+04
21	$CH2O + OH \Leftrightarrow HCO + H2O$	3.390E+03	1.200	-1.64E+03	1.180E+07	0.000	1.319E+05
22	$CH2O + H \Leftrightarrow HCO + H2$	1.000E+08	0.000	1.920E+04	7.420E+08	0.000	1.338E+05
23	$CH2O + O \Leftrightarrow HCO + OH$	1.000E+08	0.000	2.220E+04	1.000E+08	0.000	1.460E+05
24	$CH2O + M \Leftrightarrow HCO + H + M$	3.310E+10	0.000	3.389E+05	1.410E-01	1.000	-4.92E+04
25	$CH2O + CH3 \Leftrightarrow HCO + CH4$	1.000E+04	0.500	2.512E+04	2.090E+04	0.500	8.851E+04
26	$CH2O + HO2 \Leftrightarrow HCO + H2O2$	1.000E+06	0.000	3.349E+04	1.090E+05	0.000	2.760E+04
27	$CH2O + O2 \Leftrightarrow HCO + HO2$	1.000E+08	0.000	1.340E+05	2.880E+06	0.000	8.791E+03
28	$CH3O + M \Leftrightarrow CH2O + H + M$	5.000E+07	0.000	8.786E+03	9.910E-04	1.000	-1.07E+04
29	$CH3O + O2 \Leftrightarrow CH2O + HO2$	1.000E+06	0.000	2.510E+04	1.280E+05	0.000	1.346E+05
30	$HCO + OH \Leftrightarrow CO + H2O$	5.000E+07	0.000	0.000E+00	1.170E+08	-0.500	3.824E+05
31	$HCO + O2 \Leftrightarrow CO + HO2$	3.300E+07	-0.40	0.000E+00	1.878E+05	0.000	7.761E+04
32	$HCO + O \Leftrightarrow CO + OH$	3.000E+07	0.000	0.000E+00	2.880E+08	0.000	3.678E+05
33	$HCO + H \Leftrightarrow CO + H2$	7.000E+07	0.000	0.000E+00	1.310E+09	0.000	3.770E+05
34	$HCO + M \Leftrightarrow CO + H + M$	7.100E+08	0.000	7.030E+04	1.140E+03	0.000	9.980E+03
35	$HCO + O \Leftrightarrow CO2 + H$	3.000E+07	0.000	0.000E+00	9.690E+09	0.000	4.611E+05
36	$HCO + CH3 \Leftrightarrow CH4 + CO$	3.000E+05	0.500	0.000E+00	5.140E+07	0.500	3.787E+05
37	$CHCO + H \Leftrightarrow CH2 + CO$	3.000E+07	0.000	0.000E+00	6.380E-02	2.200	1.122E+05
38	$CHCO + O \Leftrightarrow CO + CO + H$	1.200E+06	0.000	0.000E+00	0.000E+00	0.000	0.000E+00
39	$C2H + O2 \Leftrightarrow CO + HCO$	1.000E+07	0.000	2.929E+04	8.900E+06	0.000	5.791E+05
40	$C2H + O \Leftrightarrow CH + CO$	5.012E+07	0.000	0.000E+00	3.160E+07	0.000	2.487E+05
41	$C2H2 + M \Leftrightarrow C2H + H + M$	1.000E+08	0.000	4.770E+05	1.110E-03	1.000	3.220E+03
42	$C2H2 + O2 \Leftrightarrow HCO + HCO$	3.980E+06	0.000	1.172E+05	1.000E+05	0.000	2.659E+05
43	$C2H2 + H \Leftrightarrow C2H + H2$	1.995E+08	0.000	7.953E+04	4.160E+07	0.000	5.527E+04
44	$C2H2 + OH \Leftrightarrow C2H + H2O$	6.310E+06	0.000	2.929E+04	5.370E+06	0.000	6.845E+04
45	$C2H2 + OH \Leftrightarrow CH2CO + H$	3.230E+05	0.000	8.370E+02	3.160E+06	0.000	8.732E+04
46	$C2H2 + O \Leftrightarrow C2H + OH$	3.230E+09	-0.60	7.113E+04	2.950E+08	-0.600	3.810E+03
47	$C2H2 + O \Leftrightarrow CH2 + CO$	6.760E+07	0.000	1.674E+04	1.250E+07	0.000	2.287E+05
48	$C2H2 + OH \Leftrightarrow CH3 + CO$	1.202E+06	0.000	2.090E+03	2.500E+06	0.000	2.427E+05
49	$C2H2 + O2 \Leftrightarrow CH2 + CO2$	6.000E+07	0.000	1.674E+05	3.400E+08	0.000	5.107E+05
50	$C2H2 + O2 \Leftrightarrow CHCO + H$	4.300E+08	0.000	5.070E+04	4.870E+11	-0.860	1.337E+05
51	$C2H3 + O2 \Leftrightarrow C2H2 + HO2$	1.585E+07	0.000	4.186E+04	1.000E+06	0.000	7.477E+04
52	$C2H3 + M \Leftrightarrow C2H2 + H + M$	7.940E+08	0.000	1.318E+05	1.230E-01	1.000	-4.33E+04
53	$C2H3 + O2 \Leftrightarrow CH2O + HCO$	1.070E+05	0.000	-1.04E+03	4.470E-25	8.340	2.935E+05
54	$C2H3 + H \Leftrightarrow C2H2 + H2$	2.000E+07	0.000	0.000E+00	3.850E-19	7.390	2.137E+05

55	C2H4 + OH ⇔ C2H3 + H2O	4.786E+06	0.000	5.150E+03	1.200E+06	0.000	5.560E+04
56	C2H4 + H ⇔ C2H3 + H2	1.514E+01	2.000	2.511E+04	1.730E+00	2.000	2.138E+04
57	C2H4 + M ⇔ C2H3 + H + M	3.800E+11	0.000	4.107E+05	2.000E+05	0.000	0.000E+00
58	C2H4 + M ⇔ C2H2 + H2 + M	2.600E+11	0.000	3.320E+05	4.600E+00	1.000	1.528E+05
59	C2H4 + OH ⇔ CH2O + CH3	2.000E+06	0.000	4.002E+03	6.000E+05	0.000	6.899E+04
60	C2H4 + O ⇔ CH3 + HCO	1.600E+03	1.200	3.096E+03	1.600E-03	2.370	1.061E+05
61	C2H4 + O ⇔ CH2 + CH2O	2.500E+07	0.000	2.092E+04	3.020E+06	0.000	6.564E+04
62	C2H4 + C2H4 ⇔ C2H3 + C2H5	5.012E+08	0.000	2.708E+05	1.490E+08	0.000	-1.09E+04
63	C2H5 ⇔ C2H4 + H	2.340E+26	-4.24	1.810E+05	1.170E+08	-0.620	7.238E+03
64	C2H5 + O2 ⇔ C2H4 + HO2	1.000E+06	0.000	2.093E+04	1.300E+05	0.000	5.732E+04
65	C2H5 + O ⇔ CH3CHO + H	5.000E+07	0.000	0.000E+00	5.360E-01	2.540	2.893E+05
66	C2H6 + H ⇔ C2H5 + H2	5.400E-04	3.500	2.180E+04	9.720E-04	3.500	1.143E+05
67	C2H6 + OH ⇔ C2H5 + H2O	6.300E+00	2.000	2.700E+03	9.780E+29	-6.550	1.627E+05
68	C2H6 + O ⇔ C2H5 + OH	3.000E+01	2.000	2.140E+04	6.940E+28	-6.320	1.078E+05
69	C2H6 + CH3 ⇔ C2H5 + CH4	5.500E-07	4.000	3.470E+04	2.291E+08	0.000	1.001E+05
70	CO + O2 ⇔ CO2 + O	3.140E+05	0.000	1.573E+05	1.900E+07	0.000	2.266E+05
71	CO + OH ⇔ CO2 + H	4.400E+00	1.500	-3.09E+03	1.380E+08	0.000	1.072E+05
72	CO + O + M ⇔ CO2 + M	5.900E+03	0.000	1.716E+04	5.500E+15	-1.000	5.516E+05
73	CO + HO2 ⇔ CO2 + OH	5.800E+07	0.000	9.581E+04	6.600E+08	0.000	3.546E+05
74	CH2 + O2 ⇔ HCO + OH	1.000E+08	0.000	1.549E+04	4.070E+07	0.000	3.204E+05
75	CH2 + O ⇔ CH + OH	1.900E+05	0.680	1.046E+05	5.860E+04	0.680	1.085E+05
76	CH2 + H ⇔ CH + H2	2.512E+05	0.670	1.076E+05	1.900E+05	0.670	1.201E+05
77	CH2 + OH ⇔ CH + H2O	2.512E+05	0.670	1.076E+05	8.120E+05	0.670	1.836E+05
78	CH2 + CH3 ⇔ C2H4 + H	4.000E+07	0.000	0.000E+00	4.380E+10	0.000	2.466E+05
79	CH2 + O ⇔ CO + H + H	5.000E+07	0.000	0.000E+00	0.000E+00	0.000	0.000E+00
80	CH2 + O2 ⇔ CO + H + OH	8.640E+04	0.000	-2.09E+03	2.270E-07	1.550	2.284E+05
81	CH2 + O2 ⇔ CO + H2O	1.870E+04	0.000	-4.18E+03	3.070E+00	1.400	7.276E+05
82	CH2 + O2 ⇔ CO2 + H + H	1.590E+06	0.000	4.184E+03	3.010E+01	0.230	3.442E+05
83	CH2 + NO ⇔ HCNO + H	1.390E+06	0.000	-4.61E+03	2.340E+08	0.000	-1.04E+05
84	CH2 + N2 ⇔ HCN + NH	2.800E+06	0.000	1.256E+05	6.800E+05	0.000	0.000E+00
85	CH2 + NO ⇔ HCN + OH	1.390E+06	0.000	-4.61E+03	1.658E+06	0.000	2.581E+05
86	CH + NO ⇔ HCN + O	1.100E+08	0.000	0.000E+00	2.600E+09	0.000	2.971E+05
87	CH + N2 ⇔ HCN + N	8.000E+05	0.000	4.605E+04	7.200E+06	0.000	3.893E+04
88	CH + H2O ⇔ CH2O + H	1.170E+09	-.750	0.000E+00	1.512E+08	0.000	2.396E+05
89	CH + CO2 ⇔ HCO + CO	3.400E+06	0.000	2.888E+03	4.200E+05	0.000	2.752E+05
90	CH + H ⇔ C + H2	1.500E+08	0.000	0.000E+00	5.300E+08	0.000	9.617E+04
91	CH + O2 ⇔ CO + OH	1.349E+05	0.670	1.075E+05	5.120E+05	0.670	7.766E+05
92	CH + O2 ⇔ HCO + O	1.000E+07	0.000	0.000E+00	1.340E+07	0.000	3.010E+05
93	CH + O ⇔ CO + H	4.000E+07	0.000	0.000E+00	5.490E+08	0.150	7.343E+05
94	CH2CO + H ⇔ CH3 + CO	1.096E+07	0.000	1.423E+04	2.399E+06	0.000	1.682E+05
95	CH2CO + O ⇔ HCO + HCO	1.000E+07	0.000	1.004E+04	3.467E+05	0.000	1.402E+05
96	CH2CO + OH ⇔ CH2O + HCO	2.818E+07	0.000	0.000E+00	2.754E+07	0.000	7.740E+04
97	CH2CO + M ⇔ CH2 + CO + M	1.995E+10	0.000	2.510E+05	4.572E-02	0.000	0.000E+00
98	CH3CHO + H ⇔ CH3CO + H2	4.000E+07	0.000	1.760E+04	8.420E+10	-1.370	9.719E+04
99	CH3CHO + O ⇔ CH3CO + OH	5.000E+06	0.000	7.500E+03	7.390E+09	-1.420	7.979E+04
100	CH3CHO + OH ⇔ CH3CO + H2O	1.000E+07	0.000	0.000E+00	9.910E+11	-1.650	1.459E+05
101	CH3CO ⇔ CH3 + CO	1.000E+10	0.000	0.000E+00	0.000E+00	0.000	0.000E+00
102	H2 + OH ⇔ H + H2O	2.200E+07	0.000	2.155E+04	9.300E+07	0.000	8.490E+04
103	H2 + O ⇔ H + OH	1.800E+04	1.000	3.711E+04	8.300E+03	1.000	2.890E+05
104	H2 + O2 ⇔ OH + OH	1.360E+07	0.000	2.015E+05	4.480E+05	0.000	1.253E+05
105	H2 + HO2 ⇔ H + H2O2	7.300E+05	0.000	7.820E+04	1.700E+06	0.000	1.540E+04
106	H + HO2 ⇔ OH + OH	2.500E+08	0.000	7.500E+03	1.200E+07	0.000	1.630E+05
107	H + H + M ⇔ H2 + M	6.400E+05	-1.00	0.000E+00	2.400E+09	0.000	4.812E+05
108	H + OH + M ⇔ H2O + M	1.413E+11	-2.00	0.000E+00	2.200E+10	0.000	4.390E+05
109	H + O2 + M ⇔ HO2 + M	1.590E+03	0.000	-4.18E+03	2.400E+09	0.000	1.921E+05
110	O + O + M ⇔ O2 + M	4.700E+03	-0.28	0.000E+00	5.100E+09	0.000	4.810E+05
111	H2O2 + M ⇔ OH + OH + M	1.690E+18	-2.00	2.023E+05	3.250E+10	-2.000	0.000E+00
112	HO2 + OH ⇔ H2O + O2	5.000E+07	0.000	4.180E+03	1.000E+08	0.000	3.091E+06
113	HO2 + HO2 ⇔ H2O2 + O2	1.000E+07	0.000	4.200E+03	6.800E+07	0.000	1.782E+05
114	H2O2 + H ⇔ H2O + OH	3.200E+08	0.000	3.751E+04	1.140E+03	1.360	3.176E+05

115	H + O2 ⇔ OH + O	1.200E+11	-0.91	6.910E+04	1.300E+07	0.000	0.000E+00
116	H2O + O ⇔ OH + OH	1.500E+04	1.140	7.213E+04	1.500E+03	1.140	0.000E+00
117	OH + M ⇔ H + O + M	8.000E+13	-1.00	4.339E+05	1.000E+04	0.000	0.000E+00
118	HO2 + H ⇔ H2 + O2	2.500E+07	0.000	2.929E+03	5.000E+08	-0.280	2.243E+05
119	HO2 + O ⇔ O2 + OH	2.000E+07	0.000	0.000E+00	2.810E+08	-0.330	2.141E+05
120	H2O2 + OH ⇔ H2O + HO2	1.000E+07	0.000	7.531E+03	2.800E+07	0.000	1.372E+05
121	C + N2 ⇔ CN + N	3.624E+02	0.000	1.591E+05	1.040E+09	-0.500	0.000E+00
122	C + NO ⇔ CN + O	6.600E+07	0.000	0.000E+00	7.300E+13	0.000	1.588E+05
123	C + N2O ⇔ CN + NO	1.000E+07	0.000	0.000E+00	1.330E+12	0.000	3.454E+05
124	C + O2 ⇔ CO + O	2.000E+07	0.000	0.000E+00	4.182E+07	0.000	5.793E+05
125	CN + OH ⇔ NH + CO	6.000E+06	0.000	0.000E+00	1.600E+07	0.000	2.512E+05
126	CN + O2 ⇔ NO + CO	6.000E+06	0.000	0.000E+00	6.800E+06	0.000	4.605E+05
127	CN + H2 ⇔ H + HCN	2.950E-01	2.450	9.364E+03	6.587E+03	0.000	8.037E+04
128	HCN + O ⇔ NH + CO	3.450E-03	2.640	2.085E+04	2.110E+06	0.000	1.646E+05
129	HCNO + H ⇔ HCN + OH	1.000E+08	0.000	5.023E+04	4.210E+06	0.000	-4.79E+03
130	HNO3 + OH ⇔ NO3 + H2O	5.400E+04	0.000	0.000E+00	2.446E+08	0.000	3.271E+05
131	NH + H ⇔ N + H2	1.000E+08	0.000	0.000E+00	4.536E+08	0.000	1.222E+05
132	N + NO ⇔ O + N2	3.270E+06	0.300	0.000E+00	1.670E+08	0.000	3.174E+05
133	N + O2 ⇔ O + NO	6.400E+03	1.000	2.629E+04	3.880E+06	0.000	1.666E+05
134	N + OH ⇔ H + NO	3.800E+07	0.000	0.000E+00	1.200E+08	0.000	2.024E+05
135	NO + HO2 ⇔ NO2 + OH	8.700E+05	0.000	0.000E+00	6.000E+06	0.000	3.349E+04
136	NO + O + M ⇔ NO2 + M	5.800E-02	1.000	-3.60E+04	1.100E+10	0.000	2.721E+05
137	NO + NO + O2 ⇔ NO2 + NO2	4.900E-06	1.000	-2.51E+03	4.000E+06	0.000	1.130E+05
138	NO + O2 + M ⇔ NO3 + M	7.650E-06	1.000	-7.11E+03	1.200E+05	0.000	1.340E+04
139	NO + NH ⇔ N2O + H	4.300E+08	-0.50	0.000E+00	2.575E+04	0.000	-1.65E+05
140	NO + NO ⇔ N2 + O2	1.410E+09	0.000	3.558E+05	2.850E+10	0.000	5.358E+05
141	NO2 + H ⇔ NO + OH	2.900E+07	0.000	0.000E+00	3.500E+05	0.000	1.231E+05
142	NO2 + O ⇔ NO + O2	1.000E+07	0.000	2.512E+03	2.200E+06	0.000	1.926E+05
143	NO2 + OH + M ⇔ HNO3 + M	9.305E+04	0.000	-7.27E+04	6.000E+08	0.000	1.260E+05
144	N2O + M ⇔ N2 + O + M	1.600E+08	0.000	2.159E+05	8.373E+10	0.000	3.750E+06
145	N2O + O ⇔ NO + NO	1.000E+08	0.000	1.180E+05	2.254E+06	0.000	2.744E+05
146	N2O + H ⇔ N2 + OH	7.600E+07	0.000	6.363E+04	2.778E+06	0.000	3.342E+05
147	NO3 + NO ⇔ NO2 + NO2	1.500E+04	0.000	5.442E+03	7.800E+05	0.000	1.005E+05
148	NO3 + M ⇔ NO2 + O + M	1.000E+11	0.000	1.800E+05	2.800E+01	1.000	-3.26E+04

ISSN: 0128-7680
Pertanika J. Sci. & Technol. **17 (2)**: 291 – 297 (2009)

Low Sm Doping Effects on the Low-Field Magnetoresistive Properties in $(La_{1-x}Sm_x)_{0.67}Sr_{0.33}MnO_3$ Perovskite

Lim Kean Pah*, Abdul Halim Shaari, Chen Soo Kien, Ng Siau Wei, Zalita Zainuddin and Ye Chau Yuen
Department of Physics, Faculty of Science, Universiti Putra Malaysia, 43400 UPM, Serdang, Selangor, Malaysia
**E-mail: kplim@science.upm.edu.my*

ABSTRACT

A series of polycrystalline samples $(La_{1-x}Sm_x)_{0.67}Sr_{0.33}MnO_3$ (X=0.00, 0.05 and 0.10) were prepared using the conventional solid-state reaction method. The XRD analysis indicated that all the samples were fully crystalline and in a single phase with a rhombohedral structure after a sintering at 1200ºC for 24 hours in air. Meanwhile, the Atomic Force Microscopy measurements showed that a small amount of Sm doping in La sites affected the grain growth and this might affect the grain boundary layer, thus resulting in the reduction of the Curie temperature, T_C. Extrinsic magnetoresistance (MR) was observed for all the samples with a large negative MR at low field (0-0.1 or 0.2T) region, followed by a slower varying MR at high field (0.1 or 0.2-1T). The highest low-field MR value of -4.6% (at 0.1T) and -6.1% (at 0.2T) were observed for sample X=0.10 and X=0.05, respectively. Hence, these indicated that the extrinsic MR was grain size dependent and was therefore enhanced with a small amount of Sm substitution in La sites.

Keywords: **Low-field magnetoresistance, polycrystalline manganites**

ABBREVIATIONS

Magnetoresistance (MR),
Low Field Magnetoresistance (LFMR),
X-ray Diffraction (XRD),
Atomic Force Microscope (AFM)
Vibrating Sample Magnetometer (VSM)

INTRODUCTION

Doped manganite oxides of the ferromagnetic compounds, $A_{1-x}B_xMnO_3$ (where A=La, Pr, Nd etc. and B=Ba, Sr, Ag, etc.) (Ibarra *et al*., 1998; Im *et al*., 2007; Urushibara *et al*., 1995; Cheng *et al*., 2004) which show Colossal Magnetoresistance (CMR) effect have received huge attraction due to their potential in the application as a magnetic sensing element. Manganites usually exhibit metal-insulator transition (T_{MI}) accompanied by a simultaneous magnetic phase transition or Curie temperature (T_C). The double exchange mechanism, proposed by Zener (1951) and the Jahn-Teller (JT) effect (Millis *et al*., 1995) are commonly used to explain the above phenomena. When a significant high magnetic field is applied, the temperature of T_{MI} changes and the resistivity decreases correspondingly. These changes show a maximum near T_C or T_{MI} for single crystal compounds or epitaxial thin films commonly recognized as an intrinsic magnetoresistance (MR) effect (Mukovskii

Received: 4 April 2008
Accepted: 13 June 2008
*Corresponding Author

et al., 1999). Therefore, a number of works have been carried out to tailor the material with higher magnetoresistance in lower field and proper temperature range (room temperature). By tuning the composition of these compounds (e.g. doping A or B site with other ions of different sizes or charges), one can actually control or modify its transport or magnetic properties. The recent reports confirm that polycrystalline compounds do not only show an intrinsic MR effect but also an extrinsic MR effect in a relatively lower filed (i.e. the effect which is commonly known as the Low-Field Magnetoresistance, LFMR) (Nam *et al*., 2001). This effect is believed to be due to the spin-polarized tunnelling or spin-dependent scattering across the disordered grain boundaries layers (Miller *et al*., 2000; Xia *et al*., 2007; Zhang *et al*., 2007) and is mostly affected by the grain size, grain size distribution and the preparation conditions. Many works have been carried out to enhance the LFMR effect by introducing weak links at the grain boundaries (Zhang *et al*., 2007; Lu *et al*., 2006) or by introducing doping at the A or B site (Cheng *et al*., 2004; Zhang *et al*., 2006). In this paper, the effects of Samarium (Sm) substitution in the La site, concluded from an investigation on the structure, electrical properties and magnetic properties of the samples, are reported.

MATERIALS AND METHODS

Polycrystalline samples of $(La_{1-x}Sm_x)_{0.67}Sr_{0.33}MnO_3$ with X=0.00, 0.05 and 0.10 were prepared using the conventional solid-state reaction method. Appropriate amounts of high-purity La_2O_3, Sm_2O_3, $SrCO_3$ and MnO_2 powders (purity >99.5%) were mixed and pre-sintered at 900ºC for 12 hours in air. After the pre-sintered powder was ground, it was pressed into a pellet and then sintered at 1200ºC for 24 hours in air. X-ray diffraction (XRD) with the Cu K_α radiation and the Atomic Force Microscope (Quesant AFM: Q-Scope 350) were respectively used to characterize the structure and microstructure of the samples. The temperature dependence of the magnetization of the sample was measured at 313K to 393K by a Vibrating Sample Magnetometer (VSM, LakeShore 7400) and the magnetoresistance effect was measured using a DC four-point probe technique with an applied filed of 1 Tesla from 100K to 300K.

RESULTS AND DISCUSSION

Fig. 1 shows the XRD spectra of the samples, before and after the sintering process. In all cases the samples were shown to have more peaks before the sintering than after it. By comparing the XRD patterns, before and after the sintering process, one can deduce that the partially reacted starting powder during the calcination process (at 900ºC for 12 hours) has indeed reacted well and formed the end product of the bulk sample after the sintering process (at 1200ºC for 24 hours). Those missing peaks (marked with *) observed might be the ones of the starting precursor powder (La_2O_3, Sm_2O_3, $SrCO_3$ and MnO_2) which had not fully been reacted to form the single phase $(La_{1-x}Sm_x)_{0.67}Sr_{0.33}MnO_3$ powder which was only obtained after the sintering process. All the XRD patterns for the sintered samples, which were measured at room temperature, matched with the ICDD standard (reference code 00-050-0308), where all the samples are in the single phase rhombohedral structure with no detectable secondary phases which agrees with an earlier report (Im *et al*., 2007; Urushibara *et al*., 1995). Hence, crystallization was completed after sintering at 1200ºC for 24 hours in air. Sm has a smaller ionic radius (0.964Å) as compared to Lanthanum (La) (1.06Å). When smaller atom (Sm) is replaced with a bigger atom (La), one would expect some reduction in the lattice parameter, which is indicated by the increase of the 2 Theta angle shown in *Fig. 1*.

The distribution of the grains was characterized using the Atomic Force Microscope (AFM). *Fig. 2* shows the AFM images obtained at the room temperature for all the samples. The pure sample (X=0.00) has a relatively bigger grain size distribution, ranging from 2.5±0.1μm to 3.7±0.1μm.

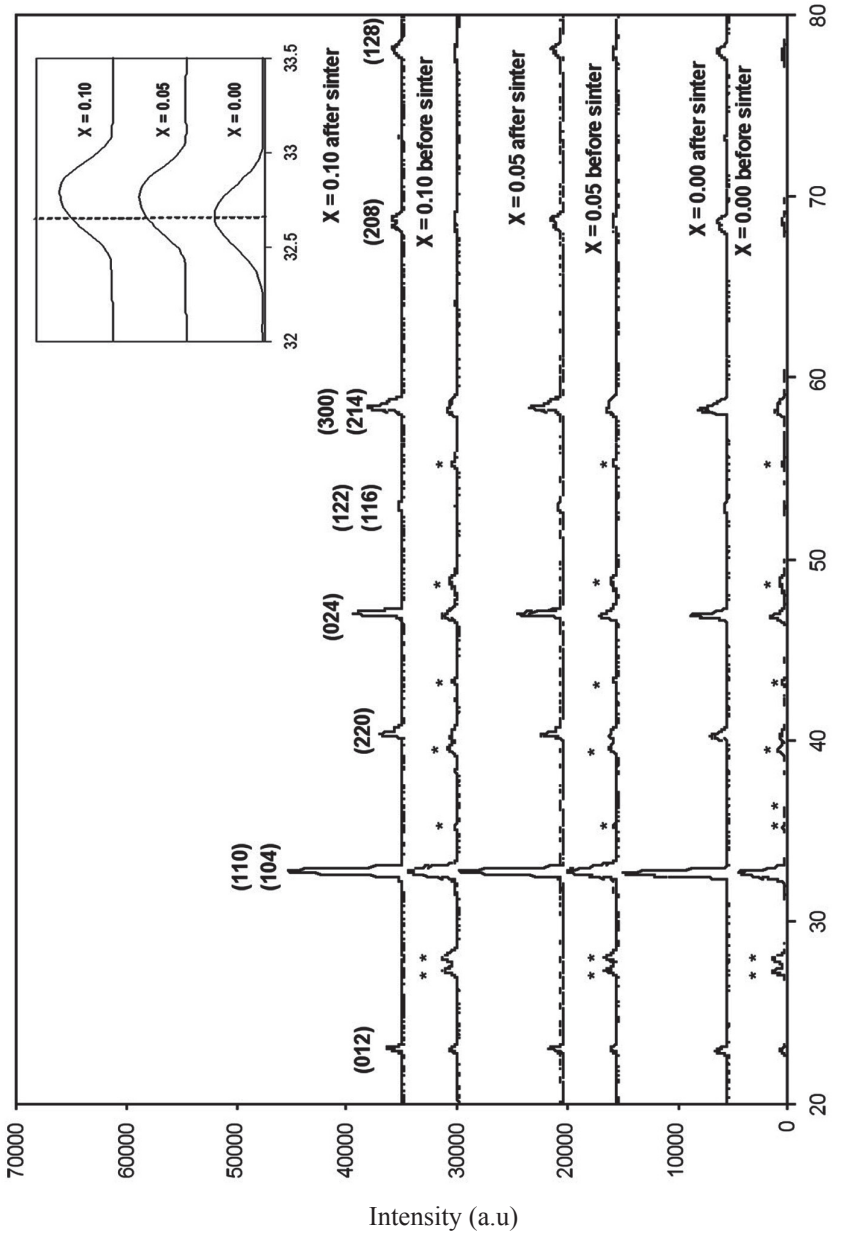

*Fig. 1: XRD pattern of $(La_{1-x}Sm_x)_{0.67}Sr_{0.33}MnO_3$ before and after sintering at open air. Peak marked with * represents the peak for the starting powder (La_2O_3, Sm_2O_3, $SrCO_3$ and MnO_2). The inset shows the shift of the main peak (32.6°) position due to the substitution of Sm*

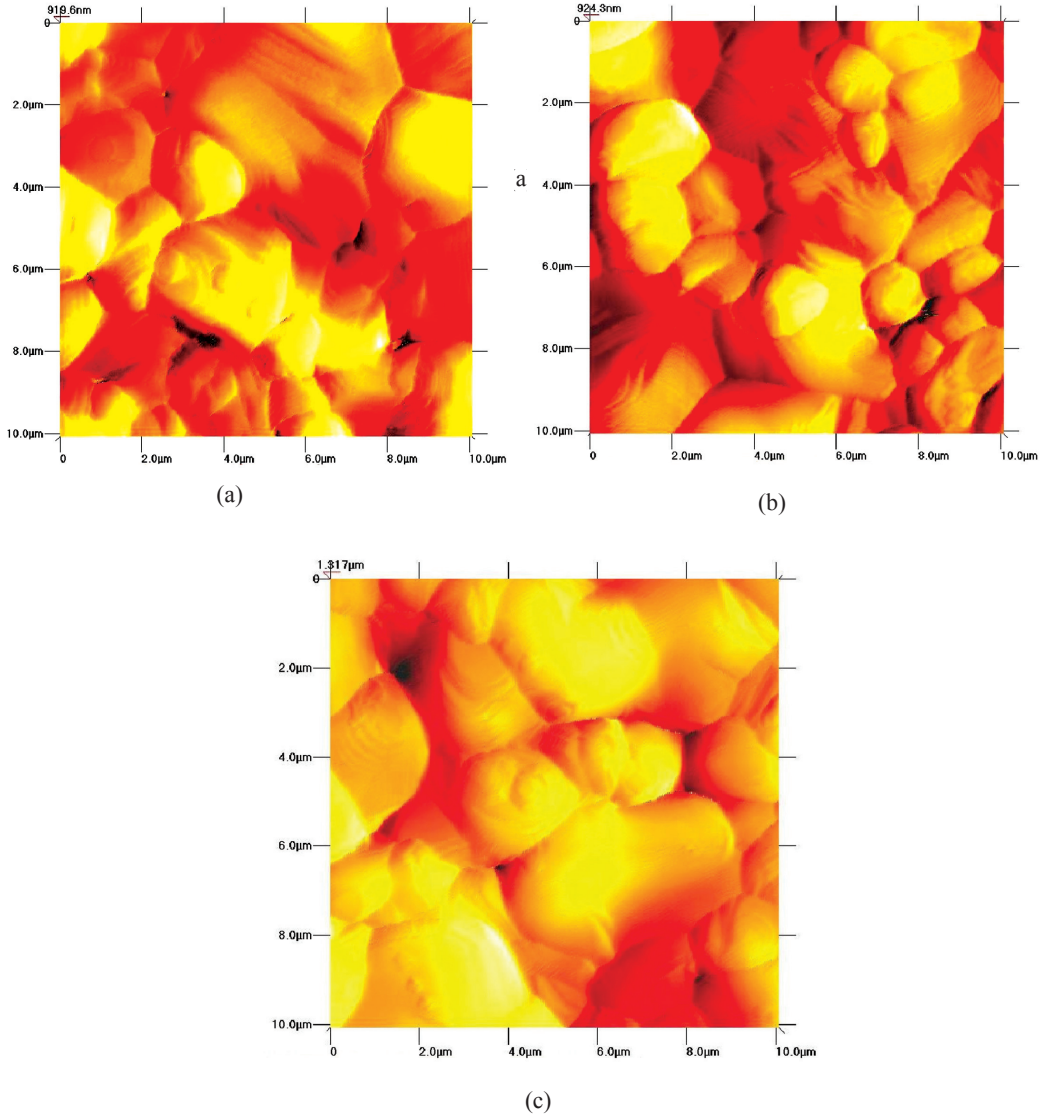

Fig. 2: AFM micrograph of $(La_{1-x}Smx)_{0.67}Sr_{0.33}MnO_3$ samples (a) X=0.00, (b) X=0.05 and (c) X=0.10

Furthermore, the distribution of the grain sizes is reduced to 1.8±0.1µm to 2±0.1µm when X=0.05 of Sm is substituted. When more Sm is introduced (X=0.10), the distribution of the grain sizes is once againd increased to 2.2±0.1µm to 2.7±0.1µm, indicating that substituting a small amount of Sm in the La site will affect the growth of grain.

The temperature dependences of magnetization in all the samples are shown in *Fig. 3(a)*. All the samples show a significant transition of paramagnetic to ferromagnetic phase which occurs at the temperature called the Curie temperature, T_C [defined as the temperature where dm/dt is minimum as shown in *Fig. 3(b)*]. The Curie temperature for the pure sample is 370K. This value

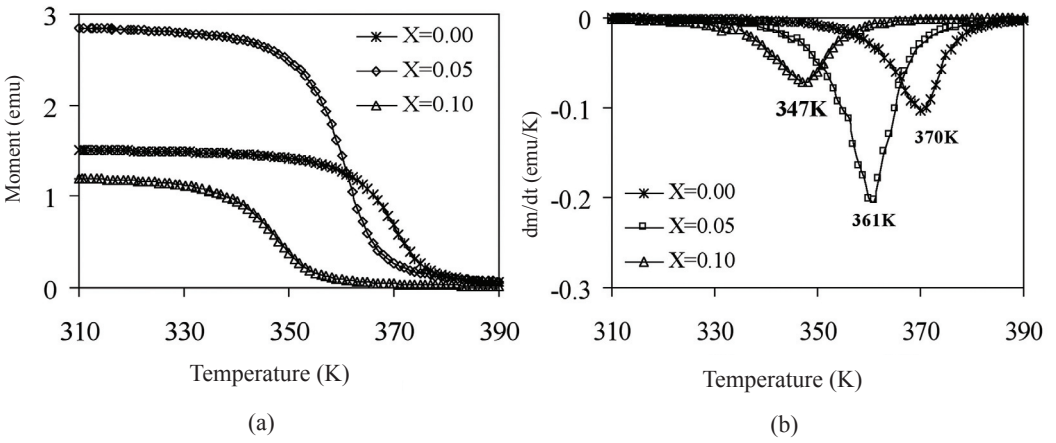

Fig. 3: (a) Moment vs. temperature, and (b) dm/dt vs temperature for $(La_{1-x}Sm_x)_{0.67}Sr_{0.33}MnO_3$ sample

is in agreement with the report by Cheng *et al*. (2004). When La is substituted with Sm (X=0.05), the Curie temperature drops to 361K and continues to decrease to 347K for X=0.10. This might be due to the change in the structure dimension (lattice spacing), as indicated in the XRD results. The La substitution by Sm changes the Mn-O-Mn chains, which then forces the magnetic ordering to occur at lower temperature.

Figs. 4(a), (b), and *(c)* show the MR ratio versus the external magnetic field H curves for all the samples at several temperatures. The MR ratio is calculated as $MR=(R_H - R_O)/R_O$. All the curves exhibit the behaviour similar to the samples with grain boundaries structure. A large negative MR at low field (0-0.1 or 0.2T) region, followed by a slower varying MR at a high field (0.1 or 0.2-1T) region is therefore observed. This behaviour, known as the Low-Field Magnetoresistance (LFMR) is commonly observed in polycrystals and believed to be influenced by the grain boundaries (Nam *et al*., 2001; Miller *et al*. 2000; Xia *et al*. 2002; Zhang *et al*., 2007). The MR is almost linear with H and it continuously decreases without any sign of saturation up to the highest measuring field. Samples X=0.00 (*Fig. 4(a)*) and X=0.10 (*Fig. 4(b)*) show a similar behaviour in the two regions of MR (0 to 0.1T and 0.1 to 1T) but the MR value is found to be larger for X=0.10. However, for X=0.05 [*Fig. 4(c)*], the MR pattern is slightly different from that of the other samples, where the small field region is 0 to 0.2T. These might be related to the size of the grain, in which smaller grain size in sample X=0.05 might have larger or thicker grain boundaries that require higher field to align the magnetic spin in the grain or at the grain boundary. Therefore, the results reveal that extrinsic MR is enhanced with small Sm substitution and grain size dependent. Overall, the highest low-field MR value of -4.6% (at 0.1T) and -6.1% (at 0.2T) are observed for samples X=0.10 and X=0.05, respectively. However, the room temperature high-field MR (at 1T) of -10.5% is given by sample X=0.05. The temperature dependence of the MR for all the samples is shown in *Fig. 4(d)*. The MR ratio drops monotonically with the decreases of the temperature. As for samples X=0.00 and X=0.10, they gave similar slopes, being higher compared to that of sample X=0.05. This might be related to the difference in the grain distribution shown by the AFM results, whereby smaller grains need higher field to fully align the magnetic spin.

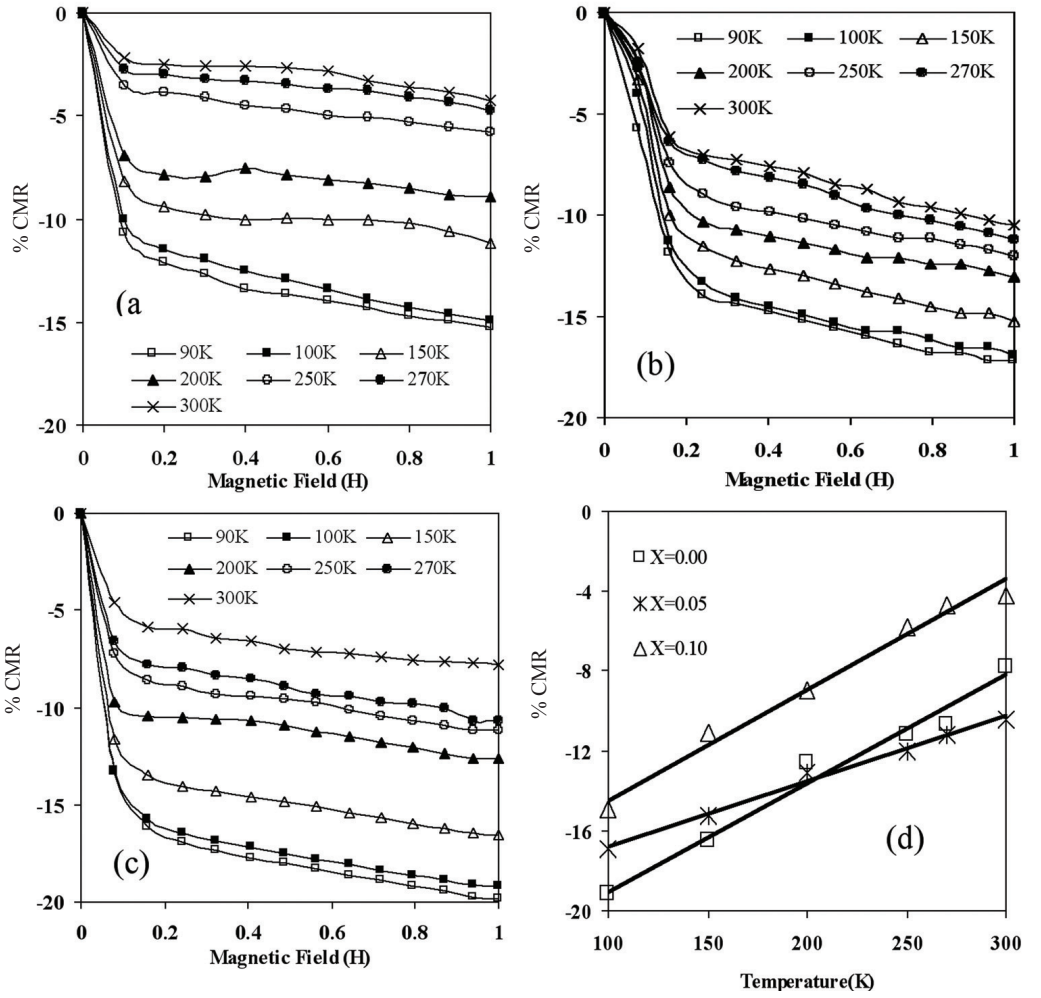

Fig. 4: Field dependence of the MR curve at different temperatures for (a) X=0.00, (b) X=0.05, (c) X=0.10, (d) temperature dependence of the MR ratio in 1 Tesla field

CONCLUSIONS

In this study, the structure, the magnetic and the MR effect in bulk polycrystalline $(La_{1-x}Sm_x)_{0.67}Sr_{0.33}MnO_3$ (X=0.00, 0.05 and 0.10) samples were investigated. The replacement of La by a small amount of Sm has been shown to change its properties. It affects the grain growth and reduces the magnetic phase transition, T_C. However, the extrinsic MR behaviour or known as the Low-Field Magnetoresistance is enhanced. The highest low-field MR value of -4.6% (at 0.1T) and -6.1% (at 0.2T) are observed for samples X=0.10 and X=0.05, respectively.

ACKNOWLEDGEMENT

The authors gratefully acknowledge the Ministry of Science, Technology and Innovation (MOSTI) for the Science Fund grant vote: 03-01-04-SF0088 (Fabrication of multilayer manganites thin films having LFMR effect using Pulsed Laser Ablation Technique).

REFERENCES

Cheng, Z.X., Silver, T.M., Li, A.H., Wang, X.L. and Kimura, H. (2004). Effect of progressive substitution of La^{3+} by Bi^{3+} on the structure, magnetic and transport properties of $La_{0.67}Sr_{0.33}MnO_3$. *Journal of Magnetism and Magnetic Materials, 283,* 143-149.

Ibarra, M.R. and De Teresa, J.M. (1998). Colossal magnetoresistance in manganese oxide perovskites. *Journal of Magnetism and Magnetic Materials, 177-181,* 846-849.

Im, H.S., Chon, G.B., Lee, S.M., Koo, B.H., Lee, C.G. and Jung, M.H. (2007). Preparation and characterization of $La_{0.7}AE_{0.3}MnO_3$ (AE = Ca, Sr, Ba): Perovskite structured manganites. *Journal of Magnetism and Magnetic Materials, 310,* 2668–2670.

Lu, W.J., Sun, Y.P., Zhu, X.B., Song, W.H. and Du, J.J. (2006). Low-field magnetoresistance in $La_{0.8}Sr_{0.2}MnO_3$/ ZrO_2 composite system. *Materials Letters*, *60*(27), 3207-3211.

Millis, A.J., Littlewood, P.B. and Shraiman, B.I. (1995). Double exchange alone does not explain the resistivity of $La_{1-x}Sr_xMnO_3$. *Physics Review Letters*, *74,* 5144-5147.

Miller, D.J., Lin, Y.K., Vlasko-Vlasov, V. and Welp, U. (2000). Grain boundary structures in $La_{2/3}Ca_{1/3}MnO_3$ thin films. *Journal of Applied Physcis, 87*(9), 6758-6760.

Mukovskii, Y.M. and Shmatok, A.V. (1999). CMR effect in mono- and polycrystalline $La_{0.7}Sr_{0.3}MnO_{3-z}$ thin film. *Journal of Magnetism and Magnetic Materials, 196-197,* 136-137.

Nam, Y.S., Ju, H.L. and Park, C.W. (2001). Low field magnetoresistance in intrinsic granular system $La_{1-x}Ba_xMnO_3$. *Solid State Communications, 119*, 613-618.

Urushibara, A., Moritomo, Y., Arima, T., Asamitsu, A., Kido, G. and Tokura, Y. (1995). Insulator-metal transition and giant magnetoresistance in $La_{1-x}Sr_xMnO_3$. *Physical Review B*, *51*(20), 14103-14109.

Xia, Z.C., Yuan, S.L., Tu, F., Tang, C.Q., Peng, G.., Zhang, G.Q., Liu, L., Liu, J., Li, Z.Y., Yang, Y.P., Xiong, C.S. and Xiong, Y.H. (2002). Grain boundaries and low-field transport properties in colossal magnetoresistance materials. *Journal of Physics D: Applied Physics*, *35,* 177-180.

Zener, C. (1951). Interaction between the d-Shells in the Transition Metals II. Ferromagnetic compounds of manganese with perovskite structure. *Physics Review, 82,* 403-405.

Zhang, M.J., Li, J., Peng, Z.H., Li, S.L., Zheng, D.N., Jin, A.Z., Gu, C.Z., Li, R.Y. and Liu, C.C. (2007). Enhanced extrinsic magnetoresistance in $La_{0.67}Sr_{0.33}MnO_3$ artificial grain boundaries induced by ion implantation. *Journal of Magnetism and Magnetic Materials, 316,* L1-L4.

Zhang, C. J., Kim, B. H., Kim J. S. and Park, Y. W. (2006). Lattice effects on magnetic and transport properties in La site doping $La_{0.67}Sr_{0.33}CoO_3$. *Physics Letters. Section A, 348,* 58-65.

ISSN: 0128-7680
Pertanika J. Sci. & Technol. **17 (2)**: 299– 306 (2009)

Observation of Cotton-like Bismuth Oxide (β-$Bi_2O_{2.5}$) Prepared via Pulsed Laser Ablation Deposition

Samaila Bawa Waje[1*], Noorhana Yahya[1,3] and Irmawati Ramli[1,2]
[1]Advanced Materials and Nanotechnology Laboratory, Institute of Advanced Technology, Universiti Putra Malaysia, 43400 UPM, Serdang, Selangor, Malaysia
[2]Department of Chemistry, Faculty of Science, Universiti Putra Malaysia, 43400 UPM, Serdang, Selangor, Malaysia
[3]Electrical and Electronics Engineering Department, Universiti Teknologi PETRONAS, Bandar Seri Iskandar, 31750, Tronoh, Perak, Malaysia
[*]E-mail: samaila@hotmail.com

ABSTRACT

Monoclinic bismuth oxide (α-Bi_2O_3) nanoparticles were prepared via precipitation method and irradiated with a pulsed laser forming thin films. Their phase and surface morphological properties were investigated using x-ray diffraction (XRD), atomic force microscopy (AFM), scanning electron microscopy (SEM) and high resolution transmission electron microscopy (HR-TEM). The XRD analysis shows the phase transformation to a partially crystalline tetragonal phase β-Bi_2O_3 thin film. The SEM micrograph of the nanoparticles, with an average crystal size of 72 nm, was seen to form a thin film with a peculiar structure, coined as "cotton-like", is attributed to the high surface energy absorbed by the nanoparticles during ablation. The HR-TEM micrograph shows the particulate with a clearly defined interlayer spacing.

Keywords: Nanostructures, thin film, laser ablation, X-ray diffraction

INTRODUCTION

Bismuth oxide is one of the most important transition metal oxides. It plays a significant role in a modern solid-state technology due to its properties such as band gap, refractive index, dielectric properties, etc. These properties made it suitable for a large range of applications such as optical coatings, photovoltaic cells, microwave integrated circuits (George *et al*., 1987; Chopra and Das, 1983), etc. Along with these applications, recently introduced applications of Bi_2O_3 are in fuel cells, oxygen sensors and oxygen pumps (Switzer *et al*., 1999; Shuk *et al*., 1996 and Azad *et al*., 1994). The oxide finds extensive application as catalysts for industrial selective oxidation reactions, especially for propylene selective oxidation and ammoxidation to acrolein and acrylonitrile, respectively (Irmawati *et al*., 2004; Hanna, 2004 and Arora *et al*., 1996). This is owing to its high oxygen-ion conductivity characteristic which provides oxygen for the α-hydrogen abstraction to form a symmetric allyl intermediate (Gleiter, 1991). Hanna (2004) revealed other important role of bismuth in promoting oxygen mobility in the lattice.

In this work, Bi_2O_3 was prepared via precipitation method and subsequently vaporized to form a thin film. Rather than simply evaporating the material to produce supersaturated vapor, a pulsed laser ablation was used to vaporize the target material (the as-prepared Bi_2O_3) so as to produce a thin film which is tightly confined, both spatially and temporally. The resulting product shows a remarkable "cotton-like" structure, which to authors' knowledge, has not been reported before.

Received: 25 April 2008
Accepted: 22 October 2008
[*]Corresponding Author

The precipitation method is preferred in providing powders with narrow particle size distribution in the range of few nanometers (Dhage *et al*., 2003), which is crucial to most applications of nanopowders, as it provides a precisely tailored set of properties for demanding applications. More so, the properties of the respective films strongly are dependent on their structure (crystalline size and shape, phase composition, presence of amorphous phase, etc.) which in turn, are determined by the deposition method and the preparation conditions (Leontie *et al*., 2001).

EXPERIMENTAL DETAILS

Preparation of Bi_2O_3

The Bismuth oxide nanoparticles were first prepared using the precipitation method, as reported in Patil *et al*. (2005). The Bismuth nitrate pentahydrate and standard ammonium hydroxide solution of AR grade were used for the preparation of bismuth oxide (Bi_2O_3). A known quantity of 4g $Bi(NO_3)_3.5H_2O$, 99.2% (HmbG chemicals) was dissolved in 50mL of 1M of nitric acid (Scharlau) and the molarity of bismuth in the resultant solution was 0.20 M. Ammonium hydroxide 25% extra pure (Scharlau) was added drop-wise to precipitate the bismuth as hydroxide. The resulting hydrate bismuth hydroxide ($Bi(OH)_3$), corresponding to JCPDS (card file number 00-001-0898), was washed several times and refluxed for 6 hours using a mantle stirrer (GLHMS 250 CC), maintaining the temperature at ≈373 K. The crystalline powder formed was dried in an oven for overnight and calcined at 673 K for 6 hours, employing the heating rate of ≈4.5 K/min. The resulting product was then characterized using the XRD, EDX and SEM.

Preparation of the Thin Film

To prepare the thin film, 0.5g of the as-prepared Bi_2O_3 was compressed into round pellet shape, using a hydraulic press with a force of 5 kN, irradiated using a pulsed laser and deposited onto unheated glass substrates. In the experiment, an Nd: YAG laser with wavelength 532 nm and a pulse-pulse width of 140 ns was used. The power, current, pressure and frequencies used were 10.24W, 25A, 5 Torr and 5 kHz, respectively (detailed steps on the setup was published elsewhere by Noorhana *et al*., 2005). The reaction process was carried out in an inert atmosphere, under the influence of Argon flown at 250 mL/min.

During the vaporization process, the flowing argon gas sweeps the produced soot from the target onto the substrate located 3cm away and parallel to the target. Furthermore, the gas leads to the confinement of the plume and a deceleration of the ablated particles, which consequently decreases its cooling rate. The process involves the bombardment of photons on the target material, leading to the emission and condensation of the particles on the substrate. The entire process includes the formation of the plasma plume with high energetic species and the subsequent transfer of the ablated material through the plasma plume onto the unheated substrate.

Characterization Techniques

For the x-ray diffraction (XRD) measurements, Philips X'Pert-MPD diffractometer, equipped with CuK_α target, operating in ambient temperature at 40kV and 30 mA, was used to generate diffraction patterns from the samples in ambient temperature, at a scanning rate of 0.33°/min for 2θ from 20° to 80°. The SEM was performed using the ZEISS SUPRA 35 VP FESEM equipped with the EDX. The SEM micrographs performed using field emission gun operating at 5-15 keV, while EDX was performed with a noise level of 40 eV. Meanwhile, the HR-TEM was performed using Philip Tecnai 20, with an accelerating voltage of 200kV. The densities and surface area were measured

using AccuPyc1330 helium Picnometer and BELSORP-mini high precision measuring apparatus, respectively. The crystallite size was calculated using the Scherrer's equation.

$$D_{hkl} = \frac{k\lambda}{B \cos \theta} \text{ Å} \quad (1)$$

where 'λ' is x-ray wavelength (1.542 Å), Θ the Bragg's angle at which the peak is observed, and 'B' is the full width of diffraction line at half of the maximum intensity.

RESULTS AND DISCUSSION

The structural analysis of the bismuth oxide films was carried out at varying diffraction angles 2θ from 20° to 60°, as shown in *Fig. 1a*. The observed values were in good agreement with the standard values in JCPDS card file number: 01-071-2274, confirming the formation of monoclinic α-Bi_2O_3. The crystallite size of (-1 2 1) plane-oriented α-Bi_2O_3 particles were estimated using the Debye Scherer's formula and was found to be about 124.4 nm. The calculated lattice parameters by the least square fit are a = 5.8486Å, b = 8.1661Å and c = 7.5059Å, and the cell volume (V) calculated from monoclinic crystal V = abc sinβ was found to be 330.15Å^3.

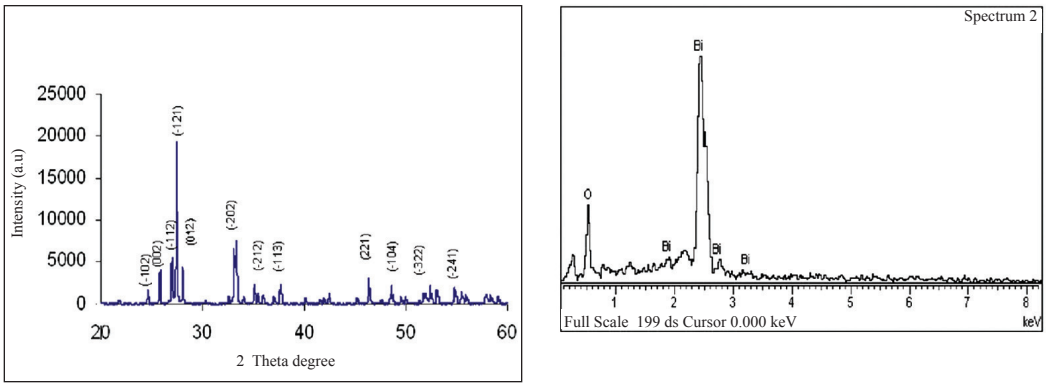

Fig. 1: (a) XRD pattern and (b) EDX profile of the as-prepared α-Bi_2O_3 nanoparticles

Fig. 1b reveals that the sample is of high purity, as only Bi and O peaks were visible in the spectrum. Furthermore, a close correlation was observed in the theoretical and experimental weight percent, having 11.20 and 10.30 wt% for oxygen and 88.80 and 89.70 wt% for bismuth for the observed and theoretical values, respectively.

Fig. 2 shows the SEM micrograph of the as-prepared α-Bi_2O_3. It can be seen that the sample is a flake-like structure described by vectors of unequal lengths. This structure is in agreement with the XRD result, which describes the sample as monoclinic. The size of the particles, as revealed by the SEM, ranges from 50 – 100 nm. The slight discrepancy observed with the calculated value using the XRD result is attributed to the non-ideal situation in the crystals, as against the assumptions of the Scherer's formula. Such inherent factors as crystal imperfections were not taken care of by the Scherer's formula. Acknowledging the fact that density is a fundamental parameter contributing to the characterization of a product, the density of the resulting product as recorded by AccuPyc1330

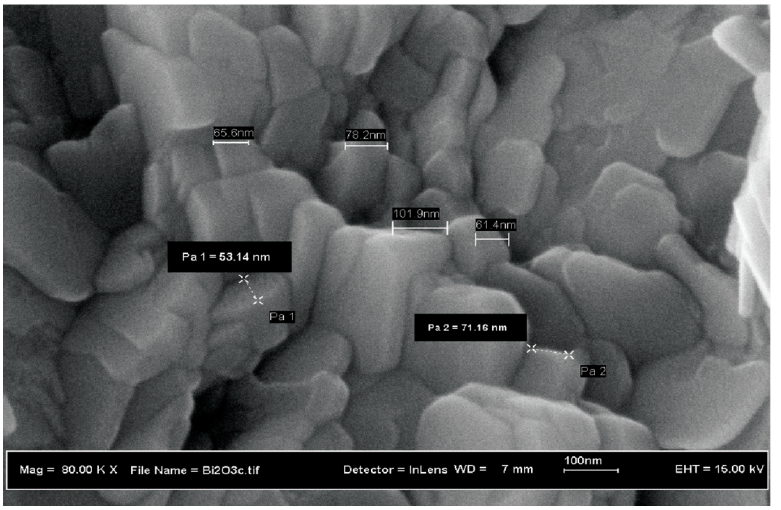

Fig. 2: SEM micrographs of the as-prepared α-Bi_2O_3 nanoparticles

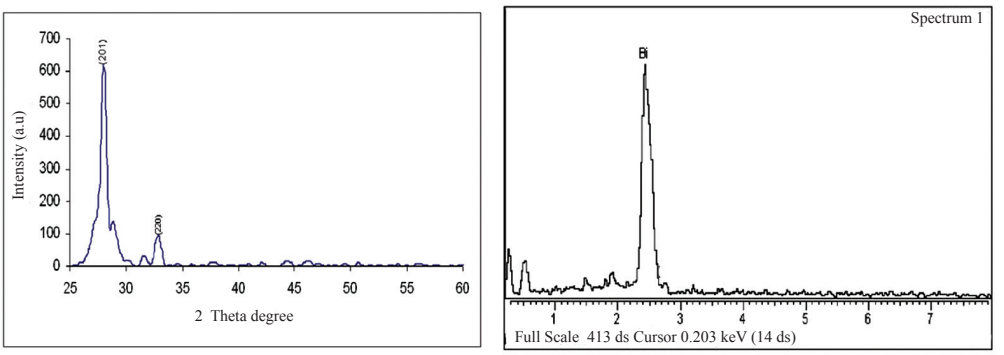

Fig. 3: (a) XRD pattern and (b) EDX spectrum of the deposited "cotton-like" β-$Bi_2O_{2.5}$ thin film

Picnometer was 8.91g/cm^3, which is very close to the theoretical density of the bismuth oxide (8. 90g/cm^3). The BET surface area of the oxide was 0.836m^2/g.

For the XRD pattern of the thin film as shown in *Fig. 3a*, it reveals a change of phase of the Bi_2O_3. The highly crystalline monoclinic α-Bi_2O_3 changes to a partially crystalline tetragonal non-stoichiometric phase β-$Bi_2O_{2.5}$ corresponding to standard values in JCPDS card files number: 01-074-1999. Consequently, the deficiency of oxygen atoms may have led to the formation of $Bi_2O_{2.5}$ phase in the film (Gujar *et al*., 2006). The amount of oxygen required for the phase formation is dependent on the thermodynamic stability of the desired oxide phase (Norton, 2004). The interaction of ablated species with the background gas produces sub-oxide species in the ablation plume. These sub-oxide species facilitate oxide phase formation. In addition to actively participating in the chemistry of the bismuth oxide growth, the background gas reduces the kinetic energies of the ablated Bi_2O_3. This means that with further annealing, $Bi_2O_{2.5}$ may be converted into Bi_2O_3 by taking oxygen from the surrounding medium.

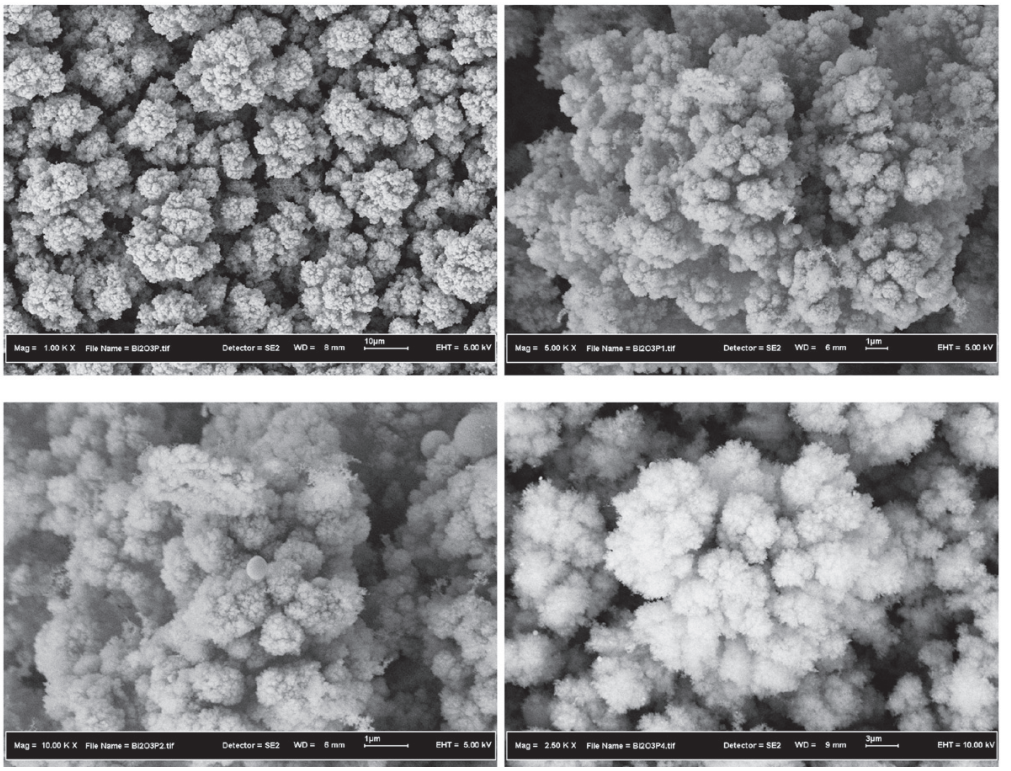

Fig. 4: SEM micrographs of the "cotton-like" β-$Bi_2O_{2.5}$ thin film with different magnifications (a) 1000 X, (b) 5,000 X, (c) 10,000X and (d) 2,500X

The XRD pattern of the as-deposited film revealed a partially crystalline structure. A reduced intensity of the thin film was observed, and this could be attributed to the formation of dangling bonds in the thin film deposited onto the glass substrate. This also suggested that the dangling bonds had given a rise to the interface states within the energy band gap of the glass consequence to the ablation process. The partially crystalline film growth depends on the surface mobility of the bismuth adatom (vapour atoms). Normally, the adatom diffuses through several atomic distances before sticking to a stable position within the newly formed film (Xu *et al*., 2006), and thus, the surface temperature of the substrate determines the surface diffusion ability of the adatom. High temperature favours rapid and defect free crystal growth, whereas low temperature or large supersaturation crystal growth may be overwhelmed by energetic particle impingement, resulting in disordered or even amorphous structures.

The EDX spectrum of the deposited thin film, shown in *Fig. 3b*, further confirms the presence of bismuth and oxygen in the sample. The surface morphology of as-deposited Bi_2O_3 thin films was studied from the SEM micrographs given in *Fig. 4*. At lower magnifications, the micrographs (*Fig. 4a* and *4b*) showed some spherical-like structures for the deposited film with defined nucleation points; however, a careful observation at high magnification (*Fig. 4c* and *4d*) showed the presence of well-grown "cotton-like" structures. These structures can be attributed to the properties and the composition of the plume evolved in this short time as a result of collisions between the bismuth particles within the plume and interaction between the plume and the laser. The

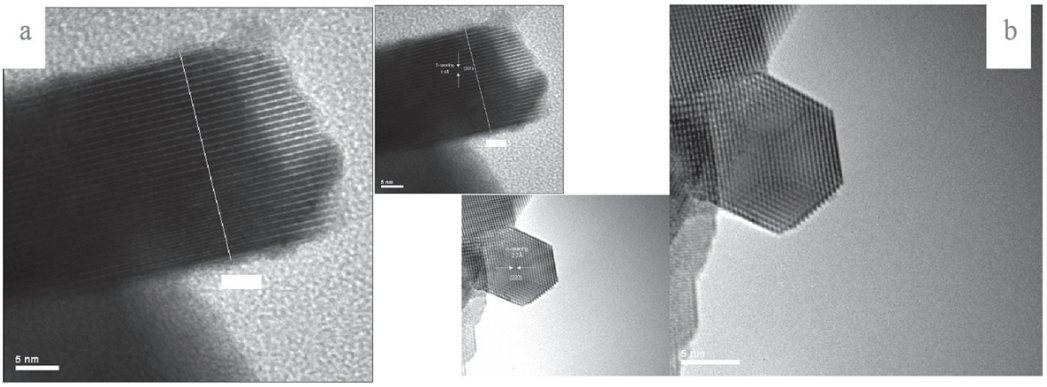

Fig. 5: HR-TEM micrograph of the deposited "cotton-like" $Bi_2O_{2.5}$ thin film (a) d-spacing of 3.1Å (b) average d-spacing of 2.7Å

components of these bismuth particle layers, (ions, electrons, atoms, radicals or clusters), travel at an extreme speed through the vacuum chamber until they have impinged on the surface of the substrate.

Since the sensitivity of a thin film is dependent both on the nature and the condition of the target material, and on the laser pulse parameters such as the wavelength, intensity, fluence, pulse duration, etc. (Satyanarayana *et al*., 2007)), the low melting point of the target material (Bi_2O_3), which is 817ºC and the high intensity of the Nd: YAG laser used for this work (5.2kW/cm^2) resulted in this wonderful structure. Further observation revealed a change in the density as a consequence to the ablation, and the resulting density of the thin film is 16.3844 g/cm^3. The increase in the density (as observed in the thin film) was attributed to the decrease in the bismuth-oxygen ratio, in addition to the decrease in the particle size of the resulting thin film. A tremendous increase in the BET surface area to 6.7304m^2/g was also observed, a situation attributed to the decrease in the crystal size consequent to ablation process.

To have a closer look at this cotton-like structure, the HR-TEM was used. The HR-TEM image of the deposited thin film (*Fig. 5a*) shows a clearly defined d-spacing, with an average d-spacing of 3.1Å, as estimated by the J-image software running on Linux. In *Fig. 5b*, the result exhibits a hexagonal shaped structure with an average d-spacing of 2.7Å. Abstracting the data from the XRD data in *Fig. 3(a)*, the values of *Figs. 5(a)* and *5(b)* were found to correspond to (201) and (220) planes, respectively.

When the dimensions were decreased from the micron level to the nano level, the specific surface area was found to increase by 3 orders of magnitude. In such a case, large proportions of the atoms will either be at or near the grain boundaries (Suryanaraya, 2005). Consequently, the quantum confinement would result in photocatalytic activities consequence to the immobilization of the high surface area nanostructures. These results suggest that the as-prepared bismuth oxide thin film would find the application in facilitating oxygen mobility in the oxide lattice in catalysis, and also result in a small shift of the reduction maximum toward lower temperature (Liu *et al*., 2003). Within the molecular sheets of bismuth, the intermolecular forces are involved in the covalent bonding and the forces between the sheets are primarily Van der Waals bonds (Evans, 1964). Due to the quasi-layered structure of elemental Bismuth, the formation mechanism of the Bi nano-

tubes reported by Liu *et al*. (2003), the observed structure might also be catalytically useful in the growth of carbon nanotubes. However, this view is still limited and further study is in progress.

CONCLUSIONS

Pure phase monoclinic α-Bi_2O_3 of an average crystal size of 72 nm was obtained using the gel-precipitation technique and the bismuth oxide thin films were prepared using a pulsed laser ablation technique. The as-prepared films were polycrystalline with the phase of tetragonal β-$Bi_2O_{2.5}$. The surface morphological study revealed the total coverage of substrates with well-developed grains. From the SEM studies, a "cotton-like" structure was observed for the bismuth oxide films. The HR-TEM micrographs showed a clearly defined d-spacing and the ablation process was seen to result in the break up of the particulate of the as-prepared α-Bi_2O_3 to a tetragonal β-$Bi_2O_{2.5}$ with average grain sizes of 10 nm as deposited on the substrate. This means the effect of the ablation process, with the power of 10.24 W, resulted in further breaking up of the Nanoparticles and a change of phase. The large surface area consequence to the small size structure is believed to result in an improved reactivity and diffusivity.

ACKNOWLEDGMENTS

The authors are grateful for the financial support given by the Ministry of Science, Technology and Innovation, Malaysia, under the EAR research grant vote number 54430 and the Universiti Putra Malaysia for the Graduate Research Fellowship.

REFERENCES

Arora, N., Deo, G., Wachs, I.E. and Hirt, A.M. (1996). Surface aspects of bismuth–Metal oxide catalysts. *Journal of Catalysis, 159,* 1-13.

Azad, A.M., Larose, S. and Akbar, S.A. (1994). Bismuth oxide-based solid electrolytes for fuel cells. *Journal of Materials Science, 29,* 4135-4151.

Chopra, K.L. and Das, S.R. (1983). *Thin Film Solar Cells* (Chaps. 6 and 7). New York and London: Plenum Press.

Dhage, S.R., Khollam, Y.B., Deshpande, S.B. and Ravi, V. (2003). Co-precipitation technique for the preparation of nanocrystalline ferroelectric $SrBi_2Ta_2O_9$. *Materials Research Bulletin, 38,* 1601-1605.

Evans, R.C. (1964). *An Introduction to Crystal Chemistry*. Cambridge, MA: Cambridge University Press.

Fu, J. (1997). Electrical properties of glasses in the systems Bi_2O_3-RO-Li_2O (R_Ca, Sr, Ba). *Journal of Material Science Letters, 16,* 1433-1436.

George, J., Pradeep, B. and Joseph, K.S. (1987). Preparation of heat mirrors using bismuth oxide films. *Physica Status Solid (a), 100,* 513-519.

Gleiter, H. (1991). Nanocrystalline solids. *Journal of Applied Crystallography, 24,* 79-90.

Gujar, T.P., Shinde, V.R. and Lokhande, C.D. (2006). Spray pyrolysed bismuth oxide thin films and their characterization. *Materials Research Bulletin, 41*(8).

Hanna, T.A. (2004). The role of bismuth in the SOHIO process. *Coordination Chemistry Review, 248*(56), 429-440.

Irmawati, R., Noorfarizan Nasriah, Y.H., Taufiq-Yap and Abdul Hamid, S.B. (2004). Characterization of bismuth oxide catalysts prepared from bismuth trinitrate pentahydrate: influence of bismuth concentration. *Catalysis Today, 93-95,* 701-709.

Shuk, P., Wiemhofer, H.D., Guth, V., Gopel, W. and Greenblatt, M. (1996). Oxide ion conducting solid electrolytes based on Bi_2O_3 Solid *State Ionics, 89,* 179-196.

Switzer, J.A., Shumsky, M.G. and Bohannan, E.W. (1999). Electrodeposited ceramic single crystals. *Science, 284*, 293-296. 1558-1564.

Leontie, L., Caraman, M., Deliba, M. and Rusu, G. I. (2001). Optical properties of bismuth trioxide thin films. *Materials Research Bulletin, 36*(9), 1629-1637.

Liu, X., Zeng, J., Zhang, S., Zheng, R., Xian-ming, L. and Yi-tai Qian. (2003). Novel bismuth nanotube arrays synthesized by solvothermal method. *Chemical Physics Letters, 374*(3-4), 348.

Noorhana, Y., Beh, H.G and Mansur, H. (2005). Development of pulsed laser deposition system for the formation of web-liked carbon nanotubes. *American Journal of Applied Sciences, 2*(11), 1509-1515.

Norton, D.P. (2004). Carbon nanotubes: Properties and application. *Material Science and Engineering R: Reports, 43*(5-6), 139-247.

Patil, M.M., Deshpande, V.V., Dhage, S.R and Ravi, V. (2005). Synthesis of bismuth oxide nanoparticles at 100°C. *Materials Letters, 59*(19-20), 2523-2525.

Satyanarayana, V.N.T , Kuchibhatla, Karakoti, A.S., Bera, D. and Seal, S. (2007). One dimensional nanostructured materials. *Progress in Materials Science, 52,* 5699-913.

Suryanarayana, C. (2005). Recent developments in nanostructured materials. *Advanced Engineering Material, 7,* 983.

Xu, X.H., Zhang, R.Q., Dong, X.Z. and Gehring, G.A. (2006). A study of the optimization of parameters for pulsed laser deposition using Monte Carlo simulation. *Thin Solid Films, 515*(4), 2754-2759.

ISSN: 0128-7680
Pertanika J. Sci. & Technol. **17 (2):** 307– 312 (2009)

Xanthones from *Calophyllum inophyllum*

G.C.L. Ee*, V.Y.M. Jong, M.A. Sukari, M. Rahmani and A.S.M. Kua
Department of Chemistry, Faculty of Science,
Universiti Putra Malaysia, 43400 UPM, Serdang,
Selangor, Malaysia
**E-mail: gwen@fsas.upm.edu.my*

ABSTRACT

The roots of *Calophyllum inophyllum* (Guttiferae), furnished six xanthones which are brasilixanthone (**1**), 1,3,5-trihydroxy-2- methoxy xanthone (**2**), caloxanthone A (**3**), pyranojacareubin (**4**), caloxanthone B (**5**) and tovopyrifolin (**6**), Structural elucidations of these compounds, were achieved through 1D and 2D NMR and MS techniques. In this paper, the isolation and structural elucidation data for these xanthones are reported.

Keywords: ***Calophyllum inophyllum*, xanthones, NMR, MS**

INTRODUCTION

Calophyllum inophyllum, which is also known as 'bintangor' by the locals in Malaysia, belongs to the Guttiferae family. Several species of this genus are known to be used in folk medicine (Dharmaratne and Wanigasekera, 1996). The wood has been used in general construction and boatbuilding, as well as for flooring, furniture, musical instruments, handicrafts, and a variety of other purposes (Shalan and Locksley, 1971). This genus has been found to be rich in xanthones (Iinuma *et al*., 1995; Kijoa *et al*., 2000; Ee *et al*., 2004*,* 2006), coumarins (Kashman *et al*., 1992; McKee *et al*., 1996) and flavonoids (Cao *et al*., 1997). Several coumarins isolated from two *Calophyllum* species were found to inhibit HIV-1 replication and cytopathicity activities (Pengsuparp *et al*., 1996; Kashman *et al*., 1992). The present work concentrates on the isolation of xanthones from the roots of *Calophyllum inophyllum.*

EXPERIMENT

Plant Material

The root bark of *Calophyllum inophyllum* was collected from UPM campus and identified by Dr. Rusea Go from the Department of Biology, UPM.

General

Infrared spectra were measured in KBr/NaCl pellet on a Perkin-Elmer FTIR Spectrum BX spectrometer. EIMS were recorded on a Shimadzu GCMS-QP5050A spectrometer. NMR spectra were obtained using a Unity INOVA 500MHz NMR/JEOL 400MHz FT NMR spectrometer, using tetramethylsilane (TMS) as an internal standard. UV spectra were recorded in $CHCl_3$ on a Shimadzu UV-160A, UV-Visible Recording Spectrophotometer. Melting points were measured using a leica Galen III microscope, equipped with Testo 720 temperature recorder.

Received: 30 April 2008
Accepted: 23 October 2008
*Corresponding Author

Extraction and Isolation

The dried roots of *Calophyllum inophyllum L.* (1.4 kg) were extracted with distilled n-hexane for 48 hours for three times. The combined n-hexane extract was concentrated under reduced pressure in a rotary evaporator. The same sample was then re-extracted twice each with distilled chloroform, followed by methanol for 48 hours. Eleven g of n-hexane extract, 60 g of chloroform extract and 21 g of methanol extract were obtained. The hexane, chloroform and methanol extracts were chromatographed through silica gel using hexane, chloroform, ethyl acetate and methanol as eluting solvents. The column chromatography on the crude hexane extract gave brasilixanthone **(1)** (5mg). 1,3,5-Trihydroxy-2-methoxy xanthone **(2)** (4 mg) and caloxanthone A **(3)** (15 mg) were obtained from the chloroform extract. Meanwhile, the methanol extract furnished pyranojacareubin **(4)** (4 mg), caloxanthone B **(5)** (6mg) and tovopyrifolin (**6**) (5 mg).

Brasilixanthone (1). Yellow crystals with m.p. 181-182ºC (Lit 181-182°C, Marques *et al*., 2000). UV ($CHCl_3$) λ_{max} nm: 317, 247. IR ν_{max} cm^{-1} (KBr): 3504, 2924, 1624, 1540, 1454, 1125, 1120, 750. EI-MS *m/z*: 392, 378, 377, 369, 347, 319, 279, 237, 203, 152, 115, 91, 77, 181 and 41. ^{1}H NMR (400 MHz, $CDCl_3$): δ 13.62 (s, 1-OH,), δ 8.02 (d, 1H, *J*=10.0Hz, H-16), *δ* 6.83 (s, 1H, 6-OH), *δ* 6.72 (d, 1H, *J*=10.0Hz, H-12), δ 6.27 (s, 1H, H-5), *δ* 6.26 (s, 1H, H-4), *δ* 5.82 (d, 1H, *J*=10.0 Hz, H-17), *δ* 5.57 (d, 1H, *J*=10.0Hz, H-11), *δ* 1.47 (s, 6H, 14-CH_3, 15-CH_3), *δ* 1.50 (s, 6H, 19-CH_3, 20-CH_3). ^{13}C NMR (100 MHz, $CDCl_3$):*δ* 156.5 (C-1), *δ* 103.9 (C-2), *δ* 153.0 (C-3), *δ* 94.3 (C-4), *δ* 157.8 (C-4a), *δ* 102.4 (C-5), *δ* 150.9 (C-6), *δ* 136.8 (C-7), *δ* 119.7 (C-8), *δ* 108.5 (C-8a), *δ* 182.5 (C-9), *δ* 104.4 (C-9a), *δ* 160.0(C-10a), *δ* 108.5 (C-11), *δ* 132.3 (C-12), *δ* 77.3 (C-13), *δ* 28.3 (C-14 & C-15), *δ* 120.9 (C-16), *δ* 127.2 (C-17), *δ* 77.3 (C-18), *δ* 27.3 (C-19 & C-20).

1,3,5-trihydroxy-2-methoxy xanthone (2). Pale yellow powder with m.p 182-184ºC (Lit 183-185°C, Iinuma *et al*., 1997). IR ν_{max} cm^{-1} (KBr): 3468, 1658, 1616, 1541, 1164, 1124, 854. EI-MS *m/z*: 274, 259, 231, 202, 187, 161, 147, 136, 107, 93, 77, 65, 51 and 41. ^{1}H NMR (400 MHz, $CDCl_3$): *δ* 13.11 (s, 1H, 1-OH), *δ* 9.48 (s, 1H, 5-OH), *δ* 9.26 (s, 1H, 3-OH), *δ* 7.64 (dd, 1H, *J* = 7.3, 1.8 Hz, H-8), *δ* 7.32 (dd, 1H, *J* = 8.2, 1.8 Hz, H-6), *δ* 7.26 (t, 1H, *J* = 15.6 Hz, H-7), *δ* 6.52 (s, 1H, H-4), *δ* 3.86 (s, 3H, 2-OMe). ^{13}C NMR (100 MHz, $CDCl_3$): *δ* 182.1 (C-9), *δ* 159.2 (C-3), *δ* 155.3 (C-1), *δ* 153.8 (C-4a), *δ* 146.9 (C-5), *δ* 146.0 (C-10a), *δ* 131.5 (C-2), *δ* 124.8 (C-7), *δ* 121.7 (C-8a), *δ* 121.3 (C-6), *δ* 116.1 (C-8), *δ* 103.9 (C-9a), *δ* 94.7 (C-4), *δ* 60.7 (2-OMe).

Caloxanthone A (3). Yellow needles with m.p. 136-138ºC (Lit 136-137°C, Iinuma *et al*., 1994). UV (EtOH) λ_{max} nm: 388, 494. IR ν_{max} cm^{-1} (KBr): 3516, 2982, 1650, 1612, 1650, 1450. EI-MS *m/z* : 394, 379, 323, 295, 281, 267, 237, 203, 175, 162, 148, 115, 105, 91, 77 and 55. ^{1}H NMR (400 MHz, $CDCl_3$): *δ* 13.89 (s, 1H, OH-1), *δ* 7.44 (s, 1H, H-8), *δ* 6.66 (d, *J* = 10.1Hz, 1H, H-11), *δ* 6.33 (s, 1H, H-4), *δ* 5.70 (d, *J* = 10.1Hz, 1H, H-12), *δ* 5.31 (t, *J* = 7.3Hz, 1H, H-17), *δ* 3.61 (d, *J* = 7.3Hz, 1H, H-16), *δ* 1.88 (s, 3H, C-19), *δ* 1.65 (s, 3H, H-20), *δ* 1.45 (s, 6H , H-14, H-15). ^{13}C NMR (100 MHz, $CDCl_3$): *δ* 180.8 (C-9), *δ* 160.6 (C-3), *δ* 158.3 (C-1), *δ* 158.0 (C-4a), *δ* 152.3 (C-10a), *δ* 150.8 (C-6), *δ* 143.4 (C-7), *δ* 132.5 (C-18), *δ* 128.5 (C-12), *δ* 122.4 (C-17), *δ* 116.6 (C-5), *δ* 115.9 (C-11), *δ* 113.2 (C-8a), *δ* 106.2 (C-8), *δ* 104.8 (C-2), *δ* 103.5 (C-9a), *δ* 95.3 (C-4), *δ* 78.7 (C-13), *δ* 28.4 (C-14), *δ* 28.4 (C-15), *δ* 25.8 (C-19), *δ* 23.0 (C-16), *δ* 18.1 (C-20).

Caloxanthone B (5). Yellow crystals with melting point 152-158ºC (Lit. 160.5ºC, Iinuma *et al*., 1994). UV (EtOH) λ_{max} nm: 317, 247. IR ν_{max} cm^{-1} (KBr): 3388, 2968, 1648, 1606, 1572, 1480, 1250. EI-MS *m/z*: 410, 395, 367, 352, 339, 337, 325, 176. ^{1}H NMR (400 MHz, $CDCl_3$): *δ* 13.75

(s, 1H, 1-OH), δ 7.28 (s, 1H, 6-OH), δ 6.84 (s, 1H, H-7), δ 6.26 (s, 1H, H-2), δ 5.38 (t, 1H, J=7.2Hz, H-17), δ 4.54 (q, 1H, J =6.6 Hz, H-14), δ 4.02 (s, 3H, 5-OCH_3), δ 4.01 (d, 2H, J=7.2 Hz, H-16), δ 1.78 (d, 3H, J=1.2Hz, 20-CH_3), δ 1.75 (s, 3H, 19-CH_3), δ 1.62 (s, 3H, 13-CH_3), δ 1.43 (s, 3H, 15-CH_3), δ 1.33 (s, 3H, 12-CH_3). ^{13}C NMR (100 MHz, $CDCl_3$): δ 182.1 (C-9), δ 165.6 (C-3), δ 164.6 (C-1), δ 153.4 (C-6), δ 151.7(C-4a), δ 151.0 (C-10a), δ 142.1 (C-8), δ 133.3 (C-18), δ 132.2 (C-5), δ 122.3 (C-17), δ 113.3 (C-7), δ 112.1 (C-8a), δ 103.9 (C-9a), δ 94.0 (C-2), δ 90.6 (C-14), δ 61.9 (5-OCH_3), δ 33.6 (C-16), δ 25.9 (C-19), δ 25.6 (C-13), δ 21.6 (C-12), δ 18.0 (C-20), δ 14.2 (C-15).

Tovopyrifolin (**6**) Pale yellow crystals with m.p. 258-259ºC (Lit 256-258°C, Mesquita *et al*., 1975). UV (EtOH) λ_{max} nm: 313, 244, 217. IR ν_{max} cm^{-1} (KBr): 3468, 1584, 1464, 1218. EI-MS *m/z*: 274, 259, 231, 228, 136, 92. ^{1}H NMR (400 MHz, $CDCl_3$): δ 13.11 (s, 1H, 1-OH), δ 9.48 (s, 1H, 3-OH), δ 9.26 (s, 1H, 5-OH), δ 7.64 (dd, 1H, J = 7.5Hz, 1.8 Hz, H-8), δ 7.34 (dd, 1H, J = 8.2Hz, 1.8 Hz, H-6), δ 7.28 (t, 1H, J = 7.5Hz, H-7), δ 6.52 (s, 1H, H-4), δ 3.86 (s, 3H, 2-OCH_3). ^{13}C NMR (100 MHz, $CDCl_3$):δ 182.1 (C-9), δ 159.2 (C-3), δ 155.3 (C-1), δ 153.8 (C-4a), δ 146.9 (C-5), δ 146.1 (C-10a), δ 131.5 (C-2), δ 124.8 (C-7), δ 121.7 (C-8a), δ 121.3 (C-6), δ 116.1 (C-8), δ 104.0 (C-9a), δ 94.7 (C-4), δ 60.7 (OCH_3).

RESULTS AND DISCUSSION

Pyranojacareubin **(4)**(10 mg) was obtained as fine yellow crystals with a m.p. of 185-189ºC (Lit. 187-189°C, Waterman and Crichton, 1980). The mass spectra data shows a molecular ion peak at *m/z* 392, indicating a molecular formula of $C_{23}H_{20}O_6$. The *m/z* peak of 377 was due to the loss of one methyl group, suggesting the existence of CH_3 as a side chain group.

The ^{1}H NMR spectrum showed the presence of one chelated hydroxyl group at δ 13.20. Two tall and sharp singlet peaks, at δ 1.36 and δ 1.41, which were integrated for 6 protons each, suggested four methyl groups. The COSY spectrum also indicated that the proton signal at δ 6.59 was coupled to the proton signal at δ 5.49. Meanwhile, the proton signal at δ 6.31 was coupled to the proton signal at δ 5.62. Thus, the four signals were assigned to the protons which were attached to C-11, C-12, C-16 and C-17. Four doublet peaks were observed at δ 6.59, δ 5.49, δ 6.31 and δ 5.62. These peaks have the same coupling constant value of 10.1 Hz, and the signals were assigned to H-11, H-12, H-16 and H-17, respectively.

The total number of carbon atoms observed in the ^{13}C NMR spectrum was 23. Meanwhile, the HMBC spectrum showed that two of the four methyl groups were attached to a similar carbon at C-13. Another two CH_3 groups were attached to C-18. The pyrano ring was obvious from the HMBC spectrum, indicating that the proton which was correlated to C-1 and C-3 was at C-11, and the proton at C-12 was correlated to C-2 via a ^3J coupling.

The HMBC spectrum also gave a ^2J correlation between the proton H-12 and C-13, while a ^3J correlation between proton H-11 and C-13 was observed. Meanwhile, proton H-11 had a correlation with C-12 and C-13 via a ^2J and ^3J coupling, respectively. On the other hand, the pyrano ring on the other side was obvious from the HMBC spectrum, which indicated that the proton at C-16 was correlated to C-7 via a ^2J coupling and the proton at C-17 was correlated to C-7 via a ^3J coupling. The HMBC spectrum also gave a ^3J correlation between proton H-16 and C-18.

From the DEPT spectrum, 6 C-H groups and no methylene groups were clearly seen in the compound. There was also evidence of 12 quarternary carbons and four CH_3 groups. Hence, compound **4** was identified to be pyranojacareubin previously isolated from *Garcinia densivenia* (Waterman and Crichton, 1980).

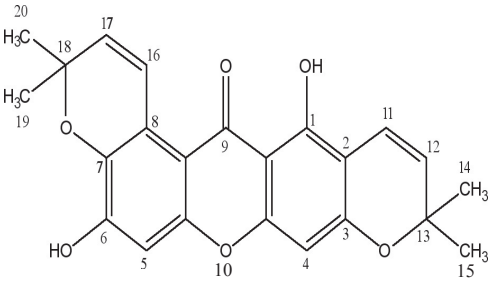

(1)

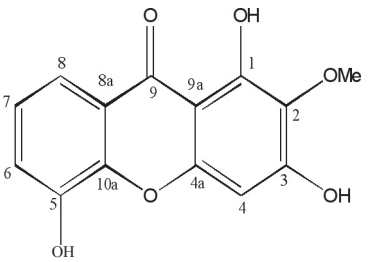

(2)

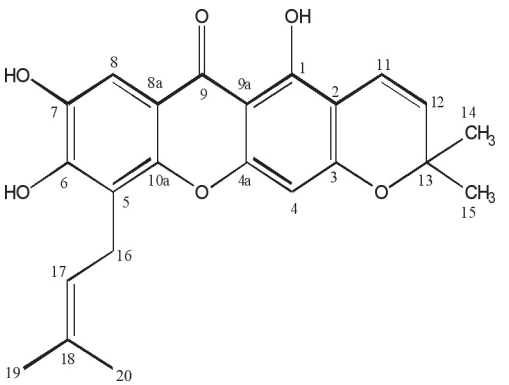

(3)

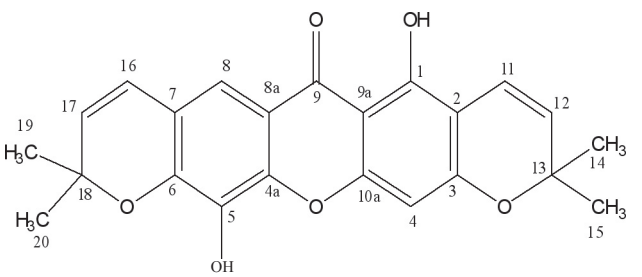

(4)

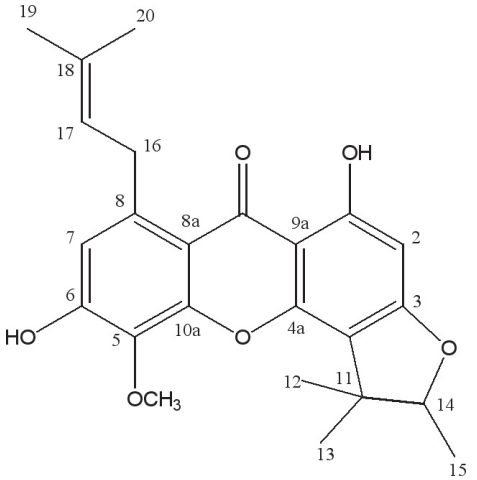

(5)

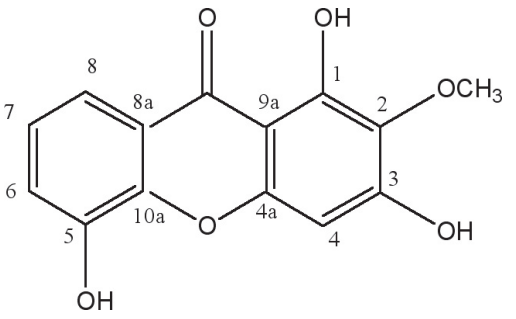

(6)

TABLE 1
^{1}H NMR (400 MHz, $CDCl_3$), ^{13}C NMR (100 MHz, $CDCl_3$)
and HMBC assignments of Pyranojacareubin **(4)**

Position	δ_H	δ_C	HMBC
1	13.20 (OH)	157.7	-
2	-	104.8	-
3	-	160.4	-
4	6.30 (1H,s)	95.3	160.4 (C-3)
4a	-	156.8	-
5	-	132.1	-
6	-	144.8	-
7	-	117.8	-
8	7.30 (1H,s)	113.5	180.2 (C-9), 121.4 (C-16),
8a	-	114.6	-
9	-	180.2	-
9a	-	103.2	-
10a	-	145.1	-
11	6.59 (1H,d, J = 10.1Hz)	115.4	78.2 (C-13), 157.7 (C-1), 160.4 (C-3)
12	5.49 (1H, d, J = 10.1Hz)	127.5	78.2 (C-13), 104.8 (C-2)
13	-	78.2	-
14	1.36 (3H,s)	28.4	28.4 (C-15), 127.5 (C-12), 78.2 (C-13)
15	1.36 (3H,s)	28.4	28.4 (C-14), 127.5 (C-12), 78.2 (C-13)
16	6.31 (1H, d, J = 10.1Hz)	121.4	78.9 (C-18), 117.8 (C-7)
17	5.62 (1H,d, J = 10.1Hz)	131.0	78.9 (C-18), 117.8 (C-7)
18	-	78.9	-
19	1.41 (3H,s)	28.5	78.9 (C-18), 131.0 (C-17), 28.5 (C-20)
20	1.41 (3H,s)	28.5	78.9 (C-18), 131.0 (C-17), 28.5 (C-19)

ACKNOWLEDGEMENTS

The authors wish to thank the Malaysian Government Science Fund for the financial support, and Mr. Johadi Iskandar from the Department of Chemistry UPM, for recording the NMR spectra.

REFERENCES

Cao, S.G., Sim, K.Y. and Goh, S.H. (1997). Biflavonoids of *Calophyllum venulosum*. *Natural Product Letters*, *60,* 1245-1250.

Dharmaratne, H.R.W. and Wanigasekera, W.M.A.P. (1996). Xanthones from root bark of *Calophyllum thwaitesii*. *Phytochemistry, 42,* 249-250.

Ee, G.C.L., Kua, A.S.M., Cheow Y.L., Lim C.K., Jong V. and Rahmani, M. (2004). A new pyranoxanthone Inophyllin B from *Calophyllum inophyllum. Natural Product Sciences, 10*(5), 220-222.

Ee, G.C.L., Kua, A.S.M., Lim, C.K., Jong, V., Sukari, M.A. and Lee, H.L. (2006). Inophyllin A, a new pyranoxanthone from *Calophyllum inophyllum. Natural Product Research*, *20*(5), 485-491.

Iinuma, M., Tosa, H., Tanaka, T. and Yonemori, S. (1994). Two xanthones from roots of *Calophyllum inophyllum*. *Phytochemistry, 35,* 527-532.

Iinuma, M., Tosa, H., Tanaka, T. and Yonemori, S. (1995). Two xanthones from the roots of *Calophyllum inophyllum*. *Phytochemistry, 38,* 725-728.

Iinuma, M., Ito, T., Tosa, H., Tanaka, T., Miyake, R., and Chelladurai, V. (1997). Prenylated xanthonoids from *Calophyllum apetalum. Phytochemistry, 46,* 1423-1429.

Kashman, Y.K., Gustafson, R., Fuller, R.W., Cardellina, J.H., McMahon, J.B., Currens, M.J., Buckheit, R.W., Hughes, S.H., Cragg, G.M. and Boyd, M.R. (1992). The Calanolide, a novel HIV-Inhibitory class of coumarin derivatives from the tropical rainforest tree. *Calophyllum lanigerum*. *Journal of Medicinal Chemistry, 35,* 2735-2743.

Kijjoa, A., Jose, M., Gonzalez, T.G., Pinto, M.M., Damas, A.M., Mondranondra, I.O., Silva, A.M.S. and Herz, W. (2000). Xanthones from *Calophyllum teysimannii*. *Phytochemistry, 55,* 833-836.

Marques, V.LD., Oliveira, F.M., Conserva, L.M, Brito, R.G. and Guilhon, G.M. (2000). Dichromenoxanthones from *Tovomita brasiliensis*. *Phytochemistry, 55*(7), 815-818.

McKee, T.C., Richard, W.F., Conni, D.C., John, H.C. II, Robert, J.G., Benjamin, L.K., James, B.M. and Michael, R. (1996). New pyranocoumarins isolated from *Calophyllum lanigerum* and *Calophyllum teysmannii*. *Journal of Natural Product, 59,* 754-758.

Mesquita, A.A.L., Oliveira, W.G. and Neiva, R.M.T. (1975). Xanthones from *Tovomita pyrifolium*. *Phytochemistry, 14,* 803-806.

Pengsuparp, T., Serit, M., Hughes, S.H., Soejarto, D.D., and Pezzuto, J.M. (1996). Specific inhibition of human immunodeficiency virus type 1 reverse transcriptase mediated by soulattrolide, a coumarin isolated from the latex of *Calophyllum tesmannii. Journal of Natural Products, 59,* 839-842.

Shalan, F. and Locksley, H.D. (1971). Xanthones in the heartwood of *Calophyllum inophyllum*; A geographical survey. *Phytochemistry, 10*(3), 603-606.

Waterman, P.G. and Crichton, E.G. (1980). Xanthones and biflavanoids from *Garcinia densivenia* stem bark.

ISSN: 0128-7680
Pertanika J. Sci. & Technol. **17 (2)**: 313 – 323 (2009)

Interval Estimation for Parameters of a Bivariate Time Varying Covariate Model

Jayanthi Arasan
Department of Mathematics, Faculty of Science,
Universiti Putra Malaysia, 43400 UPM, Serdang,
Selangor, Malaysia
E-mail:jayanthi@math.upm.edu.my

ABSTRACT

This paper investigates several asymptotic confidence interval estimates, based on the Wald, likelihood ratio and the score statistics for the parameters of a parallel two-component system model, with dependent failure and a time varying covariate, when data is censored. This model is an extension of the bivariate exponential model. The procedures are investigated via a coverage probability study using the simulated data. The results clearly indicate that the interval estimates, based on the likelihood ratio method, work better than any of the other two methods when dealing with the censored data.

Keywords: Bivariate, time varying, censoring, covariates, asymptotic, Wald, parallel, score

INTRODUCTION

The main limitation for most models, with censored data, is the fact that exact confidence intervals are impossible to compute. One alternative is to use large sample intervals, based on the asymptotic normality of the maximum likelihood estimates. However, there are some concerns over the use of the intervals which are based on asymptotic normality. Jeng and Meeker (2000) pointed out that its actual coverage probability could be significantly different from the nominal specification for a small to moderate number of failures, particularly for the one-sided confidence bounds. Cox and Hinkley (1979) mentioned that one of the disadvantages of using the Wald statistic is that it is not invariant under the transformation of the parameter of interest, unlike the methods which are based on the likelihood ratio and the score tests.

This paper investigates the interval estimates based on the Wald, likelihood ratio and the score methods, when they are applied to the parameters of the bivariate exponential model with dependent failure, time varying covariate and censored data. This is an extension of the bivariate exponential model by Freund (1961). Most of the studies, with parametric models involving time varying covariates, are in the area of political science and sociology. Works involving time varying covariates and duration dependence were done and discussed by authors such as Petersen (1986), Beck (1999), Bennet (1999), Box-Steffensmeier and Jones (1997), Tuma and Hannan (1984), Blossfield *et al*. (1989), Yamaguchi (1991), Courgeau and Leli`evre (1992), as well as Kalbfleisch and Prentice (1980).

Received: 7 May 2008
Accepted: 14 October 2008

MATERIALS AND METHODS

Bivariate Model with Time Varying Covariate

Let T_1 and T_2 be random variables representing the lifetimes of two components, A and B from a parallel system with dependent failure. Similarly, m and r are the values of the random variables representing the total number of levels of the covariate in [0, min(t_1, t_2)] and [0, min(t_1, t_2)] respectively, with an initial value of m=1. The hazard rate of component A is h=exp(-β_0-$\beta_1 x$)and the hazard rate of the component B is g=exp(-ω_0-$\omega_1 x$), where -β_0, β_1, ω_0 and ω_1 are unknown parameters. If component A fails before component B, the hazard rate of component B then changes as a function of the covariates to g'= exp(-ω^*_0-$\omega^*_1 x$), and similarly if component B fails first, then the hazard rate of component A changes to h'=exp(-β^*_0-$\beta^*_1 x$). The joint density function of T_1 and T_2 is:

$$f(t_1,t_2)=\begin{cases} h_m g_r^{'}\exp(-[(h_m+g_m)(t_1-a_{m-1})+\sum_{l=1}^{m-1}(h_l+g_l)(a_l-a_{l-1})]-[g_m^{'}(a_m-t_1) \\ +g_r^{'}(t_2-a_{r-1})+\sum_{l=m+1}^{r-1}g_l^{'}(a_l-a_{l-1})]) \\ for\ \ r>m>0\ \ and\ \ a_{m-1}<t_1\le a_m<t_2\le a_r, \\ h_m g_m^{'}\exp(-[(h_m+g_m)(t_1-a_{m-1})+\sum_{l=1}^{m-1}(h_l+g_l)(a_l-a_{l-1})]-g_m^{'}(t_2-t_1)) \\ for\ \ r=m>0\ \ and\ \ a_{m-1}<t_1<t_2\le a_m, \\ \\ g_m h_r^{'}\exp(-[(h_m+g_m)(t_2-a_{m-1})+\sum_{l=1}^{m-1}(h_l+g_l)(a_l-a_{l-1})]-[h_m^{'}(a_m-t_2) \\ +h_r^{'}(t_1-a_{r-1})+\sum_{l=m+1}^{r-1}h_l^{'}(a_l-a_{l-1})]) \\ for\ \ r>m>0\ \ and\ \ a_{m-1}<t_2\le a_m<t_1\le a_r, \\ g_m h_m^{'}\exp(-[(h_m+g_m)(t_2-a_{m-1})+\sum_{l=1}^{m-1}(h_l+g_l)(a_l-a_{l-1})]-h_m^{'}(t_1-t_2)) \\ for\ \ r=m>0\ \ and\ \ a_{m-1}<t_2<t_1\le a_m, \end{cases}$$

This paper is divided into 4 sections; Section 1 looks into some of the background studies related to the current work and the objectives of this research; Section 2 explores several asymptotic confidence interval estimates based on the Wald, likelihood ratio and the score statistics for the parameters of the time varying covariate model via coverage probability study using simulated data. Meanwhile, the result of the simulation study is discussed in Section 3, and finally Section 4 offers some concluding remarks and suggestions for future work.

Asymptotic Interval Estimation

The Wald Method

Let $\hat{\theta}$ be the maximum likelihood estimator for parameter and the log-likelihood function of θ. Under mild regularity conditions, $\hat{\theta}$ is asymptotically normally distributed with mean θ and covariance matrix $I^{1}(\theta)$, where $I(\theta)$ is the Fisher information matrix, evaluated at the true value of the parameter θ, (Cox and Hinkley, 1979). The matrix $I(\theta)$ which is not available, can be replaced by the observed information matrix $I(\hat{\theta})$ whose $(j, k)^{\text{th}}$ element can be obtained from the second partial derivatives of the log-likelihood function evaluated at $\hat{\theta}$. If $z_1-\frac{\alpha}{2}$ is the $\left(1-\frac{\alpha}{2}\right)$quantile of the standard normal distribution, the 100(1-α)% confidence interval for θ_j is given by the following:

$$\hat{\theta}_j - z_{1-\frac{\alpha}{2}}\sqrt{I^{-1}(\hat{\theta}_{jj})} < \theta_j < \hat{\theta}_j + z_{1-\frac{\alpha}{2}}\sqrt{I^{-1}(\hat{\theta}_{jj})}\,.$$

The LR Method

The confidence interval, based on the likelihood ratio statistic (LR), has been described by many authors such as Cox and Hinkley (1979), Lawless (1982), Neslon (1990), Doganaksoy and Schmee (1993a) as well as Ostrouchov and Meeker (1988). Recently, there has been more emphasis on using the corrected version of the LR intervals such as the corrected signed square root of the likelihood ratio statistic by Diciccio (1988) and Bartlett's correction to the likelihood ratio statistic by Barndorff-Nielsen and Cox (1984).

For a scalar parameter of interest θ, the likelihood ratio statistic for testing the null hypothesis, $H_0: \theta = \theta_0$ versus $H_a: \theta \neq \theta_0$ is given as:

$$\Psi = -2[l(\theta_0, \tilde{\eta}) - l(\hat{\theta}, \hat{\eta})]\,.$$

where l is the log-likelihood function, η is the vector of nuisance parameters, $(\hat{\theta}, \hat{\eta})$ is the maximum likelihood estimator of (θ, η), and $\tilde{\eta}$ is the restricted maximum likelihood estimator of η under H_0. For a large sample size, Ψ is approximately $\chi^2_{(1)}$ under H_0 and an approximate 100(1-α)% confidence interval for θ can be obtained by finding the two values of θ_0, for which H_0 is not rejected at the α level of significance, that is, the values that satisfy:

$$l(\theta_0, \tilde{\eta}) = l(\hat{\theta}, \hat{\eta}) - \tfrac{1}{2}\chi^2(1; 1-\alpha),$$

with the lower confidence limit, $\theta_L < \theta$ and the upper confidence limit, $\theta_U > \theta$. The general algorithm to obtain the LR confidence limits can be found in Venzon and Moolgavkar (1988).

The Score Method

The score statistic for testing hypothesis was introduced by Rao (1948). It was further discussed by Cox and Hinkley (1979). Let's reconsider the hypothesis, $H_0: \theta = \theta_0$ versus $H_a: \theta \neq \theta_0$ for testing a certain parameter of interest θ. The score statistic is asymptotically equivalent to the likelihood ratio statistic and is therefore obtained by considering the score vector at point θ_0, $S(\theta_0, \tilde{\eta})$. A score vector which is close to 0 at point θ_0 will indicate that is $\hat{\theta}$ also close to θ_0 and thus in favour of H_0. For a parameter of interest θ, the score statistic at point θ_0 is given as:

$$Q = S'(\theta_0, \tilde{\eta})[I^{-1}(\theta_0, \tilde{\eta})]S(\theta_0, \tilde{\eta})$$

where $\tilde{\eta}$ is the restricted maximum likelihood estimator of γ under H_0 and $I^{-1}(\theta_0, \tilde{\eta})$ is the inverse of the observed information matrix evaluated at point $(\theta_0, \tilde{\eta})$. For a large sample, Q is approximately $\chi^2_{(1)}$ and an approximate 100(1-α)% confidence interval for θ can be obtained by finding the two values of θ_0, for which H_0 is not rejected at α level of significance, that is, the values that satisfy:

$$S'(\theta_0, \tilde{\eta})[I^{-1}(\theta_0, \tilde{\eta})]S(\theta_0, \tilde{\eta}) = \chi^2(1; 1-\alpha)$$

with the lower confidence limit, $\theta_L < \theta$ and the upper confidence limit, $\theta_U > \theta$. Under some regular conditions, the score has an asymptotic normal distribution with mean 0 and variance-covariance matrix equals to the information matrix.

Simulation and Coverage Probability Study

The simulation study was conducted using $N = 2000$ samples of size $n = 150, 200, 250, 300$ and 400 to compare the performance of the Wald, score and likelihood ratio confidence interval estimates. In this research, the maximum likelihood estimators of all the parameters were computed using the Newton Raphson iterative method, which was implemented using the FORTRAN programming language.

Consider an example with at most two levels of the covariate x, for each observation. These were simulated independently from the Standard Normal distribution. Let m and r be the values of the random variables representing the total number of the covariate levels in $[0, \min(t_1, t_2)]$ and $[0, \max(t_1, t_2)]$ respectively, with initial value of m=1. Recall that $0<m\leq r$, so m can take two possible values of 1 and 2. For each simulated observation, the number of covariate levels is determined by the values of m and r, where m is dependent on $(\min(t_1, t_2|x)$ and r is dependent on both $(\min(t_1, t_2|x)$ and $(\max(t_1, t_2|x))$. Since the covariate can only change its value once, then $r\leq 2$.

A total of 8 parameters were estimated. The values of 5, 1, 4.8 and 1.5 were chosen as the parameters of β_0, β_1, ω_0 and ω_1 whereas the values of 4.8, 1.5, 3.5 and 0.7 were chosen as the parameters of β_0^*, β_1^*, ω_0, ω_1^*. Three random numbers from the uniform distribution on the interval (0,1), u_{io}, u_{i1} and , were generated to produce t_{i1} and t_{i2}. Suppose there are both censored and uncensored lifetimes for subjects. Three types of data will be considered. The first is when both t_{i1} or t_{i2} are uncensored, while the second is when both t_{i1} and t_{i2} are censored and finally in the case when only t_{i1} and t_{i2} is censored.

First, generate a_{i1}~exp(v) where the value of v can be adjusted to obtain larger or smaller intervals of a_{i1}. In a real situation, the time intervals during which a covariate value remains constant, may vary or be fixed from one individual to another, depending on the covariate. If the covariate was, for example, the presence of a certain symptom, or status such as adult or juvenile, it would certainly be different among subjects. On the other hand, if the covariate was age at the beginning of the year, the intervals will then be the same for each individual. In this study, the intervals were assumed to vary between the individuals. Then,

$$t_{iA} = \begin{cases} -\dfrac{1}{h_{i1}}\log(1-u_{i0}) & \text{for} \quad u_{i0} \leq 1-e^{-h_{i1}a_{i1}}, \\ -\dfrac{1}{h_{i2}}\log(1-u_{i0}) + \left(1-\dfrac{h_{i1}}{h_{i2}}\right)a_{i1} & \text{otherwise.} \end{cases}$$

$$t_{iB} = \begin{cases} -\dfrac{1}{g_{i1}}\log(1-u_{i1}) & \text{for} \quad u_{i1} \leq 1-e^{-g_{i1}a_{i1}}, \\ -\dfrac{1}{g_{i2}}\log(1-u_{i1}) + \left(1-\dfrac{g_{i1}}{g_{i2}}\right)a_{i1} & \text{otherwise.} \end{cases}$$

Following that, if $t_{iA} < t_{iB}$, $t_{i1} = t_{iA}$. Then, if $u_{i0} \leq 1\text{-e}^{-hi1ai1}$,

$$t_{i2}=\begin{cases}-\dfrac{1}{g'_{i1}}\log(1-u_{i2})+t_{i1} & \text{for} \quad u_{i2}\le 1-e^{-g'_{i1}(a_{i1}-t_{i1})},\\ -\dfrac{1}{g'_{i2}}\log(1-u_{i2})+\left(1+\dfrac{g'_{i1}}{g'_{i2}}\right)(a_{i1}-t_{i1})+t_{i1} & \text{otherwise.}\end{cases}$$

If $u_{i0}>1\text{-}e^{-h_{i1}a_{i1}}$, $t_{i2}=-\dfrac{1}{g'_{i2}}\log(1-u_{i2})+t_{i1}$ Otherwise if $t_{iB}<t_{iA}$, $t_{i2}=t_{iB}$. Then, if $u_{i1}\le 1\text{-}e^{-g_{i1}a_{i1}}$

$$t_{i1}=\begin{cases}-\dfrac{1}{h'_{i1}}\log(1-u_{i2})+t_{i2} & \text{for} \quad u_{i2}\le 1-e^{-h'_{i1}(a_{i1}-t_{i2})},\\ -\dfrac{1}{h'_{i2}}\log(1-u_{i2})+\left(1+\dfrac{h'_{i1}}{h'_{i2}}\right)(a_{i1}-t_{i2})+t_{i2} & \text{otherwise.}\end{cases}$$

If $u_{i1}>1-e^{-g_{i1}a_{i1}}$, $t_{i1}=-\dfrac{1}{h'_{i2}}\log(1-u_{i2})+t_{i2}$.

The censoring time, c_i~exp(μ), where the value of μ would be adjusted to obtain the desired approximate censoring proportion in the data of the present study. In this research, the two levels of approximate censoring proportions, cp=0.10 and cp=0.30, were used to see how they affected the performance of the interval estimates. The values of cp=0.10 and cp=0.30 were chosen to represent both low and high levels of censoring proportions, respectively. The coverage probability is the probability that an interval contains the true parameter value. The study was conducted by calculating the left and right estimated error probabilities for each of the parameter estimates. The estimated left (right) error probability was calculated by adding the number of times the left (right) endpoint was more (less) than the true parameter value, divided by the total number of samples, *N*.

Following Doganaksoy and Schmee (1993), if the total error probability is greater than α + 2.58 s.e ($\hat{\alpha}$), the method is then termed as anticonservative, and if it is lower than α-2.58 s.e ($\hat{\alpha}$), the method is termed as conservative. The estimated error probabilities are known as symmetric when the larger error probability is less than 1.5 times the smaller one.

RESULTS AND DISCUSSION

The summary of the simulation results, comparing the performances of the Wald, LR and score intervals, is given in Tables 1 and 2. These tables display the total number of anticonservative, conservative and asymmetrical intervals, generated by each of these methods at different nominal error probabilities, and censoring proportion. Tables 3 and 4 provide some of the more detailed results and show how the intervals performed at different sample sizes. *Figs. 1* through *4* give a graphical view of some of the coverage probabilities for each of the methods when α= 0.05 and cp=10%. Tables 1 and 2 show that all the intervals produced 1 anticonservative and 2 conservative intervals, but only when the nominal level, α is high.

The LR method clearly generates intervals which are more symmetrical than the other two methods. It only produced 1 asymmetrical interval when the censoring proportion in the data is low

TABLE 1
Summary of the number of interval estimates at $\alpha = 0.05$

Type of interval	Cp=0.10			Cp=0.30		
	Wald	LR	Score	Wald	LR	Score
Anticonservative(A)	0	0	0	0	0	0
Conservative(C)	0	0	0	0	0	0
Asymetrical	9	1	9	9	3	9

TABLE 2
Summary of the number of interval estimates at $\alpha = 0.10$

Type of interval	Cp=0.10			Cp=0.30		
	Wald	LR	Score	Wald	LR	Score
Anticonservative(A)	1	1	1	0	0	0
Conservative(C)	1	1	1	1	1	1
Asymetrical	6	1	5	4	0	4

and α is 0.05, whereas the Wald and score generated 9 asymmetrical intervals. The high censoring level in the data seems to affect the LR more than the other methods, but only when α is low where it starts to produce more asymmetrical intervals. However, this number is still much lower than the number of asymmetrical intervals generated by the Wald and score intervals.

Both Wald and score methods gave almost similar results, but the score method appears to be slightly more symmetrical than the Wald. However, the Wald has more intervals with the total error probability closer to the nominal level than the score intervals. The increase in the censoring proportion does not seem to affect the performances of the Wald and score intervals. When both α and censoring proportion is high, the performances of all the intervals seem to be slightly improved, where they produce fewer asymmetrical intervals, particularly the LR interval. The reason for this is probably the highly censored data that generates wider intervals because of the larger standard errors of the parameter estimates. This produces more intervals that include the true parameter value.

All the methods seem to generate more conservative and anticonservative intervals, but fewer asymmetrical intervals when α is high. They also seem to converge to the nominal level at almost the same rate, but the LR intervals perform slightly better than the other two when the size of the sample is lower.

CONCLUSIONS

Overall, the LR method appears to perform best since it has the least number of asymmetrical intervals. It should be the preferred method, specifically when the censoring level in the data is low. Although the high censoring level and low value of α seem to affect the LR in that it produces more asymmetrical intervals, the number of these asymmetrical intervals are still relatively low. Similarly, the LR intervals are still more symmetrical than the intervals produced by the other two methods.

TABLE 3
Estimated error probabilities at $\alpha = 0.05$, cp=0.10, A="Anticonservative", C="Conservative"

		Wald			LR			Score		
		Left Error	Right Error	Total Error	Left Error	Right Error	Total Error	Left Error	Right Error	Total Error
β_0	150	0.0235	0.0280	0.0515	0.0305	0.0250	0.0555	0.0240	0.0280	0.0520
	200	0.0215	0.0250	0.0465	0.0275	0.0230	0.0505	0.0225	0.0255	0.0480
	250	0.0250	0.0270	0.0520	0.0290	0.0220	0.0510	0.0250	0.0270	0.0520
	300	0.0225	0.0265	0.0490	0.0245	0.0230	0.0475	0.0225	0.0265	0.0490
	400	0.0265	0.0275	0.0540	0.0280	0.0225	0.0505	0.0270	0.0280	0.0550
β_1	150	0.0230	0.0300	0.0530	0.0230	0.0305	0.0535	0.0225	0.0300	0.0525
	200	0.0195	0.0280	0.0475	0.0195	0.0280	0.0475	0.0195	0.0275	0.0470
	250	0.0250	0.0200	0.0450	0.0245	0.0200	0.0445	0.0250	0.0200	0.0450
	300	0.0190	0.0260	0.0450	0.0190	0.0260	0.0450	0.0190	0.0260	0.0450
	400	0.0235	0.0255	0.0490	0.0225	0.0255	0.0480	0.0235	0.0255	0.0490
ω_0	150	0.0215	0.0300	0.0515	0.0270	0.0235	0.0505	0.0215	0.0305	0.0520
	200	0.0250	0.0330	0.0580	0.0295	0.0260	0.0555	0.0255	0.0330	0.0585
	250	0.0205	0.0365	0.0570	0.0270	0.0290	0.0560	0.0205	0.0370	0.0575
	300	0.0210	0.0290	0.0500	0.0275	0.0275	0.0550	0.0215	0.0300	0.0515
	400	0.0210	0.0285	0.0495	0.0275	0.0245	0.0520	0.0220	0.0290	0.0510
ω_1	150	0.0210	0.0245	0.0455	0.0215	0.0240	0.0455	0.0210	0.0245	0.0455
	200	0.0255	0.0275	0.0530	0.0255	0.0275	0.0530	0.0255	0.0280	0.0535
	250	0.0315	0.0200	0.0515	0.0315	0.0200	0.0515	0.0315	0.0205	0.0520
	300	0.0260	0.0190	0.0450	0.0255	0.0185	0.0440	0.0260	0.0195	0.0455
	400	0.0240	0.0235	0.0475	0.0240	0.0245	0.0485	0.0240	0.0235	0.0475
β_0^*	150	0.0210	0.0335	0.0545	0.0295	0.0285	0.0580	0.0215	0.0340	0.0555
	200	0.0170	0.0360	0.0530	0.0225	0.0300	0.0525	0.0170	0.0365	0.0535
	250	0.0155	0.0295	0.0450	0.0180	0.0250	0.0430	0.0160	0.0305	0.0465
	300	0.0190	0.0250	0.0440	0.0225	0.0240	0.0465	0.0190	0.0250	0.0440
	400	0.0180	0.0300	0.0480	0.0200	0.0255	0.0455	0.0190	0.0310	0.0500
β_1^*	150	0.0225	0.0240	0.0465	0.0245	0.0255	0.0500	0.0235	0.0240	0.0475
	200	0.0305	0.0275	0.0580	0.0305	0.0265	0.0570	0.0305	0.0275	0.0580
	250	0.0205	0.0225	0.0430	0.0210	0.0225	0.0435	0.0205	0.0225	0.0430
	300	0.0170	0.0230	0.0400	0.0170	0.0235	0.0405	0.0170	0.0230	0.0400
	400	0.0205	0.0300	0.0505	0.0205	0.0300	0.0505	0.0205	0.0305	0.0510
ω_0^*	150	0.0195	0.0370	0.0565	0.0235	0.0310	0.0545	0.0195	0.0380	0.0575
	200	0.0185	0.0340	0.0525	0.0205	0.0265	0.0470	0.0185	0.0345	0.0530
	250	0.0185	0.0345	0.0530	0.0215	0.0295	0.0510	0.0185	0.0350	0.0535
	300	0.0280	0.0305	0.0585	0.0310	0.0265	0.0575	0.0280	0.0315	0.0595
	400	0.0255	0.0335	0.0590	0.0290	0.0285	0.0575	0.0255	0.0335	0.0590
ω_0^*	150	0.0255	0.0315	0.0570	0.0245	0.0310	0.0555	0.0250	0.0315	0.0565
	200	0.0235	0.0275	0.0510	0.0240	0.0280	0.0520	0.0240	0.0280	0.0520
	250	0.0285	0.0215	0.0500	0.0280	0.0215	0.0495	0.0285	0.0215	0.0500
	300	0.0290	0.0235	0.0525	0.0290	0.0240	0.0530	0.0290	0.0235	0.0525
	400	0.0255	0.0325	0.0580	0.0255	0.0325	0.0580	0.0255	0.0325	0.0580

TABLE 4
Estimated error probabilities at $\alpha = 0.05$, cp=0.30, A="Anticonservative", C="Conservative"

		Wald			LR			Score		
		Left Error	Right Error	Total Error	Left Error	Right Error	Total Error	Left Error	Right Error	Total Error
β_0	150	0.0220	0.0330	0.0550	0.0320	0.0285	0.0605	0.0235	0.0335	0.0570
	200	0.0245	0.0300	0.0545	0.0305	0.0210	0.0515	0.0245	0.0305	0.0550
	250	0.0200	0.0230	0.0430	0.0245	0.0200	0.0445	0.0215	0.0230	0.0445
	300	0.0265	0.0285	0.0550	0.0325	0.0260	0.0585	0.0265	0.0295	0.0560
	400	0.0255	0.0285	0.0540	0.0315	0.0260	0.0575	0.0255	0.0285	0.0540
β_1	150	0.0210	0.0225	0.0435	0.0220	0.0225	0.0445	0.0205	0.0225	0.0430
	200	0.0185	0.0235	0.0420	0.0185	0.0235	0.0420	0.0185	0.0235	0.0420
	250	0.0245	0.0250	0.0495	0.0245	0.0250	0.0495	0.0245	0.0250	0.0495
	300	0.0235	0.0215	0.0450	0.0230	0.0230	0.0460	0.0235	0.0215	0.0450
	400	0.0260	0.0270	0.0530	0.0255	0.0270	0.0525	0.0260	0.0270	0.0530
ω_0	150	0.0200	0.0265	0.0465	0.0290	0.0215	0.0505	0.0205	0.0265	0.0470
	200	0.0200	0.0290	0.0490	0.0245	0.0255	0.0500	0.0200	0.0290	0.0490
	250	0.0270	0.0315	0.0585	0.0300	0.0290	0.0590	0.0270	0.0315	0.0585
	300	0.0200	0.0295	0.0495	0.0245	0.0265	0.0510	0.0200	0.0300	0.0500
	400	0.0240	0.0305	0.0545	0.0290	0.0270	0.0560	0.0245	0.0310	0.0555
ω_1	150	0.0215	0.0250	0.0465	0.0215	0.0250	0.0465	0.0215	0.0250	0.0465
	200	0.0240	0.0265	0.0505	0.0240	0.0265	0.0505	0.0240	0.0265	0.0505
	250	0.0330	0.0190	0.0520	0.0330	0.0190	0.0520	0.0330	0.0190	0.0520
	300	0.0235	0.0170	0.0405	0.0240	0.0165	0.0405	0.0235	0.0170	0.0405
	400	0.0275	0.0230	0.0505	0.0280	0.0230	0.0510	0.0275	0.0230	0.0505
β^*_0	150	0.0200	0.0305	0.0505	0.0255	0.0260	0.0515	0.0210	0.0315	0.0525
	200	0.0150	0.0375	0.0525	0.0185	0.0300	0.0485	0.0150	0.0380	0.0530
	250	0.0175	0.0295	0.0470	0.0235	0.0255	0.0490	0.0180	0.0305	0.0485
	300	0.0185	0.0275	0.0460	0.0230	0.0210	0.0440	0.0185	0.0275	0.0460
	400	0.0185	0.0345	0.0530	0.0220	0.0305	0.0525	0.0185	0.0345	0.0530
β^*_1	150	0.0215	0.0180	0.0395	0.0210	0.0175	0.0385	0.0210	0.0185	0.0395
	200	0.0290	0.0230	0.0520	0.0275	0.0225	0.0500	0.0295	0.0225	0.0520
	250	0.0205	0.0230	0.0435	0.0210	0.0230	0.0440	0.0205	0.0230	0.0435
	300	0.0155	0.0240	0.0395	0.0150	0.0240	0.0390	0.0155	0.0240	0.0395
	400	0.0250	0.0290	0.0540	0.0255	0.0280	0.0535	0.0255	0.0290	0.0545
ω^*_0	150	0.0195	0.0410	0.0605	0.0235	0.0325	0.0560	0.0205	0.0420	0.0625
	200	0.0175	0.0335	0.0510	0.0210	0.0255	0.0465	0.0175	0.0345	0.0520
	250	0.0230	0.0300	0.0530	0.0265	0.0230	0.0495	0.0230	0.0305	0.0535
	300	0.0200	0.0295	0.0495	0.0235	0.0245	0.0480	0.0200	0.0295	0.0495
	400	0.0250	0.0305	0.0555	0.0280	0.0270	0.0550	0.0250	0.0305	0.0555
ω^*_1	150	0.0205	0.0220	0.0425	0.0205	0.0210	0.0415	0.0205	0.0230	0.0435
	200	0.0235	0.0315	0.0550	0.0235	0.0290	0.0525	0.0235	0.0315	0.0550
	250	0.0255	0.0200	0.0455	0.0265	0.0195	0.0460	0.0260	0.0200	0.0460
	300	0.0245	0.0290	0.0535	0.0245	0.0295	0.0540	0.0245	0.0290	0.0535
	400	0.0255	0.0290	0.0545	0.0250	0.0285	0.0535	0.0255	0.0290	0.0545

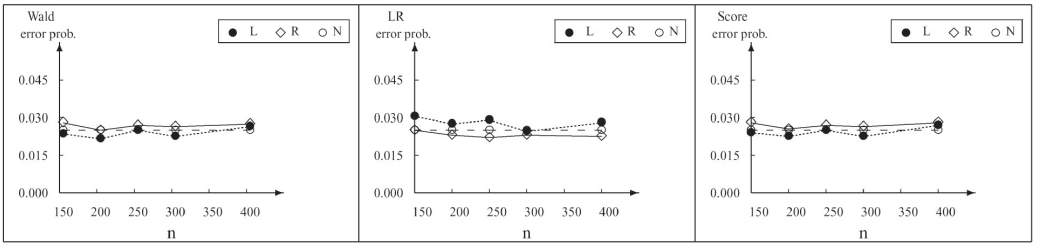

Fig. 1: Estimated error probabilities for β_0 at α= 0.05 and cp=0.1

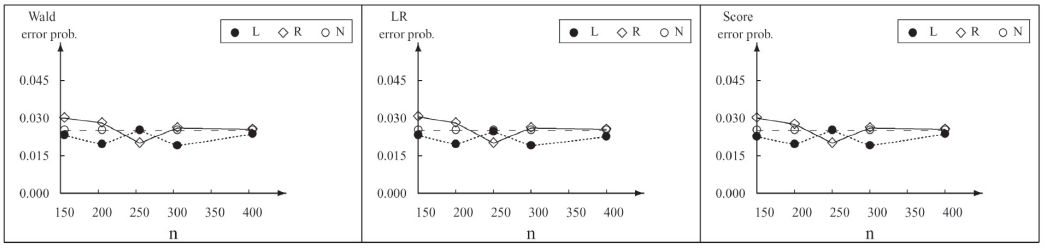

Fig. 2: Estimated error probabilities for β_1 at α= 0.05 and cp=0.1

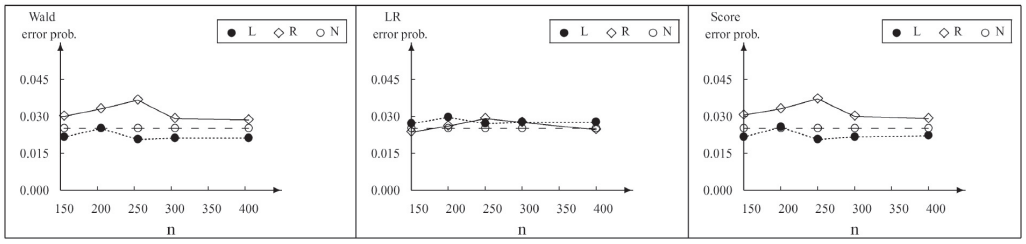

Fig. 3: Estimated error probabilities for ω_0 at α= 0.05 and cp=0.1

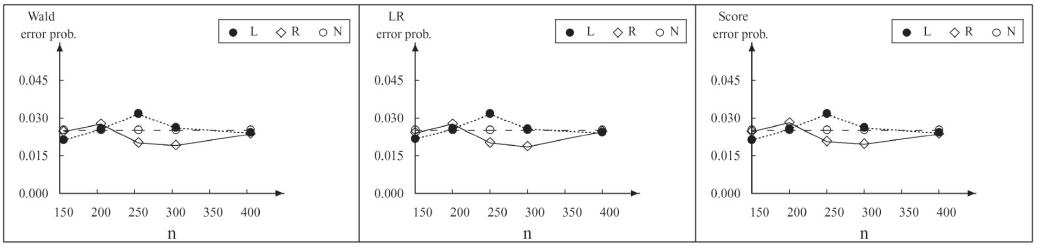

Fig. 4: Estimated error probabilities for ω_1 at α= 0.05 and cp=0.1

Thus, the Wald method can be considered when both α and the censoring proportion are high, or when a simpler and faster method is required. It is probably not advisable to consider applying the Wald intervals in other settings because it generally generates the most number of asymmetrical intervals. The score method may perform as good as the Wald, but it involves a lot of computational effort. Thus, this method should not be considered, unless as a measure of comparison. These findings are consistent with the results of Doganaksoy and Schmee (1993) who found the Wald intervals to be highly asymmetrical as compared to the LR, when dealing with censored data. However, the LR method involves a great deal of computational effort, which may not actually justify its improved performance when compared to the much more straightforward Wald method.

The discussion on the model involving time varying covariates has been restricted to two intervals, during which the covariates value remains constant. It would be possible to carry out further work to include models involving more intervals and this could be programmed relatively easily. The model can also be extended to consider the case, in which the components have the Weibull lifetime distribution.

REFERENCES

Barndorff-Nielsen, O.E. and Cox, D.R. (1984). Bartlett adjustments to the likelihood ratio statistic and the distribution of the maximum likelihood estimator. *Journal of Royal Statistical Society, B*(46), 483–495.

Beck, N. (1999). *Modelling Space and Time: The Event History Approach.* In S. Elinor and T. Eric (Eds.), *Research Strategies in the Social Sciences: A Guide to New Approaches.* Oxford: Oxford University Press.

Bennet, D.S. (1999). Parametric models, duration dependence and time-varying data revisited. *American Journal of Political Science, 43,* 256–270.

Blossfield, Hans-Peter, Hamerle, A. and Mayer, K.U. (1989). *Event History Analysis*. Hillsdale, New Jersey: Lawrence Erlbaum Associates.

Box-Steffensmeier, J.M. and Jones, B.S. (1997). Time is of the essence: Event history models in political science. *American Journal of Political Science, 41,* 1414–1461.

Courgeau, D. and Lelièvre, E. (1992). *Event History Analysis in Demography*. Oxford: Clarendon Press.

Cox, D.R. and Hinkley, D.V. (1979). *Theoretical Statistics*. New York: Chapman and Hall.

Diciccio, T.J. (1988). Approximate inference for generalised gamma distribution. *Technometrics, 29,* 33–40.

Doganaksoy, N. and Schmee, J. (1993a). Comparison of approximate confidence intervals for distributions used in life-data analysis. *Technometrics, 35*(2), 175–184.

Doganaksoy, N. and Schmee, J. (1993b). Comparison of approximate confidence intervals for smallest extreme value distribution simple linear regression model under time censoring. *Communications in Statistics-Simulation and Computation, 2,* 175–184.

Freund, J.E. (1961). A bivariate extension of the exponential distribution. *Journal of American Statistical Association, 56,* 971–977.

Jeng, S.L. and Meeker, W.Q. (2000). Comparison for approximate confidence interval procedure for type I censored data. *Technometrics, 42*(2), 135–148.

Kalbfleisch, J.D. and Prentice, R.L. (1980). *The Statistical Analysis of Failure Time Data*. New York: Wiley.

Lawless, J.F. (1982). *Statistical Models and Methods for Lifetime Data*. New York: Wiley.

Nelson, W. (1990). *Accelerated Testing: Statistical Models, Test Plans, and Data Analysis*. New York: Wiley.

Ostrouchov, G. and Meeker, W.Q. (1988). Accuracy of approximate confidence bounds computed from interval censored Weibull and lognormal data. *Journal of Statistical Computation and Simulation, 29,* 43–76.

Petersen, T. (1986). Fitting parametric survival models with time-dependent covariates. *Journal of Applied Statistics, 35*(3), 281–288.

Rao, C.R. (n.d.). Large sample tests of statistical hypotheses concerning several parameters with applications to problems of estimation. *Proceedings of the Cambridge Philosophical Society, 44,* 50-57, 1948.

Tuma, B.N. and Hannan, M.T. (1984). *Social Dynamics: Models and Methods*. Orlando, Florida: Academic Press.

Yamaguchi, K. (1991). *Event History Analysis*. New York: Sage Publications.

Venzon, D.J. and Moolgavkar, S.H. (1988). A method for computing profile-likelihood-based confidence intervals. *Applied Statistics, 37,* 87–94.

ISSN: 0128-7680
Pertanika J. Sci. & Technol. **17 (2)**: 325– 335 (2009)

Effects of Tillage Methods and Sowing Rates on the Grain Yields and Yield Components of Rain Fed Wheat

H.T. Shamsabadi[1*], A. Biabani[2] and Desa Ahmad[3]
[1]Department of Farm Machinery,*
University of Agricultural Sciences & Natural Resources, Gorgan, Iran
[2]Department of Agricultural Sciences,
University of Agricultural Sciences & Natural Resources, Gorgan, Iran
[3]Department of Biological and Agricultural Engineering, Faculty of Engineering,
Universiti Putra Malaysia, 43400 UPM, Serdang, Selangor, Malaysia
[*]E-mail: Hshamsabadi@yahoo.com

ABSTRACT

A field study was conducted on the effect of four primary tillage implements and three seed densities on the grain yield of rain fed wheat (Tajan cultivar), using a drill planting machine with the end wheels. The experimental design was a split plot design in a 4×3 factorial with three replications. In this study, the main plots were the tillage treatments, namely Mouldboard plough, Disc Plough, Chisel Plough, Offset Disc, and sub-plots were seed rates of 350, 400 and 450 seeds.m^{-2}. Determinations included grain yield and selected yield components. The results showed that grain yield was not affected by the densities of seed and tillage machine treatments. The use of Chisel Plough, with 400 seeds.m^{-2} sowing rate, had the highest grain yield of wheat grown in the Golestan province (Iran), a region with an average annual rainfall of 450 mm.

Keywords: Seed rate, tillage, wheat, yield, planting density

ABBREVIATIONS

T.M. = Tillage Machine
M.P. = Mouldboard plough
D.P. = Disc Plough
C.P. = Chisel Plough
O.D. = Offset Disc
S.R. = Sowing Rate
M.H. = Mean Height
M.S.S. = Mean no. of seed or kernel in each spike or cluster
W.P. = Weight of product in each plot
G.Y. = Grain Yield
M.S. = Mean Squares
W.P. = weight of product/crop in each plot

Received: 30 April 2008
Accepted: 20 January 2009
[*]Corresponding Author

INTRODUCTION

The bread supplied from the wheat is prevailing food which is highly used by the population in Iran. Therefore, there is a need to increase wheat production to meet the local food demand. Most researches conducted in Iran have focused mainly in the field of genetic and less work has been carried out on discovering or improving technical and production systems such as sowing rate, application of tillage implements, and planting. Thus, research on the tillage methods is very important because it utilizes 60% of the consumed energy in agricultural practices (Iqbal *et al*., 1994).

The purposes of tillage are to create an appropriate environment for germination of seed, growth of stem, weed control, preservation of soil moisture and stabilization of soil to ensure good seed contact with soil, reduce soil erosion, burying vegetative debris or vestiges, mixing of fertilizers, fungicides, herbicides, pesticides, as well as reforming materials with soil and unsettling soil capillary pipes to reduce evaporation (Mansoori Rad, 2005). To achieve these objectives, certain tillage implements had independently been applied based on a given situation. However, if appropriate machine is not used, it can lead to soil compaction, development of hardpan and degradation of soil which may finally lead to yield reduction and increase of the mechanization costs (Hargrave *et al*., 1982). However, in most subculture lands in Iran, crop production without proper tillage practice does not have satisfying results (Hemat and Asadi, 1997).

Similarly, for every climate and region, appropriate seed density varies with agro-ecology. Seed density (sowing rate) has been shown to have important effect on the final yield. In specific, if seed density is less or more than the optimal rate, it will lead to a yield reduction. For instance, when the seed rate is more than the optimal amount, the grains or kernels will become weak and shrinkage, and this will consequently lead to lower yields.

Among the three yield components, heads per unit area and kernel per head are considered as more important than kernel weight in determining wheat grain yield (Donaldson *et al*., 2001; Schillinger *et al*., 2005). Heads per unit area is generally the most important yield component for wheat (Garcia Del Moral *et al*., 2003), but under drought conditions, kernel per head often has the greatest effect on grain yield (Arnon, 1972; Schillinger and Young, 2004). High sowing rates often result in the increase in the head per unit area (Guberac *et al*., 2000; Stougaard and Xue, 2004), with a corresponding reduction in the kernel per head (Carr *et al*., 2003). In relation to the increasing sowing rate, the number of plants will generally rise, but the yield per area unit will not be increased because of the mentioned reason (Paulsen, 1987).

The most widely recommended sowing rate for dry land spring wheat in the northern Great Plains and the Pacific Northwest is 200 seeds.m^{-2} (Paulsen, 1987), but some farmers sow up to 350 seeds.m^{-2}. Considerable variability in optimum sowing rate for cereals often involves interaction effects with tillage, cultivar and environmental factors. The common sowing rate for dry land spring cereals, in the less than 300 mm annual precipitation zone of the Pacific North west, is 195 seeds.m^{-2}. Sowing rate as high as 800 seeds.m^{-2} has been reported for oat production in Finland (Peltonensainio and Jarvinen, 1995). In particular, the sowing rate of rain-fed wheat in the north of Iran is subject to change, and depends on the climate condition and based on weight of 1000 kernel or seed, is between 100 to 250 kg.ha^{-1}.

A study conducted by Touchton and Johnson (1982) showed that the yield of soya bean was not affected by the tillage methods but the yield of wheat in the chisel ploughed plot was found to be less than the mouldboard ploughed plot. It was therefore suggested that the soil should be ploughed using mouldboard or chisel plough before planting, since the yield is better than no tillage. Cox (1986) studied the effects of different methods of soil preparation, under two different types of wheat seed on the yield. However, no significant difference was reported in the yield among all

the treatments. Baloch *et al*. (1991) compared the yields in the farm ploughed with implements like mouldboard plough, disc plough, chisel plough and cultivator. The results showed that the disc plough required more tension strength in loam–clay soil as compared to the loam-silt. They also reported that the product yield of the farm ploughed by cultivator was increased by 48.5% when compared to when the Mouldboard Plough was used and 59.1% when compared with the Disc Plough.

Lal (1981) suggested that no tillage system should be recommended if no tillage system was found to have any considerable effect relative to other tillage systems in tropical countries because this system decreases the mechanization cost. To achieve the desired conditions of the crop, mechanical operation was carried out on the soil. Arvidsson and Feiza (1998) reported that tillage operation, using mouldboard plough and chisel plough, showed a significant effect on the tensile tolerance of silt-clay Swedish soil. Several researches carried out in Denmark showed that the compaction of subsoil was a general problem (Schjenning and Rasmussen, 1998; Schjenning *et al*., 2001; Djurhus and Olesen, 2000). Meanwhile, Perfect and Kay (1994) and Macks *et al*. (1996) reported less tensile tolerance for the soil under minimum tillage as compared to the soil tilled with conventional method. One of the reasons for the increase of soil tensile tolerance is soil compaction as a result of using tillage machines. According to these studies, very strong compaction is often found under the plough layer. For instance, Schjenning and Young (2004) showed that conventional land preparation machines usually cause compaction of subsoil.

The field experiments by Khosravani *et al*. (1995) showed that ploughing of one hectare of land using the Moudboard Plough utilized more fuel compared to the Chisel Plough, while the field capacity of latter was about two times as much. The main objectives of the primary tillage operation are unsettling the soil compaction and root growth. The soil compaction causes reduction of the moisture and oxygen penetration inside the soil and increasing energy consumption (Tebrugge, 2002). Tillage operation has an influence on the physical properties of soil structure (Hamblin and Tennant, 1987) and it will reform specific gravity of dry soil, apparent tolerance, thermal conductivity, water distribution, porosity distribution, root distribution and crop yield (Lal *et al*., 1994).

The study by Raoufat and Matbooei (2007) on the two methods of ploughing, namely disking followed by Chisel Plough and disking ahead of a planter, showed that equipping available planters with row cleaners was successful in reduced tillage corn production system. In addition to the environmental benefits, it also has advantages such as saving time, fuel and labour. Improved infiltration of rain water into the soil potentially increases water availability to plants, reduces surface runoff and improves ground water recharge (Lipic *et al*., 2005). Reduced soil cultivation decreases energy requirements and overall farming costs as less area needs to be tilled (Monzon *et al*., 2006). The investigation by Qin *et al*. (2006) showed that up to 80% of maize roots could be concentrated in the 0-30cm layer under no tillage systems. The sharp decline in soil water in sandy soil could also be attributed to the drainage out of the sampling depth. The conservation tillage (no till and reduced tillage) practices simultaneously conserve soil and water resources, reduce farm energy usage and increase crop production. These practices lead to positive changes in the physical, chemical and biological properties of soil (Bescansa *et al*., 2006). The physical properties of soil which are influenced by conservation tillage include bulk density, infiltration and water retention (Osunbitan *et al*., 2004).

This study was carried out to determine the effects of different primary tillage methods on the grain yield and selected yield components of Tajan wheat variety and to identify the optimum seed rate of Tajan wheat variety using drill planting with end wheels (Danish) in the Gonbad rain fed region of Iran.

MATERIALS AND METHODS

Experimental Site

The experiment was conducted in a research farm of Gonbad Agricultural Faculty, Golestan Province, Iran, during 1997-2000 cropping season on a silt clay loam (64% silt, 30% clay, 6% sand) soil type with an electrical conductivity (EC) of 1.5mμ.m^{-1} and acidity (pH) 7.8. Experimental site is located on the southeast of the Caspian Sea with longitude 37°, 20´N, latitude 55°, 25´E and an altitude of 160 m above the sea level. This region, as characterized by the Ambrotermic meteorology records, enjoys the Mediterranean climate condition. The average annual rainfall of the experimented region is more than 450 mm. Rainfall occurs mainly in autumn, winter and early spring (September to April and May). Meanwhile, the average annual temperature of the region is 17.7°C.

Experimental Layout

The experimental design was arranged with a factorial treatment consisting four primary tillage machines, namely mouldboard plough (MP), disc plough (DP), chisel plough (CP) and off-set disc (OD), with equal ploughing depth of 25 cm and three seed rates (350, 400, 450 seeds.m^{-2}). The plots were pegged out in October for the first year of the experiment and then maintained in the subsequent years. The treatments were set up in a split-plot design with three replications done each year. The main plot factors were allocated to the tillage machines (with an area of 4×18 m for one treatment excluding the borders). The seed density factor, at three levels, was allocated in the sub-plots (with an area of 6×16 m for each treatment excluding the borders in one replication). Each plot was separated by a small rotary cultivator with 1 m working pathway or border to avoid interaction effects of the treatments of one plot with the next when crop was growing.

Soil moisture was about 20% (dry basis) based on the soil texture at the time of ploughing and at the end of ploughing. A tandem disc (conventional disc harrow) was applied on the already ploughed plots. Planting was carried out with equal planting depth of 3-5cm and with three seeding rates using a drill planting machine with end wheels (Danish) having 21 rows with 12cm between crop rows.

A MF285 tractor (Massey Fergusson) was used to provide the pulling power. Tajan wheat seed variety, a domestic high producing rain-fed cultivar with 13-16% moisture content, was used in this experiment. Percentage purity, germination and weight of 1000 seeds were 100%, 95% and 39 g, respectively. To prevent fungal diseases or hidden apparent smut, carboxin and vitavax fungicide poisons were used at the rate of 150 gr per 100 kg seed. Planting depth was approximately 3cm at the tractor forward speed of 8-10 km.h^{-1}. Seeding practice was carried out immediately, i.e. after the preparation of soil (late December to early January). Crop protection practices containing weeding, controls of pests and diseases, as well as chemical fertilizers were applied, based on the soil analysis. Phosphate fertilizer of 100 kg.ha^{-1} was applied while planting, and this was followed by 75 kg.ha^{-1} while top-dressing carried out in the month of March.

After top-dressing or digitising until the growth of main stems (20-25 cm), weeds were controlled using herbicides; 100 g.ha^{-1} Granestar and 1 lit. Pumasuper applied by motorized back sprayer. The amount of the herbicide used was determined based on weed densities and the type of the Sprayer. It was 1-1.5 litres of weedicide with 200–400 lit.water.ha^{-1}. Two litres of zineb poison in 1000 litres of water was applied using a sprayer in crop maintenance.

Data Collection

During harvesting time, grain yield and some of yield components, such as mean height, weight of 1000 kernel, mean number of seed in each cluster and weight of crop, were measured from each plot. Time of harvest (the moisture content was 14-16%, leaves were yellow and seeds were firm) was determined in the late spring season. After deletion of the borders, 8 m^2 from each plot was cut using scissors from the under mast level, put in gunny sacks which had been labelled accordingly and transferred to the Agricultural Research Centre of Gonbad for threshing using a small and special combine machine. The yield at each m^2 and at each hectare was finally determined using the following equation:

$$H= b \times s \times w \times 10000$$

Where

H=The yield per hectare, b= average number of bunch per m^2 , s= average number of seeds in each bunch, and w= average weight of a seed.

Before harvesting, a 0.25 m^2 area at the middle of each plot was chosen for determining some yield components such as mean height, weight of 1000 kernel in each plot, mean number of seed in each cluster and weight of crop in each plot, and grain yield of wheat, at each square meter and for each hectare.

Statistical Analysis

The effects of tillage machines and seed rates, on grain yields and some yield components, were evaluated. Tillage machines and seed rates were the sources of variations when the grain yield and yield components of the rain-fed wheat were analyzed. Mean squares of the treatments were obtained using the least significant difference (LSD) or the Duncan multiple test at $p<0.05$. On the other hand, the probability levels of 0.001, 0.01 and 0.05 were considered to determine the level of significance between the treatment means.

RESULTS AND DISCUSSION

Seasonal Rainfall and Parameters

The results presented in Table 1 indicate that there was a significant difference in the grain yield of the rain-fed wheat between the cropping years. The average annual precipitation in the first cropping year of the experiment (1997–1998) was 593.4 mm and this was 369.2 and 582.3 mm for the second and third cropping years, respectively. The average annual rainfall, in the first and third year of experiment, was higher than the average annual rainfall in the long-term (450 mm), while the rainfall during the second year of experiment was lower, and the distribution of rainfall was uniform. The amount of precipitation and having fallow of research farm before the first year of conducting the experiment led to significant differences ($p<0.01$) in terms of grain yield of the rain-fed wheat within the three years of conducting the experiment. The remaining residues or stubbles in the second and third years of the experiment, the irregular distribution of rainfall throughout the growing season of the third year of the experiment might have some effects on the grain yields.

Fabrizzi *et al*. (2005) reported that the scarce and poorly distributed precipitation during the growing season could negatively affect the growth and yields of corn and wheat. However, soil water storage was greater under no-tillage (chemical weed control during the fallow period and seeding directly into the standing residues of the previous crop) than under the minimum tillage

TABLE 1
Comparison of the mean grain yield of the rain-fed wheat and the amount of rainfall with regard to different years

Amount of rainfall (mm)	Amount of grain yield (kg/ha)	Year
593.4	4664.1 a	1997 – 1998
369.2	3554.8 b	1998 – 1999
582.3	2364.5 c	1999 – 2000

Means followed by different letters within a column are significantly different at $p<0.01$

(chisel plough and two disking). It means that the tillage operation had affected the soil storage capacity which could consequently lead to a reduction in the growth and yields of corn and wheat. The conservation tillage such as using chisel plough during soil preparation leaves most or parts of the crop residues on the soil surface, thus affecting the chemical, biological and physical properties of soil.

The replication treatment was found to produce a significant effect on the grain yield ($p<0.01$) and weight of crop ($p<0.05$). This result could be attributed to the prepared conditions of the climate and unsuitable distributed precipitation during the growing season (heavy rainy at two times). In this condition, disc plough for land preparation with 400 seeds.m^{-2} plant density were indicated to be slightly better than the others.

Meanwhile, changes in the physical properties of soil, due to using no-tillage, are dependent on several factors including differences in soil properties, weather conditions, history of management, intensity and type of tillage (Mahboubi *et al*., 1993).

Grain Yield and Other Inspected Characteristics/Parameters

In this study, the type of tillage machines (Table 2) had no significant difference on the grain yield of the rain-fed wheat ($p>0.05$). However, its effects on the weight and the mean number of 1000 seeds in every spike were significant at 5% and 1% levels, respectively. This could be attributed to the role and nature of the tillage implement in the preparation of soil, but the factors such as its interaction effects within cultivar and environment could also be affected (Paulsen, 1987). Although disc plough prepared the soil at the better conditions related to others and affected the number of seeds in the cluster ($p<0.01$), it had not affected the grain yield significantly. Garcia Del Moral *et al*. (2003) reported that the number of spikes per unit area was generally the most important yield component for wheat, but under drought conditions, kernel per spike or cluster often has the greatest effect on grain yield (Arnon, 1972; Schillinger and Young, 2004). This result contrasts the result of the present study, largely because of the fact that the experimental site condition was not under drought conditions.

Chisel plough with one time of disking harrow prepared a better seedbed as compared to other methods. It shows an increase in grain yield up to 2.5% compared to the mouldboard plough, 3.3% with the disc plough and 4.5% with the offset disc. The chisel plough normally needs less pulling power or tensile strength, and therefore it can be used at higher speeds, in addition to its capacity to cover a wider area as well (field capacity). Other advantages include energy saving, better fuel consumption and time for the soil preparation (Mansoori Rad, 2005).

TABLE 2
Analysis of variance for different factors within three years of experiment

Resources of variations	G.Y. ($Kg.ha^{-1}$)		W. 1000 S. (gr)		W.P. (gr)		M.S.S.		M.H. (cm)	
	F value	M.S.	F value	M.S.	F value	M.S.	F value	M.S.	F value	M.S.
Year	10.97 **	1.4×10^{7}	1.66 ns	5.91	3.58 ns	1.19	0.92 ns	11.75	0.0001	0.01
Replication	8.76 **	1.2×10^{7}	2.31 ns	8.02	4.78 *	1.49	0.63 ns	8.07	1.69 ns	31.11
T.M.	0.11 ns	121757.2	2.96 *	11.13	0.77 ns	0.26	5.24 **	88.99	1.06 ns	89.75
S.R.	0.63 ns	712374.9	0.58 ns	2.17	0.85 ns	0.29	0.71 ns	12.13	1.04 ns	88.57
T.M. × S.R.	0.31 ns	356530.2	1.13 ns	4.24	1.662 ns	0.56	0.93 ns	15.87	1.25 ns	106.57
Error	—	1134363	—	3.76	—	0.34	—	16.99	—	85.06

** significant at 1% level. * significant at 5% level. **ns** not significant.
T.M. = tillage machine, S.R. = sowing rate, M.H. = mean height,
M.S.S. = mean no. of seed in each spike, W.P. = weight of product in each plot,
G.Y. = grain yield, M.S. = mean squares, W.P. = weight of product/crop in each plot.

TABLE 3
Comparison between the mean treatments for 3 years

Tillage machine	G.Y. (Kg.ha^{-1})	W. 1000 S. (gr)	W.P. (gr)	M.S.S.	M.H. (cm)
M. P.	3530 ^{a}	34.29 $^{ab\ 2}$	2.46 ^{a}	23.89 $^{a\ 1}$	70.69 ^{a}
D. P.	3500 ^{a}	33.47 ^{a}	2.71 ^{a}	29.14 ^{c}	74.08 ^{a}
C. P.	3619 ^{a}	33.36 ^{a}	2.65 ^{a}	27.45 ^{bc}	72.65 ^{a}
O. D.	3461 ^{a}	35.04 ^{a}	2.49 ^{a}	26.02 ^{ab}	68.80 ^{a}
Sowing Rate (seed. m^{-2})					
350	3577 ^{a}	34.35 ^{a}	2.47 ^{a}	26.74 ^{a}	72.96 ^{a}
400	3637 ^{a}	34.02 ^{a}	2.69 ^{a}	27.23 ^{a}	73.15 ^{a}
450	3369 ^{a}	33.75 ^{a}	2.56 ^{a}	25.87 ^{a}	69.61 ^{a}

Means between treatments followed by similar letters do not differ significantly ($p>0.05$)
1. Means between treatments followed by different letters differ significantly ($p<0.01$)
2. Means between treatments followed by different letters differ significantly ($p<0.05$)
MP = mouldboard plough, DP = disc plough, CP = chisel plough, OD = offset disc

The reports by French and Schultz (1984) and Barzegar *et al*. (1984) proved the same gained results. Tanaka (1989) compared the yield of peas using the tillage methods including no tillage, reduced tillage and mouldboard plough (the current method), and they concluded that the difference in the yield with the mentioned tillage methods was not significant, and that no tillage method showed trend towards more yield. Ciha (1982) reported that ploughing done using the chisel plough had greater yield as compared to other tillage methods for the production of wheat. Similar results were reported by Hodgson *et al*. (1989). Afuni and Mosaddeghi (2001) and Mahboubi *et al*. (1993) recommended the applications of either of the two methods of soil preparation, i.e. chisel plough or disc plough. However, other researchers found that mouldboard plough had significant effects on the yield of irrigated wheat when compared with other tillage methods (Hemat and Asadi, 1997).

Nevertheless, seed density factor did not show any significant effect ($p>0.05$) on the grain yield and yield components of the rain-fed wheat (Table 2). This result could be due to the low interval of sowing rates. Although seed density or sowing rate did not show any significant effect on the grain yield and yield components of the rain-fed wheat, the comparison of the average yield of the rain-fed wheat with different seed densities (Table 3) showed that the rate of 400 seeds.m^{-2} produced more yield, and this was followed by 350 seeds.m^{-2} (~2% decreasing crop) and 450 seeds.m^{-2} (7% decreasing crop). This could be attributed to the deficit of soil nutrition and moisture with bush increase, decrease in the number of spikelet into the spike of wheat in the plots of high sowing rates, and the shortage of seeds per area unit in the plots of low sowing rates. Therefore, the recommended seed rates were between 400 seeds.m^{-2} ~ 150 kg.ha^{-1} to reduce production costs. Khajehpoor (1986) found similar results in the seed densities of 70, 100, 150 kg.ha^{-1}, and he recommended 100 kg.ha^{-1}. However, Seif (1975) in his report showed that seed density had no significant effect on the grain yield of the product, but recommended the seed rate of 180 kg.ha^{-1} instead.

The interaction effect between the tillage machine and seed density showed no significant difference ($p>0.05$) in the grain yield of the rain-fed wheat and other parameters (Table 2). This result indicates that every understudied factor was independently effective. On the other hand, the mentioned factors (tillage machine and seed density) in this experiment had equal or similar effects on the yield of Tajan rain-fed wheat and yield components.

CONCLUSIONS

The presence of plant residues or stubbles in the second and third years of experiments had positive influence on the weight of 1000 seed and the mean number of seeds in each spike or cluster versus tillage machine treatments.

Tillage implements and seeding rates had no significant effects on the yield of rain-fed wheat. The optimum seed density recommended was between 350 seeds.m^{-2} (140 kg. ha-1) and 400 seeds.m^{-2} (150 kg.ha-1) to increase the grain yield at reduced production costs. Among the ploughing machines, the chisel plough showed increased yield in comparison with the others.

ACKNOWLEDGMENTS

The authors are grateful to field staff and personnel at the Soil and Agronomy Laboratories of the Agricultural Faculty and Eng. Jafarzade, Dr. Soltani, F. Shamsabadi for their help and valuable technical assistance in this experiment.

REFERENCES

Afuni, M. and Mosadeghi, M.R. (2001). Effect of tillage methods on the physical properties of soil and bromide movement. *Science and Technology of Agricultural and Natural Resources Magazine, 2*(5), 39-55.

Arnon, I. (1972). *Crop Production in Dry Regions. Volume I: Background and Principles*. London: Leonard Hill.

Arvidsson, J. and Feiza, V. (1998). Conventional and ploughless tillage systems with normal and low tyre inflation traffic. *Swed. Journal of Agricultural. Research, 28,* 73-82.

Baloch, J., Mirani, A.N. and Bukhari, S. (1991). Power requirements of tillage implements. *AMA., 22*(1), 34-38.

Barzegar, A.R., Asoodar, M.A., Khadish, A., Hashemi, A.M. and Herbert, S.J. (2003). Soil physical characteristics and chickpea yield responses tillage treatment. *Soil and Tillage Research, 71,* 49-57.

Bescansa, P., Imaz, M.J., Virto, I., Enrique, A. and Hoogmoed, W.B. (2006). Soil water retention as affected by tillage and residue management in semi-arid spain. *Soil and Tillage Research, 87,* 19-27.

Carr, P.M., Horsley, R.D. and Poland, W.W. (2003). Tillage and seeding rate effects on wheat cultivars: II.Yield components. *Crop Science, 43,* 210-218.

Ciha, A.J. (1982). Yield and component of four sowing wheat cultivars grown under three tillage systems. *Agronomy Journal, 74,* 317-320.

Cox, J.K. (1986). Winter survival response of winter wheat, tillage and cultivar selection. *Agronomy Journal, 78,* 795-801.

Djurhuus, J., and Olesen, J.E. (2000). Characterizations of four sites in Denmark for long-term experiments on crop rotations for organic farming. DIAS-Report No. 33 Plant Production. Danish Institute of Agricultural Sciences, pp. 74.

Donaldson, E., Schillinger, W.F. and Dofing, S.M. (2001). Straw production and grain yield relationships in winter wheat. *Crop Science, 41,* 100-106.

Fabrizzi, K.P., Gacia, F.O., Costa, J.L. and Picone, L.I. (2005). Soil water dynamic, physical properties and corn and wheat responses to minimum and no-tillage systems in the southern Pampas of Argentina. *Soil and Tillage Research, 81,* 57-69.

French, R.J. and Schultz, J.E. (1984). Water use efficiency of wheat in a mediterranian type environment. The relation between yield, water use and climate. *Journal of Agricultural Research, 35,* 743-764. Australia.

Garcia Del Moral, L.F., Rharrabti, Y., Villegas, D. and Royo, C. (2003). Evaluation of grain yield and its components in durum wheat under Mediterranean conditions: An ontogenic approach. *Agronomy Journal, 95,* 266-274.

Guberac, V., Martincic, J., Maric, S., Jurisic, M. and Rozman, V. (2000). Grain yield components of winter wheat new caltivars in correlation with sowing rate. *Cereal Research Communications, 28,* 307-314.

Hamblin, A.P. and Tennant, D. (1987). Root length density and water uptake in cereals and grain legume: how well are they correlated? *Australia Journal of Agricultural Research, 38,* 513-527.

Hargrave, W.L., Reid, J.T., Touchton, J.T. and Gallaher, R.N. (1982). Influence of tillage practices on the fertility status of acid soil double-cropprd to wheat and soybean. *Agronomy Journal, 74,* 684 - 687.

Hemat, A. and Asadi, A. (1997). Effects of planting directly, minimum tillage and conventional tillage on the yield of autumn wheat. *Iran Agricultural Sciences Magazine*, *28*(1), 19-33.

Hodgson, D.R., Kipps, N.A. and Braim, M.A. (1989). Direct drilling compared with ploughing for winter wheat grown continuously and the effects of subsoiling. *Soil Use Management, 5,* 189–194.

Iqbal, M., Younis, M., Sabir, M.S. and Azhar, Atl. (1994). Draft requirements of selected tillage implements. *AMA, 25*(1), 13-16.

Khajepoor, M.R. (1986). Effects of row planting and seed rate on yield and component of autumn wheat. Monograph. p. 1-10. Agricultural Faculty, Esfehan University, Iran.

Khosravani, A., Loghavi, M. and Solhjo, A.A. (1995). Final report of research plant about evaluation and development of pull trial of moderate and conventional tractors in Iran. Research education and propagation of agricultural organization. Institute of Technical and Engineering in Agriculture, *42,* 1-24.

Lal, R. (1981). Clearing a tropical forest. II. Effects on crop performance. *Field Crops Research, 4,* 345–354.

Lal, R., Mahboubi, A.A. and Fausey, N.R. (1994). Long-term tillage and rotation effect on properties of a central Ohio soil. *Soil Science Society. American Journal, 58,* 517-522.

Lipic, J., Kus, J. and Stowinska-Jurkiewicz, A. (2005). Soil porosity and water infiltration as influenced by tillage methods. *Soil and Tillage Research, 89,* 210-220.

Macks, S.P., Murphy, B.W., Cresswell, H.P. and Koen, T.B. (1996). Soil friability in relation to management history and suitability for direct drilling. *Australian Journal of Soil and Tillage Research*, *34,* 343-360.

Mahboubi, A.A., Lal, R. and Favsey, N.R. (1993). Twenty-eight years of tillage effect on two soil in Ohio. *Soil Science Society American journal, 57,* 506-512.

Mansoori Rad, D. (2005). *Tractors and Agricultural Machinery*. p. 339-344. Boalisina Uni. Press.

Monzon, J.P., Sadras, V.O. and Andrade, F.H. (2006). Follow soil evaporation and water storage as affected by stubble in sub-humid (Argentina) and semi arid (Australia) environments. *Field Crops Research, 98,* 83-90.

Osunbitan, J.A., Qyedele, D.J. and Adekalu, K.O. (2004). Tillage effect on bulky density, hydraulic conductivity and strength of a gloomy sand soil in south western Nigeria. *Soil and Tillage Research, 82,* 57-64.

Paulsen, G.M. (1987). Wheat stand establishment. In E.G. Heyne(Ed.), *Wheat and Wheat Improvement* (p. 384-389). Agronomy Monograph 13. 2nd ed. ASA, CSSA, and SSSA, Madison, WI.

Peltonensainio, P. and Jarvinen, P. (1995). Seeding rate effects on tillering grain yield and yield components of oat at high latitude. *Field Crops Research, 40,* 49-56.

Perfect, E. and Kay, B.D. (1994). Influence of corn management on dry aggregate tensile strenht: Weibull analysis. *Soil and Tillage Research, 32,* 149-161.

Qin, R., Stamps, P. and Richner, W. (2006). Impact of tillage on maize rooting in a combisol and luvisol in Switzerland. *Soil and Tillage Research, 85,* 50-61.

Raoufat, M. H. and Matbooei, A. (2007). Row cleaner enhance reduced tillage planting of corn in Iran. *Soil and Tillage Research, 93,* 152-161.

Saif, H. (1976). Cereal seed improvement and better agronomy methods conference. Esfehan Uni. Iran.

Schillinger, W., Wellsandt, D., Schafer, H., Schofstoll, S. and Papendick, R. (2005). Tillage method and sowing rate relations for dry land spring wheat, barley and oat. PNW Handbook Series No. 30, chapter 2:1-13.

Schillinger, W.F. and Young, D.L. (2004). Cropping systems research in the world's driest rainfed wheat region. *Agronomy Journal, 96,* 1182-1187.

Schjenning, P. and Rasmussen, K.J. (1998). Long-term reduced cultivation. I. Soil strength and stability. *Soil and Tillage Research, 15,* 79-90.

Schjenning, P., Elmholt, S.E., Munkholm, L.J. and Debosz, K. (2001). Soil quality aspects of humid sandy loams as influenced by different long-term management. *Agriculture Ecosystem Environment* (in press).

Stougaard, R.N. and Xue, Q.W. (2004). Spring wheat seed size and seeding rate effects on yield loss due to wild oat (AVena fatua) interference. *Weed Science, 52,* 133-141.

Tanaka, D.L. (1989). Spring wheat plant parameters as affected by fallow methods in the Northern Great Plains. Soil Science Society. *American Journal, 53,* 1506–1511.

Tebrugge, F. (2002). Conservation tillage as a toll to improve soil-water and air quality. In *Proceeding of the Eighth International Congress Mechanization and Energy in Agriculture*, Kusadas1. Turkey.

Touchton, J.T. and Johnson, J.W. (1982). Soybean tillage and planting methods effects on yield of double - cropped wheat and soybeans. *Agronomy Journal, 74,* 57 - 59.

ISSN: 0128-7680
Pertanika J. Sci. & Technol. **17 (2)**: 337– 345 (2009)

Spatial Regression with Conditional Autoregressive (CAR) Errors for Annual Mean Relative Humidity in Peninsular Malaysia

Mahendran Shitan[1, 2*] and Kok Wei Ling[2]
[1]Applied and Computational Statistics Laboratory,
Institute for Mathematical Research (INSPEM), Universiti Putra Malaysia,
[2]Department of Mathematics, Faculty of Science, Universiti Putra Malaysia,
43400 UPM, Serdang, Selangor, Malaysia
[*]E-mail: mahen698@gmail.com

ABSTRACT

Modelling observed meteorological elements can be useful. For instance, modelling rainfall has been an interest for many researchers. In a previous research, trend surface analysis was used and it was indicated that the residuals might spatially be correlated. When dealing with spatial data, any modelling technique should take spatial correlation into consideration. Hence, in this project, fitting of spatial regression models, with spatially correlated errors to the annual mean relative humidity observed in Peninsular Malaysia, is illustrated. The data used in this study comprised of the annual mean relative humidity for the year 2000-2004, observed at twenty principal meteorological stations distributed throughout Peninsular Malaysia. The modelling process was done using the S-plus Spatial Statistics Module. A total of twelve models were considered in this study and the selection of the model was based on the *p*-value. It was found that a possible appropriate model for the annual mean relative humidity should include an intercept and a term of the longitude as covariate, together with a conditional autoregressive error structure. The significance of the coefficient of the covariate and spatial parameter was established using the Likelihood Ratio Test. The usefulness of the proposed model is that it could be used to estimate the annual mean relative humidity at places where observations were not recorded and also for prediction. Some other potential models incorporating the latitude covariate have also been proposed as viable alternatives.

Keywords: Relative humidity, environment, spatial regression, Simultaneous Autoregressive errors, Conditional Autoregressive errors

INTRODUCTION

Climatic changes have been occurring for the past hundred years or so, and some of these changes are attributable to human activities like deforestation, changes in land use, etc. Many meteorological elements are observed at meteorological stations like rainfall, sunshine, air temperature, radiation, atmospheric pressure, wind velocity, evaporation and the like. One of the elements observed or recorded at a meteorological station is relative humidity which is defined as the ratio of the mass of water vapour actually present in unit volume of the air to that required to saturate it at the same temperature. Relative humidity is usually expressed in percentage.

Modelling the observed meteorological elements can be useful. For instance, modelling rainfall has been an interest for many researchers. Le Cam (1961), Waymire and Gupta (1981) and Cox and Isham (1988) have adopted point process based models. Time series models, bivariate models and variogram analysis have been presented by Smith (1994). One of the early studies on rainfall

Received: 5 July 2007
Accepted: 13 April 2009
[*]Corresponding Author

analysis in Malaysia (Todorov and Abraham, 1982) used the traditional statistical methods to identify dry areas and variability in the annual rainfall. A modelling technique, known as the Trend Surface Analysis, was used to fit models for the agricultural land value data for 1977-8 in Iowa (Cliff and Ord, 1981) and to study the forest landscape patterns (Jin-Ping, Guo and Yang, Xiao, 1999). More recently, the trend surface analysis of the annual rainfall in Peninsular Malaysia was undertaken by Isthrinayagy (2001). It was suggested that if the residuals were spatially autocorrelated, the modelling procedure should then take into consideration the correlation reflecting the spatial structure. In fact, whenever dealing with spatial data, it is vital to be thoughtful of the spatial correlation.

Shitan (2004) modelled the annual mean relative humidity with Simultaneous Autoregressive (SAR) errors for the year 2001. Another error structure is the Conditional Autoregressive (CAR) type and Shitan *et. al*. (2005) fitted a spatial regression with the CAR errors to the same data set. In both these studies, it was concluded that an appropriate model for the annual mean relative humidity should include an intercept and a term of the longitude (i.e. $Y_i = \beta_{00} + \beta_{01}x_2 + \varepsilon_i$). There is also another common error structure known as the Moving Average (MA) errors. Shitan and Kok (2007) have also modelled the same data set with the MA error structure. In their study, it was concluded in that the quadratic model $Y_i = \beta_{00} + \beta_{01}\, x_2 + \beta_{20}x_1^2 + \varepsilon_i$, as an appropriate one since the linear model was not computable due to the numerical difficulties for the MA error structure. However, in all these studies, the data set used was only for one year. The research could be strengthened by considering more data and for this reason, the data for five years (2000 to 2004) were used in the present research.

In this project, the modelling of the annual mean relative humidity was concentrated on and the objective was to fit and illustrate the spatial regression with the Conditional Autoregressive (CAR) errors covariance structure. In Section 2, the methodology of the study is described, followed by the results in Section 3 and finally the conclusions are drawn in Section 4.

METHODOLOGY

The data set for this study included the annual mean relative humidity (Table 1) from 2000 to 2004, observed at twenty (20) principal meteorological stations distributed throughout Peninsular Malaysia and operated by the Malaysian Meteorological Service. These principal meteorological stations are located at Batu Pahat, Kluang, Mersing, Senai, Alor Setar, Langkawi, Kota Bharu, Kuala Krai, Melaka, Kuantan, Temerloh, Ipoh, Lubok Merbau, Sitiawan, Chuping, Bayan Lepas, Butterworth, Subang, Petaling Jaya and Kuala Terengganu. Cameron Highlands was excluded from this study because it is situated at 1,545 metres above the mean sea level, which is located much higher than the other stations, where height ranges only from 3 to 88 metres.

The psychrometer or hygrometer, which is a combination of dry bulb and wet bulb thermometers, was used to obtain the relative humidity necessitated for the study. If the air is dry, evaporation occurs rapidly, and this thus lowers the reading of the wet bulb thermometer; the differences in the reading for the dry bulb and wet bulb were used to compute the relative humidity. For the continuously recording relative humidity, on the other hand, the standard instrument is the hair hygrograph where the humidity sensitive element is a bundle of hair which has the property of altering in length with changes in the relative humidity. Both these instruments were kept in a Stevenson screen at the principal meteorological stations.

A class of models incorporating the correlation reflecting the spatial structure is of the form, $Y_i = \mu_i + \varepsilon_i$, where Y_i is the random variable at site i, μ_i is the mean at site i which is modelled in

TABLE 1
Co-ordinates, annual mean relative humidity and neighbours of principal meteorological stations

	Meteorological Station	Latitude (degrees North)	Longitude (degrees East)	Annual Mean Relative Humidity (%)					Neighbours
				2000	2001	2002	2003	2004	
1	Batu Pahat	1.917	103.00	87.9	87.3	86.8	87.8	87.1	Kluang, Mersing, Senai, Melaka
2	Kluang	2.067	103.42	86.5	86.3	85.1	86.4	85.2	Batu Pahat, Mersing, Senai
3	Mersing	2.333	103.83	87.9	88.3	86.3	86.9	86.0	Kluang, Batu Pahat, Senai
4	Senai	1.600	103.63	86.1	86.2	84.7	85.3	84.6	Kluang, Batu Pahat, Mersing
5	Alor Setar	6.117	100.42	83.7	83.0	78.7	80.1	79.0	Chuping, Langkawi, Butterworth, Bayan Lepas
6	Langkawi	6.333	99.83	79.5	79.6	77.0	78.1	78.1	Chuping, Alor Setar
7	Kota Bharu	6.100	102.25	81.9	82.9	81.5	81.8	81.0	Kuala Krai
8	Kuala Krai	5.533	102.22	86.1	85.2	84.4	85.7	84.9	Kota Bharu, Kuala Terengganu
9	Melaka	2.333	102.28	82.4	82.4	80.1	81.4	80.5	Petaling Jaya, Batu Pahat
10	Kuantan	3.800	103.33	85.2	84.4	81.4	83.7	85.1	Temerloh
11	Temerloh	3.450	102.53	85.1	84.2	82.8	84.3	83.7	Petaling Jaya, Subang, Kuantan
12	Ipoh	4.567	101.05	83.3	83.7	81.6	81.9	80.9	Lubok Merbau, Sitiawan
13	Lubok Merbau	4.817	100.87	84.3	83.3	81.1	82.9	82.1	Ipoh,Butterworth, Bayan Lepas, Sitiawan
14	Sitiawan	4.217	100.72	84.3	84.0	83.5	85.3	81.7	Ipoh, Lubok Merbau
15	Chuping	6.500	100.25	83.6	82.9	81.7	82.6	81.7	Alor Setar, Langkawi
16	Bayan Lepas	5.200	100.18	80.9	80.5	75.1	77.1	77.3	Butterworth, Alor Setar, Lubok Merbau
17	Butterworth	5.400	100.35	82.3	80.9	79.5	81.3	80.8	Bayan Lepas, Alor Setar, Lubok Merbau
18	Subang	3.200	101.58	79.2	79.2	77.9	80.0	79.8	Petaling Jaya, Temerloh
19	Petaling Jaya	3.083	101.67	77.8	79.0	77.0	78.2	77.4	Subang, Melaka, Temerloh
20	Kuala Terengganu	5.333	103.12	84.3	84.0	81.3	82.4	81.1	Kuala Krai

terms of the covariates and ε_i the random error terms. Furthermore, ε_{ii} could be allowed to be a function of the neighbouring sites as:

$$\varepsilon_i = \sum_{\substack{j=1 \\ j \neq i}}^{n} g_{ij}\varepsilon_j + \delta_i \quad i = 1, 2, ..., n \tag{1}$$

with $\{g_{ij}\}$ a sequence of constants, $\{\delta_i\}$ a sequence uncorrelated errors with $E(\delta_i) = 0$ and $Var(\delta_i) = \sigma^2$. This is what is known as a Simultaneous Autoregressive (*SAR*) Model (*see* Cliff and Ord, 1981).

This model can be written in the matrix forms as, $\varepsilon = \mathbf{G}\,\varepsilon + \boldsymbol{\delta}$, where vector $\varepsilon^T = (\varepsilon_1, \varepsilon_2, \ldots, \varepsilon_n)$, vector $\boldsymbol{\delta}^T = (\delta_1, \delta_2, \ldots, \delta_n)$, $\varepsilon \sim \mathbf{MVN}(\mathbf{0}, \boldsymbol{\Sigma})$ $\boldsymbol{\delta} \sim \mathbf{MVN}(\mathbf{0}, \sigma^2\mathbf{I})$ and the matrix **G** is given as follows:

$$\mathbf{G} = \begin{bmatrix} 0 & g_{12} & g_{13} & \cdots & g_{1n} \\ g_{21} & 0 & g_{23} & \cdots & g_{2n} \\ g_{31} & g_{32} & 0 & \cdots & g_{3n} \\ \vdots & \vdots & \vdots & \ddots & \vdots \\ g_{n1} & g_{n2} & \cdots & \cdots & 0 \end{bmatrix}. \tag{2}$$

If we let $\varepsilon_i^* = \{\varepsilon_j, j \neq i\}$, where ε_i^* denotes $\boldsymbol{\varepsilon}$ after deletion of ε_i, the Conditional Autoregressive (*CAR*) Model is then:

$$E(\varepsilon_i | \varepsilon_i^*) = \sum_{\substack{j=1 \\ j \neq 1}}^{n} g_{ij}\varepsilon_j \text{ and } Var(\varepsilon_i | \varepsilon_i *) = \sigma_i^2 \text{ for } i = 1, 2, ..., n \tag{3}$$

When each conditional distribution is normal, the matrix form of the joint distribution becomes $\varepsilon \sim$ MVN *(***o, Σ***),* where $\boldsymbol{\Sigma}^{-1} = \mathbf{D}(\mathbf{I}-\mathbf{G})$, $\mathbf{D}^{-1} = diag\,(\sigma_1^2, \sigma_2^{2,} \cdots \sigma_n^2)$, G is given in equation (2), where DG and G must necessarily be symmetric for the *CAR* model.

Since g_{ij} are constants which need estimation and too many of these constants are to be estimated, some simplifications can be made by allowing $\mathbf{G} = \rho\mathbf{W}$, where ρ is an unknown constant which can be estimated for a given data set, and

$$\mathbf{W} = \begin{bmatrix} 0 & w_{12} & w_{13} & \cdots & w_{1n} \\ w_{21} & 0 & w_{23} & \cdots & w_{2n} \\ w_{31} & w_{32} & 0 & \cdots & w_{3n} \\ \vdots & \vdots & \vdots & \ddots & \vdots \\ w_{n1} & w_{n2} & \cdots & \cdots & 0 \end{bmatrix}, \tag{4}$$

is a matrix of known weights. Suppose we let $\sigma_i^2 = \sigma^2$, for all *i*, the covariance matrix, $\boldsymbol{\Sigma}$would then be given as $\sigma^2(\mathbf{I}-\rho\mathbf{W})^{-1}$ for the *CAR* model.

To obtain the weights, the researcher first had to ascertain or define the neighbouring sites and then worked out the weights. For this study, the neighbours for a given meteorological station were defined as all meteorological stations located within a radius of one(1) degree from the station of interest. The weights, $w_{ij} = 1$, if stations *i* and *j* were neighbours and $w_{ij} = 0$, if otherwise. The neighbours of the twenty meteorological stations considered in this study are listed in Table 1.

Various models of increasing complexity (as discussed in the results section in Section 3), were fitted to the relative humidity data and the modelling process was done using the S-plus Spatial Statistics Module (Kaluzny *et al.,* 1998).

To evaluate between the competing models, the test statistic (Cressie, 1993) used in this study was:

$$U^2 = 2\left(\frac{n-p-r}{n}\right)(L_p - L_{p+r}) \sim \chi^2(r), \tag{5}$$

where n is the number of data points, p is the number of parameters estimated, r is the additional number of the parameters estimated, L_p is the negative log likelihood for the smaller model and L_{p+r} is the negative log likelihood for the larger model.

The log likelihood function for the *CAR* model is given by:

$$-\frac{n}{2}\log(2\pi) - \frac{n}{2}\log(\sigma^2) + \frac{1}{2}\log|\mathbf{I} - \rho\mathbf{W}| - \frac{1}{2\sigma^2}\varepsilon^{\mathrm{T}}(\mathbf{I} - \rho\mathbf{W})\varepsilon \tag{6}$$

To determine whether any of the coefficients of the covariates were significant or not, the Likelihood Ratio Test given as $-2\log\lambda \sim \chi^2(k)$ was used (*see* Maddala, 1989, 84), where k is the number of restrictions and:

$$\lambda = \frac{\text{maximum of Likehood under restriction}}{\text{maximum of Likehood without restriction}} \tag{7}$$

RESULTS

A scatter plot of the annual mean relative humidity versus the latitude and longitude are shown respectively in *Figs. 1* and *2*. From these figures, it is clearly shown that there is some sort of relationship between the mean relative humidity and geographical co-ordinates.

The test for the spatial correlation was also conducted using the Moran and Geary Statistics (Cliff and Ord, 1981). The Moran spatial correlation was found to be 0.6231, with the standard error of 0.08828. The computed z-statistic value was 7.173 and a p-value of 7.329×10^{-13}. The Geary spatial correlation value was 0.5128, with the standard error of 0.09752. The computed z-statistic value was −4.996 and a p-value of 5.844×10^{-7}. These tests indicated that the observations were spatially correlated due to the extremely small p-value, thereby rejecting the null hypothesis of the no spatial correlation. Hence, various models of increasing complexity were fitted into the data, as follows:

Let Y_i be the annual mean relative humidity recorded at station i, x_1 be the latitude and x_2 be the longitude position of the stations.

The models considered in this study were:

$$Y_i = \beta_{00} + \varepsilon_i, \quad \text{(Model 1)}$$
$$Y_i = \beta_{00} + \beta_{10}x_1 + \varepsilon_i, \quad \text{(Model 2)}$$
$$Y_i = \beta_{00} + \beta_{01}x_2 + \varepsilon_i, \quad \text{(Model 3)}$$
$$Y_i = \beta_{00} + \beta_{20}x_1^2 + \varepsilon_i, \quad \text{(Model 4)}$$
$$Y_i = \beta_{00} + \beta_{11}x_1x_2 + \varepsilon_i, \quad \text{(Model 5)}$$
$$Y_i = \beta_{00} + \beta_{10}x_1 + \beta_{01}x_2 + \varepsilon_i, \quad \text{(Model 6)}$$
$$Y_i = \beta_{00} + \beta_{10}x_1 + \beta_{20}x_1^2 + \varepsilon_i, \quad \text{(Model 7)}$$

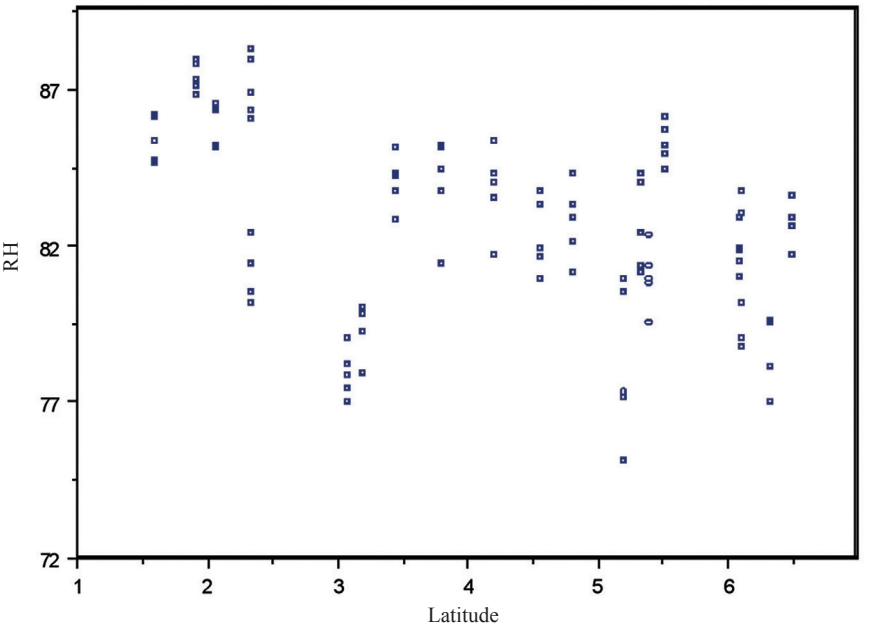

Fig. 1: Plot of annual mean relative humidity vs. latitude

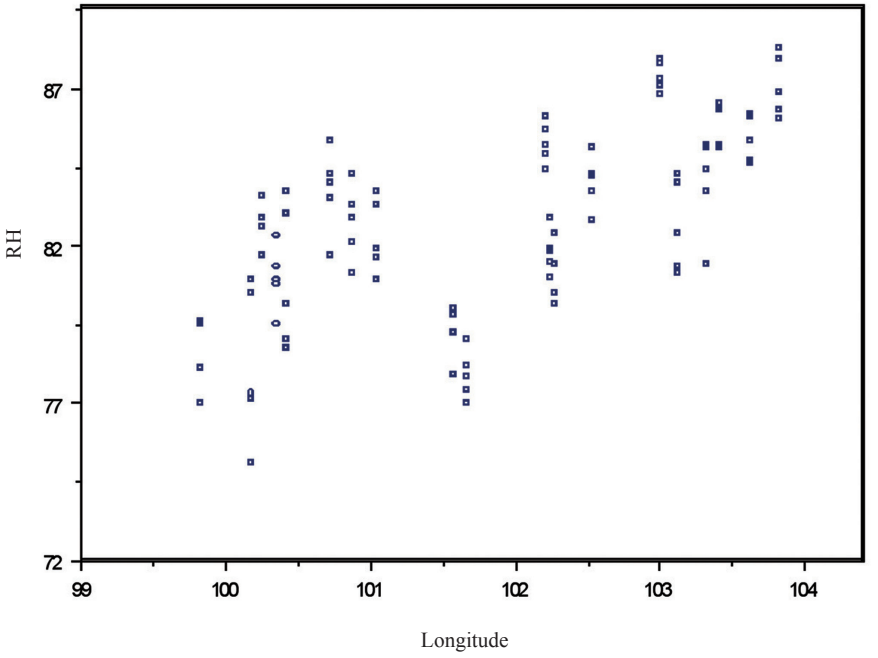

Fig. 2: Plot of annual mean relative humidity vs. longitude

$$Y_i = \beta_{00} + \beta_{11}x_1x_2 + \beta_{20}x_1^2 + \varepsilon_i, \quad \text{(Model 8)}$$
$$Y_i = \beta_{00} + \beta_{01}x_2 + \beta_{20}x_1^2 + \varepsilon_i, \quad \text{(Model 9)}$$
$$Y_i = \beta_{00} + \beta_{10}x_1 + \beta_{01}x_2 + \beta_{20}x_1^2 + \varepsilon_i, \quad \text{(Model 10)}$$
$$Y_i = \beta_{00} + \beta_{10}x_1 + \beta_{11}x_1x_2 + \beta_{20}x_1^2 + \varepsilon_i, \quad \text{(Model 11)}$$
$$Y_i = \beta_{00} + \beta_{10}x_1 + \beta_{01}x_2 + \beta_{11}x_1x_2 + \beta_{20}x_1^2 + \varepsilon_i, \quad \text{(Model 12)}$$

The parameter estimates of the fitted models for the *CAR* error structures in the present study are given in Table 2. Using equation (5), the test statistic U^2 were computed for the various models considered in this study and are also tabulated in Table 2, together with the *p*-values.

Based on the data presented in Table 2, it could be observed that the estimated parameter coefficients takes on a wide variety of values, which were both positive and negative. The estimate for σ^2 remained in the interval of 4.233 to 5.045, while for ρ it is in the range between 0.182 and 0.312 for the models considered in this study. The log likelihood remained in the vicinity of −318.74 to −302.46, while U^2 did not exceed 30.281.

However, the most crucial thing which needs to be observed in Table 2 is the *p*-values, which range from 7.58×10^{-7} to 0.759. The *p* value indicates whether or not a particular model significantly differs from the null model (Model 1). Then, a smaller *p*-value would clearly assist in the selection of a model. Among the models considered in this study, model $Y_i = \beta_{00} + \beta_{01}x_2 + \varepsilon_i$ (Model 3) has the smallest *p*-value of 7.58×10^{-7} and it is therefore highly significant at 0.001 level. The significance of the coefficient of the longitude covariate was established by the Likelihood Ratio Test, which gave the value, $\chi^2 = 25.487$ with 1 degree of freedom and *p*-value of 4.453×10^{-7}. Hence, this coefficient is highly significant at 0.001 level, indicating that β_{01} is not zero. In order to test the significance of ρ, the Likelihood Ratio Test gave a value, $\chi^2 = 11.049$, with 1 degree of freedom and *p* value of 0.001. This is also highly significant at the 0.01 level.

Following closely behind Model 3 are Models 9, 12, 6, 10 and 11 which have the *p*-values of 4.20×10^{-6} , 4.29×10^{-6} , 4.58×10^{-6} , 1.64×10^{-5} and 5.67×10^{-4}, respectively. The other models can be safely discarded.

CONCLUSIONS

The objective of this research was to fit and illustrate a spatial regression modelling which takes into account the spatial correlation amongst its neighbours. It was found that model $Y_i = \beta_{00} + \beta_{01}x_2 + \varepsilon_i$ (Model 3) is an appropriate one to be used as it has the smallest *p* value when compared to the null model (Model 1). Using more data, this consolidates the previous studies undertaken. The coefficient β_{01} was also found to be significant. The parameter ρ was highly significant at 0.01 level, and this explains the importance of taking the spatial correlation between the neighbouring sites into consideration in the modelling process. The usefulness of this model is that it is simple and it will help to estimate the mean annual relative humidity at places where no observations were recorded for the year 2000 to 2004. It would therefore be useful for predicting future values.

There are also other potential models, including Models 9, 12, 6, 10 and 11 which also have small *p* values. In any future study, these potential models need to be given due consideration as they are viable alternatives.

Similar further studies can be undertaken for the data observed for other years apart from the ones considered in this research. Different neighbourhood structures and weights can also be attempted in any future study. Alternatively, further research can be done to fit the spatial regression models with Moving Average (*MA*) errors and make comparison with the proposed model in this research.

TABLE 2
Results of fitted models for the *CAR* error structures

	Estimated parameter Coefficients	$\hat{\sigma}$	$\hat{\rho}$	Log Likelihood	U^2	p-value
Model 1	$\hat{\beta}_{00} = 82.205$	4.837	0.289	− 318.74	-	-
Model 2	$\hat{\beta}_{00} = 83.522$ $\hat{\beta}_{10} = -0.275$	5.045	0.275	− 318.48	0.499	0.480
Model 3	$\hat{\beta}_{00} = -64.124$ $\hat{\beta}_{01} = 1.438$	4.241	0.225	− 306.00	24.461	7.58×10^{-7}
Model 4	$\hat{\beta}_{00} = 82.912$ $\hat{\beta}_{20} = -0.029$	5.000	0.279	− 318.46	0.538	0.463
Model 5	$\hat{\beta}_{00} = 83.154$ $\hat{\beta}_{11} = -0.002$	5.005	0.280	− 318.62	0.230	0.632
Model 6	$\hat{\beta}_{00} = -73.545$ $\hat{\beta}_{10} = 0.153$ $\hat{\beta}_{01} = 1.524$	4.234	0.232	− 305.80	24.586	4.58×10^{-6}
Model 7	$\hat{\beta}_{00} = 81.972$ $\hat{\beta}_{10} = 0.397$ $\hat{\beta}_{20} = -0.068$	4.977	0.285	− 318.45	0.551	0.759
Model 8	$\hat{\beta}_{00} = 73.167$ $\hat{\beta}_{11} = 0.038$ $\hat{\beta}_{20} = -0.396$	4.310	0.312	− 317.22	2.888	0.236
Model 9	$\hat{\beta}_{00} = -75.000$ $\hat{\beta}_{01} = 1.540$ $\hat{\beta}_{20} = 0.021$	4.234	0.230	− 305.71	24.757	4.20×10^{-6}
Model 10	$\hat{\beta}_{00} = -71.768$ $\hat{\beta}_{10} = -0.803$ $\hat{\beta}_{01} = 1.524$ $\hat{\beta}_{20} = 0.111$	4.327	0.216	− 305.51	24.872	1.64×10^{-5}
Model 11	$\hat{\beta}_{00} = 86.620$ $\hat{\beta}_{10} = -29.780$ $\hat{\beta}_{11} = 0.271$ $\hat{\beta}_{20} = 0.249$	4.586	0.235	− 309.45	17.465	5.67×10^{-4}
Model 12	$\hat{\beta}_{00} = -335.944$ $\hat{\beta}_{10} = 56.962$ $\hat{\beta}_{01} = 4.059$ $\hat{\beta}_{11} = -0.540$ $\hat{\beta}_{20} = -0.198$	4.233	0.182	− 302.46	30.281	4.29×10^{-6}

ACKNOWLEDGEMENTS

The researchers would like to thank the reviewers and the editor for their useful comments and valuable suggestions to improve the quality of the paper. We would also express our thanks to the Department of Mathematics and the Institute of Mathematical Research, Universiti Putra Malaysia for their support.

REFERENCES

Cliff, A.D. and Ord, J.K. (1981). *Spatial Processes: Models and Applications*. Pion, London.

Cox, D.R. and Isham, V. (1988). A simple spatial-temporal model of rainfall. In *Proceedings of the Royal Society of London*.

Cressie, N.A.C. (1993). *Statistics for Spatial Data*. New York: Wiley.

Isthrinayagy, K. (2001). Trend surface analysis of annual rainfall in Peninsular Malaysia. Master of Science (Applied Statistics) Project Report.

Jin Ping, Guo and Yang, Xiao. (1999). Trend surface analysis of forest landscape pattern in Guandishan forest region of Shanxi, China. *Journal of Environmental Sciences*.

Kaluzny, S.P., Vega, S.C., Cardoso T.P. and Shelly, A.A. (1998). *S+SpatialStats User's Manual for Windows and UNIX*. New York: Springer.

LeCam, L. (1961). Stochastic description of precipitation. In J. Neyman and Berkeley C. A. (Eds.), *Proceedings of the Fourth Berkely Symposium on Mathematical Statistics and Probability*. University of California Press.

Maddala, G.S. (1989). *Introduction to Econometrics*. New York: Macmillan Publishing Company.

Mahendran Shitan. (2004). Trend surface analysis with Simultaneous Autoregressive (SAR) errors for annual mean relative humidity in Peninsular Malaysia. In *Proceedings of Ecological and Environmental Modelling (ECOMOD 2004)*, 15-16 September 2004, Penang, Malaysia.

Mahendran Shitan, Pauline Mah Jin Wee, Lim Ying Chin and Lim Ying Siew. (2005). Spatial regression with Conditional Autoregressive (CAR) and Simultaneous Autoregressive (SAR) errors for annual mean relative humidity in Peninsular Malaysia. In *Proceedings of International Conference on Quantitative Sciences and Its Applications (ICOQSIA 2005),* 6-8 December, 2005, Malaysia.

Mahendran Shitan and Kok Wei Ling. (2007). A comparative study of spatial regression with MA, CAR and SAR error structure for annual mean relative humidity in Peninsular Malaysia. In *Proceedings of the 2nd Regional Conference on Ecological and Environmental Modelling (ECOMOD 2007)*, 28 -30 August 2007, Penang.

Smith, R.L. (1994). *Spatial Modelling of Rainfall Data, Statistics for the Environment 2: Water Related Issues*. New York: Wiley.

Todorov, A.V. and David Abraham. (1982). Recent rainfall trends in Malaysia. *MARDI Report*, 79.

Waymire, E.D. and Gupta, V.K. (1981). The mathematical structure of rainfall representations: Some applications of the point process theory to rainfall processes. *Water Resources Research*, *17*.

ISSN: 0128-7680
Pertanika J. Sci. & Technol. **17 (2)**: 347 – 354 (2009)

The Effect of Effective Diameter on Fluidization Quality in Compartmented Fluidized Bed Gasifier

Wee Siaw Khur*, Chok Vui Soon, Alexander Gorin, Chua Han Bing and Yan Hong Ming
Curtin University of Technology, CDT 250, 98009 Miri, Sarawak, Malaysia
**E-mail: wee.siaw.khur@stud.curtin.edu.my*

ABSTRACT

Compartmented Fluidized Bed Gasifier (CFBG), consisting of two compartments - the combustor and gasifier, uses air blown instead of pure oxygen for syngas production in bubbling fluidization mode, eliminating the need of air separation unit, and reducing the capital cost, thus distinguishes it from other traditional ones. Fluidization quality is a determining factor in the CFBG to guarantee its well-lifted behaviour. Previous study, without solid circulation at ambient conditions, brought to the fore the necessity of considering the effect of the minimum allowable effective diameter. The study was then performed in the CFBG cold physical model of 0.66m overall diameter (effective diameter for combustor and gasifier is 0.413m and 0.257m) to investigate the fluidization quality and compare it with the results obtained from the previous cold model of about 1.36 times smaller, but with the same compartmented ratio of 65:35. Different inert particles (river sand, quartz sand and alumina) were used, over a range of aspect ratios, for the aforementioned objective. The results showed that the fluidization quality in the gasifier has not been achieved and the degradation of fluidization quality in the combustor is still observed, notwithstanding the fact that the condition of the minimum allowable effective diameter has been met. The reduction of distributor free area, to increase the distributor pressure drop, showed a marginal effect on the quality. The effect of the minimum allowable effective diameter on fluidization quality in CFBG as well as the interplay of geometric and operational parameters require further studies be carried out. The fluidization quality of the binary mixture is also currently under investigation.

Keywords: Channelling, Compartmented Fluidized Bed Gasifier (CFBG), effective diameter, fluidization, fluidization quality

INTRODUCTION

It is of great importance to be able to estimate the quality of fluidization for an efficient and economic use of gas-fluidized beds when the operating parameters are changed. An idealized fluidization consists of a completely lifted and uniform suspension of inert particles. Fluidization quality, Q, is used as a distinctive indicator to show the fluidization characteristic in the compartmented fluidized bed gasifier (CFBG).

The CFBG is a unique compartmented reactor which consists of two reactors, namely the combustor and the gasifier, partitioned vertically inside at a ratio of 65:35, based on the heating requirement during the high-temperature operation. The significance of the CFBG is that it uses air blown instead of pure oxygen for syngas production in bubbling fluidization mode, eliminating the need for air separation unit and thus reducing the capital cost, which distinguishes it from the traditional ones. The idea of having compartmented reactors arises when the construction of several reactors is not economically viable, owing to the need of solids to be circulated through different

Received: 6 May 2008
Accepted: 20 May 2008
*Corresponding Author

reaction zones in many gas-solid reactions. In this paper, the combustor or gasifier compartment is neither a full cylindrical nor semi-cylindrical, but rather a segment of a cylindrical, as shown in *Fig. 1*. A few studies on non-cylindrical fluidized bed have been carried out elsewhere (Bhattacharya *et al*., 1999; Singh *et al*., 2005; He, 1993; Yan, 1995), but hitherto none has addressed the type of geometry in the CFBG. This has thus invited a strong interest in the study of fluidization characteristics in the CFBG.

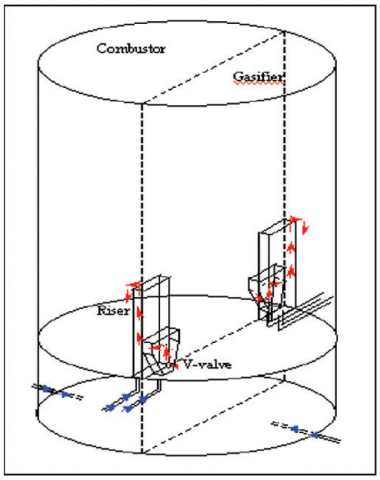

Fig. 1: Isometric view of CFBG

A previous study by Wee *et al*. (2007) brought to the fore the necessity of considering the effect of the minimum allowable effective diameter, without solid circulation at ambient conditions. The study was carried out (in this paper) at the expanded CFBG cold physical model of 36% increment in the overall diameter, compared to the previous one. The objectives of this paper were to investigate the fluidization quality, at each compartment, with different inert particles and sizes being used (river sand, quartz sand and alumina) for a range of aspect ratios as well as to compare it with the results obtained from the previous model.

THEORY

Fluidization is defined as a process, in which particles are transformed into a fluid-like state, through contact with either a gas or a liquid. The fluidization quality indicator, Q, is conventionally defined as the ratio of experimental bed pressure drop to the theoretical bed pressure drop, or in short, Q = Experimental ΔP/ Theoretical ΔP, where theoretical bed pressure drop is simply the weight of the particles over the cross-sectional area of the compartment.

It is essential to find the effective diameter for the CFBG reactor of the non-uniform and uncommon shape. Hence, the effective diameter, D_e (Nicholas *et al*., 1984) was representatively used in this study.

$$D_e = 4\text{x}\ \frac{\textit{mean cross sectional area of flow channels through bed}}{\textit{mean wetted perimeter of flow channels}} \qquad (1)$$

Distributor free area is the percentage of the area which is occupied by orifices, as described in equation (2).

$$Free\ area = \frac{Total\ Orificers\ Area}{Distributor\ Plate\ Area} \times 100\% \quad (2)$$

EXPERIMENTAL METHOD

The experimental set up used in this study is shown in *Fig. 2*. The CFBG is custom-made using mild steel as the body structure, and Perspex material as the cover to ease the visual observation during the experiment. The overall diameter of the CFBG is 0.66m, with a height of 1.8m, and partitioned into two compartments, namely the combustor and the gasifier by a vertical diving wall in a ratio of 65:35, respectively. Meanwhile, perforated plate distributor, with orifice diameter of 3mm was used to uniformly distribute the fluidizing agent, ambient air into the beds of the particle, at the free area of 0.27% and 0.32% in triangular pitch arrangement for gasifier and combustor accordingly. The effective diameter for combustor and gasifier is 0.413m and 0.257m correspondingly. Meanwhile, 100 micron mesh was employed on top of the distributor to avoid the particles from weeping through the orifices. The air is regulated in the range of 1 – 2 minimum fluidization velocity, U_{mf}, to maintain the bubbling mode of fluidization. Water manometer is utilized to gauge the pressure drop across the beds and the distributors.

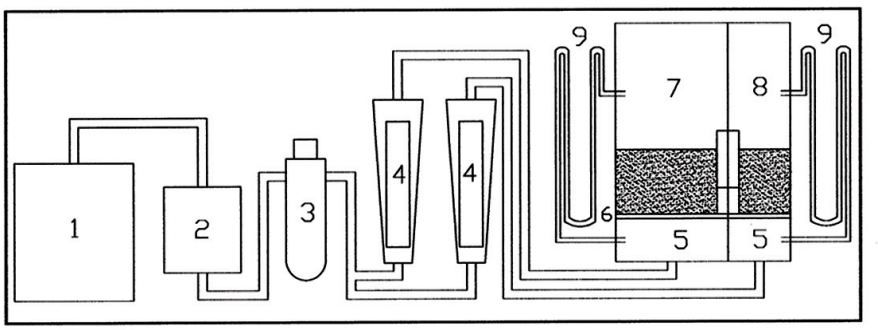

Fig. 2: Experimental set up (1: compressor; 2: dryer; 3: pressure regulator; 4: rotameter; 5: plenum; 6: perforated plate distributor; 7: combustor; 8: gasifier; 9: water manometer)

The particles used in the experiment are mostly natural river sand. However, alumina of different properties, and sized as a perspective heat carrier for pilot plant and quartz sand with free-impurities-surfaces and physical properties were tested on the quality of fluidization. Their physical properties are tabulated in Table 1.

TABLE 1
Physical properties of particles

Particle	River sand	Alumina	Quartz sand	Quartz sand
Size, d_p	272 μm	360 μm	256 μm	362.5 μm
Density, ρ_p	2620 kg/m^3	3992 kg/m^3	2638 kg/m^3	2638 kg/m^3
Theoretical (Wen & Yu) minimum fluidization velocity, U_{mf} (Kunii, 1991)	0.060 m/s	0.154 m/s	0.053 m/s	0.105 m/s

RESULTS AND DISCUSSION

The Effect of Effective Diameter

Fig. 3 compares the fluidization quality at different effective diameters, using river sand at bed height of 0.34m, over a range of free area from 0.27% to 0.32%. The results were then compared with the ones obtained from Wee *et al*. (2007) who obtained D_e = 0.173m, 0.234m and 0.290m. As can be observed from the graph, only the diameter of 0.290m was found to achieve good fludization quality, whereas the rest exhibited the opposite quality. It was also expected that the diameter which was bigger than 0.290m achieved a good fluidization quality (Wee *et al*., 2007); however, the trend of D_e = 0.413m was notwithstanding the fact that the condition of the minimum allowable effective diameter had been met. Further studies need to be done to verify the reasons contributing to it. The flow behaviour of a gas solid fluidized bed is very complex and highly sensitive to scale (Nicholas *et al*., 1984). Hence, the wall effect, which has a strong relationship with D_e, is a determining factor which leads to the fluidization quality. Werther (1968) and other researchers showed that the wall effect became progressively more significant as the bed diameter was decreased. As the diameter was decreased, the friction at the wall was found to support a larger and larger fraction of the weight of the bed, as a result of which the bed became more loosely packed (Srivastava *et al*., 2002). This leads to a decrease in the internal friction and a corresponding decrease in the normal stress exerted at the wall, creating a preferential path at wall side, which facilitates the air to flow through it. This eventually contributes to increasing bed pressure to drop with increasing air velocity which demonstrates the intermediate channelling behaviour (Nicholas *et al*., 1984). Profiles which are below 1.0 indicate channelling bed. This offset suggests that the beds are not completely fluidized.

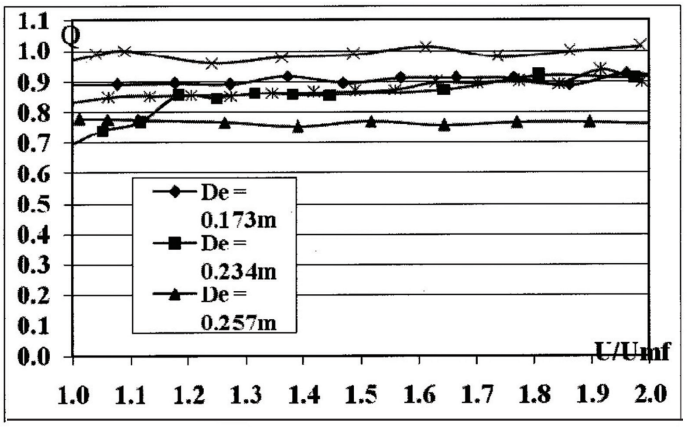

Fig. 3: Fluidization quality, Q versus U/U_{mf} at different effective diameters (river sand, bed height = 0.34m)

The Effect of Free Area

In order to improve the fluidization quality, the study was done to investigate the effect of the distributor free area. *Fig. 4* shows the fluidization quality of different free areas, e.g. 0.23% and 0.32% at the aspect ratio of 1.09 and the river sand was used. The higher free area shows a more satisfactory trend in relative to the smaller free area; nevertheless, the desirable quality of fluidization is still unachievable. The graph shows the inability of the fluidized bed to be fully lifted by the incoming gas rate at U_{mf} and obviously one can observe that channelling occurs in the system studied. Channelling can be a result of the non-uniformities and inhomogeneities in the bed due to the perturbation, where there is a localized higher velocity through the bed, causing a localized expansion. Thus, it changes the pressure drop through that portion of the bed. Channelling becomes more pronounced if the localized pressure drop through the bed-distributor system decreases with the increased velocity (Robert, 1976).

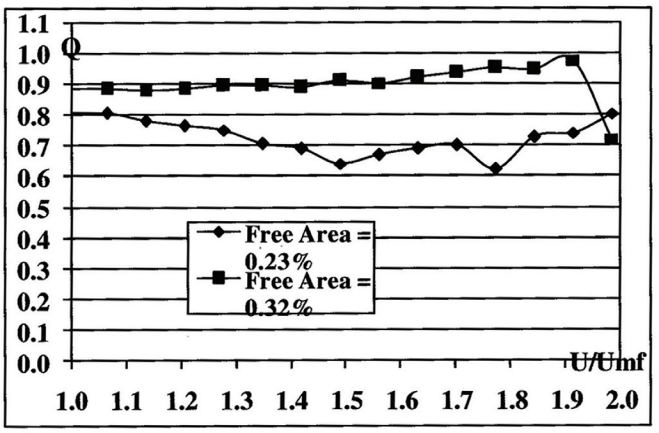

Fig. 4: Fluidization quality, Q versus U/U_{mf}, at different distributor free areas (river sand, H/D = 1.09, D_e = 0.413m)

The Effect of Different Particles

A comparison was also done between the alumina and quartz sand of identical size in the gasifier compartment, as shown in *Fig. 5*. It was observed from the fluidization quality curve that the quartz sand showed a better behaviour as compared to alumina. According to Wee *et al*. (2007), the physical properties of the particles play the key effect to the hydrodynamics of the bed.

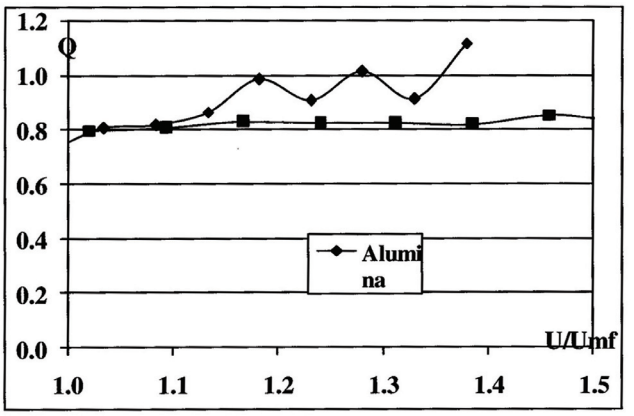

Fig. 5: Fluidization quality, Q versus U/U_{mf}, using different particles (free area = 0.27%, H/D = 1.36, D_e = 0.257m)

The shape and density of the particles are factors which affect channelling (Nicholas *et al*., 1984). Channelling always takes place due to the appreciable cohesive force between the particles (Wang *et al*., 1997). Thus, it is observed that the quartz sand and alumina shows through and intermediate channelling, respectively. The through channelling can be distinguished when the Q is less than 1, whereas the intermediate channelling will have an increasing large fluctuation along the Q=1 (Wee *et al*., 2007).

The Effect of Different Particle Sizes

A comparison of the different particle sizes was made in the gasifier compartment of shallow bed, as can be seen in *Fig. 6*. None of the sizes showed a quantitatively good fluidization quality. It was also observed that smaller size particles had a tendency to show through channelling, while larger ones show intermediate channelling. Therefore, the increasing of size in diameter would result in a high propensity of intermediate channelling to occur in shallow bed. This is because smaller size particle diameter leads to a less porous bed, leading to a more complex bed structure, and making it more difficult to fluidize and less bed expansion compared to larger size particles.

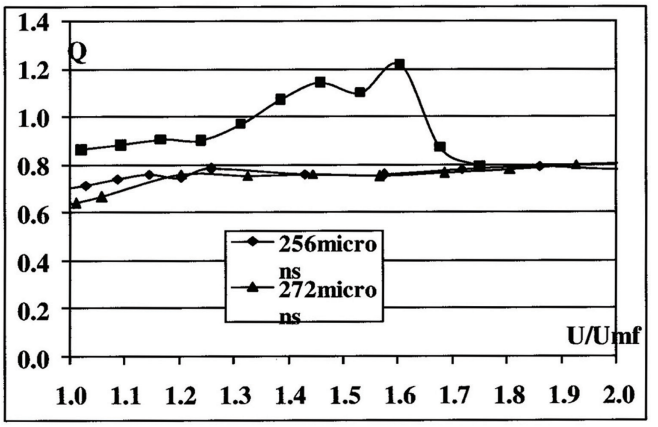

Fig. 6: Fluidization quality, Q versus U/U_{mf} at different particles size (free area = 0.27%, H/D = 0.78, D_e = 0.257m)

The Effect of Aspect Ratio

Fig. 7 shows the fluidization quality in relation to different aspect ratios, using river sand at the distributor free area of 0.27% and a diameter of 0.257m. As can be observed from the graph, no distinctive differences are discernible in progression of the aspect ratio. The average quality which can be obtained over the range of the aspect ratio is approximately 0.8.

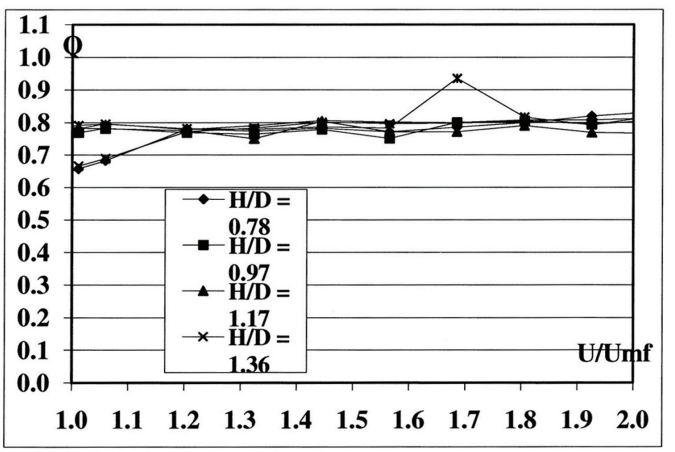

Fig. 7: Fluidization quality, Q versus U/U_{mf} at different aspect ratios (river sand, free area = 0.27%, D_e = 0.257m)

CONCLUSIONS

The study was carried out to investigate the fluidization quality in the expanded CFBG cold model. One can summarize the findings as below:

1. The expanded CFBG cold model, which results in a bigger combustor compartment (D_e = 0.413m), does not achieve the desirable quality of fluidization, even when the diameter is bigger than the minimum allowable effective diameter (D_e = 0.290m), as obtained in the previous cold model.
2. The effects of different distributor free areas, different particles used, different particle sizes and different aspect ratios to the fluidization quality were also tested; the results showed similar results for all, i.e. the occurrence of channelling was consistent in both compartments.

The effect of the minimum allowable effective diameter on fluidization quality in the CFBG and the interplay of geometric and operational parameters invite further study. In addition, the fluidization quality of the binary mixture is currently under investigation.

REFERENCES

Bhattacharya, B., Sathiyamoorthy, D., Govardhana Rao, V. and Mahajan, S.P. (1999). Solid circulation in a compartmented gas fluidized bed. *Power Technology, 101,* 191-204.

He, Y. (1993). Hydrodynamics of a compartmented dense phase circulating fluidised bed. Ph.D. Dissertation, Department of Chemical Engineering, University of Queensland, Australia.

Kunii, D. and Levenspiel, O. (1991). *Fluidization Engineering*. USA: Butterworth-Heinemann.

Nicholas, P.C. and Paul, P.C. (1984). *Hydrodynamics of Gas-Solids Fluidization*. Houston: Gulf Pub. Co.

Robert, S. (1976). Effect of distributor plate-to-bed resistance ratio on onset of fluidized-bed channeling. *AIChE Journal, 22*(3), 590-592.

Singh, R.K. and Roy, G.K. (2005). Prediction of minimum bubbling velocity, fluidization index and range of particulate fluidization for gas-solid fluidization in cylindrical and non-cylindrical beds. *Powder Technology, 159,* 168-172.Srivastava, A. and Sundaresan, S. (2002). Role of wall friction in fluidization and standpipe flow. *Powder Technology, 124,* 45-54.

Wang, Z., Kwauk, M. and Li, H. (1997). Fluidizaton of fine particle. *Chemical Engineering Science, 53*(3), 377-95.

Wee, S.K., Chok, V.S., Srinivasakannan, C., Chua, H.B. and Yan, H.M. (2007). Fluidization Quality Study in Compartmented Fluidized Bed Gasifier. *Bio-energy outlook*, Singapore.

Werther, J. (1968). Influence of the bed diameter on the hydrodynamics of gas fluidized beds. *AIChE Symposium Series, 141*(70), 53-62.

Yan, H.M. (1995). Development and modelling of coal combustion and gasification in a compartmented fluidised bed gasifier. Ph.D. Dissertation, Department of Chemical Engineering, University of Queensland, Australia.

ISSN: 0128-7680
Pertanika J. Sci. & Technol. **17 (2)**: 355 – 362 (2009)

Production of Carbon Dioxide Using Direct Pyrolysis-Combustion from *Aquilariella malaccensis* or Karas Woods Under Argon Atmosphere

Noraishah Othman[1,2*], Siti Kartom Kamarudin[1], Muhd Noor Md Yunus[2], Abd. Halim Shamsuddin[3], Siti Rozaimah[2] and Zahirah Yaakob[2]

[1]Nuclear Malaysia Agency (Nuclear Malaysia) Bangi, 43000 Kajang, Selangor, Malaysia

[2]Chemical Engineering Department, Faculty of Engineering, National University of Malaysia, 43000 Bangi, Selangor, Malaysia

[3]Mechanical and Materials Engineering Department, Faculty of Engineering, National University of Malaysia, 43000 Bangi, Selangor, Malaysia

[*]E-mail: noraishah@nuclearmalaysia.gov.my

ABSTRACT

The production of carbon dioxide from *Karas* woods under argon atmosphere was investigated using a direct pyrolysis-combustion approach. Direct burning was used in this study, using argon for pyrolysis and oxygen during combustion to look at the yield of carbon dioxide, produced at different parameters, such as the temperature, retention time and flow rate of argon, as the carrier gas. In this study, a new methodology, 2^3 response surface central composite design was successfully employed for the experimental design and analysis of results. Central composite experimental design and response surface method were utilized to determine the best operating condition for a maximum carbon dioxide production. Appropriate predictable empirical linear model was developed by incorporating interaction effects of all the variables involved. The results of the analysis revealed that linear equation models fitted well with the experimental for carbon dioxide yield. Nevertheless, the R-Squared obtained using the direct pyrolysis-combustion was 0.7118, indicating that the regression line was not at the best-fitted line.

Keywords: **Argon, carbon dioxide production, direct pyrolysis-combustion, *Karas*, response surface method**

ABBREVIATIONS

ANOVA- Analysis of variance
CO_2 - Carbon dioxide

INTRODUCTION

Nuclear Malaysia Radiocarbon Dating Laboratory has been equipped by conventional radiometric method in order to determine the age of archaeological, hydrological and environmental samples. This conventional technique encompasses production of carbon dioxide, production of acetylene and trimerization, respectively. The yield of the carbon dioxide using combustion technique is a prominent stage since it determines the yield of the subsequent process. The sufficient amount of CO_2 will determine the scientific age of the archaeological samples found. A complete combustion produces carbon dioxide, water and char, but the process is not controllable and this

Received: 14 April 2008
Accepted: 16 May 2008
[*]Corresponding Author

leads to inconsistent amount of carbon dioxide produced from the same amount of samples due the consumption of oxygen at the surface of semi-coke during combustion, which negligibly diffused into its pore, causing the wood not to burn directly but undergo thermal degradation precedes the combustion (Browne, 1958). Joel (1994) and Fang *et al*. (2006) used a direct burning of biomass for CO_2 production, and found that the yield was unsatisfactorily inconsistent with the amount of 63% and 60%, respectively from the existing carbon in the samples. Browne (1958), and Wen and Stanley (1979) reported that the pyrolysis of wood would introduce more evolved gases compared to combustion, but this was most preferred because it is a controlled process, in which the desired yield could be determined accordingly. Besides, the yield of products would also be the same although the wood components such as cellulose, hemicelluloses and lignin were separately pyrolyzed. The increased amount of the char, formed at lower temperature during pyrolysis, was due to the fact that slow heating would make the woods to decompose in an orderly manner, in which there is stepwise formation of increasingly stable molecules, richer in carbon and converging toward the hexagonal structure of graphitic carbon (Browne, 1958).

In this study, the influence of argon was characterized as carrier gas onto the wood samples using a direct pyrolysis-combustion by statistical approach. The pyrolysis-combustion method was introduced in this study to obtain the efficiency of the carbon dioxide with respect to several parameters, including the temperature of pyrolysis, residence time and concentration of argon in maximizing the amount of CO_2 from the same amount of samples. Statistical design of experiments (DOE) is a well-known efficient experimentation technique and has been applied in a wide range of disciplines, particularly in industries. In this paper, 2^3central composite design (CCD) was used to predict the optimum numerical conditions for a maximum CO_2 production by applying the response surface method (RSM) using the Design-Expert 6.10.0 (Minneapolis, Inc., USA). The RSM is a collection of mathematical and statistical techniques for empirical model building. The estimated mathematical model was examined using the analysis of variance (ANOVA) at 5% level of significance.

MATERIALS AND METHODS

Sample Pre-treatment

Karas woods were taken from Nuclear Malaysia Reserved Forest as degraded woods cum archaeological samples. Karas woods are among the oldest species found in the rainforest of Asian countries like Malaysia and Indonesia. Karas woods were cut into smaller pieces, milled and then washed with distilled water prior to oven drying. About 50g of the sample underwent the hot-solvent Soxhlet extraction to get rid of resins and wax. Benzene and ethanol, with the ratio of 2:1, were used to eliminate wax and resin, followed by 95% ethanol and distilled water, respectively (Gupta and Polach, 1985). The sample was then refluxed for 8 hours for each solvent before it was oven dried at 50^{o}C for 3 days so that the samples would have totally dried prior to the pyrolysis-combustion process.

Direct Pyrolysis-combustion Reaction

About 5g of the milled Karas wood was spread in the 20cm length of the sample boat and inserted into a 50cm length quartz chamber. The schematic set up of the direct pyrolysis-combustion is shown in *Fig. 1*. It consists of a quartz chamber inserted with thermocouple Type-K integrated with temperature controller and monitor, while purification system, water and carbon dioxide traps were laid out in series and should be vacuumed before the experiment could be started. The quartz tube was heated up at designated temperatures (265, 300, 350, 400, 434^{o}C) using the flames from

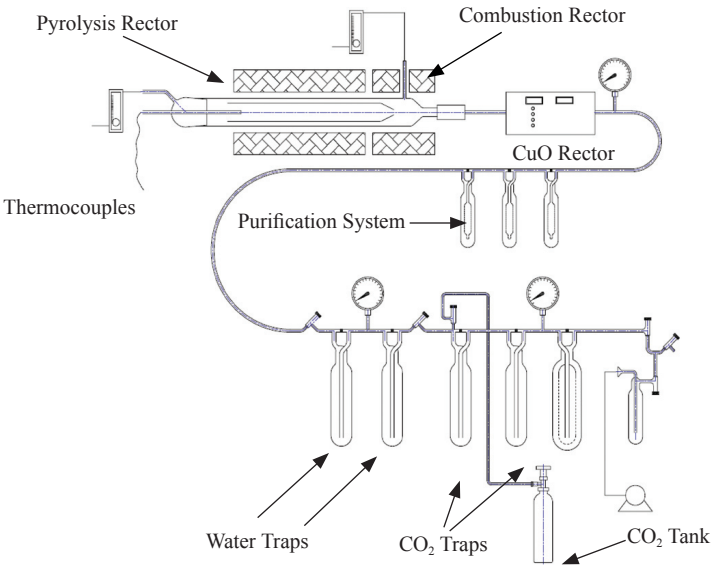

Fig. 1: Schematic diagram of pyrolysis-combustion set up in radiocarbon dating laboratory

TABLE 1
Experimental ranges and levels of process variables for wt% CO_2

Independent variables	Unit	Ranges and Levels				
Coded levels		-1.68179	1	0	1	+1.68179
temperature	°C	266	300	350	400	434
Time	Minutes	15	20	27.5	35	40
Flow rates	cm^3/min	195	400	700	1000	1204

the burners and the temperature monitor indicating the intended temperature; all the traps were fixed at their places. Finally, liquid nitrogen was used to trap the incoming carbon dioxide since the freezing point of liquid nitrogen is –196°C, and dry ice was also used to trap water produced during the experiment.

Initially, the argon was supplied at the inlet of quartz tube at selected flow rates (195,400,700, 1000, 1204 cm^3/min) for the pyrolysis to occur, and the oxygen in excess was supplied at the end tip of the quartz tube simultaneously; hence, the reactor experienced integrated pyrolysis and combustion reaction. After experiencing the integrated pyrolysis-combustion, at the designated retention times of 14, 20, 27.5, 35 and 40 minutes, the remaining char in the sample boat was combusted using oxygen, and the argon supply was automatically ceased. The purified carbon dioxide was cryogenically collected for further synthesis. In this study, the system should be free from any leakages so that it would not contaminate the results yielded. All the nominated parameters were obtained from the Design-Expert 6.10.0 (State-Ease, Minneapolis, USA) software layout as illustrated in Tables 1 and 2. Generally, the volatile matters released during pyrolysis reaction were oxidized at intended

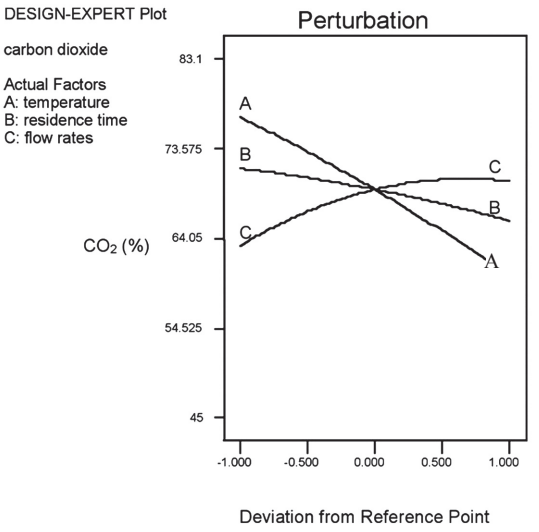

Fig. 2: Effect of temperature, time and flow rates with respect to carbon dioxide production

TABLE 2
Central composite design matrix of wt% CO_2

	Factor 1	Factor 2	Factor 3	Response
Run	T	time	flow rates	CO_2
	^oC	minute	cm^3/m	%
1	350	27.5	700	73.5
2	300	20	1000	83.1
3	350	27.5	700	67.5
4	400	20	1000	67
5	400	20	400	73.5
6	350	27.5	700	73
7	350	27.5	700	69.9
8	300	35	1000	75.9
9	300	35	400	68.7
10	300	20	400	79.5
11	400	35	1000	59
12	400	35	400	52
13	350	27.5	700	70.1
14	350	27.5	195.46	47
15	350	40.11	700	66
16	350	14.89	700	60.2
17	434.09	27.5	700	45
18	350	27.5	1204.54	68
19	350	27.5	700	69
20	265.91	27.5	700	80

residence time, while the remaining char after the reaction was oxidized by switching the inlet from argon to oxygen supply.

RESULTS AND DISCUSSION

Experimental Design and Statistical Analysis

The results from the Design-Expert showed that the maximum CO_2 production was achieved when the temperature was set at 300°C; meanwhile, the retention time was set at 20 minutes for the 1000ml/min argon supplied as shown in Table 2. Moreover, *Fig. 2* shows that the low temperature of the pyrolysis, short retention time and excess argon flow rates had caused the amount of CO_2 production from the Karas woods to increase. This results were also supported by ANOVA, which gave the value $P<0.001$ for the low temperature, and $P< 0.0043$ for shorter residence time, respectively (Table 3). The small P value also indicated that the low temperature of pyrolysis and shorter residence time were the most significant effects of increasing the amount of CO_2 production as compared to the flow rate of argon, with $P<0.02$ (Chiang and Chang, 2006). The ANOVA also showed that the linear model chosen was less than 0.05 or was with 95% confidence, indicating that the model could be considered as statistically significant, and demonstrated that the terms in the model had a significant effect on the response (Chiang and Chang, 2006).

As the temperature increased, there was a decrease in the yield of carbon dioxide due to the decrease in the char yield, when the temperature was higher than 300°C. According to Fang (2006), the amount of char would increase when the temperature was lower. Similarly, Fuwape (1996) and Lua *et al*. (2006) stated that the temperature higher than 300°C would generate char which was less than 50%. During the slow pyrolysis, hydrolysis and dehydration reactions could proceed in an orderly manner to uncover the still macro-molecular cellulose and lignin fragments. Thus, less interaction exists between carbon to carbon bonds in glucosan and aromatic rings, leaving time for the carbon residues to condense into charcoal. According to Qinfeng *et al*. (2005), the cellulose pyrolysis between 300 to 400°C involved a depolymerization of the glycosyl units to levoglucosan, and H_2O, CO, CO_2 and char to decompose. In addition, the secondary reactions involved were oxidization of volatiles and char, respectively, since the slow pyrolysis reactor was purged with oxygen. Moreover, Robert and Todd (2001) also reported that the elemental carbon (i.e. char) produced the highest emission of CO_2 as compared to various solid fuels like biomass.

Thermal treatments, both pyrolysis and combustion, are important reactions of depolymerization of volatiles and scission of carbon chain in the wood samples. The large amount of volatiles produced, consisting of H_2O, CO_2, CO, C_2H_6, CH_4 and tar, would be in direct contact with the excess oxygen so that all the volatiles were completely oxidized. The volatiles released from the pyrolyzed matters react with oxygen to produce carbon dioxide. Thus, integrating the pyrolysis-combustion will boost up the yield of carbon dioxide. According to Liang and Kozinski (2000), oxidation of char comes from the following reaction:

$$\text{Char} + O_2 \longrightarrow CO_2 + \text{ash} \quad (1)$$

While the oxidation of volatile matters are from this reaction:

$$CH_mO_n + O_2 \longrightarrow CO_2 + H_2O \quad (2)$$

TABLE 3
Analysis of Variance (ANOVA) table

Source	Mean Square	F-Value	p-value	
Block	135.34			
Model	496.82	15.25	<0.0001	significant
A	902.20	27.70	<0.0001	
B	367.87	11.30	0.0043	
C	220.38	6.77	0.0200	
Residual	32.57			
Lack of fit	41.47	5.12	0.0643	Not significant

Fig. 2 shows that the time extension did not contribute in increasing the CO_2 yield based on the observation made; in this case, the smoke emitted was depleted after 15 minutes and totally ceased after 25 minutes. The smoke produced indicated that the volatiles were released, during the pyrolysis, and combusted after reacting with oxygen, as indicated by Equations 1 and 2. As time increased, other products produced CH_4, H_2 and C_2H_2 and secondary reaction could occur (Wen and Stanley, 1979). Secondary reaction could be very active due to the catalyzation from charcoal and this led to the formation of more highly combustible products. For example, carbon dioxide and water vapor react with carbon to form carbon monoxide, hydrogen and formaldehyde (Fang *et al*., 2006).

A higher concentration of argon was needed to increase the production of CO_2, as shown in *Fig. 2*. A higher concentration was also required to ensure that a complete degradation of woods occurred during the pyrolysis, with the complete cracking and splitting of C-O and C-C for high production of CO_2 and CO (Qinfeng *et al*., 2005). *Fig. 3* illustrates that R^2 was 0.7531, indicating that 75.31% of the variability in the data was explained by this model and the regression line was not at the best fitted line. This effect might be due to the flaming process, which could not give consistent and optimum amount of carbon dioxide. The integrated process, using direct flaming as a tool of heating, led to a homogenous heating to the samples, and thus, caused the fluctuation in reading and produced non-reproducible result. In addition, *Fig. 4* shows that all the points fell in the allowable ranges between –3.50 to 3.50, showing that there were no significant influential factors during the experiments (Bursali *et al*., 2006).

Mathematical model was built through regression, based on the coded experimental plan and the response results (Table 2). The following linear equation explains the experimental data for CO_2 production.

$$\text{(Actual factor)}Y = +134.57 - 0.163T - 0.692t + 0.0133Q \quad (3)$$

$$\text{(Coded factor)}\ Y = +68.02 - 8.13A - 5.19B + 4.02C \quad (4)$$

Where Y is CO_2 production in %, T is temperature in ^oC, t is retention time in minutes and Q is flow rate of argon in ml/min, similarly for the coded factor where A, B and C were for temperature, time and flow rate, respectively. In this study, all the three parameters gave significant effects to the CO_2 yield.

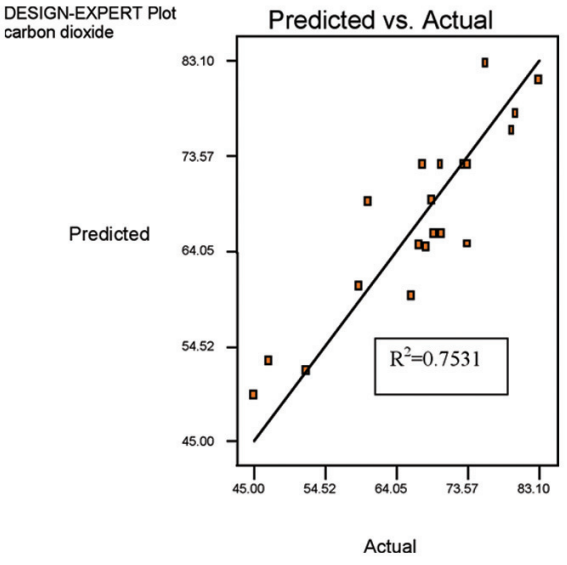

Fig. 3: Regression line of CO_2 production from Karas woods

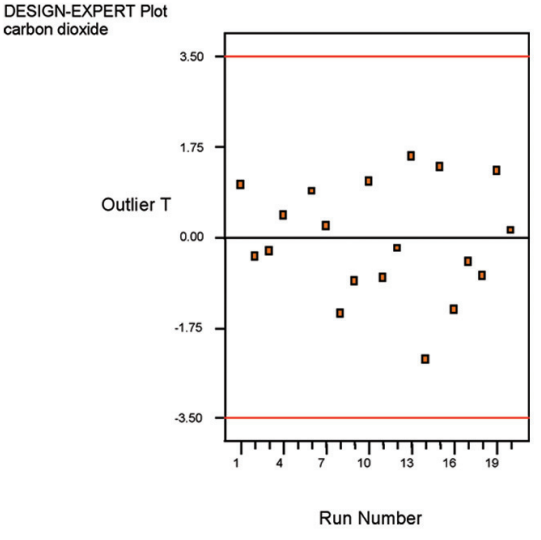

Fig 4: The outlier with respect to the run number of experiments

CONCLUSIONS

The objective of this study was to investigate the influence of temperature, residence time of pyrolysis and the concentration of argon on the production of carbon dioxide during direct pyrolysis-combustion process. The result from the Design-Expert showed that the maximum CO_2 production was achieved when the temperature was set at 300°C, and the retention time was at 20 minutes for 1000ml/min argon supplied. These show that the low temperature of pyrolysis, short retention time and excess argon flow rates will increase the amount of CO_2 production from the Karas woods.

The results were also supported by ANOVA using the central composite design by giving the value P<0.001 for the low temperature, and P< 0.0043 for shorter residence time, respectively. The small P value also indicated that the low temperature of pyrolysis and shorter residence time were the most significant effects which increased the amount of CO_2 production as compared to the flow rate of argon, in which P<0.02. The study also showed that the low temperature of pyrolysis at 300°C would increase the amount of char production, whereas the oxidization of the char during combustion would add up to another increment of CO_2.

ACKNOWLEDGEMENT

The work described above was fully supported by Nuclear Malaysia Agency through the grant Project No: NM-RND-07-07 from the Ministry of Science, Technology and Innovation Malaysia (MOSTI).

REFERENCES

Browne, F.L. (1958). *Theories on the combustion of wood and its control*. US forest Prod. Lab Report. 2136.

Bursali, N., Ertunc, S. and Akay, B. (2006). Process improvement approach to the saponification reaction by using statistical experimental design. *Chemical Engineering and Processing, 45*, 980-989.

Chiang, K.T. and Chang, F.P. (2006). Application of response surface methodology in the parametric optimization of a pin-fin type heat sink. *International Communications in Heat and Mass Transfer, 33*, 836-845.

Fang, M.X., Shen, D.K., Li, Y.X., Yu, C.J, Luo, Z.Y. and Cen, K.F. (2006). Kinetic study on pyrolysis and combustion of wood under different oxygen concentrations by using TG-FTIR analysis. *Journal of Analytical and Applied Pyrolysis, 77*, 22-27.

Fuwape, J.A. (1996). Effects of carbonization temperature on charcoal from some tropical trees. *Bioresource Technology, 57,* 91-94.

Gupta, S. and Polach, H. (1985). *Radiocarbon Dating Practices at ANU*. Handbook: Australia Publishing.

Joel, S.L. (ed.). (1994). *Biomass Burning and the Production of Greenhouse Gases*. New York: John Wiley and Sons.

Liang, X.H. and Kozinski, J.A. (2000). Numerical modelling of combustion and pyrolysis of cellulosic biomass in thermogravimetric systems. *Fuel, 79,* 1477- 1486.

Lua, A.C., Fong, Y.L. and Jia, G. (2006). Influence of pyrolysis conditions on pore development of oil-palm-shell activated carbons. *Journal of Analytical and Applied Pyrolysis,76,* 96-102.

Qinfeng, L., Chunxiang, L., Yonggang, Y., Fu, H. and Licheng, L. (2005). Study on the pyrolysis of wood-derived rayon fiber by thermogravimetry-mass spectrometry. *Journal of Molecular Structure, 733,* 193-302.

Robert, H. and Todd, L. (2001). Minimizing net carbon dioxide emissions by oxidative co-pyrolysis of coal/ blends. Technical report for research project (10/2000-3/2001).

Wen, C.Y. and Stanley, L.E. (1979). *Coal Conversion Technology, Advanced Book Program Reading*. Massachusetts: Addison-Wesley Publishing Company.

ISSN: 0128-7680
Pertanika J. Sci. & Technol. **17 (2)**: 363 – 370 (2009)

A Thermodynamic Equilibrium Analysis on Oxidation of Methane to Higher Hydrocarbons

Nor Aishah Saidina Amin* **and Soon Ee Peng**
Chemical Reaction Engineering Group, Faculty of Chemical and Natural Resources Engineering, Universiti Teknologi Malaysia, 81310 UTM Skudai, Johor, Malaysia
**E-mail: noraishah@fkkksa.utm.my*

ABSTRACT

Thermodynamic chemical equilibrium analysis using, total Gibbs energy minimization method, was carried out for methane oxidation to higher hydrocarbons. For a large methane conversion and a high selectivity to higher hydrocarbons, the system temperature and oxygen concentration played a vital role, whereas, the system pressure only slightly influenced the two variables. Numerical results showed that the conversion of methane increased with the concentration of oxygen and reaction temperature, but it decreased with pressure. Nevertheless, the presence of oxygen suppressed the formation of higher hydrocarbons which mostly consisted of aromatics, but enhanced the formation of hydrogen. As the system pressure increased, the aromatics, olefins and hydrogen yields diminished, but the paraffin yield improved. Carbon monoxide seemed to be the major oxygen-containing equilibrium product from methane oxidation, whilst almost no H_2O, CH_3OH and HCOH were detected although traces amount of carbon dioxide were formed at relatively lower temperature and higher pressure. The total Gibbs energy minimization method is useful to theoretically analyze the feasibility of methane conversion to higher hydrocarbons and syngas at the selected temperature and pressure.

Keywords: Thermodynamic chemical equilibrium, Gibbs energy minimization, methane conversion, higher hydrocarbons

INTRODUCTION

The study on thermodynamic equilibrium composition was used in investigating the feasibility of many types of reaction such as simultaneous partial oxidation and steam reforming of natural gas (Chan and Wang, 2000; Lutz *et al*., 2003; Lutz *et al*., 2004; Zhu *et al*., 2000). Meanwhile, the minimization of Gibbs free energy using Lagrange's multiplier was applied by Lwin *et al*. (2000), Douvartzides *et al*. (2003), Chan and Wang (2000;2004), and Liu *et al*. (2003) for solving thermodynamic equilibrium analysis of autothermal methanol reformer, solid oxide fuel cells, natural-gas fuel processing for fuel cell applications, and catalytic combustion of methane, respectively.

Following the oil crisis in the 1970s, there seems to be many efforts focusing on synfuel production (Hutching and Scurrel, 1998). Hence, the development of a simple and commercially advantageous process for converting methane, the major constituent of natural gas, to more valuable and easily transportable chemicals and fuel becomes a great challenge to the science of catalysis. However, methane is the most stable and symmetric organic molecule consisting of four C-H covalence bonds with bond energy of 440 kJ/mol (Banares, 1999). Thus, effective methods to activate methane are desired.

Received: 5 March 2008
Accepted: 18 August 2008
*Corresponding Author

Thermodynamic constraints on the reactions in which all four C–H bonds of CH_4 are totally destroyed, such as CH_4 reforming into synthesis gas, are much easier to overcome than the reactions in which only one or two of the C–H bonds are broken under either oxidative or non-oxidative conditions. For this reason, only indirect conversions of CH_4 via synthesis gas into higher hydrocarbons or chemicals are currently available for commercialization [Xu *et al*., 2003]. Nonetheless, heat management issues are common to CH_4 reforming. With steam reformation, large quantities of heat must be supplied, whereas, with catalytic partial oxidation, a large amount of heat is released at the front end of the catalyst bed as CH_4 undergoes total oxidation ($CH_4 + 2O_2 \rightarrow CO_2 + 2H_2O$) (Lunsford, 2000).

As an alternative approach, the transformation of methane to aromatics has also attracted great interests from many researchers (Shepeley and Ione, 1983; Anderson and Tsai, 1985; Han *et al*., 1994). They reported that only the trace amount of aromatics could be detected if CH_4 reacted with O_2 or NO over HZSM-5 zeolite, and the main products would be CO_x and H_2O. In an attempt to avoid the use of oxygen, several researches tried to transform methane into higher hydrocarbon in the absence of oxygen. Mo supported on HZSM-5 zeolite which has been reported as the most active catalyst for non-oxidative aromatization of methane (Xu *et al*., 2003; Xu and Lin, 1999; Li *et al*., 1999), but its activity and stability are still inadequate for the aromatization process to be commercialized. Previous work have also shown that the conversion of methane to liquid fuels is promising using metal modified ZSM-5 (or with MFI structure) zeolite as catalysts (Amin and Anggoro, 2002; 2003).

The main objective of this paper was to perform a thermodynamic chemical equilibrium analysis of possible equilibrium products formed in a methane reaction under oxidative and non-oxidative conditions. In this analysis, the effect of various conditions, such as temperature, CH_4/O_2 feed ratio and system pressure, on the chemical equilibrium are discussed. The thermodynamics analysis is important to study the feasibility of reactions in a reacting system, and also to determine the reaction conditions and a range of possible products that which be formed.

METHODOLOGY

The total Gibbs energy of a single-phase system with specified temperature T and pressure P, ($G^t_{T,P}$ is a function of the composition of all gases in the system and can be represented as,

$$(G^t)_{T,P} = g(n_1, n_2, n_3, \ldots n_N) \quad (1)$$

At equilibrium condition, the total Gibbs energy of the system has its minimum value. The set of n_i's, which minimizes $(G^t)_{T,P}$, is found using the standard procedure of the calculation for gas-phase reactions and is subject to the constraints of the material balances. The procedure, based on the method by Lagrange's undetermined multipliers, is described in detail by Smith *et al*. (1996).

In this paper, the gas equilibrium compositions of a system, containing CH_4, C_2H_6, C_2H_4, C_3H_8, C_3H_6, C_4H_{10}, C_4H_8, C_5H_{12}, C_5H_{10}, C_6H_6, C_7H_8, C_8H_{10}, CO, CO_2, H_2, H_2O, CH_3OH and HCOH species at 900-1100K, various oxygen/methane mole ratio and 1-10 bar were calculated. These products were chosen as they were likely to be produced from the reaction between CH_4 and O_2. The oxygen/methane mole ratio was set to be 0.04, 0.05, 0.1 and 0.2. Meanwhile, the condition without oxygen was also simulated. In the preliminary calculations, the compositions of O_2 and C_{6+} aliphatic hydrocarbons are always less than 1E-10 mol%, and for that reason, the subsequent calculations only involved the C_1-C_5 aliphatic hydrocarbons.

TABLE 1
The effect of oxygen/methane mole ratio on the methane equilibrium conversions, at 900K – 1100K and 1 bar

Temperature (K)	CH_4 Conversion (%)				
	0.00*	0.04*	0.05*	0.10*	0.20*
900	6.64	8.21	10.02	19.08	33.74
1000	14.07	13.65	13.82	20.22	39.41
1100	25.07	25.29	25.28	26.29	40.24

* : O_2/CH_4 ratio

TABLE 2
The effect of system pressure on methane equilibrium conversions at 900K - 1100K and oxygen/methane mole ratio = 0.1

Temperature (K)	CH_4 Conversion (%)				
	1 bar	2 bar	3 bar	5 bar	10 bar
900	19.08	17.61	16.35	14.54	12.41
1000	20.22	19.86	19.72	19.04	17.40
1100	26.29	22.07	20.83	20.23	19.89

RESULTS AND DISCUSSION

Methane Conversion

Based on the carbon number basis, the methane conversion and the equilibrium compositions (Tables 1 and 2) increase with system temperature at all conditions. The results are in agreement with the equilibrium conversion of methane by Zhang *et al.* (1998) based on reaction (2):

$$6CH_4 \rightarrow C_6H_6 + 9H_2 \quad (2)$$

The equilibrium methane conversions, at temperatures 973K, 1023K, 1073K, 1123K and 1173K, were reported as 11.3%, 16%, 21%, 27% and 33% respectively, but lower than the results calculated in this work for the non-oxidative conditions since they considered only benzene as the hydrocarbon product.

The effect of oxygen/methane ratio on methane conversion is tabulated in Table 1. The conversion of methane is enhanced by increasing the oxygen/methane ratio as methane can easily be oxidized into carbon oxides in the presence of oxygen. Nevertheless, the methane conversion decreases as the system pressure increases. By examining the calculated equilibrium compositions, it is apparent that the conversion of methane involves the following reactions:

Partial oxidation: $CH_4 + \frac{1}{2}O_2 \rightarrow CO + 2H_2$ (υ=1½) (3)
Total oxidation: $CH_4 + 20_2 \rightarrow CO_2 + 2H_2O$ (υ=0) (4)
To aromatic: $xCH_4 \leftrightarrow C_x H_{(2x-6)} + (x+3) H_2$, $x \geq 6$ (υ=4) (5)
To paraffins: $xCH_4 \leftrightarrow C_x H_{(2x+2)} + (x-1) H_2$, x=2 ($\upsilon$=0) (6)

TABLE 3
Distribution of product concentration > 0.01 mole% as a function of system temperature and oxygen/methane mole ratio

Temperature	O_2/CH_4	Concentration > 0.01 mole%						
900K	0	-	-	H_2	-	C_2H_4	C_2H_6	Aromatics
	0.04	CO	CO_2	H_2	H_2O	-	C_2H_6	-
	0.05	CO	CO_2	H_2	H_2O	-	C_2H_6	-
	0.1	CO	CO_2	H_2	H_2O	-	-	-
	0.2	CO	CO_2	H_2	H_2O	-	-	-
1000K	0	-	-	H_2	-	C_2H_4	C_2H_6	Aromatics
	0.04	CO	-	H_2	-	C_2H_4	C_2H_6	Aromatics
	0.05	CO	-	H_2	-	C_2H_4	C_2H_6	Aromatics
	0.1	CO	CO_2	H_2	H_2O	C_2H_4	C_2H_6	-
	0.2	CO	CO_2	H_2	H_2O	-	-	-
1100K	0	-	-	H_2	-	C_2H_4	C_2H_6	Aromatics
	0.04	CO	-	H_2	-	C_2H_4	C_2H_6	Aromatics
	0.05	CO	-	H_2	-	C_2H_4	C_2H_6	Aromatics
	0.1	CO	-	H_2	-	C_2H_4	C_2H_6	Aromatics
	0.2	CO	CO_2	H_2	H_2O	C_2H_4	-	-

To olefins: $xCH_4 \leftrightarrow C_x H_{2x} + xH_2$, x=2 ($\upsilon$=1) (7)

Except for Equations (4) and (6), Equations (3), (5) and (7) have positive υ value. The increase in the system pressure shifts the reaction with the positive υ to the left (Smith *et al.*, 1996), resulting in the decrease of methane equilibrium conversion which is consistent with other some results reported in the literature (Liu *et al.*, 2003; Istadi and Amin, 2005).

Aromatics, Paraffin and Olefin Yields

Table 3 shows the distribution of products with concentrations > 0.01mol%, as a function of the system temperature and oxygen/methane mole ratio. It is interesting to note that no aromatics were formed when the levels of CO_2 and H_2O yields became noticeable. This observation is consistent with the report in the literature on methane oxidation over Mo/HZSM-5 (Tan *et al.*, 2002; Yuan *et al.*, 1999) and $La_2O_3 + Mo_3$/HZSM-5 (Liu *et al.*, 1998) catalysts. The existence of CO_2 and H_2O not only suppressed the active carbon surface species on the catalysts, but the aromatics were converted into CO and H_2, via steam and carbon dioxide reforming, as shown in the following equations:

$$C_xH_{(2x-6)} + xH_2O \rightarrow xCO + (2x-3)H_2 \quad (8)$$

$$C_xH_{(2x-6)} + xCO_2 \rightarrow 2xCO + (x-3)H_2 \quad (9)$$

The results in Table 3 clearly reveal that reactions (8) and (9) are thermodynamically favourable at the given conditions and are only curtailed when the concentrations of CO_2 and H_2O are low.

The effects of the system pressure on the equilibrium aromatics (Table 4) show that the aromatic yield decreases with the increase in the system pressure. Based on Equation (5), the increment of the system pressure shifts the reaction to the left, and suppresses the formation of aromatics due to the positive υ in the stoichiometric reaction.

TABLE 4
The effect of system pressure on aromatic equilibrium yield at equilibrium at 900K - 1100K and oxygen/methane mole ratio = 0.1

Temperature (K)	Aromatics yield				
	1 bar	2 bar	3 bar	5 bar	10 bar
900	≈0	≈0	≈0	≈0	≈0
1000	0.0643	0.00456	0.00104	≈0	≈0
1100	5.61	1.55	0.478	0.0776	0.00604

TABLE 5
The effect of system pressure on (a) paraffin and (b) olefin equilibrium yields, at equilibrium at 900K - 1100K and oxygen/methane mole ratio = 0.1

(a)

Temperature (K)	Paraffin yield				
	1 bar	2 bar	3 bar	5 bar	10 bar
900	0.0245	0.0283	0.0322	0.0392	0.0531
1000	0.0615	0.0627	0.064	0.0677	0.0792
1100	0.100	0.129	0.139	0.143	0.148

(b)

Temperature (K)	Olefin yield				
	1 bar	2 bar	3 bar	5 bar	10 bar
900	0.00516	0.00325	0.00267	0.0022	0.00187
1000	0.0785	0.0405	0.0279	0.0183	0.0118
1100	0.513	0.381	0.284	0.175	0.00929

The equilibrium yields of paraffin and olefin are also affected by the system pressure. The paraffin yield increases with pressure, but the olefin yield decreases as the system pressure increases, as shown in Table 5. The results may be attributed to the positive υ, as shown in Eqn (7). Similar trends have also been observed in the literature (Istadi and Amin, 2005).

Table 6 shows the dependency of hydrogen equilibrium yield, based on hydrogen number basis, on the system pressure. The yield decreases with the system pressure. Meanwhile, the reacted oxygen is converted to mostly CO with trace amounts of CO_2. Yields of CH_3OH and HCOH can be neglected for the fact that the yields are below 3.0×10^{-5} % at the given conditions.

Figs. 1 and *2* illustrate the effect of oxygen/methane ratio at T, P constant and the effect of system pressure on carbon oxide (CO_x) yield at fixed T and oxygen/methane ratio, respectively. Overall, the total CO_x yield increases with the increasing oxygen content in the system, as oxygen conversion is 100% in all cases. As shown in *Fig. 2*, at methane to oxygen ratio equal to 0.2,

TABLE 6
The effect of system pressure on hydrogen equilibrium yields at equilibrium at 900K - 1100K and oxygen/methane mole ratio = 0.1

Temperature (K)	Hydrogen yield				
	1 bar	2 bar	3 bar	5 bar	10 bar
900	18.78	16.88	15.31	13.10	10.22
1000	20.02	19.75	19.48	18.69	16.64
1100	24.47	21.39	20.50	20.08	19.57

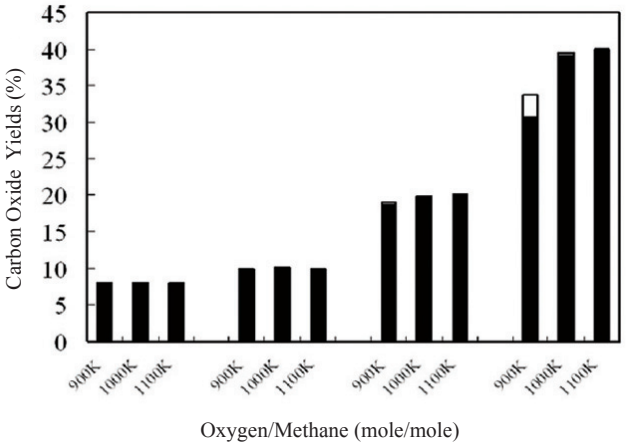

Fig. 1: The effect of oxygen/methane mole ratio at initial unreacted state and system temperature on carbon monoxide. (■) and carbon dioxide (□) yields

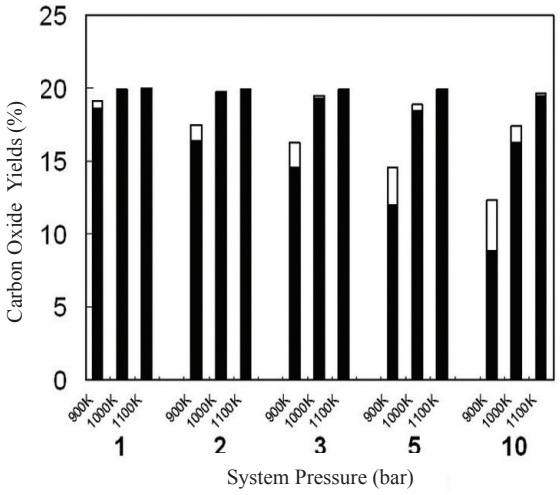

Fig. 2: The effect of system pressure and system temperature on carbon monoxide (■) and carbon dioxide (□) yields. Oygen/methane mole ratio =0.2

some of the oxygen is converted to CO_2 at 900K and this causes a slight reduction in the total CO_x equilibrium yield. The CO_x yield does not seem to be greatly affected by the reaction temperature, except for the conditions where the oxygen concentration and the pressure are high. When the system pressure increases, lowering the system temperature will increase the CO_2 yield, but the CO and overall CO_x yields are reduced.

CONCLUSIONS

The effects of system pressure, temperature and oxygen/methane mole ratio on the methane conversion and product distribution at equilibrium have been studied. The formation of CH_3OH, HCOH, CO_2, H_2O, paraffins and olefins are unfavourable at the selected temperature, pressure and oxygen/methane mole ratio. Meanwhile, CO, H_2 and aromatics are the major equilibrium products. In order to achieve high methane conversion and high aromatics yield, the system temperature should be kept as high as possible, while the system pressure and oxygen/methane mole ratio should be kept low. The production of aromatics and syngas is theoretically feasible at the selected temperature, pressure, and oxygen/methane ratio.

ACKNOWLEDGEMENTS

The work described above was fully supported by a grant (Project number: 09-02-06-0057 SR0005/09-07) from the Ministry of Science, Technology and Innovation (MOSTI) Malaysia. E.P. Soon is also grateful to MOSTI for providing the scholarship under the National Science Fellowship (NSF).

NOTATION

Greek symbols

λ_k Lagrange multiplier of element k.

υ the total stoichiometric number.

Φ_i fugacity coefficient of species i in solution. The Φ_i are all unity if the assumption of ideal gases is justified in all cases.

REFERENCES

Amin, N.A.S. and Anggoro, D.D. (2003). Characterization and activity of Cr, Cu and Ga modified ZSM-5 for direct conversion of methane to liquid hydrocarbons. *Journal of Natural Gas Chemistry, 12,* 123-134.

Amin, N.A.S. and Anggoro, D.D. (2004). Optimization of direct conversion of methane to liquid fuels over Cu loaded W/ZSM-5 catalyst. *Fuel, 83,* 487-494.

Anderson, J.R. and Tsai, P. (1985). Oxidation of methane over H-ZSM5 and other catalysts. *Applied Catalysis A, 19,* 141-152.

Banares, M.A. (1999). Supported metal oxide and other catalysts for ethane conversion: A review. *Catalysis Today, 51,* 319-348.

Chan, S.H. and Wang, H.M. (2000). Themodynamic analysis of natural-gas fuel processing for fuel cell application. *International Journal of Hydrogen Energy,* 25, 441-449.

Chan, S.H. and Wang, H.M. (2004). Thermodynamic and kinetic modelling of an autothermal methanol reformer. *Journal of Power Sources,* 126, 8-15.

Douvartzides, S.L., Coutelieris, F.A. and Demin A.K. et al. (2003). Fuel options for solid oxide fuel cells: A thermodynamic analysis. *AIChE Journal, 49,* 248-257.

Han, S., Martenak, D.J., Palermo, R.E., Pearson, J.A. and D.E. Walsh. (1994). Direct partial oxidation of methane over ZSM-5 catalyst: Metals effects on higher hydrocarbon formation. *Journal of Catalysis, 148,* 134-137.

Hutching, J. and Scurrell, M.S. (1998). *Methane Conversion by Oxidative Processes*. New York: Van Nostrand Reinhold.

Istadi and Amin, N.A.S. (2005). Co-generation of C2 hydrocarbons and synthesis gases from methane and carbon dioxide: A thermodynamic analysis. *Journal of Natural Gas Chemistry, 14,* 140-150.

Li, S., Zhang, C., Kan, Q., Wang, D., Wu, T. and Lin, L. (1999). The function of Cu(II) ions in the Mo/Cu-HZSM-5 catalyst for methane conversion under non-oxidative condition. *Applied Catalysis A, 187,* 199-206.

Liu, W., Ch, Xu Y.P. and Tian, Z.J. et al. (2003). A thermodynamic analysis on the catalytic combustion of methane. *Journal of Natural Gas Chemistry,* 12, 237.

Liu, Y., Lin, J. and Tan, K.L. (1998). Conversion of methane to styrene over the mixed catalyst La2O3 + Mo3/HZSM-5. *Catalysis Letters, 50,* 165-168.

Lunsford, J.H. (2000). Catalytic conversion of methane to more useful chemicals and fuels. *Catalysis Today, 63,* 165-174.

Lutz, A.E., Bradshaw, R.W. and Bromberg, L. et al. (2004). Thermodynamic analysis of hydrogen production by partial oxidation reforming. *International Journal of Hydrogen Energy, 29,* 809-816.

Lutz, A.E., Bradshaw, R.W. and Keller, J.O. (2003). Thermodynamic analysis of hydrogen production by steam reforming. *International Journal of Hydrogen Energy, 28,* 159-167.

Lwin, Y., Daud, W.R., Mohamad, A.B. and Yaakob, Z. (2000). Hydrogen production from steam-methanol reforming: Thermodynamic analysis. *International Journal of Hydrogen Energy, 25,* 47-53.

Shepelev, S.S. and Ione, K.G. (1983). Preparation of aromatic hydrocarbons from methane in the presence of O2. *Reaction Kinetics Catalysis Letters, 23,* 323-325.

Smith, J.M., Ness, H.C.V. and Abbott, M.M. (1996). *Introduction to Chemical Engineering Thermodynamics* (5th Edition). New York: The McGraw-Hill Companies.

Tan, P.L., Leung, Y.L. and Au, C.T. (2002). Methane aromatization over 2wt% Mo/HZSM-5 in the presence of O2 and NO. *Catalysis Letters, 78,* 251-258.

Xu, Y. and Lin, L. (1999). Recent advances in methane dehydro-aromatization over transition metal ion-modified zeolite catalysts under non-oxidative conditions. *Applied Catalysis A, 188,* 53-67.

Xu, Y., Bao, X. and Lin, L. (2003). Direct conversion of methane under nonoxidative conditions. *Journal of Catalysis, 216,* 386-395.

Yuan, S., Li, J., Hao, Z., Feng, Z., Xin, Q., Ying, P. and Li, C. (1999). The effect of oxygen on the aromatization of methane over the Mo/HZSM-5 catalyst. *Catalysis Letters, 63,* 73-77.

Zhang, H., Zeng, J., Xiong, Z., Lin, G. and Tsai, K.R. (1998). Nonoxidative dehydrogenation and aromatization of methane over Mo-based catalysts supported on different types of zeolytes. *Journal of Catalysis Letters, 53,* 119-124.

Zhu, J., Zhang, D. and King, K.D. (2000). Reforming of CH4 by partial oxidation: Thermodynamic and kinetic analysis. *Fuel, 80,* 899-905.

ISSN: 0128-7680
Pertanika J. Sci. & Technol. **17 (2)**: 371 – 380 (2009)

Adsorption of Phenol Using Activated Carbon Adsorbent from Waste Tyres

Nurulhuda Amri, Ridzuan Zakaria* and Mohamad Zailani Abu Bakar
School of Chemical Engineering, Engineering Campus,
Universiti Sains Malaysia, 14300 USM, Nibong Tebal, Penang, Malaysia
**E-mail: chduan@eng.usm.my*

ABSTRACT

The adsorption of phenol, from aqueous solutions on activated carbon from waste tyres, was studied in a batch system at different initial concentrations (100-500mg/L) at 30°C for 48 hours. The activated carbon was prepared using the two-step physiochemical activation, with potassium hydroxide (KOH) at ratio KOH/char = 5. The carbonization process was done at 800°C for 1 hour with nitrogen flow rate 150ml/min, followed by the activation with the carbon dioxide flow rate 150ml/min at 800°C for 2 hours. The adsorption isotherms were determined by shaking 0.1g of activated carbon with 100ml phenol solutions. The initial and final concentrations of phenol in aqueous solution were analyzed using the UV-Visible Spectrophotometer (Shimadzu, UV-1601) at a wavelength of 270nm. Experimental isotherm data were analyzed using the Langmuir and Freundlich isotherm models. The equilibrium data for phenol adsorption could fit both isotherm models well with the R^2 value of 0.9774 and 0.9895, respectively. The maximum adsorption capacity of the adsorbent obtained from the Langmuir model was up to 156.25 mg/g.

Keywords: Adsorption, phenol, activated carbon, adsorption capacity

ABBREVIATIONS

C_o = initial adsorbate concentration, mg/L
C_e = equilibrium adsorbate concentration, mg/L
C_t = adsorbate concentration at time, mg/L
K_f = empirical constants depending on several environmental factors, $(mg/g)(L/mg)^{1/n}$
K_L = Langmuir constant related with affinity of the points of union (L/mg)
n = empirical parameter representing the energetic heterogeneity of the adsorption sites
Q^o = maximum adsorption capacity corresponding to complete monolayer coverage (mg/g)
q_e = adsorption capacity at equilibrium solute concentration, C_e (mg/g)
R^2 = correlation coefficient
V = volume of solution, L
w = weight of adsorbent, g

INTRODUCTION

Phenol and related compounds are toxic to human and aquatic life, creating an oxygen demand in receiving waters. Chronic toxic effects, due to the phenol pollution reported in humans, include vomiting, anorexia, difficulty in swallowing, liver and kidney damage, headache, fainting and other mental disturbances (Fawell, 1988). The demand for the removal of organic compounds including phenol has been increased by the increasing the industrial wastewaters. The Department

Received: 5 March 2008
Accepted: 20 May 2008
*Corresponding Author

of Environment (DOE) of Malaysia has set the maximum concentration of phenol as 0.001mg/L for standard A and 1.0mg/L for standard B in the industrial effluent discharge to Malaysia inland waters (Environment Quality Act, 2001).

These organics compounds are considered as priority pollutants since they are harmful to organisms at low concentrations, and can be toxic when present at elevated levels and are suspected to be carcinogens (Ozkaya, 2006). Therefore, it is necessary to remove phenol from industrial effluents before discharging them into the water stream. The adsorption by activated carbon (AC) is the most frequently used treatment method to separate toxic pollutant from water environment. In waste water treatment, activated carbon is powerful adsorbent because it has a large surface area and pore volume which allows the removal of organic compounds, heavy metal ions and colours (Hsieh and Teng, 2000). Although activated carbon adsorption is considered as the best available technologies for the removal of organic compounds, it is still considered highly expensive based on the market price of the commercial activated carbon available. Therefore, more inexpensive and effective activated carbon adsorbents need to be found for removal of phenol in wastewater treatment so that the strict regulation on the concentration of phenol in wastewater can be implemented.

Recently, there has been an increasingly amount of literature devoted to the study of preparation activated carbon from agricultural and solid wastes for cheaper adsorbent which can be used in removing organic compounds such as phenol (Mukherjee *et al*., 2006; Kennedy *et al*., 2007; Wu *et al*., 2006; Tseng *et al*., 2006; Srivastava *et al*., 2006; Tanthapanichakoon *et al*., 2005; Ariyadejwanich *et al.*, 2003; Miguel *et al*., 2003; Nakagawa *et al*., 2004). In relation to the literature studies, it was proven that activated carbons prepared from waste tires are considered as highly mesoporous among solid wastes, and they have a remarkably high adsorption capacity for large molecules (Tamai *et al*., 1999). In some applications, especially those involving large molecules or macromolecules which cannot easily penetrate into the micropores (<2 nm diameter) and adsorb onto them, the activated carbons should possess not only micropores but also interconnecting mesopores (Hsieh and Teng, 2000; Tamai *et al*., 1999).

The purpose of this work was to determine the adsorption potential prepared activated carbon from waste tires to be used to remove phenol from wastewater. Laboratory batch isotherm studies were conducted to evaluate the adsorption capacity of the activated carbon adsorbent. The effects of contact time and initial phenol concentration were also investigated. Langmuir and Freundlich isotherm models were tested for their applicability with the experimental data.

MATERIALS AND METHODS

Preparation of Activated Carbon Using the Physiochemical Activation Method

The experiments started with the carbonization of waste tires. Approximately 100 gram of waste tires (diameter = 0.425 mm) was put on the tray and placed inside the batch muffle furnace. The temperature was increased from the ambient temperature to 800ºC and kept for 1 hour under nitrogen flow rate. The char product was then cooled down to room temperature and stored in a dessicator.

The experiment was continued with an impregnation procedure. The tyre char was dispersed uniformly in the KOH solutions in a stainless steel beaker with water:KOH:char equal to 5:5:1 by mass, denoted as the KOH/char ratio = 5. The beaker was immersed in a constant temperature shaker bath. The mixing was performed at 30ºC for 3 hr to make sure that potassium hydroxide pellets were completely dissolved. For dehydrating purposes, the beaker was then placed inside an oven at 110ºC for 24 hours for dehydrating purpose.

The chemically treated char was placed inside a batch muffle furnace reactor and heated at 800ºC under the nitrogen flow of 150 ml/min. After the temperature had reached the setting point, the gas flow was switched to carbon dioxide at the flow rate of 150 ml/min for 2 hours. The activated products were then cooled under the nitrogen flow to room temperature. The sample was then poured to a beaker containing 0.1M HCl (250cm^3) and stirred for 1 hour. They were finally washed with hot water until the conductivity of the filtrate became less than 10μs. This was to ensure that all the KOH used for activation had been removed before the carbon was taken for adsorption study. The carbon was dried at 105°C until it was bone dry and stored in a dessicator.

Procedures for the Adsorption Experiments

The activated carbon was characterized for its adsorption capacity using phenol. A phenol solution of 1500mg/m^3 concentration was prepared in an appropriate volumetric flask. The stock solution was diluted to the desired initial concentrations (100-500 mg/L) for batch equilibrium studies. About 0.1g of activated carbon was introduced into a 100ml of 100 to 500mg/L of phenol solution, and kept in a laboratory shaker for 48 hours at 30°C. The samples were withdrawn at appropriate time interval, using a glass syringe to determine the residual concentration of the solutions. For high concentrations, 0.1 cm^3 of the solution was withdrawn and diluted to 50 cm^3 using deionized water before determining the residual concentration using UV-Spectrophotometer at 270nm wavelength for phenol.

The amounts of adsorbates adsorbed at time, q_t and at equilibrium condition, q_e were calculated using Equations (1) and (2) below.

$$q_t = \frac{(C_o - C_t)V}{w} \tag{1}$$

$$q_e = \frac{(C_o - C_e)V}{w} \tag{2}$$

Where C_o and C_e are initial and equilibrium adsorbate concentrations, mg/L. C_t is the adsorbate concentration at time, mg/L. V is volume of solution, L and w is weight of adsorbent, g.

RESULTS AND DISCUSSION

Textural Characterization of the Prepared Activated Carbon

The BET surface area of the prepared activated carbon was found to be 273.26m^2/g, with a total pore volume of 0.585cm^3/g. The average pore diameter was found to be 5.84nm. This indicates that the pores on the prepared activated carbon are in the meso range.

Fig. 1 shows the SEM image of the char and the prepared activated carbon. Metals on the surface of the char could clearly be seen in the SEM images of the char. However, after the activation process, the SEM images showed that the inorganic components on the surface of the prepared activated carbon were partially removed. The pore development was also increased after the activation process, as shown in the SEM images of the prepared activated carbon.

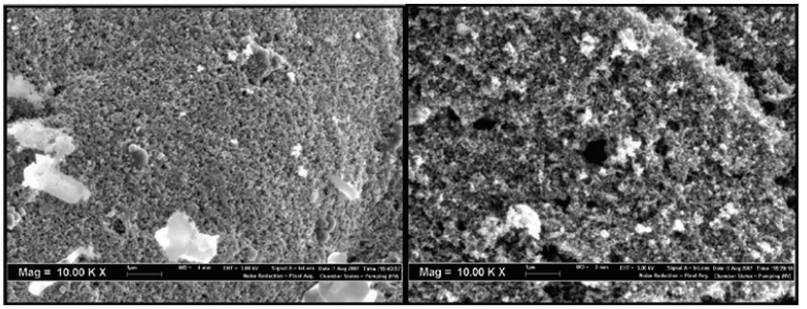

Fig. 1: SEM image of (a) tyre char and (b) activated carbon at 10Kx magnification

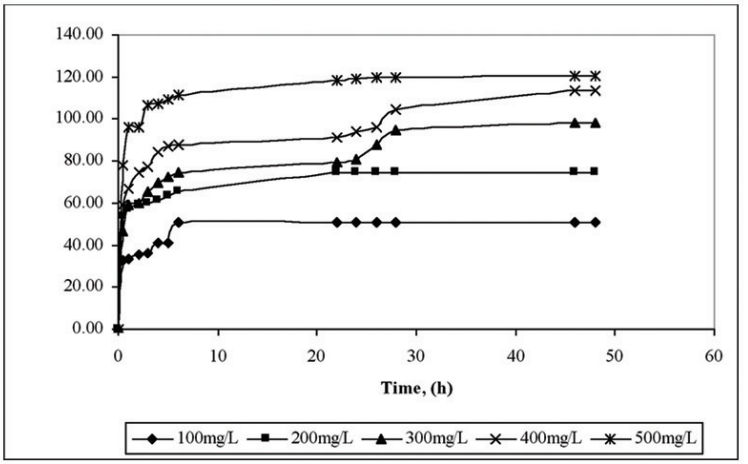

Fig. 2: Effect of initial phenol concentration on the adsorption of phenol onto the prepared activated carbon

Effect of Initial Concentration Phenol

The effect of the initial concentration phenol, on the adsorption capacity, as a function of time, is shown in *Fig. 2*. The amount of phenol adsorbed per unit weight of adsorbent increased with the increase in the phenol concentration. This means, when the initial concentration increased from 100 to 500 mg/L, the adsorption capacity also increased from 50.62 mg/g to 120.80 mg/g. It was because the initial concentration plays an important role which provided the necessary driving force to overcome the resistances to the mass transfer of phenol between the aqueous and the solid phases (Srivastava *et al*., 2006). The interaction between phenol and the prepared activated carbon adsorbent was also found to enhance with the increase in the initial concentration. Thus, it can be concluded that higher initial concentration enhances the adsorption uptake of phenol.

Effect of Contact Time

Aqueous phenol solutions, with different initial concentrations ranging from 100 to 500 mg/L, were kept in contact with the adsorbents for 48 hour. The available adsorption results reveal that the uptake of the adsorbate is fast at the initial stage of the contact period, and it then becomes slower near to the equilibrium. The rate of adsorption is nearly constant between of these two stages

of the uptake (Srivastava *et al*., 2006). It is because the number of adsorption sites available is higher at the initial stage of contact time, and the driving force for the mass transfer is also greater. Therefore, it is much easier for the adsorbate to reach the adsorption site. After a lapse of time, the number of active sites becomes less and the adsorbent becomes crowded inside the particles, and thus impeding the movement of the adsorbate (Kennedy *et al*., 2007). This fact is in agreement with the results presented in *Fig. 2*. The fastest removal was showed at the initial concentration of 100 mg/L, which is within 6 hours to reach equilibrium. For the initial concentrations of 200 and 300 mg/L, the equilibrium was achieved within 22 and 28 hours, respectively. Meanwhile, for high initial concentration of 400 and 500 mg/L, it gradually increased to attain equilibrium at 46 hour.

Adsorption Isotherms

An adsorption isotherm describes the relationship between the amount of adsorbate which is adsorbed on the adsorbent and the concentration of dissolved adsorbate in the liquid at equilibrium (Roostaei and Tezel *et al*., 2004). The equilibrium adsorption isotherm is fundamentally important in the design of adsorption systems. The amount of phenol adsorbed at equilibrium, was plotted against the equilibrium condition, C_e, as shown in *Fig. 3*. The result shows that the value of q_e is increased with the increase in the concentration of phenol.

The adsorption isotherm of phenol onto the prepared activated carbon was fitted by several well-known isotherms models, namely the Langmuir and Freundlich models, to assess their utility. The Langmuir model is obtained under the ideal consumption of a totally homogeneous adsorption surface, whereas the Freundlich model is suitable for a highly heterogeneous surface. In this work, both models were used to describe the relationship between the amount of phenol adsorbed and its equilibrium concentration.

Langmuir Isotherms

The Langmuir adsorption isotherm is often used for adsorption of the solute from a liquid solution. The Langmuir adsorption isotherm is perhaps the best known of all the isotherms describing adsorption, and it is often expressed as:

$$q_e = \frac{Q^o K_L C_e}{\left(1 + K_L C_e\right)} \tag{3}$$

Where:

q_e = Adsorption capacity at equilibrium solute concentration, C_e (mg/g)
C_e = Concentration of adsorbate in solution (mg/L)
Q^o = Maximum adsorption capacity corresponding to complete monolayer coverage (Mg/g)
K_L = Langmuir constant related with affinity of the points of union (L/mg)

The above equation can be rearranged to create the following linear form:

$$\frac{C_e}{q_e} = \frac{1}{Q^o K_L} + \frac{C_e}{Q^o} \tag{4}$$

The linear form can be used for the linearization of experimental data by plotting C_e/q_e against C_e. Meanwhile, the Langmuir constant Q^o and K can be evaluated from the slope and intercept of linear equation, respectively, as shown in *Fig. 4*. The essential characteristics of the Langmuir equation can be expressed in terms of dimensionless separation factor, R_L, defined as:

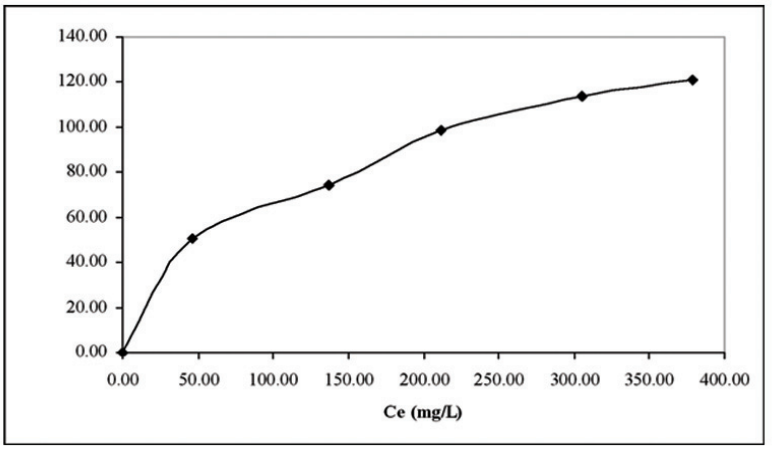

Fig. 3: Equilibrium adsorption isotherm of phenol onto prepared activated carbon at 30ºC

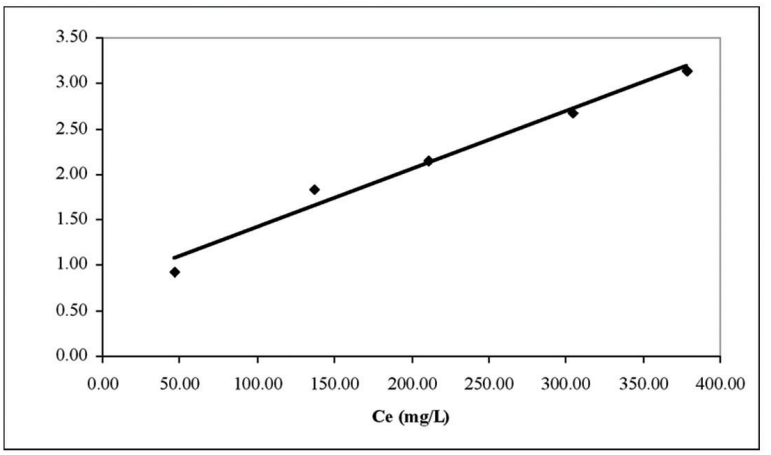

Fig. 4: Langmuir adsorption isotherm of phenol onto activated carbon at 30ºC

$$R_L = \frac{1}{(1 + K_L C_o)} \tag{5}$$

Where C_o is the highest initial solute concentration. The R_L value implies the adsorption to be favourable (R_L >1), linear (R_L =1), favourable (0< R_L <1), or irreversible (R_L =0). The value of R_L was found to be 0.1947 and this confirmed that prepared activated carbon is favourable for the adsorption of phenol under conditions used in the present study (Aktas and Cecen, 2007).

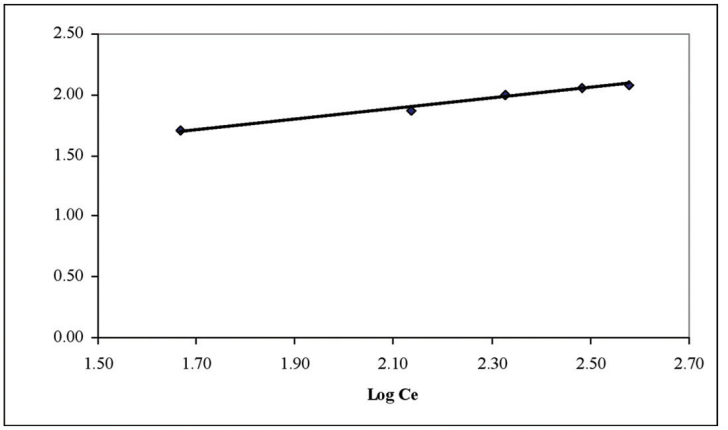

Fig. 5: Freundlich adsorption isotherm of phenol onto activated carbon at 30°C

Freundlich Isotherms

The Freundlich isotherm is the earliest known relationship describing the adsorption equation which is often expressed as:

$$q_e = K_f C_e^{1/n} \tag{6}$$

Where:

q_e = Adsorption capacity at equilibrium solute concentration, C_e (mg/g)
C_e = Concentration of adsorbate in solution (mg/L)
K_f = Empirical constants depending on several environmental factors
n = Empirical parameter representing the energetic heterogeneity of the adsorption sites

The equation is conveniently used in the linear form by taking the logarithmic of both sides as:

$$\log q_e = \log K_f + \frac{1}{n} \log C_e \tag{7}$$

A plot of $(\log q_e)$ against $(\log C_e)$ yields a straight line which indicates the confirmation of the Freundlich isotherm for adsorption. The constant can be obtained from the slope and the intercept of the linear plot of the experimental data, as shown in *Fig. 5*. The value of n indicates favourable adsorption when $1<n<10$. The n value was found to be 2.3348. Therefore, the present adsorption systems appear to be favourable (Ozkaya, 2006).

The Langmuir constants Q^o and K_L and the Freundlich constants K_F and n are given in the Table 1. Both isotherm models were found to fit the adsorption data of the prepared activated carbon with correlation coefficient, R^2 value 0.9774 and 0.9895, respectively. The adsorption capacity of the adsorbent was obtained from the Langmuir model up to 156.250 mg/g. This result shows that the prepared activated carbon in this study has a very high adsorption capacity as compared to the other works listed in Table 2. This is probably be due to the different activation methods used, which eventually resulted in different surface characteristics (Aktas and Cecen, 2007).

TABLE 1
Langmuir and Freundlich isotherm constants for phenol on the prepared activated carbon at 30ºC

Type of adsorbent	Langmuir isotherm model				Freundlich isotherm model		
	Q^o (mg/g)	K_L (1/mg)	Correlation Coefficient, R^2	R_L	K_F (mg/g)(L/mg)$^{1/n}$	n	Correlation Coefficient, R^2
Activated carbon	156.250	0.0083	0.9774	0.1947	2.6717	2.3348	0.9895

TABLE 2
Comparison of the maximum monolayer adsorption capacity of phenol onto activated carbon adsorbents from waste tires

Adsorbent	Maximum adsorption capacity (mg/g)	Method of activation	References
Activated carbon	156.25	Physiochemical activation	Present work
Tyre rubber derived carbon	106.00	Steam activation	(Miguel *et al.,* 2003)
Activated carbon	43.06	Steam activation	(Laszlo *et al.,* 1997)

CONCLUSIONS

The experimental data of the adsorption studies on phenol using prepared activated carbon was described well by both Langmuir and Freundlich isotherm models. This indicates that the adsorption of phenol from aqueous solutions could be either monolayer or multilayer. The adsorption capacity of the adsorbent, obtained from the Langmuir model, was up to 156.25 mg/g. The present study concludes that the production of the activated carbon adsorbents, from waste tire rubber, can provide a two-fold environmental and economic benefit; a recycling path is created for waste vehicles tires and new low-cost adsorbents are produced for commercial use in wastewater treatment.

ACKNOWLEDGEMENTS

The authors acknowledge the Long-term IRPA grant provided by MOSTI for the present work. The authors are also very thankful to the school of Chemical Engineering, Universiti Sains Malaysia for providing the facilities necessitated and constant encouragement.

REFERENCES

Aktas, O. and Cecen, F. (2007). Adsorption, Desorption and bioregeneration in the treatment of 2-chlorophenol with activated carbon. *Journal of Hazardous Materials, 141,* 769 - 777.

Ariyadejwanich, P., Tanthapanichakoon, W., Nakagawa, K., Mukai, S.R. and Tamon, H. (2003). Preparation and characterization of mesoporous activated carbon from waste tires. *Carbon, 40-41,* 157 - 164.

Environmental Quality Act, Sewage and Industrial Effluent in Environment Quality Act and Regulations, Laws of Malaysia (12th Edn.). p. 61. Malaysia: MDC Publisher Printers Sdn. Bhd.

Fawel, J.K. and Hunt, S. (1988). *Environmental Toxicology: Organic Pollutants.* New York: Halstd Press, John Wiley & Sons 398.

Hsieh, C.T. and Teng, H. (2000). Influence of mesopore volume and adsorbate size on adsorption capacities of activated carbons in aqueous solutions. *Carbon, 38,* 863 - 869.

Kennedy, L.J., Vijaya, J.J., Kayalvizhi, K. and Sekaran, G. (2007). Adsorption of phenol from aqueous solutions using mesoporous carbon prepared by two stage process. *Chemical Engineering Journal, 132,* 279 - 287.

Laszlo, K., Bota, A. and Nagy, L.G. (1997). Characterization of activated carbons from waste materials by adsorption from aqueous solutions. *Carbon, 35,* 593 - 598.

Miguel, G.S., Fowler, G.D. and Sollars, C.J. (2003). A study of the characteristics of activated carbons produced by steam and carbon dioxide activation of waste tyre rubber. *Carbon, 41,* 1009 - 1016.

Mukherjee, S., Kumar, S., Misra, A.K. and Fan, M. (2006). Removal of phenols from water environment by activated carbon, bagasse ash and wood charcoal. *Chemical Engineering Journal, 129,* 133 - 142.

Nakagawa, K., Namba, A., Mukai, S.R., Tamon, H., Ariyadejwanich, P. and Tanthapanichakoon, W. (2004). Adsorption of phenol and reactive dye from aqueous solution on activated carbons derived from solid wastes. *Water Research, 38,* 1791 - 1798.

Ozkaya, B. (2006). Adsorption and desorption of phenol on activated carbon and a comparison of isotherm models. *Journal of Hazardous Materials, B129,* 158 - 163.

Roostaei, N. and Tezel, F.H. (2004). Removal of phenol from aqueous solutions by adsorption. *Journal of Environment Management, 70,* 157 - 164.

Srivastava, V.C., Swamy, M.M., Mall, I.D., Prasad, B. and Mishra, I.M. (2006). Adsorptive removal of phenol by bagasse fly ash and activated carbon: Equilibrium, kinetics and thermodynamics. *Colloids and Surfaces, 272,* 89 - 104.

Tamai, H., Yoshida, T., Sasaki, M. and Yasuda, H. (1999). Dye adsorption on mesoporous activated carbon fiber obtained from pitch containing yttrium complex. *Carbon, 37,* 983 - 989.

Tanthapanichakoon, W., Ariyadejwanich, P., Japthong, P., Nakagawa, K., Mukai, S.R. and Tamon, H. (2005). Adsorption-desorption characteristics of phenol and reactive dys from aqueous solution on mesoporous activated carbon prepared from waste tires. *Water Research, 39,* 1347 - 1353.

Tseng, R.L., Tseng, S.K. and Wu, F.C. (2006). Preparation of high surface area carbons from corncob with KOH etching plus CO_2 gasification for the adsorption of dyes and phenols from water. *Colloids and Surfaces, 279,* 69 - 70.

Wu, F.C. and Tseng, R.L. (2006). Preparation of highly porous carbon from fir wood by KOH etching and CO_2 gasification for adsorption of dyes and phenols from water. *Colloids and Interface Science, 294,* 21 - 30.

ISSN: 0128-7680
Pertanika J. Sci. & Technol. **17 (2)**: 381 – 388 (2009)

Biohydrogen Production by Local Isolate of *Clostridium butyricum:* Initial Nutrients Optimization Study

Mohd. Sanusi Che Kadir, Jamaliah Md. Jahim*, Nurina Anuar, Mohd. Sobri Takrif and Zahira Yaakub
Department of Chemical and Process Engineering, Faculty of Engineering, Universiti Kebangsaan Malaysia, 43600 UKM, Bangi, Selangor, Malaysia
**E-mail: jamal@vlsi.eng.ukm.my*

ABSTRACT

In this study, an anaerobic mesophilic bacterial strain, namely *Clostridium butyricum* KBH1, was isolated from a natural source. This strain grew well and produced biogas with an average hydrogen concentration of 60% (v/v) in the Reinforced Clostridial Media (RCM). To study the basic nutrient requirements, three main nutrients namely peptone (Pep), yeast extracts (Yes) and glucose (Glu) were chosen as factors, using an experimental design. The experiments were run according to 2^3 Full Factorial Design, followed by the Response Surface Method (RSM). The fermentation was performed in 30 ml serum bottles with 20 ml working volume in a sterile and anaerobic condition at 37°C with 5% inoculums. The results from the Analysis of Variance (ANOVA) for the factorial design showed that all the three factors had significantly affected the gas production by the *C. butyricum*. The response surface plot of the gas production by *C. butyricum* showed that the gas production could be enhanced by increasing peptone and yeast extract concentrations up to 15 g/l and 24 g/l respectively, without showing any substrate inhibition. Meanwhile, the glucose concentration showed an optimum at the middle point (8 g/l) with possible substrate inhibition at a high concentration (12 g/l). The total biogas production could be correlated to the three factors, using the quadratic equation: Gas = 0.17 + 7.11Glu - 0.02Pep + 0.77Yes - $0.53Glu^2$ + 0.09Glu*Pep. The experimental results showed that the strain could grow well in substrate with high organic nitrogen content such as POME and might be not suitable for substrate with high sugar content due to substrate inhibition.

Keywords: Anaerobic fermentation, biohydrogen, *Clostridium*, optimization

INTRODUCTION

Pollution to the environment due to the use of conventional fuels, in conjunction with concerns on the depletion of oil reserves, necessitate the intensification of research for alternative energy sources. Amongst many alternative energy sources, hydrogen (H_2) offers tremendous potential as a clean, renewable energy. According to Levin *et al*. (2004), hydrogen has the highest gravimetric energy density of any known fuel and is compatible with electrochemical and combustion process for energy conversion without producing carbon-based emissions. Therefore, hydrogen fuel cells are considered as the main technology which makes the utilization of hydrogen energy possible (Lin *et al*., 2007).

Hydrogen may be produced by various processes such as electrolysis of water, thermo catalytic reformation of hydrogen rich compounds, and biological processes. Biological production of hydrogen (biohydrogen) using micro-organisms is an exciting new area which offers tremendous potential in using various renewable raw materials (Levin *et al*., 2005). Two main methods for biohydrogen production are possible via photo and dark fermentation. On the contrary to photolytic

Received: 28 February 2008
Accepted: 3 June 2008
*Corresponding Author

production, dark fermentation has the advantages for high hydrogen production rate, without the need for illumination and capability to utilize organic wastes. Many types of bacteria which have been reported as capable of generating hydrogen in dark fermentation such as the species of *Enterobacter* (Shin *et al*., 2007), as well as *Bacillus* and *Clostridium* (Chen *et al*., 2005).

Several studies on biohydrogen production reported that the hydrogen gas yields are determined by its fermentation pathway and the end-products such as acetic acid and butyric acid. Chen *et al*. (2006) indicated that process operating conditions such as pH, nutrient levels, mixing, levels of carbon dioxide, shock loads, metabolites in liquid phase and gas partial pressure could also affect metabolic balance and alter the hydrogen production.

The Response Surface Methodology (RSM) is widely used to study individual and interactive effects of various factors affecting the final results in any experiment. For instance, Wang *et al*. (2005) used the RSM to study the effect of pH, temperature and substrate concentration on the production of biohydrogen by mixed culture using sucrose as the main carbon source. They reported that all the factors gave a significant influence on biohydrogen production.

The commercial Reinforced Clostridial Medium (RCM) is widely used for isolation and cultivation of Clostridial strains. The RCM contains only 5 g/l glucose while the main nutrients composition are peptone (10 g/l), meat extract (10 g/l) and yeast extract (3 g/l). In this study, three main nutrients, namely Glucose, Peptone and Yeast Extract, were chosen as parameters. Peptone is rich in organic nitrogen content, while yeast extract mainly provides vitamins and amino acids necessary for growth.

The aim of the present study was to isolate, characterize and identify dark fermentative bacteria from the local sources. An initial study on the effect of nutrients concentration was done using the Response Surface Methodology (RSM). The results obtained from the RSM could then be used as a guideline to further optimize raw substrate such as Palm Oil Mill Effluent (POME). This may include amending POME with specific organic nutrients for higher biohydrogen production and simultaneous COD reduction.

MATERIALS AND METHODS

Culture of Micro-organism

Hydrogen producing bacteria was isolated from the water samples of Sungai Langat nearby UKM Bangi, in Selangor. The samples were cultured and purified using the Reinforced Clostridial Medium (RCM) (Oxoid, UK). RCM contains: glucose (5 g/l), peptone (10 g/l), yeast extract (3 g/l), meat extract (10 g/l), starch (1 g/l), NaCl (5 g/l), $NaC_2H_3O_2$ (3 g/l), Agar (0.5 g/l) and Cysteine HCl (0.5 g/l).

Samples were heat shocked at 100ºC for 5 minutes, and 2 ml was transferred into 30 ml serum bottles, containing 18 ml of liquid RCM. The bottles were incubated at 37°C overnight. Then, the cultures which produced gases were sub-cultured into another bottle. The cultures were then streaked onto the RCM agar and incubated at 37°C inside an anaerobic jar (HP00011A, Oxoid, UK). A single colony obtained from agar plate was incubated and analyzed for hydrogen production. Hydrogen producing strains were then stored at 4°C as stock cultures. The morphological identification and observations were performed using a light electron microscope (Nikon YS100, Japan). Bacteria sample were sent to Vivantis Technologies Sdn. Bhd. (Shah Alam, Selangor) for identification using the 16S/18S rRNA sequencing method.

Analytical Methods

Cell density was analyzed by measuring the optical density (OD) of the cell suspension, at a wavelength of 600 nm, using a spectrophotometer (Thermo spectronic, Model Genesys 10_{UV}).

Hydrogen and carbon dioxide were measured by gas chromatography (GC-8A, Shimadzu, Japan) with thermal conductivity detectors; TCD equipped with a stainless steel column packed with Porapak Q. Nitrogen was used as a carrier gas at a flow rate of 30 ml/min. The temperatures of the injection port, oven and detector were 100, 50 and 100ºC, respectively.

Nutrients Optimization

Glucose (Sigma-Aldrich, USA), Peptone (Bacto Peptone, Difco, UK) and Yeast Extract (Bacto Yeast Extract, Difco, UK) were chosen as factors in this study. The experiment was performed in 30 ml serum bottles containing 18 ml medium, with 2 ml inoculums. The amount of glucose, peptone and yeast extracts were varied, while the other ingredients such as NaCl (5 g/l) and $NaC_2H_3O_2$ (3 g/l) were kept constant. The concentration of glucose ranged from 4 to 12 g/l, Peptone from 12 to 24 g/l and yeast extract 5-15 g/l. The evolved gas was collected every 3 hour using a syringe.

A factorial central composite design was used to study the effect of nutrients concentration on gas production. Design expert software version 6.0 (Stat-Ease. Inc., MN, USA) was used for regression and graphical analyses of the experimental data. The optimum levels of the selected variables were obtained by solving the regression equation and analyzing the response surface contour and surface plots. The quality of the fit of quadratic model was expressed by the coefficient of determination R^2, and its statistical significance was checked using the F-test in the same program.

RESULTS AND DISCUSSION

Microbe and Growth Profile

A hydrogen producing bacteria was isolated from a small river stream of Sungai Langat, located near UKM, Bangi. It was observed as a spore former, rod shape, and gram positive bacteria. The result obtained from 16S rRNA sequencing confirmed that the bacteria were closely related to *Clostridium butyricum* species with 99% similarity.

Fig. 1 shows the typical time course profile of pH, growth and gas production of *C. butyricum*. The time course profile is similar as reported by other researchers such as Chen *et al*. (2005) and Pan *et al*. (2007). The differences in terms of yields are due to the different media used and operating condition. The biomass growth, during the exponential phase, was accompanied by pH drop, due to the accumulation of acetic and butyric acid liquid product. The composition of hydrogen, from the GC analysis in a cumulative form, was in the average of 60% v/v and the remaining was CO_2.

Effect of Nutrients Concentration

The present study aimed to see the effects of nutrient concentration on the growth of *C. butyricum* and biohydrogen production. The *Clostridium* species have two different metabolic pathways for the production of H_2 from carbohydrates fermentation; these are acidogenesis which produces mainly organic acids like acetate and butyrate, and solventogenesis which generates solvents such as acetone, and ethanol. Thus, when environmental conditions are favourable, *Clostridium* is able to modify their metabolism to any of these pathways. A pH decrease could therefore be used to induce the shift to solventogenesis along with H_2 production decline. Cheng *et al*. (2002) studied the use of peptone and found that it avoided the abrupt pH drops in the system and allowed for further exploration of organic acids and pH effects on H_2 production.

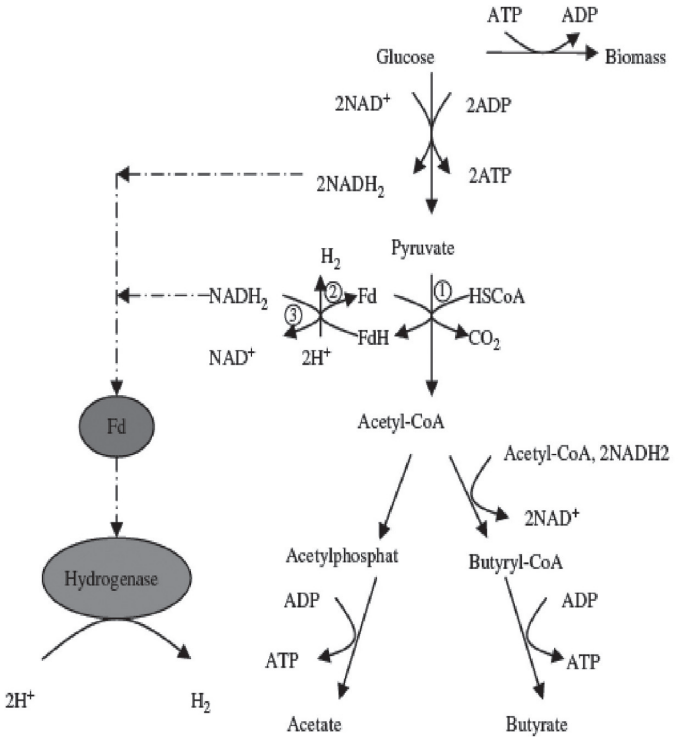

Fig. 1: Metabolic pathway of glucose by Clostridium butyricum *under anaerobic conditions. 1 Pyruvate: ferredoxin oxidoreductase (PFOR); 2 Hydrogenase; 3 NADH: ferredoxin oxidoreductase (Chen* et al., *2006)*

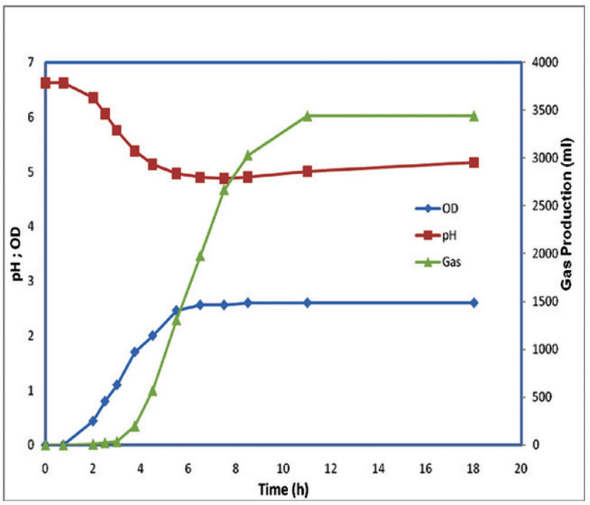

Fig. 2: Typical time course profile for pH, OD and gas production of C. butyricum *growth on RCM with 1.5L working volume*

TABLE 1
Result for the 2^3 full factorial experiments

Run	Factor 1 A: Glucose, g/L	Factor 2 B: Peptone, g/L	Factor 3 C: Yeast, g/L	Response 1 R1 Gas (ml)
1	4	15	5	*31*
2	4	15	15	*35*
3	4	25	5	33
4	4	25	15	*37*
5	12	15	5	*33*
6	12	15	15	*45*
7	12	25	5	*44*
8	12	25	15	*53*

TABLE 2
Effect list and model selection

	Term	Effect	% Contribution
Model	A	9.75	46.05
Model	B	5.75	16.02
Model	C	7.25	25.46
Model	AB	3.75	6.81
Model	AC	3.25	5.12
Error	BC	-0.75	0.27
Error	ABC	-0.75	0.27

Table 1 shows the results for the 2^3 full factorial designs. The analysis of this experimental design yielded seven model terms consisting of three main effects (A = glucose, B = peptone and C = yeast), four interactions (AB, AC, BC & ABC) and one intercept. Table 2 illustrates the model terms which were selected based on the effect or percentage of contribution. Meanwhile, the ANOVA of the selected factorial model showed that the model and all the model terms are significant.

Response Surface Method

The main goal of the response surface analysis was to find the optimum combination of variables in order to maximize the response. The result of the replicate experiments at the middle point is shown in Table 3. Meanwhile, the purpose of the repetition at the middle point was to measure the consistency of the experimental result. Thus, to complete the RSM, experiments were done at the star point, as depicted in Table 4. The first three runs of the star point were used to measure the effect of nutrient concentration deficiency, while the next three runs measured the effect of excessive nutrient concentration.

TABLE 3
Repetition at middle point

Run	Factor 1 A: Glucose, g/L	Factor 2 B: Peptone, g/L	Factor 3 C: Yeast, g/L	Response 1 R1 Gas (ml)
9	8	20	10	*45*
10	8	20	10	*44*
11	8	20	10	*45*
12	8	20	10	*46*
13	8	20	10	*45*
14	8	20	10	*45*

TABLE 4
Star point

Run	Factor 1 A: Glucose, g/L	Factor 2 B: Peptone, g/L	Factor 3 C: Yeast, g/L	Response 1 R1 Gas (ml)
15	1.27	20	10	22
16	8	11.59	10	37
17	8	20	1.59	37
18	14.73	20	10	17
19	8	28.41	10	53
20	8	20	18.41	51

The RSM for the three factors would yield a quadratic model with nine model terms. In this study, however, the model was reduced to only five most significant model terms. After estimating the coefficients of the quadratic model, the amount of the total biogas could be predicted using the following quadratic equation:

$$Gas = 0.17 + 7.11Glu-0.02Pep+0.77Yes-0.53Glu^2 + 0.09Glu*Pep. \quad (1)$$

The three dimensional plots are based on Eq. (1), with one variable kept constant at its optimum level, and varying the other two variables within the experimental range. *Fig. 3* shows the response surface plot of the effect of glucose, peptone and yeast to biogas production by *C. butyricum*. The plot also demonstrates that the production of gas could be enhanced by increasing peptone and yeast extract concentrations up to 15 g/l and 24 g/l respectively, without showing any substrate inhibition. Meanwhile, the concentration of glucose was shown as optimum at the middle point (8 g/l), with possible substrate inhibition at high concentration (12 g/l). The substrate inhibition by glucose was likely due to the high osmotic pressure at higher glucose concentration.

It is crucial to highlight that peptone provides the bacteria with a readily available organic nitrogen source. Peptone and Yeast Extract also contains sources for minerals such as iron. The production of biological hydrogen is also dependent on the activity of hydrogenases, which are iron-containing enzymes directly responsible for the formation of hydrogen.

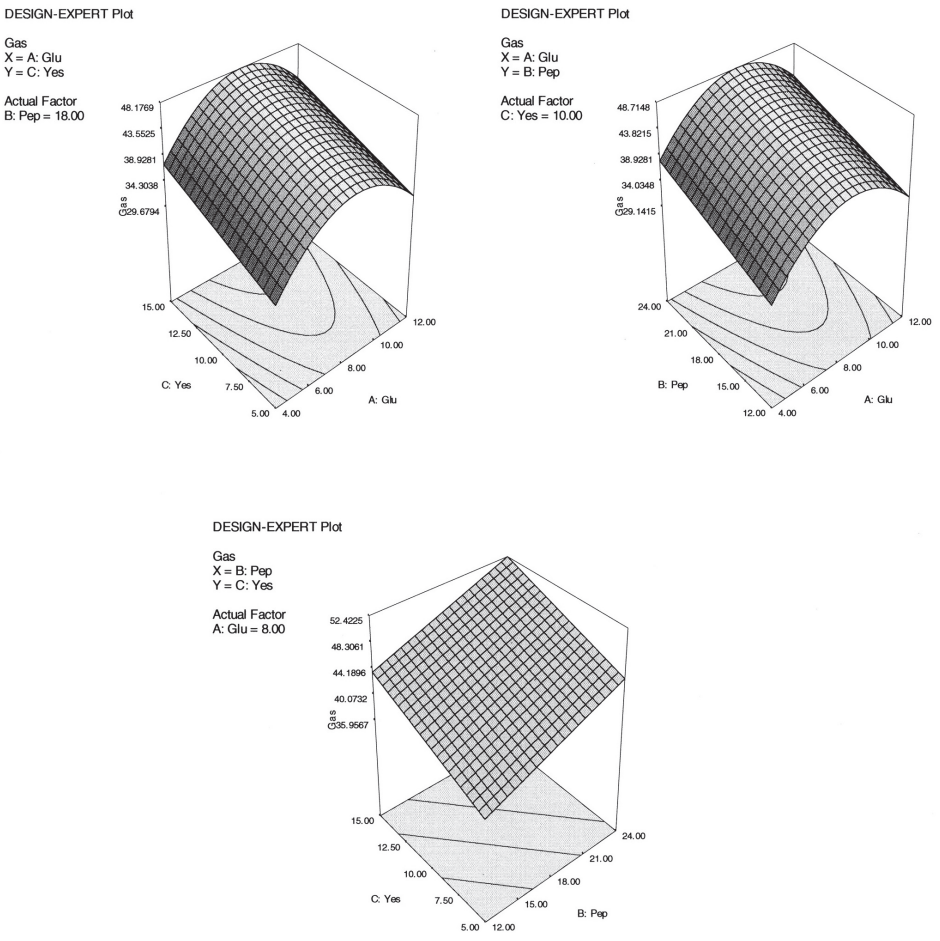

Fig. 3: Model graphs of the effect of glucose, peptone and yeast extract to biogas production

From the results of this study, the *C. butyricum* was shown to grow better on high concentration of organic nitrogen content. This information may be used to improve the yield of culture on substrate already high on organic content, such as Palm Oil Mill Effluent (POME). Thong *et al*. (2007) studied the thermophilic H_2 production bacteria and found that organic nitrogen amended medium improved the H_2 production, compared to inorganic nitrogen amended medium.

CONCLUSIONS

An anaerobic mesophilic bacterial strain with high production rate and yield of H_2 known as *Clostridium butyricum* KBH1was isolated. The results from the Response Surface Methodology (RSM) showed that peptone and yeast extracts are the limiting nutrients while glucose exhibits a substrate inhibition at high concentration. Peptone and yeast extracts provide sources for organic nitrogen, amino acids, vitamin and other growth factors. This bacterium is suitable for the production of biohydrogen using substrate with high organic loading. This optimization experiment was able to show the nutrients requirements for the growth and biohydrogen production of the isolated strain.

ACKNOWLEDGEMENT

The authors wish to thank the Ministry of Science, Technology and Innovation Malaysia, for funding this project under the grant number UKM-MGI-NBD0016-2007.

REFERENCES

Chen, W.M., Tseng, Z.J., Lee, K.S. and Chang, J.S. (2005). Fermentative hydrogen production with *Clostridium butyricum* CGS5 isolated from anaerobic sewage sludge. *International Journal of Hydrogen Energy*, *30*, 1063-1070.

Chen, X., Sun, Y., Xiu, Z.H., Li, X. and Zhang, D. (2006). Stoichiometric analysis of biological hydrogen production by fermentative bacteria. *International Journal of Hydrogen Energy*, *31*, 539-549.

Cheng, S.S., Chang, S.M. and Chen, S.T. (2002). Effect of volatile fatty acids on a thermophilic anaerobic hydrogen production process degrading peptone. *Water Science Technology*, *46*(4/5), 209 214.

Levin, B.D., Pitt, L. and Love, M. (2004). Biohydrogen production: Prospects and limitations to practical application. *International Journal of Hydrogen Energy*, *29*, 173-185.

Lin, C.N., Wu, S.Y., Lee, K.S., Lin, P.J., Lin, C.Y. and Chang, J.S. (2007). Integration of fermentative hydrogen process and fuel cell for on-line electricity generation. *International Journal of Hydrogen Energy*, *32*, 802-808.

O-Thong, S., Prasertsan, P., Intrasungkha, N., Dhamwichukorn, S. and Birkeland, N.K. (2008). Optimization of simultaneous thermophilic fermentative hydrogen production and COD reduction from palm oil mill effluent by *Thermoanaerobacterium*-rich sludge. *International Journal of Hydrogen Energy*, *33*, 1221-1231.

Pan, C.M., Fan, Y.T., Xing, Y., Hou, H.W. and Zhang, M.L. (2007). Statistical optimization of process parameters on biohydrogen production from glucose by *Clostridium* sp. Fanp2. *Bioresource Technology*. Doi:10.1016/ju.biotech.2007.05.055

Shin, J.H., Yoon, J.H., Ahn, E.K. Kim, M.S., Sim, S.J. and Park, T.H. (2007). Fermentative hydrogen production by the newly isolated *Enterobacter asburiae* SNU-1. *International Journal of Hydrogen Energy*, *32*, 192-199.

Wang, G., Mu, Y. and Yu, H.Q. (2005). Response surface analysis to evaluate the influence of pH, temperature and substrate concentration on the acidogenesis of sucrose-rich wastewater. *International Journal of Hydrogen Energy*, *23*, 175-184.

ISSN: 0128-7680
Pertanika J. Sci. & Technol. **17 (2)**: 389 –398 (2009)

Dielectrophoretic Separation of Cells Using 3-D Microelectrode

Zurina Zainal Abidin[1*], Zalini Yunus[2] and Gerard H. Markx[3]
[1]Department of Chemical Engineering and Environmental,
Faculty of Engineering, 43400 UPM, Serdang, Selangor, Malaysia
[2]STRIDE, MINDEF, Taman Bukit Mewah Fasa 9, 43000, Kajang, Selangor
[3]School of Chemical and Analytical Science, University of Manchester,
Sackville Street, M60 1QD, Manchester, UK
[*]E-mail: zurina@eng.upm.edu.my

ABSTRACT

The dielectrophoretic (DEP) separation of cell, using microelectrodes structure, has been limited to small scale due to size of the substrate. This work was carried out to extend the capability of microelectrodes system by orientating the microelectrodes in three dimensions (3-D) for larger scale dielectrophoretic separation of microorganism. The designed 3-D separation chamber consists of microelectrodes on two opposing walls. Based on the FEMLAB simulation, the electric field was seen to be generated across the chamber, rather than between adjacent electrodes in the same plane like in the small scale system. This configuration led to a stronger electric field in the bulk medium. The experimental results showed that the 3-D microelectrodes chamber behaved similar to the system with microelectrodes on one wall. The effects of the main parameters such as voltage, frequency and flow rates were similar to that of the systems with all the electrodes on one wall, but on the overall, capture more cells. A gap size between 250 – 500 μm resulted in an electric field which is strong enough to hold cells while giving a reasonable cross sectional area at the same time. Although there is some improvement achieved by 3-D system, it is still not very much, as compared to the small scale system.

Keywords: 3-D, dielectrophoresis, cell separation, microelectrodes

NOMENCLATURE

ε_p^*	Complex dielectric permittivities of the particle (F/m)
ε_m^*	Complex dielectric permittivities suspending medium (F/m)
F_{DEP}	Force of DEP (N)
r^3	radius of particle (m)
ε_0	free space permittivity (F/m)
ε_m	medium permittivity (8.854×10^{-12} F/m)
$Re(fcm)$	real part of the Clausius-Mossotti factor
∇E^2	Square of the electric field gradient (V^2/m^3)
j	imaginary number

INTRODUCTION

Advances made in many bio-related areas, such as cell biology, bioprocessing and others, have generated a demand for highly efficient and improved cell separation techniques. The manipulation of the behaviour of a particle or cell in a non-uniform electric field or also known as dielectrophoresis (DEP) (Pohl, 1978; Pethig, 1996) is one of the promising methods available to be explored. The

Received: 4 April 2008
Accepted: 16 May 2008
[*]Corresponding Author

particle or cell can exhibit positive or negative DEP when suspended in a fluid medium, due to the dipole associated with charge distribution at the fluid/particle interface. Dielectrophoresis has shown many applications, such as in monitoring and purifying cell cultures (Becker *et al*., 1994; Docoslis *et al*., 1994; Markx *et al*., 1994a), detection and removal of toxic pathogens from water (Suehiro *et al*., 2003), separation of dead and live cells (Li *et al*., 2002; Markx *et al*., 1994b) as well as removal of human breast cancer from CD34+ from stem cells (Huang *et al*., 1999). The DEP has the advantage of being non-invasive and can be conducted under sterile conditions. More importantly, DEP can be integrated with other methods to achieve improved separation since the physical properties exploited this technique has little impact on the other cell separation methods.

Currently, the DEP makes use of microelectrodes which are fabricated using photolithography technique. The high field intensities, which are important for the DEP application, have become possible due to the small dimensions of the microelectrode. Furthermore, it reduces the heat and enhances heat dissipation. However, the size of the substrate limits the capability of the microelectrodes to microlitres. This is rather unattractive for industrial application, which requires more sample volumes to be processed.

In most separations, the microelectrodes are only on one planar plate. The effective surface area of electrodes has also been reduced because only one side of the chamber is typically covered with electrodes. It is theoretically possible to scale up the DEP separations using large electrodes and electrical potentials. In practice, this may however cause electrical heating and electrochemical effects which can reduce the DEP effect and kill the cells.

In this work, the main aim was to extend the microelectrodes capability by orientating the microelectrode in 3-D arrangement and investigate its effectiveness for larger scale DEP separation of cells. Furthermore, this study also served as a basis in determining the important characteristics for scaling process.

THEORY

Dielectrophoresis works because of the existence of the non-uniform AC electric field, which is vitally determined by the electrode configuration. Following established theory (Pohl, 1978; Pethig, 1979; Jones, 1995), the DEP force, F_{DEP} acting on a spherical particle of radius r, suspended in a fluid of absolute dielectric permittivity, ε_m is given by:

$$F_{DEP} = 2\pi r^3 \varepsilon_0 \varepsilon_m \, Re(fcm) \nabla E^2 \tag{1}$$

where *Re(fcm)* is the real part of the Clausius-Mossotti factor, ∇E^2 is the square of the electric field gradient, ε_m is the medium conductivities and ε_0 is the free space permittivity (8.854×10^{-12} Fm^{-1}).

$$f_{cm} = \frac{(\varepsilon_p^* - \varepsilon_m^*)}{(\varepsilon_p^* + 2\varepsilon_m^*)} \tag{2}$$

where ε_p^* and ε_m^* are the frequency-dependent complex dielectric permittivities of the particle and its suspending medium defined by:

$$\varepsilon_p^* = \varepsilon_p - j\frac{\sigma}{\omega} \tag{3}$$

where ε_p are the permittivity of the particle and its suspending medium. σ is the conductivity, ω is the angular frequency, ($\omega = 2\pi f$) and $j = \sqrt{-1}$. The Clausius-Mossotti factor is a measure of the strength of the effective polarization of a spherical particle as a function of particle and medium permittivity. Clausius Mossoti factor is dependent on the applied frequency and also the electric properties of the particle relative to the medium. Theoretically, it should have a value between +1.0 to -0.5, which means that the DEP force can be positive and negative.

MATERIALS AND METHODS

Electric Field Simulation

FEMLAB 2.3 (Comsol Ltd) was used to simulate the electric field generated by the designed electrode systems. The FEMLAB is based on finite element analysis and partial differential equations. The module used was electromagnetic module, and the electric field calculation was done in 3-D.

The chromium electrodes were modelled as a layer with 100 nm thickness, placed onto a glass substrate of 50 μm thickness. Water with electrical permittivity of 78 was used as the medium and projected as a layer of 200 μm thickness. Both the glass substrate and water were considered as insulators. All simulations were done at voltages ranging from 2-20 $V_{peak\text{-}peak}$ and at a frequency of 1 MHz.

Micro-organism Preparation

The yeast used was *Saccharomyces cerevisiae* (strain 239, isolated from Whitbread the brewers, and obtained from Mr. Ralph Cooper, University of Manchester). It was grown overnight in a 100 ml MYGP broth containing 0.3% each of yeast and malt extracts (Oxoid), 1% of glucose and 0.5% of mycological peptone (Oxoid), at 35°C in an orbital shaker with a speed of 150 rpm. The cells were centrifuged (Int. Equipment, model Centra 4MPR), washed four times and re-suspended in deionised water to reduce the conductivity. After that, the conductivity was checked using a Jenway conductivity meter (model 4010). The concentration of the cells was measured using a UV spectrophotometer (PYE Unicam 8600, Philips) in a cuvette of 1 cm path length before carrying out the experiments.

Fabrication of Microelectrodes

The microelectrodes were fabricated using a standard photolithography method described previously (Markx *et al*., 1994a). Microelectrodes were made from chromium on a glass surface (75 mm x 25 mm) in the clean room at the School of Electronic and Electrical Engineering, University of Manchester. Interdigitated parallel microelectrodes, which were drawn using AutoCAD 2002, were used to study the effectiveness of the 3-D microelectrodes system. These microelectrodes have a width of 50 μm, while the distance between the adjacent electrodes was also 50 μm.

A chamber was then prepared to carry out the DEP separation experiments. In this work, the chamber made was similar to those described by Markx and Pethig (1995). A 3-D separation system was obtained by sandwiching a Teflon spacer (50 μm depth) between two glass plates with microelectrodes which were placed opposite each other. The final depth of the chamber was found to be around 250 μm (*Fig. 1*).

Experimental Procedures

The equipment used in this study is shown schematically in *Fig. 2*. The DEP chamber was placed on top of the microscope to monitor the behaviour of cell. A Nikon camera was mounted onto the microscope (Eclipse E600) and deionised water was continuously fed into the chamber using

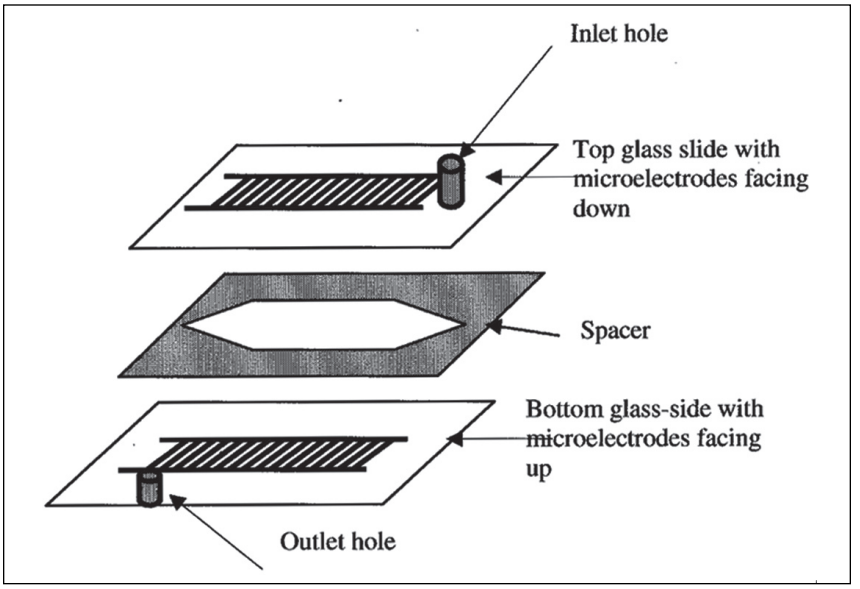

Fig. 1: Schematic presentation of dielectrophoretic separation chamber for 3-D system

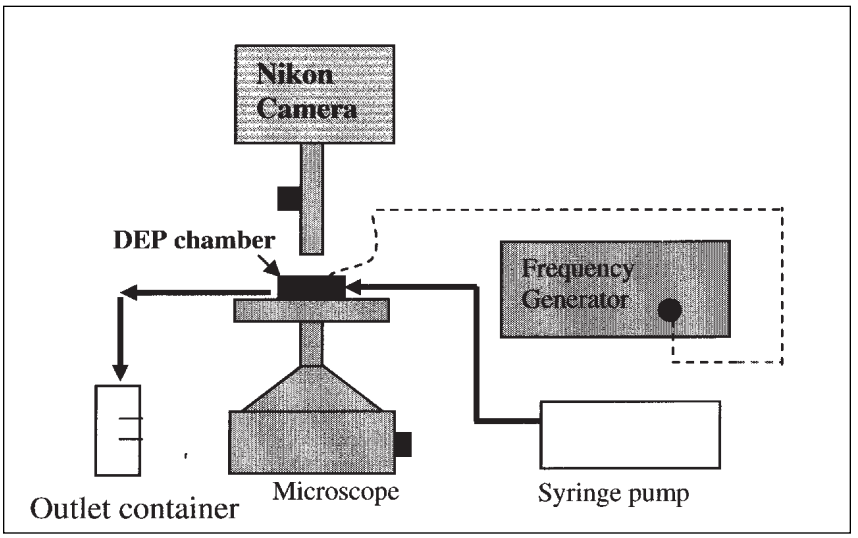

Fig. 2: Flow diagram of the system used for the dielectrophoretic separation of cells

a 10 ml syringe, which was controlled by a Sage instrument syringe pump (Model 355, Sage Instruments, USA). A measuring cylinder was placed at the outlet to collect the cell and water mixtures. Before the start of the experiments, the concentration of the cells was determined using the spectrophotometer (PYE Unicam, Philips; model 8600) at 660 nm. The optical density was adjusted until it achieved a value of 1.8 (equivalent to 2.8 x 10^8 cells per ml). The medium conductivity was 5 μScm^{-1}.

Water was let flowing into the DEP chamber prior to the introduction of the cells. The electric field was applied to the electrodes using a frequency generator (Thurlby Thandar Instruments, model TG120). Next, a pulse of cells was injected at the inlet tubing, using a syringe and the water went through the chamber was maintained to wash away the cells which were not attracted to the electrodes. After one hour, the experiment was stopped and the outlet suspension was collected to measure the optical density.

RESULTS AND DISCUSSION

In this work, two microelectrodes planes were placed opposite each other, top and bottom, and were energized with electric field. This resulted in an electric field pattern which acted between the bottom energized electrode and the top grounded electrode. The strongest electric field was found at the edges of the electrodes, while the strength of the field was found weaker away from the edges. *Fig. 3* shows the results of the FEMLAB analysis carried out for the electric field of the 3-D chamber at $x = 1.5 \times 10^{-4}$ m for 250 μm gap size at 8 $V_{pk\text{-}pk}$. The magnitude of the largest electric field strength is 2.8×10^4 Vm^{-1} at the edge of bottom electrode. The strength of the electric field declined further away from this edge before it started to peak again somewhere near the top electrode plane with a magnitude of about 1×10^4 Vm^{-1}.

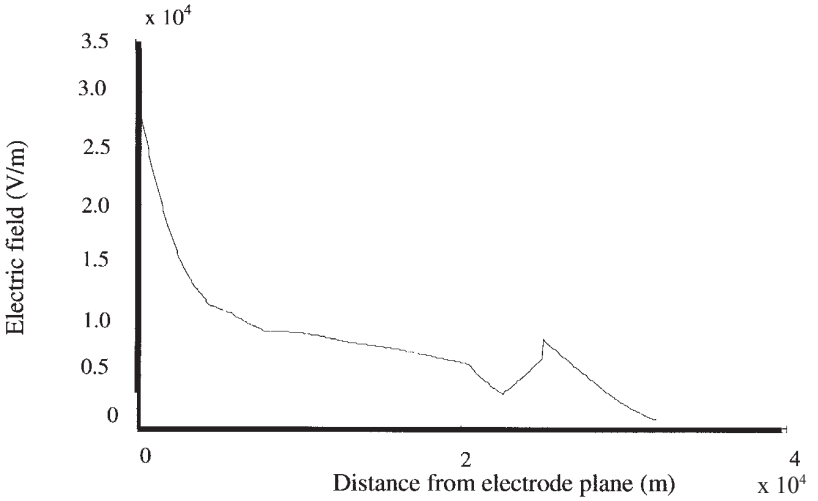

Fig. 3: The electric field pattern variations at x=1.5 × 10-4 m for 250 μm gap size at 8 Vpk-pk in z-direction. The electric field is decaying from a peak value as the distance increases. However, near the top electrode the electric field increases back slowly and reached another peak

In a system with only one wall covered with planar microelectrodes, the electric field was generated between the neighbouring electrodes in the same plane, and then decayed exponentially as a function of the height above the electrode plane (Markx *et al*., 1994b). For the system with opposing electrodes, in which the electric field was generated across the chamber, the electric field pattern was found to penetrate further into the chamber cross section, and hence the likelihood of a particle being caught in a high field region was also higher. These findings suggested that using a chamber having opposing microelectrodes could be better than using the chamber based on electrode arrays with adjacent microelectrodes. However, it should be noted that the gap between opposing

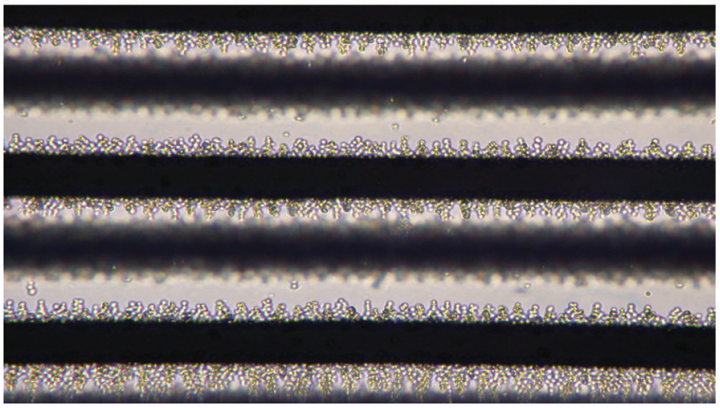

Fig. 4: Yeast cells collected at the electrode edges of both top and bottom electrodes. The applied voltage and frequency were 8V peak to peak and 1 MHz. The gap of the chamber used was 250 μm. The distance between the top and bottom neighbouring electrodes was 150 μm. The blurred arrays are the top array. The picture was taken at 20x magnification

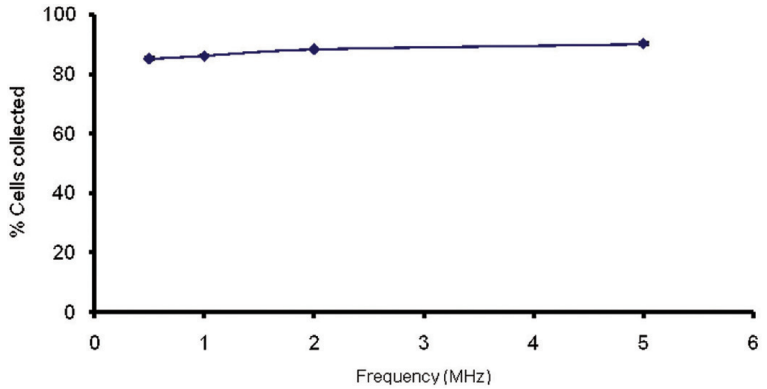

Fig. 5: The percentage of cells collected increases non-linearly as a function of the applied frequency

microelectrodes was quite large, and in this case, it was at least 250 μm between the electrode planes and 150 μm in the planes. As a result, it should be no surprise that the electric field values, in the opposing electrode system, were likely to be smaller than those in the system with adjacent microelectrode, in which the distance between the adjacent electrodes was typically 50-150 μm.

In this work, a simple 3-D separation chamber was constructed and a set of experiments was carried out to determine the performance of the new DEP chamber. The investigation was started by varying the applied frequencies, while setting the voltage and flow rate at 8 V_{pk-pk} and 9 μl min^{-1}, respectively. The gap size between the top and bottom electrodes was 250 μm, and the medium conductivity was 5 μS cm^{-1}.

Fig. 4 demonstrates a typical collection pattern of yeast cells under the influence of 1 MHz applied frequency and $8V_{pk-pk.}$ These yeast cells were seen to be collected at the electrode edges of both the top and bottom electrodes. When the frequency was increased from 0.5 MHz to 5 MHz, the number of cells attracted to the electrodes increased (*Fig. 5*). Nearly 85% of cells were found

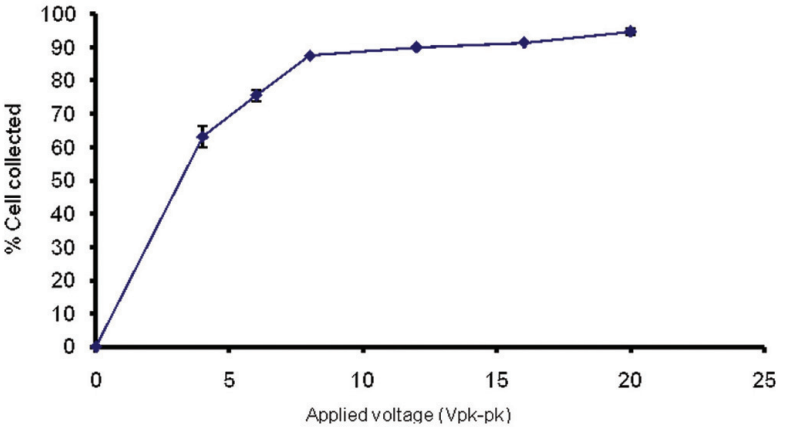

Fig. 6: Changes in the percentage of the cells collected at an applied voltage of 8 V_{pk-pk}. The percentage of the cells collected increases as the voltage increases

to be attracted at 0.5 MHz, and this was around 91% at 5 MHz. This was in concordance with the previous findings by Huang *et al*. (1992). However, pearl chain formation, which could be of advantage in capturing the other cells, was found to be less at 5 MHz than around 1 MHz.

In the next set of experiments, the voltage was varied from 2 to 20 V_{pk-pk} at 1 MHz and 9 μl min^{-1}. When there was no electric field, no cells were collected. Once the electric field was applied, the result (*Fig. 6*) showed that as voltage increased, the percentage of cells attracted to the electrodes was also increased. Nearly 65% cells were already collected at 4 V_{pk-pk}. At low voltages, the fluid drag force exerted onto some of the cells was often larger than the magnitude of the DEP force holding them. When the voltage increased, the magnitude of the electric field strength as well as the DEP force holding the cells at the electrode had also increased and resulted in less cells being washed away from the chamber.

The next investigation conducted was varying different flow rates from 9 μl/min to 193 μl/min. The gap between the slides in the separation chamber was 250 μm at 1 MHz and 8 V_{pk-pk}, respectively. *Fig. 7* illustrates that the percentage of cells attracted to the electrodes decreased as the flow rates became faster. This was rather expected because increasing the flow rates would in turn increase the drag force exerted on the cells, whilst the DEP forces holding the cells at the electrodes remained constant. Hence, more cells were flushed out from the separation chamber when the flow rate was increased. The flow in the DEP chamber would have a parabolic velocity profile. Therefore, the drag force would virtually be zero at both of the electrode planes and this was the maximum at the middle of the chamber. This contradicted the DEP force, which would be at its maximum at the electrode plane and minimum in the middle of column. It is believed that only cells which reside at the middle of chamber are likely to be washed away.

When scaling up, it is desirable to process as much sample volume as possible. One way of doing this is by increasing the cross sectional area of the chamber. This allows more sample volume to be handled at one time. The next experiments were carried out by varying the gap of chamber, i.e. from 250 μm to 1mm at 1 MHz and 8 V_{pk-pk}. Increasing the cross sectional area of the chamber was found to reduce the velocity. Thus, in order to maintain the velocity of the fluid flows for all the different gap sizes, different flow rates had to be used. The velocity needed to wash the cells

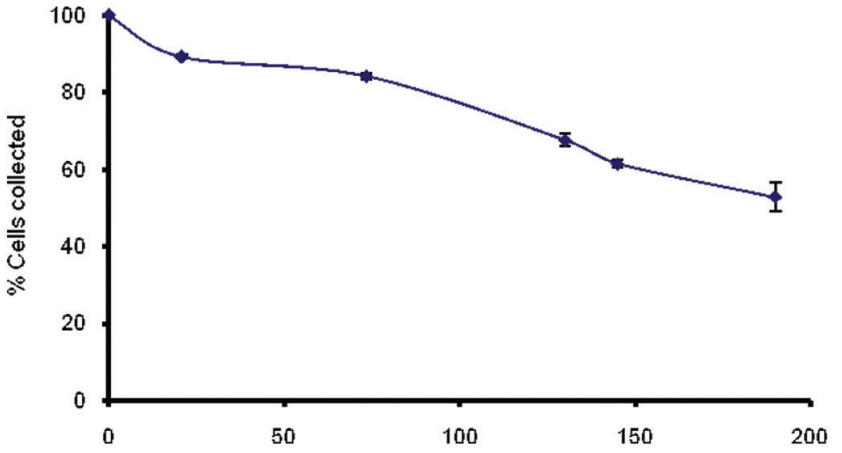

Fig. 7: The influence of the flow rate on the number of cells attracted to the electrodes. More cells are flushed out from the separation chamber at higher flow rates since increasing the flow rates will increase the drag force

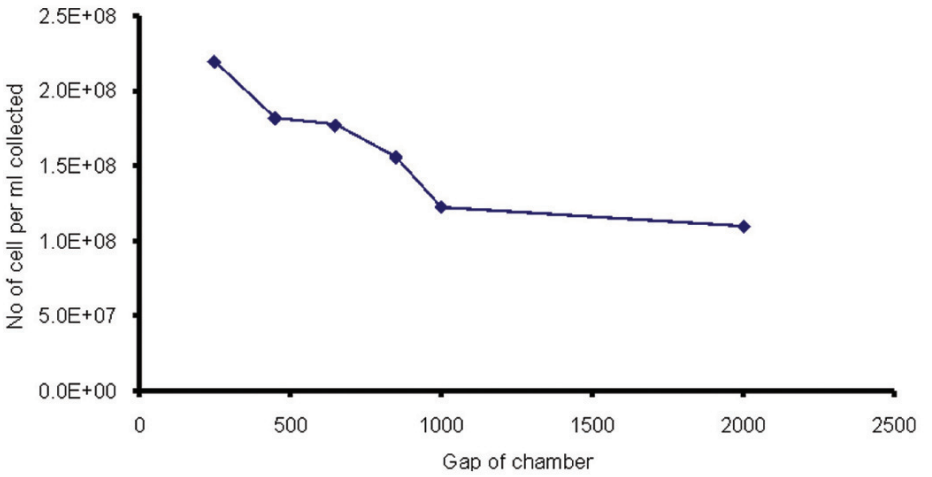

Fig. 8: The influence of the gap between the top and bottom electrodes on the number of cells attracted to the electrodes. The number of cells collected at the electrodes decreases as the gap increases

that were not attracted to the electrodes was determined for each electrode gap experimentally. The gaps used were 250 μm, 450 μm, 600 μm, 800 μm, 1000 μm, 2000 μm, 6000 μm and 10000 μm. The corresponding flow rates were 9 μl min^{-1}, 18 μl min^{-1}, 90 μl min^{-1}, 180 μl min^{-1}, 420 μl min^{-1}, 800 μl min^{-1}, ~ 24 ml min^{-1} and ~100 ml min^{-1}, respectively.

The results, shown in *Fig. 8*, indicate that the number of cells attracted to the electrodes decreased as the gap between the electrodes was increased. This is entirely due to the higher DEP force experienced by the cells, as the gap decreases. At 250 μm, these cells were observed to be attracted to both the top and bottom electrodes. However, as the gap between the electrodes was

increased to 450 μm, less cells were collected, and most of them resided at the bottom electrodes. The number of cells collected further reduced as the gap was increased to 650 μm, 850 μm, 1000 μm and 2000 μm. At 250 μm and 450 μm, the pearl chains formed by the cells were still distinct. As the gap sizes increased, pearl chain formation was less, and the cells were also more dispersed.

The bigger the gap size, the more volume sample can be processed. The above results suggest that the electric field interaction between the top and bottom electrodes will only be effective throughout the length of chamber or bulk medium for collection of cells up until a certain gap size of around 600 μm. This also means that although a bigger gap between the interacting electrodes would help process more sample volume, the effectiveness of the electric field throughout the bulk medium was reduced and hence the collection of cells. The further away the cells into the bulk medium, the drag force will be larger than the DEP force and flushes them away to the outlet. It therefore, limits the capability of this 3-D microelectrode system.

CONCLUSIONS

An extension to photolithographic approach was attempted for the DEP separation at larger scales. A 3-D separation chamber was designed with microelectrodes on two opposing walls, with the electric field generated across the chamber, rather than between the adjacent electrodes in the same plane like in the small scale system. The experimental results showed that this system behaved similar to the systems with microelectrodes on one wall, but it captured more cells. This configuration led to a stronger electric field in the bulk medium. In the experiments it performed well, giving substantial amount of cell collection. The experimental results also showed that the effects of the main parameters such as voltage, frequency and flow rates were similar to that of the systems with all the electrodes on one wall. A gap size between 250 – 500 μm gave the best results. However, in comparison to the small scale system, the improvement was still not very much. This result has a big implication in that it limits the capacity of the microelectrode system. The findings from this study also suggest that in scaling up dielectrophoretic separation, it is very important for the electrode to generate high electric field strength in the system. The electrode system must be able to fully utilized the surface area of the electrode and also rapidly dissipate any heat generated within the system. The findings also suggest the possibility of using a different approach from the conventional photolithography technique to ensure success in scaling up.

ACKNOWLEDGEMENT

We wish to thank Universiti Putra Malaysia for its financial support.

REFERENCES

Becker F.F., Wang, X.B., Huang, Y., Pethig, R., Vykoukal, J. and Gascoyne, P.R.C. (1994). The removal of human leukaemia cells from blood using interdigitated microelectrodes. *Journal of Physics D: Applied Physics, 27,* 2659-2662.

Docoslis A., Kalogerakis, N., Behie, L.A. and Kaler, K.V.I.S. (1994). A novel dielectrophoresis-based device for the selective retention of viable cells in cell culture media. *Biotechnology Bioengineering, 54*, 239-250.

Huang Y., Holzel, R., Pethig, R. and Wang, X.B. (1992). Differences in the AC electrodynamics of viable and non-viable yeast cell determined through combined dielectrophoresis and electrorotation. *Physical Medical Biology, 37*, 1499-1517.

Huang Y., Yang, J., Wang, X.B., Becker, F.F. and Gascoyne, P.R.C. (1999). Cutting edge communication: The removal of human breast cancer cells from hematopoietic CD34+ stem cells by dielectrophoretic field-flow-fractionation. *Journal of Hematotherapy and Stem Cell Research, 8*(5), 481-490.

Jones, T.B. (1995). Dielectrophoretic force calculation. *Journal of Electrostatics, 6*, 69-82.

Li, H. and Rashid, B. (2002). Dielectrophoretic separation and manipulation of live and heat-treated cells of Listeria on microfabricated devices with interdigitated electrodes. *Sensors & Actuators: B., 86*(2-3), 215-221.

Markx G.H., Huang, Y., Zhou, X.F. and Pethig, R. (1994a). Dielectrophoretic characterization and separation of microorganism. *Microbiology, 140*, 585-591.

Markx, G.H., Talary, M. and Pethig, R. (1994b). Separation of viable and non-viable yeast using dielectrophoresis. *Journal of Biotechnology, 32*, 29-37.

Markx, G.H. and Pethig, R. (1995). Dielectrophoretic of cells: Continuous separation. *Biotechnology Bioengineering, 45*, 337-343.

Pethig, R. (1996). Dielectrophoresis: Using inhomogeneous AC electric fields to separate and manipulate cells. *Critical Reviews in Biotechnology, 16*(4), 331-348.

Pethig, R. (1979). *Dielectric and Electronic Properties of Biological Materials.* J. Wiley and Sons.

Pohl, H.A (1978). *Dielectrophoresis*. Cambridge, UK: Cambridge University Press.

Suehiro, J., Zhou, G., Imamura, M. and Hara, M. (2003). Dielectrophoretic filter for separation and recovery of biological cells in water. *IEEE Transactions on Industry Applications, 39*(5), 1514-1521.

ISSN: 0128-7680
Pertanika J. Sci. & Technol. **17 (2)**: 399 – 408 (2009)

Production of Ethanol by Fed-Batch Fermentation

Ngoh Gek Cheng[1*], Masitah Hasan[1], Andri Chahyo Kumoro[2], Chew Fui Ling[1] and Margaret Tham[1]

[1]Department of Chemical Engineering, University of Malaya, 50603, Kuala Lumpur, Malaysia

[2]Separation Engineering Research Group, Department of Chemical Engineering, Faculty of Engineering, Diponegoro University, Prof. H. Sudharto, SH Road, Tembalang – Semarang, Indonesia

[*]E-mail: ngoh@um.edu.my

ABSTRACT

The production of ethanol, from glucose in batch and fed batch culture, was investigated. In the fed batch culture, the glucose feeding was added into the culture at 16th hour of fermentation. The effects of different glucose concentration feeding rates on ethanol fermentation were investigated for fed batch culture. The 2$gL^{-1}hr^{-1}$ glucose concentration feeding rate was found to give higher ethanol yield (2.47 g ethanol g $glucose^{-1}$), with respect to substrate consumed as compared to 8 $gL^{-1}hr^{-1}$ (0.23 g ethanol g $glucose^{-1}$) and 4 $gL^{-1}hr^{-1}$ (0.20 g ethanol g $glucose^{-1}$). The ethanol yield with respect to substrate consumed obtained in batch culture was 0.81 g ethanol g $glucose^{-1}$. The fed batch culture at 2 $gL^{-1}hr^{-1}$ glucose concentration feeding rate was proven to be a better fermentation system than the batch culture. The specific growth rate, specific glucose consumption rate and specific ethanol production rate for the fed batch fermentation, at 2 $gL^{-1}hr^{-1}$ glucose concentration feeding rate, were 0.065 hr^{-1}, 1.20 hr^{-1} and 0.0009 hr^{-1}, respectively.

Keywords: Batch culture, ethanol, fed batch culture, fermentation, glucose feed rate, *Saccharomyces cerevisiae*

INTRODUCTION

Due to a rapid depletion of the world's petroleum reserves and its rising prices day by day, new sources of hydrocarbons must be found to supply chemical and energy needs (Sitton and Gaddy, 1980; Lee *et al*., 1983). In this context, ethanol fermentation offers promising alternative as it can be produced from various sources of raw materials. In view of increasing importance of ethanol, as an alternative source for chemicals and liquid fuel, a great deal of research interest in ethanol fermentation has been generated in the last two decades (Vega *et al*., 1987; Converti *et al*., 1985). Many different types of processes for ethanol fermentation have been proposed including batch fermentation, continuous fermentation, continuous fermentation with cell recycling, fed-batch and repeated-batch culture (Yoshida *et al.*, 1973). The fed-batch culture with the intermittent addition of glucose and without the removal of fermentation broth is one of the most common methods for the production of ethanol in the industry. One advantage of this process is the reduction of substrate inhibition. A high concentration of sugar in fermentation medium inhibits growth and ethanol production. Other advantages of this process are higher productivity, higher dissolved oxygen in the medium, decreased fermentation time and reduced toxic effects of the medium components, which are present at high concentrations (Stanbury and Whitaker, 1984).

Received: 28 February 2008
Accepted: 16 May 2008
[*]Corresponding Author

The ethanol production, which involves fed-batch methods and using baker's yeast as biomass is a complex, time-variant, nonlinear process. Baker's yeast, one of the *S. cerevisiae* strains, has been used intensively for the production of single cell protein (SCP for human and animal consumption), and ethanol (industrial and portable alcohol) from fermentable sugar because of its GRAS (Generally Regarded as Safe) status (Solomon *et al*., 1997). This yeast strain can produce a high concentration of ethanol and it is preferred for most ethanol fermentations (Yan *et al*., 2006). Therefore, the aims of this work were to: (a) determine the switching time for fed batch fermentation, (b) investigate the optimum glucose concentration feeding rate of ethanol production by *S. cerevisiae* cells in fed batch fermentation, using glucose as the source of carbon, (c) study the kinetic parameters of the system which include specific growth rate, specific glucose uptake rate, specific ethanol production rate and the production yield of ethanol.

MATERIALS AND METHODS

Micro-organism

S. cerevisiae (Baker's yeast, Mauri-Pan), used throughout this investigation, was maintained at 4°C on agar slants. The compositions of the agar were: 5 gL^{-1}yeast extract, 5 gL^{-1} malt extract, 5 gL^{-1} peptone, 20 gL^{-1} glucose and 20 gL^{-1} agar. The cultures were maintained by sub-culturing every 20 days and the plates were incubated at 30°C for 24 hours.

Fermentation Medium

One litre of production medium was prepared according to the requirement of *S. cerevisiae*, containing 50.0 gL^{-1}glucose, 1.0 gL^{-1}yeast extract, 5.0 $gL^{-1}KH_2PO_4$, 2.0 $gL^{-1}(NH_4)_2SO_4$ and 0.4 $gL^{-1}MgSO_47H_2O$. The medium was sterilized and the pH was adjusted to 5.0.

The Preparation of Inoculums

The micro-organism was cultured in 250 mL Erlenmeyer flasks, containing 100 mL of the medium, which has the same composition as the fermentation medium. The Erlenmeyer flask was incubated at 28°C for 6 hours on a rotary shaker at 200 rpm.

The Fermentation Conditions

(i) Batch Culture

The fermentation was carried out in a 2 litre stirred tank fermentor, with a working volume of 1.5 litres. The 900 mL fermentation medium was inoculated with 100 mL inoculums and the pH was adjusted to 5.0. It was carried out at 250 rpm and temperature of 30°C, with an air flow rate of 1vvm. Samples were taken every 2 hours for the entire fermentation cycle, which was terminated after 42 hours.

(ii) Fed Batch Culture

The substrate was fed continuously into the bioreactor with a peristaltic pump, at a glucose concentration feeding rates of $2gL^{-1}hr^{-1}$, $4gL^{-1}hr^{-1}$ and $8gL^{-1}hr^{-1}$. The impeller speed was set at 250 rpm and 30°C, with the air flow rate of 1 vvm for all the runs.

The Analytical Techniques

Fermentation broth was removed from the fermentor and analyzed at a predetermined time interval. Yeast growth was evaluated by spectrophotometric measurements at 260 nm in a spectrophotometer and calibrated against cell dry weight measurements. The concentration of glucose was determined

using the 3, 5 dinitrosalicylic acid (DNS) method (Miller, 1959). Meanwhile, the concentrations of ethanol in the medium were determined by gas chromatography, using a polyethylene glycol column, nitrogen as carrier gas and flame ionization detection with the following conditions: an injection temperature of 250°C, initial oven temperature of 45°C to final temperature of 250°C at a rate of 8°C min^{-1}, a flow rate of carrier gas of 4 mL min^{-1} and an injected volume of 1 µL (Agilent Technologies, 2000).

The Kinetic Parameters

Ethanol yield was calculated with respect to both glucose consumed and biomass generated. The specific growth kinetic, specific substrate uptake rate and specific ethanol production rate were determined using a simulation method based on the MATLAB Programme. A set of system equations was derived from the material balances of cell, sugar and ethanol for the fed batch fermentation:

$$\frac{dX}{dt} = \mu X - \frac{F}{V}X \tag{1}$$

$$\frac{dS}{dt} = \frac{F}{V}(S_0 - S) - \nu X \tag{2}$$

$$\frac{dP}{dt} = QX - \frac{F}{V}P \tag{3}$$

Where X, S and P denote the concentration of cells, glucose, and ethanol, respectively. V is the culture volume, and S_o and F are the sugar concentration and feed rate of the feed medium added to the fermentor, respectively; µ, ν and Q are the specific rates of growth, glucose consumption, and ethanol production, respectively.

RESULTS AND DISCUSSION

Batch Fermentation

In order to conduct the fed batch fermentation, this batch fermentation was carried out to study the trend of cell growth, glucose consumption and ethanol formation. The switching time for the fed batch fermentation was determined from the result of the batch fermentation. Based on the data presented in *Fig. 1*, a typical batch growth phase can be observed, including the following phases: lag phase (0 - 6 hr), exponential growth phase (6 - 30 hr), deceleration phase (30 - 34 hr) and stationary phase (34 - 42 hr).

In the first 6 hours of fermentation, the yeasts adapted themselves to growth conditions. During the exponential phase, the periods of exponential growth were of limited duration due to the depletion of some rate-limiting resources. After 34 hours of fermentation, the growth rate was found to slow down as a result of glucose depletion.

Based on *Fig. 1*, the concentration of glucose is shown to remain almost constant for the first 6 hours. The concentration of glucose was then decreased as expected during the fermentation, coinciding with an increase in the production of cell and ethanol. This is due to the cells consuming the glucose in the system to increase the growth of cell and the production of ethanol. The feeding of the substrate was initiated when most of the substrates have been consumed and the growth of

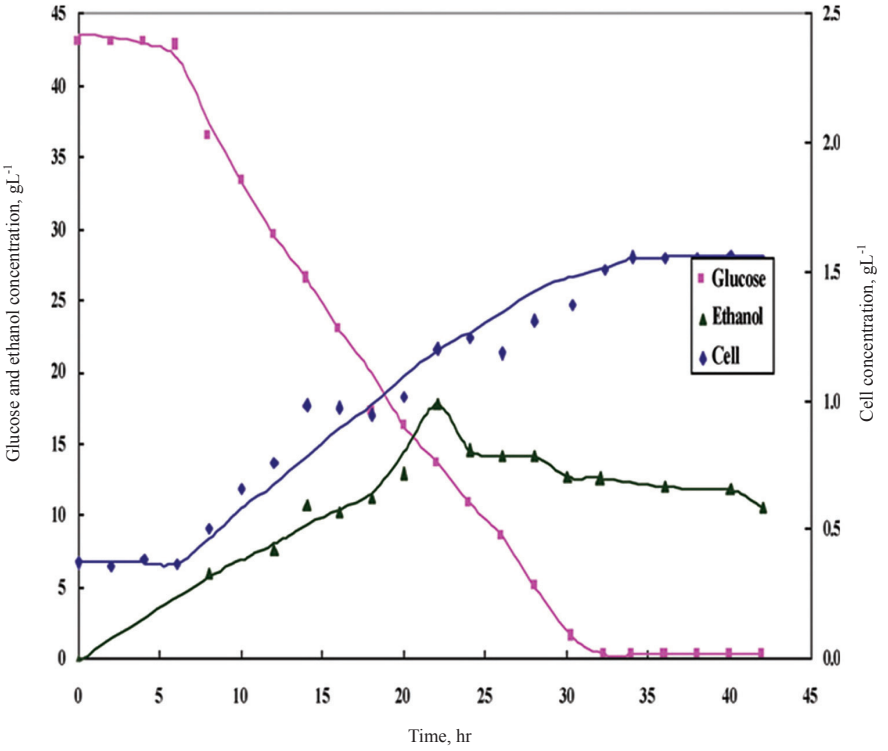

Fig. 1: Fermentation of S. cerevisiae cells during ethanol production from glucose in batch culture

yeast was in the exponential phase. It could also be observed that the system glucose was depleted after 34 hours.

The concentration of ethanol was found to increase rapidly during the first 20 hours of fermentation. It started to decrease only after achieving a maximum concentration of 18 gL^{-1} at 22 hours of fermentation. The ethanol might have been used as a carbon source by the yeast for its growth after the 22nd hours, when the concentration of glucose started to deplete (Bauchop and Elsden, 1960; Coppella and Dhurjati, 1989). By comparing the cell and the concentrations of ethanol, it can be classified as a growth-associated product in which the product is produced simultaneously with the cell growth.

Fig. 1 indicates that the optimum switching time from batch to fed batch fermentation is between 14th -18th hr. Therefore, the feeding of substrate was decided to start at 16th hours of fermentation cycle for all the fed-batch systems.

Fed Batch Fermentation

(i) Comparison of the Cell Concentration

Fig. 2 shows that the cell concentration generally remained almost constant for about 5 hours and it increased gradually throughout the fermentation. In general, there was no stationary phase observed

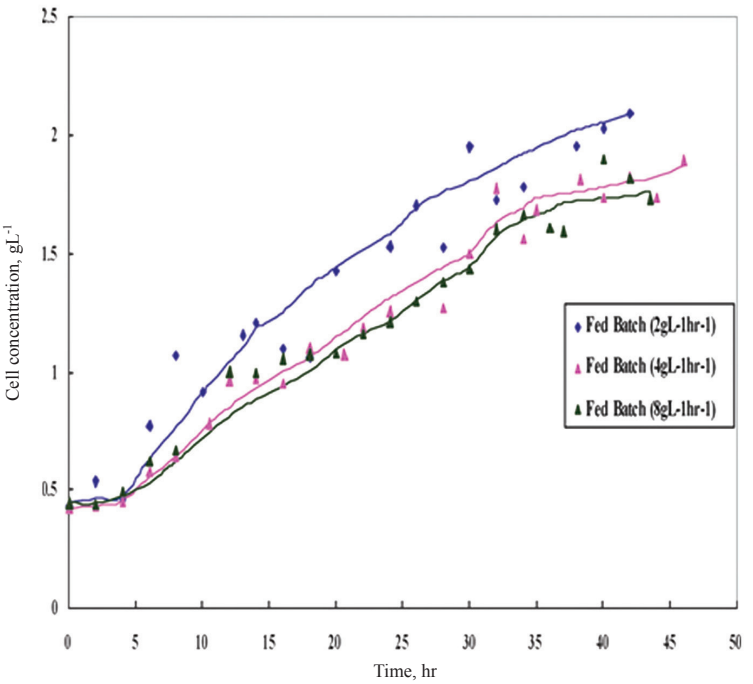

Fig. 2: Comparison of cell concentration at different glucose concentration feeding rate for fed batch fermentation

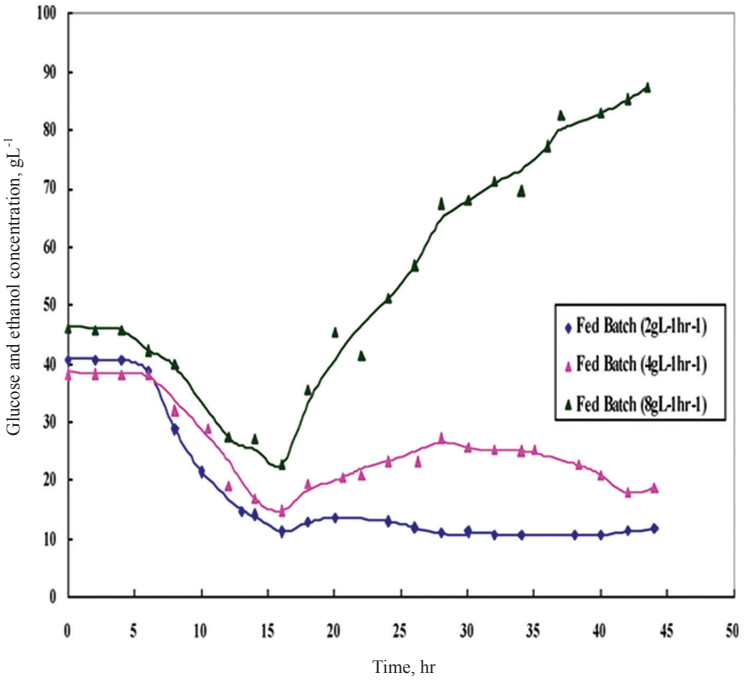

Fig. 3: Glucose concentration with time at different glucose concentration feeding rates for the fed batch fermentation

for the fed batch culture, at all the glucose concentration feeding rates. Comparatively, 2 $gL^{-1}hr^{-1}$ glucose concentration feeding rate gave a better cell concentration than 4 $gL^{-1}hr^{-1}$ and 8 $gL^{-1}hr^{-1}$. This was probably due to the 2 $gL^{-1}hr^{-1}$ glucose concentration feeding rate which had provided a better growth environment to the yeast, so that the yeast cells could divide more rapidly.

It also might be attributed to the osmotic effect contributed by the high glucose concentrations, resulting in slower proliferation of yeast cells (Thomas *et al.,* 1992). The higher concentration of substrate was also found to affect the pH, viscosity and the activity of the medium. Long hour exposure to high substrate concentration might also cause catabolic repression. The changing of the environment had somehow affected the growth rate of the cell, whereby the cell viability decreased as the sugar concentration increased during the fermentation of ethanol. This trend is in agreement with the report by Thomas and Ingledew (1992).

(ii) Comparison of the Glucose Concentration

From *Fig. 3*, glucose concentration is observed to follow the same pattern as in the batch fermentation before the fed batch fermentation was started. At 8 $gL^{-1}hr^{-1}$ glucose concentration feeding rate, the concentration of glucose was found to increase exponentially throughout the fermentation. This indicates that the glucose feeding rate is much greater than the glucose consumption rate. Consequently, there is an excess in the glucose left in the medium and it becomes a waste for the system.

Fig. 3 also indicates that the concentration of glucose at 4 $gL^{-1}hr^{-1}$ glucose concentration feeding rate is generally higher than the glucose concentration at 2 $gL^{-1}hr^{-1}$ glucose concentration feeding rate, but less than the glucose concentration at 8 $gL^{-1}hr^{-1}$ glucose concentration feeding rate. At 2 $gL^{-1}hr^{-1}$ glucose concentration feeding rate, the concentration of glucose was found to increase slightly and remain constant at about 10 gL^{-1} after 28 hours of fermentation. This was due to the amount of glucose fed into the system had been fully consumed by the yeast. It could be seen that the 2 $gL^{-1}hr^{-1}$ glucose concentration feeding rate gave the best glucose consumption.

(iii) Comparison of Ethanol Concentration

Fig. 4 shows that the overall ethanol concentration, at 2 $gL^{-1}hr^{-1}$ glucose concentration feeding rate, is higher than 4 $gL^{-1}hr^{-1}$ and 8 $gL^{-1}hr^{-1}$ in the fed batch culture. The glucose feeding rate of 2 $gL^{-1}hr^{-1}$ was indicated to produce the ethanol concentration up to the maximum 17gL^{-1}. The concentration of ethanol remained almost constant for about 14 hours before it started to decrease at 32nd hours. The decrease in the concentration of ethanol was probably due to the oxidation of ethanol to acetic acid and other components (Mian *et al.,* 1973).

For both the 4 $gL^{-1}hr^{-1}$ and 8 $gL^{-1}hr^{-1}$ glucose concentration feeding rates, the pattern of ethanol formation was similar but the 4 $gL^{-1}hr^{-1}$ glucose concentration feeding rate produced more ethanol as compared to that at 8 $gL^{-1}hr^{-1}$. The glucose concentration feeding rate at 8 $gL^{-1}hr^{-1}$ gave the lowest concentration of ethanol. This might be due to the catabolic repression and glucose overflow metabolism. When the glucose concentration exceeded a critical value, it caused excretion of ethanol.

(iv) Fed Batch Culture at 2 $gL^{-1}hr^{-1}$ Glucose Concentration Feeding Rate

The fed batch fermentation conducted at 2 $gL^{-1}hr^{-1}$ glucose concentration feeding rate was found to produce the highest ethanol production. The trend of the cell growth, glucose consumption and ethanol formation are shown in *Fig. 5*.

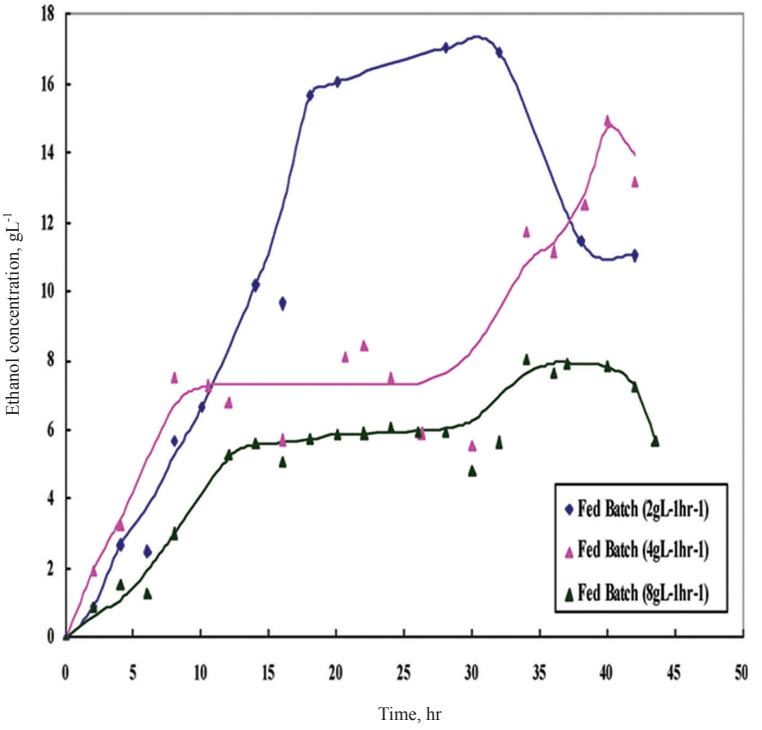

Fig. 4: Ethanol concentration at different glucose concentration feeding rates for the fed batch fermentation

The concentration of ethanol decreased at 32nd hours, although the glucose was fed into the system continuously. The maximum production of ethanol achieved was about 17 gL^{-1}. The yeast cells grew exponentially after 6 hours until the end of the fermentation cycle and no stationary phase was observed. It was found that the concentration of glucose had remained almost constant after 28 hours of fermentation. The added glucose was sufficient and it provided an optimum environment for the cell growth.

In comparison with the batch culture (*Fig. 1*), ethanol was produced constantly for a longer period in the fed batch culture at 2 $gL^{-1}hr^{-1}$ glucose concentration feeding rate. The batch culture produced the maximum ethanol at a single point, but it could not maintain the production due to the depletion of glucose.

Kinetic Parameters

The specific growth rate, glucose consumption rate, production rate and the yield coefficient are commonly adopted to assess microbial performance. The specific cell growth rate, specific glucose uptake rate and specific ethanol production rate, at three different glucose concentration feeding rates, were determined using the modelling method. The MATLAB program was also employed to solve the three ordinary differential equations derived from material balance of cell, glucose and ethanol, with the data obtained from the experiments. Table 1 shows all the kinetic parameters for both the batch and fed batch fermentations. The volume change of the fermentation medium was relatively small and it was assumed to be negligible in the system.

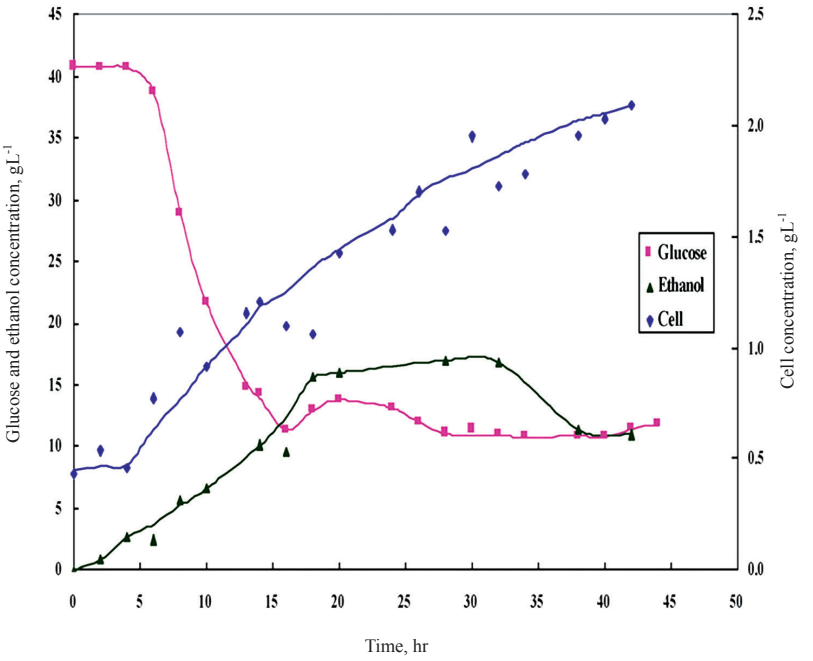

Fig. 5: Cell growth, glucose consumption and ethanol formation profile of the fed batch fermentation at $2gL^{-1}hr^{-1}$ glucose concentration feeding rate

TABLE 1
Kinetic parameters for the batch and fed batch fermentations

Kinetic Parameter	Batch Fermentation	Fed Batch Fermentation		
		$2gL^{-1}hr^{-1}$	$4gL^{-1}hr^{-1}$	$8gL^{-1}hr^{-1}$
Yield, $Y_{P/X}$ (g ethanol g $cell^{-1}$)	21.49 (22 hr)	24.75 (20 hr)	12.50 (20 hr)	9.28 (20 hr)
Yield, $Y_{P/S}$ (g ethanol g $glucose^{-1}$)	0.81 (22 hr)	2.47 (18 hr)	0.23 (20 hr)	0.20 (18 hr)
Specific cell growth rate, μ (hr^{-1})	0.0613	0.0645	0.0341	0.0313
Specific glucose uptake rate, ν (hr^{-1})	1.183	1.1953	1.4452	1.6133
Specific ethanol production rate, Q (hr^{-1})	0.0006	0.0009	0.0008	0.0005

Table 1 also illustrates that a lower glucose concentration feeding rate correlated with a higher product yield. The fed batch fermentation at $2gL^{-1}hr^{-1}$ glucose concentration feeding rate gave the highest product yield. However, the product yield at $4gL^{-1}hr^{-1}$ and $8gL^{-1}hr^{-1}$ glucose concentration feeding rate was much lower than the batch fermentation. It seemed that the carbon fraction channelling to ethanol synthesis was saturated when the glucose concentration was higher. This indicated that the higher glucose concentration feeding rate did not enhance the production of ethanol. It was due to the substrate inhibition at a higher glucose concentration in the system. The highest product yield for the fermentation was achieved in the range of 18^{th} - 22^{nd} hr.

The decrease in the specific growth rate suggested the inhibition of cell growth by increasing the glucose concentration feeding rate. The decrease in the specific growth rates showed that the rate of biosynthesis was lower at a high glucose concentration, as maintenance coefficient was increased at high glucose concentrations. Thus, it could be concluded that the fed batch fermentation is most suitable to be operated at $2gL^{-1}hr^{-1}$ glucose concentration feeding rate for this study.

The fed batch culture at 2 $gL^{-1}hr^{-1}$ glucose concentration feeding rate also supported a higher ethanol yield, specific growth rate, specific consumption rate and specific ethanol formation rate as compared to the batch culture. It was shown that an increase in the concentration feeding rate resulted in a significant decrease in the fermentation efficiency. The decreased efficiency encountered with the highest concentration treatment was probably due to the osmotic effects. Roukas *et al*. (1991) reported that above the critical substrate, the decrease of water activity and the onset of plasmolysis could cause a decrease in the rate of fermentation and the production of ethanol. These results clearly showed that the substrate concentration feeding rate had a significant effect on the kinetic parameter of *S. cerevisiae*. Carine *et al*. (2006) studied the minimization of glycerol production during the high performance fed-batch ethanol fermentation process in *S. cerevisiae* and found that a product yield of 0.34 g g^{-1}, maximum specific growth rate of 0.62 g $g^{-1}hr^{-1}$ were obtained when the fermentor was fed with a sterile concentrated glucose solution of 700 g L^{-1}.

CONCLUSIONS

In this work, the best switching time from the batch to fed batch fermentation was determined at 16^{th} hour. The $2gL^{-1}hr^{-1}$ glucose concentration feeding rate in the fed batch fermentation achieved the best ethanol production as compared to $4gL^{-1}hr^{-1}$ and $8gL^{-1}hr^{-1}$ glucose concentration feeding rates. The maximum product yield was achieved at 18^{th} - 22^{nd} hr of fermentation, and the ethanol production was maintained at 14 gL^{-1} from 16^{th} - 32^{nd} of fermentation time. The fed batch culture at 2 $gL^{-1}hr^{-1}$ glucose concentration feeding rate was a better fermentation system than the batch culture as the fed batch culture supported a higher yield of ethanol.

REFERENCES

Agilent Technologies. (2000). Capillary Column Installation Quick Reference Guide copyright@1994, 2000.

Bauchop, T. and Elsden, S.R. (1960). The growth of micro-organism in relation to their energy supply. *Journal of General Microbiology, 23*, 457.

Carine, B., Sandrine, A., Xavier, Carole, M.J., Uribelarrea, J.L. and Stéphane E. Guillouet. (2006). Minimization of glycerol production during the high-performance fed-batch ethanolic fermentation process in *Saccharomyces cerevisiae*, using a metabolic model as a prediction tool. *Applied and Environmental Microbiology, 72(3),* 2134–2140.

Converti, A.P., Lodi, P.A., Parisi, F. and Borghi M.D. (1985). A kinetic study of saccharomyces strains: Performance at high sugar concentrations. *Biotechnology Bioengineering, 27*, 1108-1114.

Coppella, S.J. and Dhurjati, P. (1989). A detailed analysis of Saccharomyces *cerevisiae* growth kinetics in batch, fed-batch and hollow-fiber bioreactors. *The Chemical Engineering Journal, 41,* B27 – B35.

Mian, F.A., Kuenzi, H.T. and Halvorson, H.O. (1997). Studies on mitochondrial membrane proteins in Saccharomyces *cerevisiae* under different degrees of glucose depression. *Journal of Bacteriology, 115*, 876.

Miller, G.L. (1959). Use of DNS reagent for the determination of reducing sugars. *Analytical Chemistry, 31*, 426-428.

Sitton, O.C. and Gaddy, J.L. (1980). Ethanol production in an immobilized cell reactor. *Biotechnology Bioengineering, 22*, 1735-1748.

Solomon, B.O., Odeseye, O.R., Betiku, E. and Pretorius, I.S. (1997). Investigation of starch degradation ability of Saccharomyces *cerevisiae* strain ZC89 in batch processes. *JNSChE, 16,* 69-76.

Stanbury, P.F. and Whitaker, A. (1984). *Principles of Fermentation Technology*. Oxford: Pergamon Press.

Thomas, K.C. and Ingledew, W.M. (1992). Production of 21% (v/v) ethanol by fermentation of Very High Gravity (VHG) wheat mashes. *Journal of Industrial Microbiology and Biotechnology, 10*, 61–68.

Vega, J.L., Clausen, E.C. and Gaddy, J.L. (1987). Acetate addition to an immobilized yeast column of ethanol production. *Biotechnology Bioengineering, 29*, 429-435.

Yan Lina and Shuzo Tanaka. (2006). Ethanol fermentation from biomass resources: current state and prospects. *Applied Microbiology Biotechnology, 69*, 627-642.

Yoshida, F., Yamane, T. and Nakamoto, K. (1973). Fed-batch hydrocarbon fermentation with colloidal emulsion feed. *Biotechnology Bioengineering, 15*, 257-270.

ISSN: 0128-7680
Pertanika J. Sci. & Technol. **17 (2)**: 409 – 424 (2009)

Analysis of Process Parameters Effect on Synthesis of Carboxymethylcellulose

Awang Bono*, Duduku Krisnaiah, Yan Yan Farm, Noor Maizura Ismail and Lee Muei Chng
Chemical Engineering Programme, School of Engineering and Information Technology, Universiti Malaysia Sabah, 88999 Kota Kinabalu, Sabah, Malaysia
**E-mail: awang@pc.jaring.my*

ABSTRACT

Synthesis of carboxymethylcellulose (CMC) from natural cellulose is an important industrial process. The effect of process parameters on the synthesis process is important information for the efficiency improvement of production process. Most of the previous studies on the effect of process parameters on the synthesis of CMC are based on the One-Factor-At-Time (OFAT); therefore, in this work, the response surface methodology (RSM) was used. Here, the cellulose was converted to CMC through carboxymethylation process using a technique of William etherification in heterogeneous system. The process parameters studied include the solvent ratio, reaction temperature and reactant ratio (molar ratio of NaOH to SMCA). Meanwhile, the analysis and optimization of the responses of the process, degree of substitution (DS) and yield were also performed using the response surface methodology. The validity of the synthesis process was identified by the determination of CMC spectrum using the fast Fourier infrared spectrometer (FTIR). The analysis of the results shows that carboxymethylation is strongly affected by combination of process parameters studied. The results obtained also show that the optimum responses, degree of substitution (DS) is 0.87 and yield is 1.80, whereas the optimum process parameters, solvent ratio is 0.70v/v, reaction temperature at 56.03°C, and molar ratio of NaOH to SMCA at 1.00mol/mol. These findings conclude that the DS and yield of carboxymethylation of cellulose are strongly affected by the combination of the process parameters.

Keywords: Carboxymethylcellulose, degree of substitution, one-factor-at-time, William etherification

ABBREVIATIONS

ANOVA	Analysis of Variance
CMC	Carboxymethylcellulose
DS	Degree of Substitution
FTIR	Fourier Transform Infrared
OFAT	One-Factor-At-Time
RSM	Response Surface Methodology

Received: 29 April 2008
Accepted: 20 May 2008
*Corresponding Author

INTRODUCTION

Modified cellulose is a form of cellulose which has become an important industrial polymer with a wide range of applications in many areas. Cellulose as raw material to cellulose derivatives production is a wonderful material in nature, and it can be found in all plant matters, including agricultural waste and forest debris to grass clippings. Intrinsic properties of this cellulose, which are unique in many ways, have caused its fundamental research and industrial applications to be hindered by its natural structures. As an example, the properties like high crystalline structure or less accessibility of its reactive sites often limit its dissolving characteristics in common organic solvents, and hence, restrict its accessibility for chemical reactions and biological and microbial treatments (McMurry, 1998). This leads to production of modified cellulose which generally enhances the functionalities of cellulose because more desirable properties are incorporated.

Various types of modified cellulose with their specific characteristic were developed. Commercial cellulose derivatives, such as cellulose diacetate, cellulose ethers, halodeoxycellulose having water solubility, organic-solvent solubility, ion-exchanging groups, or hydrophobic groups, are used as aqueous thickeners, plastics, column-supporting materials for chromatography, and others. The typical chemical modifications of the cellulose are etherification and etherification at hydroxyl groups of cellulose. One of the famous cellulose ether, which is carboxymethylcellulose, has gained its positions on the market due to its availability, economic efficiency, easy handling and low toxicity. CMC is used primarily in foods, drugs and cosmetics as a viscosifier, emulsion stabilizer, thickener and to improve texture. CMC is also used in detergent as an antiredeposition agent, textile warp-sizing aid, adhesives, latex paints and polishes.

Cellulose ethers are prepared based on the William etherification method by replacing the hydrogen on the cellulose hydroxyl groups with an alkyl group (Tijsen *et al*., 1999). The substitution reaction first involves the removal of the hydrogen by sodium hydroxide to make alkali cellulose. The alkali cellulose is then reacted with chloroacetic acid or sodium chloroacetic acid as the substituting agent. The degree of substitution (DS) is used to indicate the extent of the reaction. The DS is a major factor in the water solubility of Na CMC, below approximately 0.4 the polymer is swellable but insoluble; above this, the polymer is fully soluble with its hydro affinity increasing with increasing DS (Togrul and Arslan, 2003).

The dependence of reaction yield and degree of substitution on reagents concentration, reaction time, reaction temperature and solvent have been reported for carboxymethylation reaction using various sources of cellulose (Barai *et al*., 1996; Togrul and Arslan, 2003; Adinugrada *et al*., 2005; Dapia *et al.*, 2003; Varshney *et al*., 2006). Nonetheless, none of them analyzed the effects of the reaction parameters using response surface methodology. Most of them had analyzed based on the One-Factor-At-Times (OFAT) which is time consuming and lack information on the combined effect of the reaction parameters on carboxymethylation reaction. As compared to the OFAT, the response surface methodology involves a smaller number of runs, thereby reduces the cost and amount of time required for the experiment. The conclusions obtained from the response surface methodology include more accuracy since the OFAT may also miss out the best settings if the variables interact, that is, if the effect of a variable on the quality or performance of a process or product is dependent on the setting of another variables (Fabio *et al*., 2006; Myers and Montgomery, 1995; Bono *et al.*, 2007).

Process studies on the carboxymethylation of cellulose have not been well expanded to produce modified cellulosic materials for daily and industrial necessities. In fact, the production of this kind of product with various properties is possible, and will contribute to global economy. Most properties of the CMCs in actual applications, are dependent on a large extent, on three key parameters – molecular weight of the polymer, the average number of carboxymethyl substituents

per anhydroglucose unit (degree of substitution, DS), and the distribution of the carboxymethyl substituents along the polymer chain (Schult and Moe, 1997). In this work, the perception in the factors, which affect the carboxymethylation reaction and allow determination of the optimum operating condition using the RSM to achieve carboxymethylated cellulose with a high degree of substitution, was studied. This provides a valuable input for the development of kinetic models for the carboxymethylation process in future studies.

MATERIALS AND METHODS

Synthesis of Sodium Carboxymethylcellulose

The synthesis of the CMC was conducted in two steps, namely alkalization and etherification of cellulose under heterogeneous conditions. Alkalization work is a pre-treatment step for etherification reaction. The reaction was conducted in a temperature controlled water bath to maintain the reaction temperature at the required value. A motor running stirrer was also used to homogenize the solution and speed up the reaction. Oven was used to dry the resulted product. The dried product was blended into powder form for the DS analysis. Pure cellulose in adequate amount was suspended in 100ml of ethanol:isopropanol in an appropriate ratio under mechanical stirring. 10 ml of aqueous sodium hydroxide as swelling agent was added drop-wise and the solution then was stirred for an hour at room temperature (Pushpamalar *et al.,* 2006). Carboxymethylation reaction was started with an addition of sodium monochloroacetate (SMCA) with the reaction mixture placed in the temperature controlled water bath. The reaction mixture was then heated up to the reaction temperature and stirred for three hours of reaction time (Pushpamalar *et al*., 2006). This period of time is the optimum time for inducing better contacts between the etherifying agent and cellulose. Prolonged time increased degradation of the polymer which will lower the value of degree substitution (Bhattacharyya *et al*., 1995; Heinze and Pfeiffer, 1999). The slurry was neutralized with 90% acetic acid and then filtered. The CMC was purified by washing it with 70% ethanol four times to remove undesired byproducts. Then, the CMC was filtered and dried at 60^{o}C in an oven (Pushpamalar *et al.,* 2006).

Fourier Transform Infrared Spectroscopy of Sodium Carboxymethylcellulose

Fourier Transforms IR is a common instrument used to identify type of chemical bonds (functional group) in polysaccharides. Infrared absorption spectrum like molecular "fingerprint" was produced for this purpose. Different types of polysaccharides have distinct molecular "fingerprint" in the spectrum. With this fingerprint region, molecular compounds in polysaccharides such as cellulose and carboxymethylcellulose can be differentiated. Therefore, carboxymethylcellulose products were calibrated using the Fourier Transforms IR (FTIR) instrument in this research. The infrared spectra of the CMC samples were recorded with the FTIR. To get the spectra, a pellet made from the CMC samples was ground with KBr. Transmission was measured at the wave number range of 4000–400cm^{-1}.

Yield Measurement

Yield value is one of the responses to be optimized in this study. It indicates the amount of production based on the dry weight basis. An analytical balance was used for the yield measurement. The dry carboxymethylcellulose was weighed out and the net weight was divided with 5g of cellulose to get the yield value.

Determination of Degree of Substitution

The degree of substitution (DS) of the sample CMC was determined by the standard method (ASTM, 1961). 4 g of sample and 75ml. of 95% ethyl alcohol were agitated in 250ml. beaker for 5 min. 5 ml of nitric acid was then added. A hotplate was used to boil the solution, and this solution was then removed from the hotplate and further stirred for 10 minutes. Using a vacuum pump, liquid solution was decanted and washed 5 times with 80% ethyl alcohol (60ºC). Then, the precipitate was washed with a small quantity of anhydrous methanol and apply vacuum to remove the alcohol. Finally, the filter was dried at 105ºC for 3 hours and cooled in desiccators for half an hour. 1 to 1.5g of dry carboxymethylcellulose was added to 100ml of water and 25 ml of hydroxide 0.3N with agitation. The solution was heated to boil for 15 to 20 minutes. After the products dissolved, the mixture was titrated by 0.3N HCI. Phenolphthalein indicator was added to observe the colour change from Mexican pink (dark pink) to colourless.

To calculate the degree of substitution, equations (1) and (2) were used:

$$A = \frac{BC - DE}{F} \quad (1)$$

$$\text{Degree of substitution} = \frac{0.162 \times A}{1-(0.058 \times A)} \quad (2)$$

Where,
A = milli-equivalents of consumed acid per gram of specimen;
B = volume of Sodium hydroxide added;
C = concentration in normality of sodium hydroxide added;
D = volume of consumed chloric acid;
E = concentration in normality of Chloric acid used;
F = specimen grams used;

162 are the molecular weight of the anhydrous glucose unit and 58 is the net increment in the anhydrous glucose unit for every substituted carboxymethyl group.

Optimization of the CMC Production

The response surface methodology (RSM), combined with a Box-Behnken design, was used to find out the relationship between the response functions and the process variables, and to determine the conditions of these variables able to optimize the carboxymethylation.

Therefore, to reduce the experimental runs in reasonable limit, some variables were fixed according to the literature review (Barai *et al*., 1996; Togrul and Arslan, 2003; Adinugrada *et al*., 2005; Dapia *et al*., 2003; Pushpamalar *et al*., 2006; Varshney *et al*., 2006). The variables used are shown in Table 1. Optimization was done through the response surface methodology (RSM) using Design Expert software. This software is a statistical tool to study the process optimization efficiently through a series of design and analysis. With the range of factors in Table 2, the DS and Yield were targeted to the maximum for the optimization purpose in the software using numerical optimization.

The reaction was optimized with respect to the DS and yield varying each of the reaction parameters. There reaction parameters optimized were the volume ratio of ethanol to isoprophyl alcohol, reaction temperature and molar ratio of NaOH to SMCA. Meanwhile, the range of factors is shown in Table 2. The DS and yield were selected as quantitative responses.

TABLE 1
Values of the reaction parameters used

Factors	Value
Cellulose	5g
Weight of solvent	100ml
Time	3hr
Alkalization time	1hr
Alkalization temperature	30°C
Sodium Monochloroacetate	6.0g

TABLE 2
Range of reaction parameters for optimization

Parameter	Range
Ethanol : Isoprophyl Alcohol (v:v)	0.50 – 2.00
Reaction Temperature (°C)	30 - 60
NaOH : SMCA (mol:mol)	1 - 3

RESULTS AND DISCUSSION

Carboxymethylation Process

Fig. 2 shows the IR spectrum of the sample carboxymethylcellulose at DS 0.731. This spectrum was compared with commercial CMC spectrum at DS 0.75-0.9 (*Fig. 1*). The two spectrums have similar bands at certain peaks, illustrating the fingerprint region (highlighted in oval) of the CMC. The IR spectra show the typical absorption of the cellulose backbone and the presence of the carboxymethyl ether group at 1600cm^{-1}. The area inside the oval is the fingerprint region for the CMC.

Based on the data presented in *Fig. 2*, the bands in the region 1350-1450cm^{-1} are due to symmetrical deformations of CH_2 and OH groups. In the fingerprint region, the bands showing the ether bonds in CMC are 1250-1050cm^{-1} (Georgelt, 1996). The presence of a new and strong absorption band at 1600 cm^{-1} is confirms the stretching vibration of the carboxyl group (COO^-) and 1415cm^{-1} is assigned to carboxyl groups as its salt.

The RSM Analysis of Carboxymethylation Reaction

The experimental results of degree of the substitution (DS) and the yield value were applied to obtain the regression models. Table 3 shows the experimental design compiled in the Design-Expert software. From the compilation, there are 17 runs needed in this study to determine the optimum reaction condition. From Table 3, 17 sets of run, with relevant parameter values, were studied. A statistical analysis was also performed on the experimental results.

The quality of the models was evaluated using ANOVA, in which the repetition supplied the freedom degree to obtain the pure error. Meanwhile, the regression analysis was performed to fit the response function and experimental data, and the ANOVA was required to evaluate the second

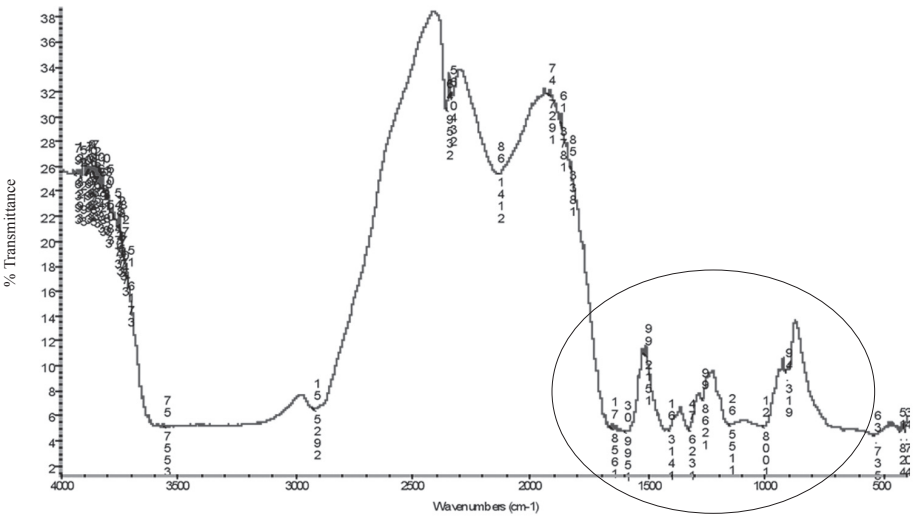

Fig. 1: FTIR spectrum for commercial CMC with DS at 0.75-0.9

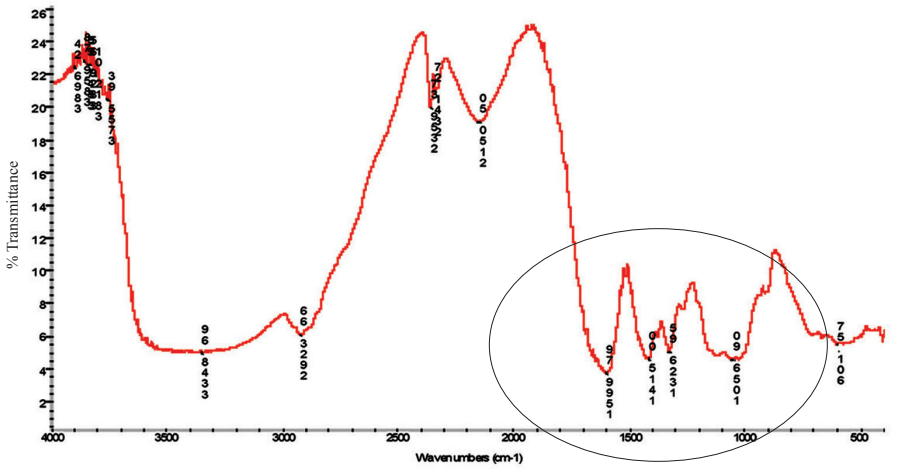

Fig. 2: FTIR spectrum for sample CMC with DS at 0.731

order model for both responses. From the ANOVA, the quadratic model for both responses was found to be significant. The quadratic models for the DS and yield, in terms of the coded factors, are shown in the following equations:

$$DS = 0.75-0.022A + 0.15B - 0.050C - 0.056A^2 - 0.16B^2 - 0.059C^2 + 0.012AB +0.071A-0.10BC \quad (3)$$

TABLE 3
Design Data for the analysis and optimization using the design expert software

Run	Block	Factor 1 A: Ethanol: Isoprophyl alcohol (v/v)	Factor 2 B: Reaction temp. (°C)	Factor 3 C: NaOH:SMCA (mol/mol)	DS	Yield
1	Block 1	1.25	45	2	0.729	1.551
2	Block 1	2.00	60	2	0.600	1.3696
3	Block 1	0.50	30	2	0.489	1.2496
4	Block 1	2.00	30	2	0.413	1.1316
5	Block 1	1.25	45	2	0.803	1.3530
6	Block 1	1.25	45	2	0.735	1.4188
7	Block 1	1.25	60	3	0.583	1.2802
8	Block 1	0.50	60	2	0.627	1.4100
9	Block 1	0.50	45	1	0.767	1.6698
10	Block 1	1.25	60	1	0.901	1.7988
11	Block 1	1.25	45	2	0.707	1.4466
12	Block 1	2.00	45	1	0.588	1.6876
13	Block 1	1.25	30	3	0.358	1.5484
14	Block 1	1.25	45	2	0.778	1.5011
15	Block 1	1.25	30	1	0.276	1.6154
16	Block 1	2.00	45	3	0.646	1.3214
17	Block 1	0.50	45	3	0.542	1.3072

$$\text{Yield} = 1.45 - 0.016A + 0.039B - 0.16C - 0.11A^2 - 0.050B^2 + 0.16C^2 + 0.019AB - 9.00\text{x}10^{-4}AC - 0.11BC \quad (4)$$

Where A represents volume ratio of ethanol to isoprophyl alcohol, B represents reaction temperature and C represents molar ratio of NaOH to SMCA.

Effect of Solvent on Carboxymethylation

The effects of the solvents on the DS and yield values, when the molar ratio of NaOH to SMCA and reaction temperature were selected at 2.00 and 45°C as the centre point, are shown in *Figs. 3* and *4*, respectively.

From the One Factor Plot in *Fig. 3*, it shows that there is an optimum DS value when the ratio of solvent medium was increased. The maximum value of the DS was found when the solvent ratio

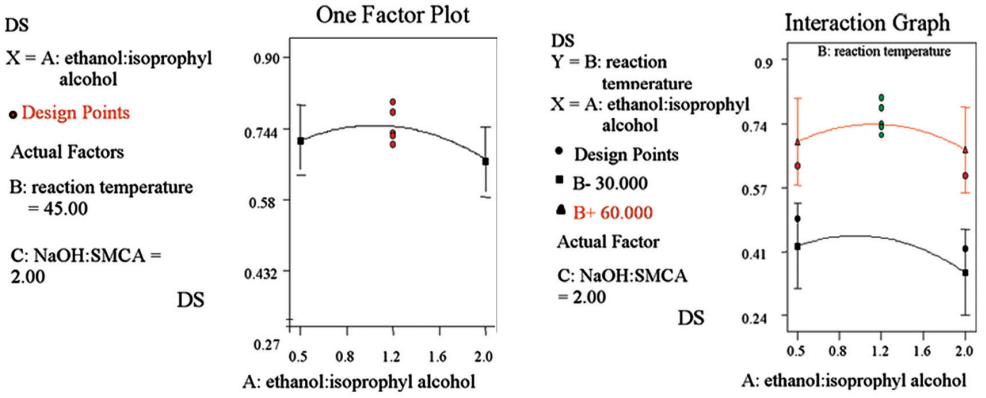

Fig. 3: The effect of the ratio between ethanol and isoprophyl alcohol on DS when the reaction temperature and molar ratio NaOH:SMCA were maintained at 45°C and 2, respectively

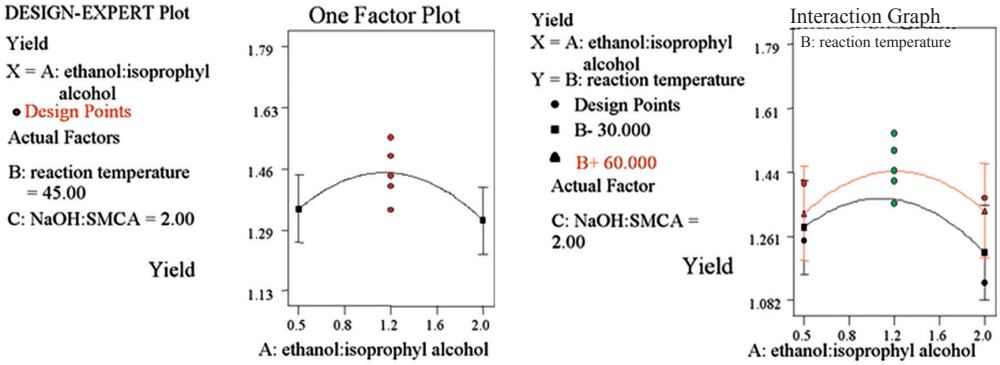

Fig. 4: The effect of the ratio between ethanol and isoprophyl alcohol on yield when the reaction temperature and molar ratio of NaOH:SMCA were maintained at 45°C and 2, respectively

near to 1.00 for reaction at 45°C. Above this value, the DS decreased. This indicates that the main reaction [equation 5(a) and 5(b)] is preferred when the concentration on ethanol and isopropanol is equal, while the interaction graph shows a simultaneous effect of the reaction temperature and solvent ratio on the DS value. It shows that the DS value is limited by the reaction temperature where the DS value can achieve the optimum points and then decreases with higher solvent ratio (higher preferences on isopropanol solvent).

From the One Factor Plot in *Fig. 4*, the yield curve shows a slight difference with the DS plot. However, the effect of the solvent ratio is the same with the DS where the yield value increases to optimum point and drops gradually with increasing solvent ratio. Nonetheless, the optimum point of the yield plot is closer to the solvent ratio at 1.25.

These figures show that appropriate solvent ratio is needed to obtain the optimum value for the DS and yield. The effect of the solvent system on the extent of the reaction is related to miscibility, which is the ability to solubilise the etherifying agents and to swell the cellulose to improved

accessibility of the etherifying agent into the cellulose structure. The interaction graph is therefore important to show the simultaneous effect of the solvent and reaction temperature on reaction. *Figs. 3* and *4* provide information on the preferences of solvent in driving carboxymethylation reaction (equation 5a) to the right at different temperatures.

$$R_{cell}OH + NaOH \leftrightarrow R_{cell}\,OH.NaOH \quad (5a)$$

$$R_{cell}OH.NaOH + ClCH_2COONa \rightarrow R_{cell}OCH_2COONa + NaCl + H_2O \quad (5b)$$

Side Reaction

$$NaOH + ClCH_2COONa \rightarrow HOCH_2COONa + NaCl \quad (6)$$

The Effect of Molar Ratio of NaOH to SMCA on Carboxymethylation

By maintaining the solvent ratio and reaction temperature at 1.25 and 45°C respectively, the effects of alkali concentration on the DS and yield were studied (*Figs. 5* and *6*). Here, the effect of alkali on reaction was studied through One Factor Plot in the RSM. The yield and DS were responses distinctively with the alkali concentration (the concentration of the SMCA was maintained at 6.0 g in this work) which are described in the following paragraph.

It was observed that the degree of substitution showed an opposite effect with the yield response when the sodium hydroxide concentration was increased. From the One Factor Plot in *Fig. 5*, it is observed that the DS value responded distinctively with the concentration of the sodium hydroxide. When the sodium hydroxide concentration was increased, the DS value was found to increase gradually to the optimum point. At lower sodium hydroxide concentration, the DS curve sloped steeply and then dropped gradually with the increasing alkali concentration. However, the DS value at lower NaOH concentration was still higher as compared to the higher concentration of NaOH. The interaction plot shows the combined effect of solvent and molar ratio of NaOH:SMCA to DS. The graph shows that the solvent with appropriate amount of sodium hydroxide and SMCA gives a better product with higher DS.

Prior to alkylation, cellulose was treated with aqueous alkali, exposing the less crystalline regions to be attacked by the reagents, where heterogeneity of the product was the consequence. Carboxymethylation reaction involves two competing reactions which take place simultaneously (equations 5 and 6) (Pushpamalar *et al*., 2006). The first reaction was between cellulose and monochloroacetic acid in the presence of alkali (equation 5). The second one was the reaction between sodium hydroxide with monochloroacetic acid to form sodium glycolate (equation 6). The first reaction seemed to prevail up to a certain NaOH concentration. Above this concentration, the second reaction was predominated with the formation of a larger amount of sodium glycolate, which decreased the DS value. By looking at the One Factor Plot in *Fig. 5*, the reaction is therefore preferential for lower NaOH concentration.

Based on the One Factor Plot in *Fig. 6*, the relationship between the sodium hydroxide concentration and yield was the opposite of the DS. In particular, higher yield was obtained at lower NaOH concentration. At particular alkali strength, the yield was decreased to minimum and then started increasing. Higher yield at lower NaOH concentration might be due to the formation of sodium glycolate which was difficult to be removed from the sample. The interaction plot gave important information, i.e. the interaction between solvent and NaOH produces the maximum yield of product.

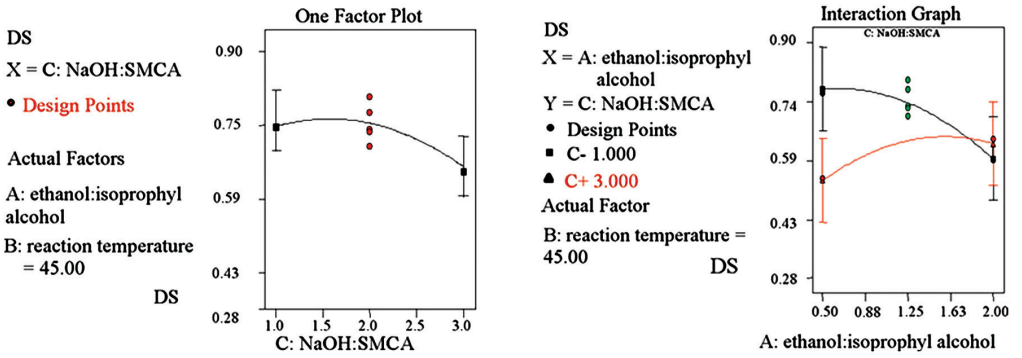

Fig. 5: The effect of the molar ratio NaOH:SMCA on DS when the ratio between ethanol and isoprophyl alcohol and the reaction temperature were maintained at 1.25 and 45°C, respectively

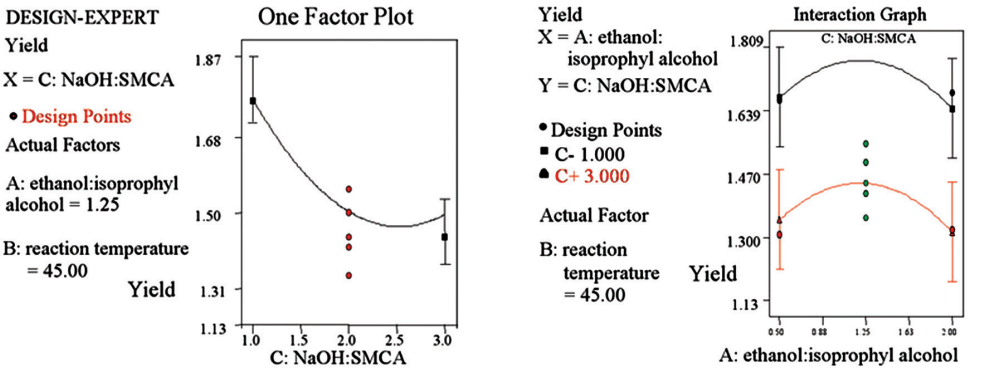

Fig. 6: The effect of the molar ratio NaOH:SMCA on yield when the ratio between ethanol and isoprophyl alcohol and the reaction temperature were maintained at 1.25 and 45°C, respectively

Effect of Reaction Temperature on Carboxymethylation

Figs. 7 and *8* show the effect of the reaction temperature on the degree of substitution and yield when the solvent ratio was maintained at 1.25 and the molar ratio of NaOH to SMCA was maintained at 2.00. It was also observed that the responses were increased by increasing the reaction temperature until the optimum point was achieved. The response values were decreased with the increasing temperature.

From *Fig. 7*, One Factor Plot quadratic curve was obtained for the DS plot. There was a significant and drastic increase in the degree of substitution with temperature, within the range between 30°C – 52.50°C for the molar ratio of NaOH to SMCA at 2.00. The increased of the DS might be due to the fact that there was a better environment created that favoured the reaction to the right (equation 5). Similarly with the DS, the effect of reaction temperature on the yield at higher NaOH concentration was increased with the reaction temperature until a maximum value thereafter decreased *(Fig. 8)*. However, the curve is not as steep as in the DS plot. This might be due to the cellulose degradation causing lost of water from cellulose (Pushpamalar *et al*., 2006). These provide information which indicates that the reaction temperature is an important factor to influence the carboxymethylation reaction for desired product.

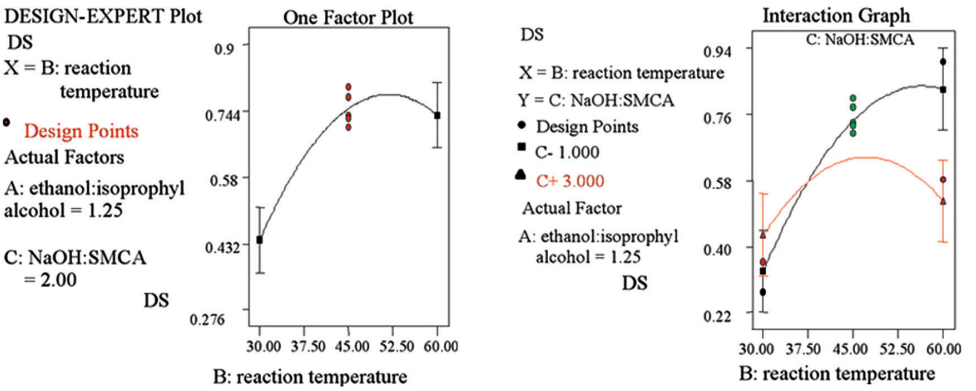

Fig. 7: The effect of the reaction temperature on DS when the ratio between ethanol and isoprophyl alcohol and the molar ratio of NaOH:SMCA were maintained at 1.25 and 2.00, respectively

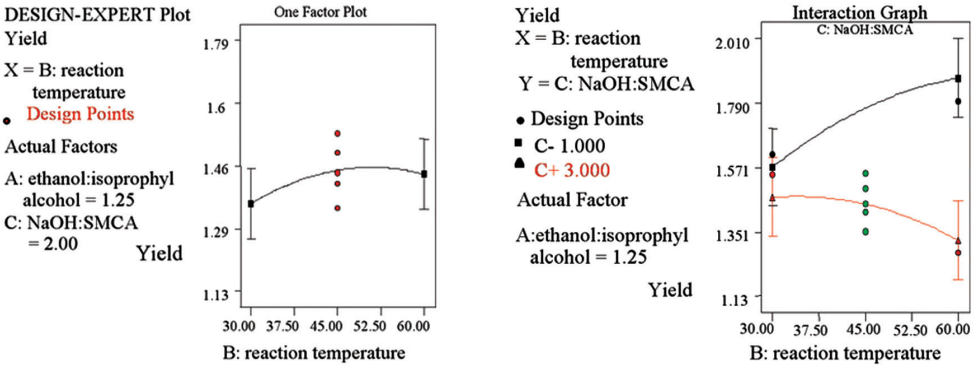

Fig. 8: The effect of the reaction temperature on yield when the ratio between ethanol and isoprophyl alcohol and the molar ratio of NaOH:SMCA were maintained at 1.25 and 2.00, respectively

From both plots, it shows that the reaction temperature gives the same effect on the responses, while they may be shown differently when the interaction with other factors are considered, as shown in the interaction graph in *Figs. 7* and *8*. Looking at the Interaction Plot depicted in *Fig. 7*, lower concentration of molar ratio NaOH:SMCA performs better in higher reaction temperature for the carboxymethylation reaction to occur. Where it could be observed that the curve sloped steeply at lower concentration of molar ratio of NaOH:SMCA when the reaction temperature increased. Similar to the DS responses, the yield value was higher when carboxymethylation reaction occurred in lower concentration and higher temperature.

Optimization of Process Parameters on Carboxymethylation Process

Based on the model, the relationship between the response and the variables is visualized by a response surface or contour plot to indicate the relative influence of the parameters, find an optimum parameter combination, and predict the experimental results for other parameter combinations. The numerical optimization was carried out with the help of Design Expert v.6.0.10, considering each value of response and three solutions were obtained, as shown in Table 4.

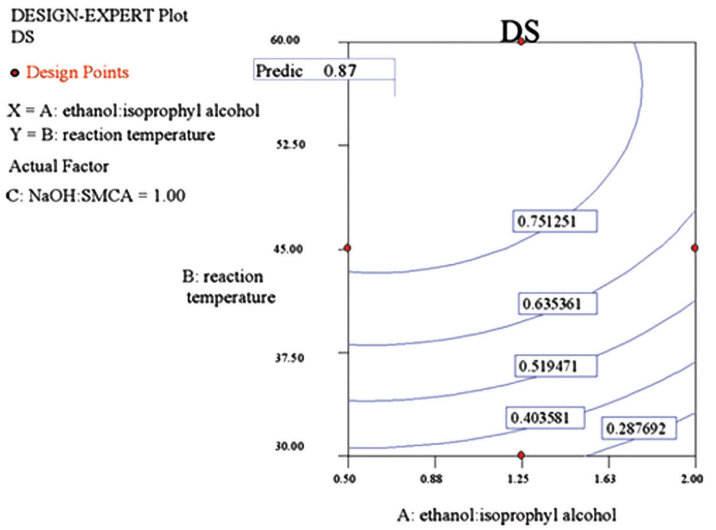

Fig. 9: Optimization contour plot on the DS value when NaOH:SMCA remained constant at 1.00

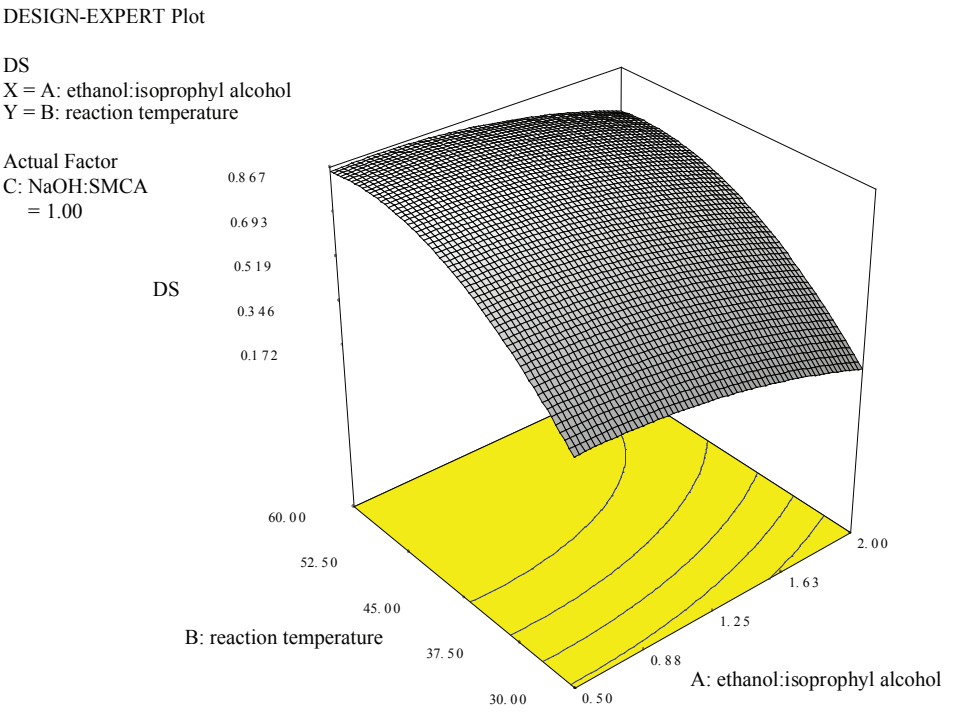

Fig. 10: Optimization of the 3D response surface on the DS value when NaOH: SMCA remained constant at 1.00

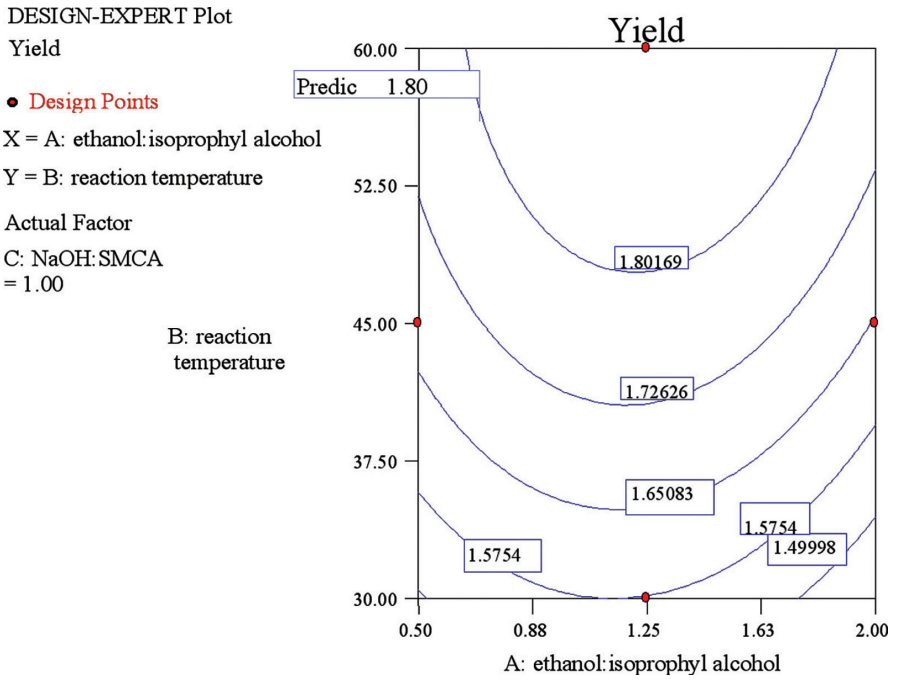

Fig. 11: Optimization contour plot on yield when NaOH:SMCA remained constant at 1.00

TABLE 4
Solutions of optimization on DS and yield

Name	Goal	Lower Limit	Upper Limit
ethanol:isoprophyl alcohol	is in range	0.5	2
reaction temperature	is in range	30	60
NaOH:SMCA	is in range	1	3
DS	Maximize	0.2760	0.901
Yield	Maximize	1.1316	1.7988

Solutions	1 (Selected)	2	3
ethanol:isoprophyl alcohol	0.70	0.77	0.87
reaction temperature	56.03	55.91	49.25
NaOH:SMCA	1.00	1.00	1.00
DS	0.87	0.87	0.83
Yield	1.80	1.81	1.79
Desirability	0.98	0.97	0.94

TABLE 5
Previous study on the carboxymethylation reaction condition

Reference	Reaction temp.	Reaction time (min)	NaOH	SMCA (g)	Cellulose (g)	Solvent (ml)	DS
Barai *et al.,* 1996 (water hyacinth)[a]	75* 30-75	360* 60-360	10% (2.5M)*	0.92 : 1(w/w)*		Isopropanol - 110	0.72*
Pushpamalar *et al.,* 2006 (sago waste)[a]	45*	180*	10ml of 25%*	6.0*	5	Pure isopropanol	0.821*
Togrul and Arslan, 2003 (sugar beet pulp cellulose)[a]	70*	360*	30% in 20ml*	3.0*	2.0	Isobutyl alcohol	0.667*
Zhao *et al.,* 2003 (cotton linter)[a]	50-60	30	NaOH/AGU: 2:1(mol)	MCA/AGU: 1.5:1(mol)	100	Benzene-ethanol	1.10*
Varshney *et al.,* 2006 (Lantana camara)[a]	55* (35-65)	210*	3.24mol/AGU, 20% (w/v)* (10-40%)	2.05*mol/AGU (1.55-2.30)	3	Isoprophyl alcohol	1.22*

*Optimized value

[a]Cellulose source

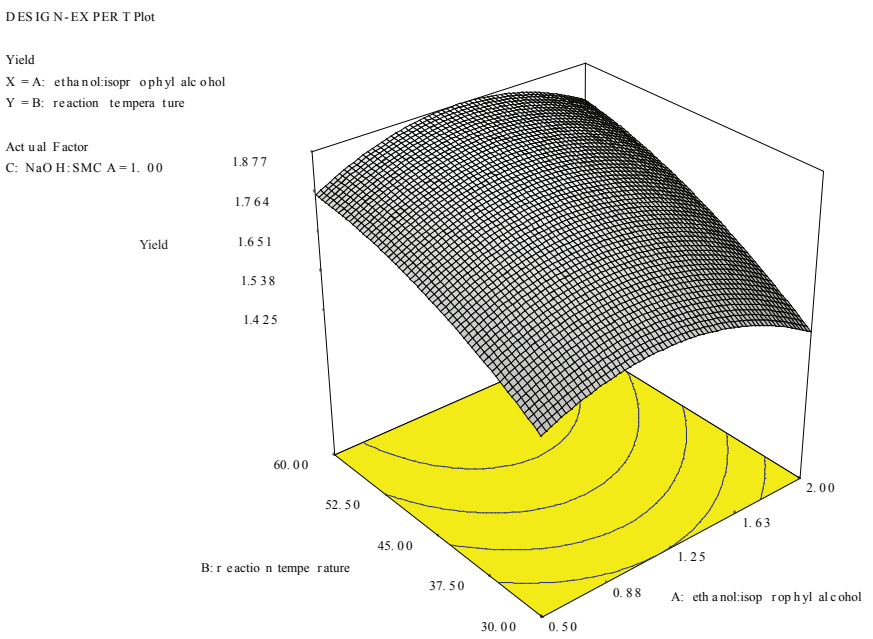

Fig. 12: Optimization of 3D response surface on Yield when NaOH:SMCA remained constant at 1.00

From Table 4, there are three solutions suggested from the numerical optimization. The best results of the DS value and yield obtained under optimized condition, selected among the three, were 0.87 and 1.80g/g, respectively. The optimized conditions were the volume ratio of ethanol to isoprophyl alcohol at 0.70, the reaction temperature at 56.03ºC, and the molar ratio of NaOH to SMCA at 1.00.

Figs. 9 through *12* show the response surfaces and the contour plot of the optimization result on the DS and yield under optimized condition. Based on these figures, the effects of the reaction condition on the responses were studied. The point identified by the flag in the contour plot was chosen in the graph, as a representative of the optimized area corresponding to the reaction condition. The contour plot in *Fig. 10* shows an elliptical and inclined profile implying the interaction effects between the reaction factors on the CMCs yield.

Table 5 shows the process parameters of carboxymethylation reaction in the previous study. These authors studied the production of carboxymethylcellulose from different sources of cellulose. However, none of them optimized the reaction condition using the RSM as in the present study. Instead, they used the one-factor-at-time (OFAT) to optimize the process parameters. However, the results reported (Table 5) were similar to the result obtained in the present study. The difference in the optimum condition could be attributed to the variation of the cellulose sources, the solvent used and the different reaction times. Nonetheless, the optimum DS obtained in the present study, which is 0.87, is similar to the previous study (0.6-1.3). This shows that the value obtained from the RSM analysis is reliable.

CONCLUSIONS

The conversion of cellulose to CMC was completed done using the carboxymethylation process of William etherification. The analysis results using the RSM show that the effects of reaction parameters are easily interpreted with less experimental runs, as compared to the OFAT conducted by most of the previous studies. The effects of the reaction parameters on the yield and DS were studied by performing the one factor plot, interaction plot, contour plot and surface plot. The results show that the DS and yield varies with the variation of combination of process parameters. The numerical optimization results also suggest that the optimum value of the DS and yield are 0.87 and 1.80, respectively, whereas the optimum condition of the process parameters, solvent ratio is 0.70v/v, reaction temperature at 56^{o}C, and the molar ratio of NaOH to SMCA at 1.00mol/mol.

REFERENCES

Adinugrada, M.P., Marseno, D.W. and Haryadi. (2005). Synthesis and characterization of sodium carboxylmethylcellulose from Cavendish banana pseudo stem (Musa cavendishii LAMBERT). *Carbohydrate Polymers*, *62*,164-169.

Barai, B.K., Singhal, R.S. and Kulkarni, P. (1996). Optimization of a process for preparing carboxymethyl cellulose from water hyacinth (Eichornia Crassipes). *Carbohydrate Polymers*, *32*, 229-231.

Bhattacharyya, D., Singhal, R.S. and Kulkarni, P.R. (1995). A comparative account of conditions for synthesis of sodium carboxymethyl starch from corn and amaranth starch. *Carbohydrate Polymers*, *27*, 247–253.

Bono, A., Rajin, M. and Krishniah, D. (2007). *Products Formulation and Process Optimization Using Response Surface Methodology*. Kota Kinabalu, Sabah: UMS Press. (In Press).

Dapia, S., Santos, V. and Parajo, J.C. (2003). Carboxymethylcellulose from totally chlorine free-bleached milox pulps. *Bioresource Technology*, *89*, 289-296.

Georgelt Schmid. (1996). *Organic Chemistry*. Mosby, USA.

Heinze, T. and Pfeiffer, K. (1999). Studies on the synthesis and charcterization of carboxymethylcellulose. Angewandte Makromolekulare. *Chemie*, *266*, 37–45.

Hua Zhao, Fa Cheng, Guifeng Li and Jingwu Zhang. (2003). Optimization of a process for carboxymethyl cellulose (CMC) preparation in mixed solvents. *International Journal of Polymeric Materials*, *52*, 749-759.

McMurry, J. (1998). *Fundamentals of Organic Chemistry* (4th edition). Singapore: Brooks/Cole Publishing Company.

Myers, D.H. and Montgomery, D.H. (1995). *Response Surface Methodology*. USA: John Wiley & Sons.

Pushpamalar, V., Langford, S.J., Ahmad, M. and Lim, Y.Y. (2006). Optimization of reactions conditions for preparing carboxymethyl cellulose from sago waste. *Carbohydrate Polymer*, *64*, 312-318.

Schult, T. and Moe, S.T. (1997). Viscosity loss and molecular weight degradation during etherification of high molecular weight cellulose. *9th International Symposium on Wood and Pulping Chemistry*, Montreal.

Tijsen, C.J., Scherpenkate, H.J., Stamhuis, E.J. and Beenackers, A.C.M. (1999). Optimization of the process conditions for the modification of starch. *Chemical Engineering Science*, *54*, 2765-2772.

Togrul, H. and Arslan, N. (2003). Production of carboxymethyl cellulose from sugar beet pulp cellulose and rheological behaviour of carboxymethyl cellulose. *Carbohydrate Polymer*, *54*, 73-82.

Varshney, V.K., Gupta, P.K., Naithani, S., Khullar, R., Bhatt, A. and Soni P.L. (2006). Carboxymethlyation of α-cellulose isolated from *Lantana Camara* with respect to degree of substitution and rheological behavior. *Carbohydrate Polymers*, *63*, 40-45.

Pertanika Journal of Science & Technology

Subject Index for Volume 17 Nos. 1 & 2 2009

Pertanika Journal of Science & Technology

Author Index for Volume 17 Nos. 1 &2 2009

REFEREES FOR THE PERTANIKA JOURNAL OF SCIENCE AND TECHNOLOGY (JST)

January – July 2009

The Editorial Board of the Journal of Science and Technology wish to thank the following for acting as referees for manuscripts submitted to JST between January and July 2009.

Abdul Halim Abdullah
Abdul Halim Shaari
Abdul Rahman Mohamed
Adeline Chua Seak May
Ahmad Husni Mohd Hanif
Ahmad Kamal Ariffin Mohd Ihsan
Amu Therwat
Ariffin Samsuri
Azlina Harun
Azmi Zakaria
Barkawi Sahari
Bassim H Hameed
Borhanuddin Mohd Ali
Chikkalingaiah
Chin Nyuk Ling
Dayang Radiah Awang Biak
Don Hee Park
Fakhru'l-Razi Ahmadun
Farah Nor Abdul Aziz
Halimah Mohamed Kamari
Ibni Hajar Rukunuddin
Intan Safinar Ismail
Irmawati Ramli
Isao Yumoto
Ismail Abu Bakar
Izian Abdul Karim
James, R
Jumiah Hassan
Kassim Haron
Law Chung Lim
Lee Teang Shui
Li Jing
Lim Chan Kiang
Low Heng Chin
Luqman Chuah Abdullah
Mahendran A/L S Shitan
Manal Ismail
Mansor Hashim
Masjuki Hassan
Masturah Markom
Md Dan Md Palil
Md Jelas Haron
Md Zahangir Alam
Megat Mohamad Hamdan Megat
Mohamad Nasir Mohamad Ibrahim
Mohd Adzir Mahdi
Mohd Amran Mohd Salleh
Mohd Khairol Anuar Mohd Ariffin
Mohd Nizar Hamidon
Mohd Sapuan Salit
Nazlina Ibrahim
Noor Akma Ibrahim
Nor Aishah Saidina Amin
Nor Aripin Shamaan
Norazah Abd Rahman
Norhafizah Abdullah
Norhashidah Awang
Othman A Karim
Prakash C Sinha
Rainbow Phillip
Raizal Saifulnaz Muhammad Rashid
Robiah Yunus
Rozi Abdullah
Shafreeza Sobri
Shahidan Radiman
Shuhaimi Mustafa
Siti Aslina Hussain
Siti Mazlina Mustapa Kamal
Siti Rozaimah Sheikh Abdullah
Siva Balasundram
Suraya Abdul Rashid
Taufiq Yap Yun Hin
Teh Boon Sung
Tey Beng Ti
Thomas Choong Shean Yaw
Wan Hamidon Wan Badaruzaman
Wan Mahmood Mat Yunus
Yap Chee Kong
Zakir A Ansari
Zurina Zainal Abidin

While every effort has been made to include a complete list of referees for the period stated above, however if any name(s) have been omitted unintentionally or spelt incorrectly, please notify the Executive Editor, *Pertanika* Journals at ndeeps@admin.upm.edu.my.

Pertanika

Our goal is to bring high quality research to the widest possible audience

Journal of Science & Technology

INSTRUCTIONS TO AUTHORS

(Manuscript Preparation & Submission Guidelines)

Revised January 2009

We aim for excellence, sustained by a responsible and professional approach to journal publishing.
We value and support our authors in the research community.

Please read the guidelines and follow these instructions carefully; doing so will ensure that the publication of your manuscript is as rapid and efficient as possible. The Editorial Board reserves the right to retum manuscripts that are not prepared in accordance with these guidelines.

About the Journal

Pertanika is an international peer-reviewed journal devoted to the publication of original papers, and it serves as a forum for practical approaches to improving quality in issues pertaining to tropical agriculture and its related fields. Pertanika Journal of Tropical Agricultural Science began publication in 1978. In 1992, a decision was made to streamline Pertanika into three journals to meet the need for specialised journals in areas of study aligned with the interdisciplinary strengths of the university. The revamped, Pertanika Journal of Science and Technology (JST) is now focusing on research in science and engineering, and its related fields. Other Pertanika series include Pertanika Journal of Tropical Agricultural Science (JTAS); and Pertanika Journal of Social Sciences and Humanities (JSSH).

JST is published in **English** and it is open to authors around the world regardless of the nationality. It is currently published two times a year i.e. in **January** and **July**.

Goal of Pertanika

Our goal is to bring the highest quality research to the widest possible audience.

Quality

We aim for excellence, sustained by a responsible and professional approach to journal publishing. JST is an international journal indexed in EBSCO.

Future vision

We are continuously improving access to our journal archives, content, and research services. We have the drive to realise exciting new horizons that will benefit not only the academic community, but society itself.

We also have views on the future of our journals. The emergence of the online medium as the predominant vehicle for the 'consumption' and distribution of much academic research will be the ultimate instrument in the dissemination of the research news to our scientists and readers.

Aims and scope

Pertanika Journal of Science and Technology aims to provide a forum for high quality research related to science and engineering research. Areas relevant to the scope of the journal include: *bioinformatics, bioscience, biotechnology and bio-molecular sciences, chemistry, computer science, ecology, engineering, engineering design, environmental control and management, mathematics and statistics, medicine and health sciences, nanotechnology, physics, safety and emergency management*, and related fields of study.

Editorial Statement

Pertanika is the official journal of Universiti Putra Malaysia. The abbreviation for Pertanika Journal of Science & Technology is *Pertanika J. Sci. Technol.*

Guidelines for Authors

Publication policies

Pertanika policy prohibits an author from submitting the same manuscript for concurrent consideration by two or more publications. It prohibits as well publication of any manuscript that has already been published either in whole or substantial part elsewhere.

Editorial process

Authors are notified on receipt of a manuscript and upon the editorial decision regarding publication.

Manuscript review: Manuscripts deemed suitable for publication are sent to the Editorial Advisory Board members and/or other reviewers. We encourage authors to suggest the names of possible reviewers. Notification of the editorial decision is usually provided within to eight to ten weeks from the receipt of manuscript. Publication of solicited manuscripts is not guaranteed. In most cases, manuscripts are accepted conditionally, pending an author's revision of the material.

Author approval: Authors are responsible for all statements in articles, including changes made by editors. The liaison author must be available for consultation with an editor of *The Journal* to answer questions during the editorial process and to approve the edited copy. Authors receive edited typescript (not galley proofs) for final approval. Changes **cannot** be made to the copy after the edited version has been approved.

Please direct all inquiries, manuscripts, and related correspondence to:

The Executive Editor
Pertanika Journals
Research Management Centre (RMC)
4th Floor, Administration Building
Universiti Putra Malaysia
43400 UPM, Serdang, Selangor
Malaysia
Phone: + (603) 8946 6192
Fax: + (603) 8947 2075
ndeeps@admin.upm.edu.my

or visit our website at http://rmc.upm.edu.my/pertanika for further information.

Manuscript preparation

Pertanika accepts submission of mainly four types of manuscripts. Each manuscript is classified as **regular** or **original** articles, **short communications**, **reviews**, and proposals for **special issues**. Articles must be in **English** and they must be competently written and argued in clear and concise grammatical English. Acceptable English usage and syntax are expected. Do not use slang, jargon, or obscure abbreviations or phrasing. Metric measurement is preferred; equivalent English measurement may be included in parentheses. Always provide the complete form of an acronym/abbreviation the first time it is presented in the text. Contributors are strongly recommended to have the manuscript checked by a colleague with ample experience in writing English manuscripts or an English language editor.

Linguistically hopeless manuscripts will be rejected straightaway (e.g., when the language is so poor that one cannot be sure of what the authors really mean). This process, taken by authors before submission, will greatly facilitate reviewing, and thus publication if the content is acceptable.

The instructions for authors must be followed. Manuscripts not adhering to the instructions will be returned for revision without review. Authors should prepare manuscripts according to the guidelines of Pertanika.

1. Regular article
Definition: Full-length original empirical investigations, consisting of introduction, materials and methods, results and discussion, conclusions. Original work must provide references and an explanation on research findings that contain new and significant findings.

Size: Should not exceed 5000 words or 8-10 printed pages (excluding the abstract, references, tables and/or figures). One printed page is roughly equivalent to 3 type-written pages.

2. Short communications
Definition: Significant new information to readers of the Journal in a short but complete form. It is suitable for the publication of technical advance, bioinformatics or insightful findings of plant and animal development and function.

Size: Should not exceed 2000 words or 4 printed pages, is intended for rapid publication. They are not intended for publishing preliminary results or to be a reduced version of Regular Papers or Rapid Papers.

3. Review article
Definition: Critical evaluation of materials about current research that had already been published by organizing, integrating, and evaluating previously published materials. Re-analyses as meta-analysis and systemic reviews are encouraged. Review articles should aim to provide systemic overviews, evaluations and interpretations of research in a given field.

Size: Should not exceed 4000 words or 7-8 printed pages.

4. Special issues
Definition: Usually papers from research presented at a conference, seminar, congress or a symposium.

Size: Should not exceed 5000 words or 8-10 printed pages.

5. Others
Definition: Brief reports, case studies, comments, Letters to the Editor, and replies on previously published articles may be considered.

Size: Should not exceed 2000 words or up to 4 printed pages.

With few exceptions, original manuscripts should not exceed the recommended length of 6 printed pages (about 18 typed pages, double-spaced and in 12-point font, tables and figures included). Printing is expensive, and, for the Journal, postage doubles when an issue exceeds 80 pages. You can understand then that there is little room for flexibility.

Long articles reduce the Journal's possibility to accept other high-quality contributions because of its 80-page restriction. We would like to publish as many good studies as possible, not only a few lengthy ones. (And, who reads overly long articles anyway?) Therefore, in our competition, short and concise manuscripts have a definite advantage.

Format

The paper should be formatted in one column format with the figures at the end. A maximum of eight keywords should be indicated below the abstract to describe the contents of the manuscript. Leave a blank line between each paragraph and between each entry in the list of bibliographic references. Tables should preferably be placed in the same electronic file as the text. Authors should consult a recent issue of the Journal for table layout.

There is no need to spend time formatting your article so that the printout is visually attractive (e.g. by making headings bold or creating a page layout with figures), as most formatting instructions will be removed upon processing.

Manuscripts should be typewritten, typed on one side of the ISO A4 paper with at least 4cm margins and double spacing throughout. Every page of the manuscript, including the title page, references, tables, etc. should be numbered. However, no reference should be made to page numbers in the text; if necessary, one may refer to sections. Underline words that should be in italics, and do not underline any other words.

Authors are advised to use Times New Roman 12-point font. Be especially careful when you are inserting special characters, as those inserted in different fonts may be replaced by different characters when converted to PDF files. It is well known that 'μ' will be replaced by other characters when fonts such as 'Symbol' or 'Mincho' are used.

We recommend that authors prepare the text as a **Microsoft Word** file.

1. Manuscripts in general should be organised in the following order:

   - **Page 1: Running title.** (Not to exceed 60 characters, counting letters and spaces). This page should **only** contain your running title/ full title of your paper. In addition, the **Subject areas** most relevant to the study must be indicated on this page. Select one or two subject areas (refer to the *Scope Form).*
     A **list** of number of **black and white / colour figures and tables** should also be indicated on this page**.**
     Figures submitted in color will be printed in colour. See "*5. Figures & Photographs"* for details.

   - **Page 2: Author(s) and Corresponding author information.** This page should **repeat** the title of your paper with name(s) of all the authors, institutions and corresponding author's name, institution and full address (Street address, telephone number (including extension), hand phone number, fax number and e-mail address) for editorial correspondence.

     Authors' addresses. Multiple authors with different addresses must indicate their respective addresses separately by superscript numbers:

     George Swan[1] and Nayan Kanwal[2]
     [1]Department of Biology, Faculty of Science, Duke University, Durham, North Carolina, USA.
     [2]Research Management Centre, Universiti Putra Malaysia, Serdang, Malaysia.

   - **Page 3**: This page should **repeat** the title of your paper with only the **Abstract** (the abstract should be less than 250 words for a Regular Paper and up to 100 words for a Short Communication). **Keywords** must also be provided on this page (Not more than eight keywords in alphabetical order).
   - **Page 4 and subsequent pages**: This page should begin with the **Introduction** of your article and the rest of your paper should follow from page 5 onwards.

   Abbreviations. Define alphabetically, other than abbreviations that can be used without definition. Words or phrases that are abbreviated in the introduction and following text should be written out in full the first time that they appear in the text, with each abbreviated form in parenthesis. Include the common name or scientific name, or both, of animal and plant materials.

   Footnotes. Current addresses of authors if different from heading.

2. **Text.** Regular Papers should be prepared with the headings **Introduction**, **Materials and Methods**, **Results and Discussion, Conclusions** in this order. Short Communications should be prepared according to "*8. Short Communications."* below.
3. **Tables.** All tables should be prepared in a form consistent with recent issues of Pertanika and should be numbered consecutively with Arabic numerals. Explanatory material should be given in the table legends and footnotes. Each table should be prepared on a separate page. (Note that when a manuscript is accepted for publication, tables must be submitted as data - .doc, .rtf, Excel or PowerPoint file- because tables submitted as image data cannot be edited for publication.)

4. **Equations and Formulae.** These must be set up clearly and should be typed triple spaced. Numbers identifying equations should be in square brackets and placed on the right margin of the text.

5. **Figures & Photographs.** Submit an original figure or photograph. Line drawings must be clear, with high black and white contrast. Each figure or photograph should be prepared on a separate sheet and numbered consecutively with Arabic numerals. Appropriate sized numbers, letters and symbols should be used, no smaller than 2 mm in size after reduction to single column width (85 mm), 1.5-column width (120 mm) or full 2-column width (175 mm). Failure to comply with these specifications will require new figures and delay in publication. For electronic figures, create your figures using applications that are capable of preparing high resolution TIFF files acceptable for publication. In general, we require **300 dpi or higher resolution for coloured and half-tone artwork** and **1200 dpi or higher for line drawings**. For review, you may attach low-resolution figures, which are still clear enough for reviewing, to keep the file of the manuscript under 5 MB. Illustrations may be produced at extra cost in colour at the discretion of the Publisher; the author could be charged Malaysian Ringgit 50 for each colour page.

6. **References.** Literature citations in the text should be made by name(s) of author(s) and year. For references with more than two authors, the name of the first author followed by 'et al.' should be used.

   Swan and Kanwal (2007) reported that …
   The results have been interpreted (Kanwal et al. 2009).

   - References should be listed in alphabetical order, by the authors' last names. For the same author, or for the same set of authors, references should be arranged chronologically. If there is more than one publication in the same year for the same author(s), the letters 'a', 'b', etc., should be added to the year.
   - When the authors are more than 11, list 5 authors and then et al.
   - Do not use indentations in typing References. Use one line of space to separate each reference. For example:
     - Jalaludin, S. (1997a). Metabolizable energy of some local feeding stuff. *Tumbuh, 1,* 21-24.
     - Jalaludin, S. (1997b). The use of different vegetable oil in chicken ration. *Mal. Agriculturist, 11,* 29-31.
     - Tan, S.G., Omar, M.Y., Mahani, K.W., Rahani, M., Selvaraj, O.S. (1994). Biochemical genetic studies on wild populations of three species of green leafhoppers *Nephotettix* from Peninsular Malaysia. *Biochemical Genetics*, *32,* 415 - 422.
   - In case of citing an author(s) who has published more than one paper in the same year, the papers should be distinguished by addition of a small letter as shown above, e.g. Jalaludin (1997a); Jalaludin (1997b).
   - Unpublished data and personal communications should not be cited as literature citations, but given in the text in parentheses. 'In press' articles that have been accepted for publication may be cited in References. Include in the citation the journal in which the 'in press' article will appear and the publication date, if a date is available.

7. **Examples of other reference citations**:
   Monographs: Turner, H.N. and Yong, S.S.Y. (2006). *Quantitative Genetics in Sheep Breeding*. Ithaca: Cornell University Press.

   Chapter in Book: Kanwal, N.D.S. (1992). Role of plantation crops in Papua New Guinea economy. In Angela R. McLean (Eds.), *Introduction of livestock in the Enga province PNG* (p. 221-250). United Kingdom: Oxford Press.

   Proceedings: Kanwal, N.D.S. (2001). Assessing the visual impact of degraded land management with landscape design software. In N.D.S. Kanwal and P. Lecoustre (Eds.), *International forum for Urban Landscape Technologies* (p. 117-127). Lullier, Geneva, Switzerland: CIRAD Press.

8. **Short Communications** should include **Introduction, Materials and Methods, Results and Discussion, Conclusions** in this order. Headings should only be inserted for Materials and Methods. The abstract should be up to 100 words, as stated above. Short Communications must be 5 printed pages or less, including all references, figures and tables. References should be less than 30. A 5 page paper is usually approximately 3000 words plus four figures or tables (if each figure or table is less than 1/4 page).

   *Authors should state the total number of words (including the Abstract) in the cover letter. Manuscripts that do not fulfill these criteria will be rejected as Short Communications without review.

STYLE OF THE MANUSCRIPT

Manuscripts should follow the style of the latest version of the Publication Manual of the American Psychological Association (APA). The journal uses British spelling and authors should therefore follow the latest edition of the Oxford Advanced Learner's Dictionary.

SUBMISSION OF MANUSCRIPTS

All articles submitted to the journal **must comply** with these instructions. Failure to do so will result in return of the manuscript and possible delay in publication.

The **four copies** of your original manuscript, four sets of photographic figures, as well as a CD with the **electronic copy in MS Word** (including text and figures) together with a **cover letter**, **declaration form**, **referral form A**, **scope form** need to be enclosed. They are available from the Pertanika's home page at http://rmc.upm.edu.my/pertanika or from the Executive Editor's office upon request.

Please do **not** submit manuscripts directly to the editor-in-chief or to the UPM Press. All manuscripts must be **submitted through the executive editor's office** to be properly acknowledged and rapidly processed:

Dr. Nayan KANWAL
Executive Editor
Research Management Centre (RMC)

4th Floor, Administration Building
Universiti Putra Malaysia
43400 UPM, Serdang, Selangor, Malaysia
email: ndeeps@admin.upm.edu.my; tel: + 603-8946 6192
fax: + 603 8947 2075

Authors should retain copies of submitted manuscripts and correspondence, as materials can not be returned.

Cover letter

All submissions must be accompanied by a cover letter detailing what you are submitting. Papers are accepted for publication in the journal on the understanding that the article is original and the content has not been published or submitted for publication elsewhere. This must be stated in the cover letter.

The cover letter must also contain an acknowledgement that all authors have contributed significantly, and that all authors are in agreement with the content of the manuscript.

The cover letter of the paper should contain (i) the title; (ii) the full names of the authors; (iii) the addresses of the institutions at which the work was carried out together with (iv) the full postal and email address, plus facsimile and telephone numbers of the author to whom correspondence about the manuscript should be sent. The present address of any author, if different from that where the work was carried out, should be supplied in a footnote.

As articles are double-blind reviewed, material that might identify authorship of the paper should be placed on a cover sheet.

Note When your manuscript is received at Pertanika, it is considered to be in its final form. Therefore, you need to check your manuscript carefully before submitting it to the executive editor (see also **English language editing** below).

Electronic copy

Preparation of manuscripts on a CD or DVD is preferable and articles should be prepared using MS Word. File name(s), the title of your article and authors of the article must be indicated on the CD. The CD must always be accompanied by four hard-copies of the article, and the content of the two must be identical. The CD text must be the same as that of the final refereed, revised manuscript. CDs formatted for IBM PC compatibles are preferred, as those formatted for Apple Macintosh are not acceptable. Please do not send ASCII files, as relevant data may be lost. Leave a blank line between each paragraph and between each entry in the list of bibliographic references. Tables should be placed in the same electronic file as the text. Authors should consult a recent issue of the Journal for table layout.

Peer review

In the peer-review process, three referees independently evaluate the scientific quality of the submitted manuscripts. The Journal uses a double-blind peer-review system. Authors are encouraged to indicate in **referral form A** the names of three potential reviewers, but the editors will make the final choice. The editors are not, however, bound by these suggestions.

Manuscripts should be written so that they are intelligible to the professional reader who is not a specialist in the particular field. They should be written in a clear, concise, direct style. Where contributions are judged as acceptable for publication on the basis of content, the Editor or the Publisher reserves the right to modify the typescripts to eliminate ambiguity and repetition and improve communication between author and reader. If extensive alterations are required, the manuscript will be returned to the author for revision.

The editorial review process

What happens to a manuscript once it is submitted to Pertanika? Typically, there are seven steps to the editorial review process:

1. The executive editor and the editorial board examine the paper to determine whether it is appropriate for the journal and should be reviewed. If not appropriate, the manuscript is rejected outright and the author is informed.
2. The executive editor sends the article-identifying information having been removed, to three reviewers. Typically, one of these is from the Journal's editorial board. Others are specialists in the subject matter represented by the article. The executive editor asks them to complete the review in three weeks and encloses two forms: (a) referral form B and (b) reviewer's comment form along with reviewer's guidelines. Comments to authors are about the appropriateness and adequacy of the theoretical or conceptual framework, literature review, method, results and discussion, and conclusions. Reviewers often include suggestions for strengthening of the manuscript. Comments to the editor are in the nature of the significance of the work and its potential contribution to the literature.
3. The executive editor, in consultation with the editor-in-chief, examines the reviews and decides whether to reject the manuscript, invite the author(s) to revise and resubmit the manuscript, or seek additional reviews. Final acceptance or rejection rests with the Editorial Board, who reserves the right to refuse any material for publication. In rare instances, the manuscript is accepted with almost no revision. Almost without exception, reviewers' comments (to the author) are forwarded to the author. If a revision is indicated, the editor provides guidelines for attending to the reviewers' suggestions and perhaps additional advice about revising the manuscript.
4. The authors decide whether and how to address the reviewers' comments and criticisms and the editor's concerns. The authors submit a revised version of the paper to the executive editor along with specific information describing how they have answered' the concerns of the reviewers and the editor.
5. The executive editor sends the revised paper out for review. Typically, at least one of the original reviewers will be asked to examine the article.
6. When the reviewers have completed their work, the executive editor in consultation with the editorial board and the editor-in-chief examine their comments and decide whether the paper is ready to be published, needs another round of revisions, or should be rejected.
7. If the decision is to accept, the paper is sent to that Press and the article should appear in print in approximately two to three months. The Publisher ensures that the paper adheres to the correct style (in-text citations, the reference list, and tables are typical areas of concern, clarity, and grammar). The authors are asked to respond to any queries by the Publisher. Following these corrections, page proofs are mailed to the corresponding authors for their final approval. At this point, only essential changes are accepted. Finally, the article appears in the pages of the Journal and is posted on-line.

English language editing
Authors are responsible for the linguistic accuracy of their manuscripts. Authors not fully conversant with the English language should seek advice from subject specialists with a sound knowledge of English. The cost will be borne by the author, and a copy of the certificate issued by the service should be attached to the cover letter.

Author material archive policy
Authors who require the return of any submitted material that is rejected for publication in the journal should indicate on the cover letter. If no indication is given, that author's material should be returned, the Editorial Office will dispose of all hardcopy and electronic material.

Copyright
Authors publishing the Journal will be asked to sign a declaration form. In signing the form, it is assumed that authors have obtained permission to use any copyrighted or previously published material. All authors must read and agree to the conditions outlined in the form, and must sign the form or agree that the corresponding author can sign on their behalf. Articles cannot be published until a signed form has been received.

Lag time
The elapsed time from submission to publication for the articles averages 5-6 months. A decision of acceptance of a manuscript is reached in 2 to 3 months (average 9 weeks).

Back issues
Single issues from current and recent volumes are available at the current single issue price from UPM Press. Earlier issues may also be obtained from UPM Press at a special discounted price. Please contact UPM Press at penerbit@putra.upm.edu.my or you may write for further details at the following address:

UPM Press
Universiti Putra Malaysia
43400 UPM, Serdang
Selangor Darul Ehsan
Malaysia.

Pertanika

Our goal is to bring high quality research to the widest possible audience

Pertanika is Indexed in Scopus & EBSCO

Pertanika is an international peer-reviewed leading journal in Malaysia which began publication in 1978. The journal publishes in three different areas — Journal of Tropical Agricultural Science (JTAS); Journal of Science and Technology (JST); and Journal of Social Sciences and Humanities (JSSH).

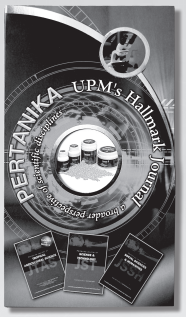

JTAS is devoted to the publication of original papers that serves as a forum for practical approaches to improving quality in issues pertaining to tropical agricultural research or related fields of study. It is published twice a year in **February** and **August**.

JST caters for science and engineering research or related fields of study. It is published twice a year in **January** and **July**.

JSSH deals in research or theories in social sciences and humanities research with a focus on emerging issues pertaining to the social and behavioural sciences as well as the humanities, particularly in the Asia Pacific region. It is published twice a year in **March** and **September**.

Why should you publish in Pertanika Journals?

Benefits to Authors

PROFILE: our journals are circulated in large numbers all over Malaysia, and beyond, in Southeast Asia. Recently, we have widened our circulation to other overseas countries as well. We will ensure that your work reaches the widest possible audience in print and online, through our wide publicity campaigns held frequently, and through our constantly developing electronic initiatives through e-pertanika and Pertanika Online.

QUALITY: Our double-blind peer refereeing procedures are fair and open, and we aim to help authors develop and improve their work. Pertanika JTAS is now over 30 years old; this accumulated knowledge has resulted in Pertanika JTAS being indexed by Scopus (Elsevier).

AUTHOR SERVICES: we provide a rapid response service to all our authors, with dedicated support staff for each journal, and a point of contact throughout the refereeing and production processes. Our aim is to ensure that the production process is as smooth as possible, is borne out by the high number of authors who publish with us again and again.

LAG TIME & REJECTION RATE: the elapsed time from submission to publication for the articles in Pertanika averages 6-8 months. A decision of acceptance of a manuscript is reached in 1 to 3 months (average 7 weeks).

Our journals have a 30% rejection rate of its submitted manuscripts, many of the papers fail on account of their substandard presentation and language (frustrating the peer reviewers).

Call for Papers

Pertanika invites you to explore frontiers from all fields of science and technology to social sciences and humanities. You may contribute your scientific work for publishing in UPM's hallmark journals either as a ***regular article***, ***short communications***, or a ***review article*** in our forthcoming issues. Papers submitted to this journal must contain original results and must not be submitted elsewhere while being evaluated for the Pertanika Journals.

Submissions in English should be accompanied by an abstract not exceeding 300 words. Your manuscript should be no more than 6,000 words or 10-12 printed pages, including notes and abstract. Submissions should conform to the Pertanika style, which is available at www.rmc.upm.edu.my/pertanika or by mail or email upon request.

Papers should be double-spaced 12 point type (Times New Roman fonts preferred). The first page should include the title of the article but no author information. Page 2 should repeat the title of the article together with the names and contact information of the corresponding author as well as all the other authors. Page 3 should contain the abstract only. Page 4 and subsequent pages to have the text - Acknowledgments - References - Tables - Legends to figures – Figures, etc.

Questions regarding submissions should only be directed to the Executive Editor, Pertanika Journals.

Remember, ***Pertanika is the resource to support you in strengthening research and research management capacity***.

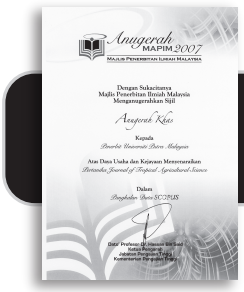

An Award Winning International-Malaysian Journal

FEB. 2008

Mail your submissions to:

The Executive Editor
Pertanika Journals
Research Management Centre (RMC)
Publication Division
4th Floor, Administration Building
Universiti Putra Malaysia
43400 UPM, Serdang, Selangor, Malaysia

Tel: +603-8946 6192
ndeeps@admin.upm.edu.my
www.rmc.upm.edu.my/pertanika

Pertanika Journal of Science & Technology
Vol. 17 (2) Jul. 2009

Contents

Research Management Centre (RMC)
4th Floor, Administration Building
Universiti Putra Malaysia
43400 UPM Serdang
Selangor Darul Ehsan
Malaysia

http://www.rmc.upm.edu.my
E-mail : pertanika@rmc.upm.edu.my
Tel : +603 8946 6185/ 6192
Fax : +603 8947 2075

UPM Press
Universiti Putra Malaysia
43400 UPM Serdang
Selangor Darul Ehsan
Malaysia

http://penerbit.upm.edu.my
E-mail : penerbit@putra.upm.edu.my
Tel : +603 8946 8855/8854
Fax : +603 8941 6172

ISSN 0128-7680
07
9 770128 768083